Analysis of the charge collection process in solid state X–ray detectors

DISSERTATION
zur Erlangung des Grades eines Doktors
der Naturwissenschaften

vorgelegt von
Dipl.-Phys. Nils Kimmel
geb. am 5 April 1976 in Castrop-Rauxel

eingereicht beim Fachbereich Physik
der Universität Siegen
Siegen, 2008

Tag der mündlichen Prüfung: 12.02.2009

Erster Gutachter:	Prof. Dr. Lothar Strüder	(Arbeitsgruppe Detektorphysik und Elektronik)
Zweiter Gutachter:	Prof. Dr. Ullrich Pietsch	(Arbeitsgruppe Festkörperphysik)

Kurzfassung

Physik mit Röntgenstrahlen befasst sich sowohl mit grosskaligen Strukturen in der Röntgenastronomie, als auch mit kleinskaligen Phänomenen bei Strukturanalysen mit Synchrotronstrahlung. In beiden der genannten Bereiche werden bildgebende Sensoren benötigt, die zusätzlich als Spektrometer im Energiebereich von 0.1 keV bis 20.0 keV arbeiten. Ursprünglich wurden pnCCDs am Halbleiterlabor der Max–Planck–Institute für Physik und extraterrestrische Physik entwickelt, um ein bildgebendes Spektrometer für die Röntgenastronomiemission XMM–Newton der ESA bereitzustellen. Das pnCCD ist ein Detektor mit Pixelstruktur, der vom Infraroten über optische und UV–Strahlung bis hin zu Röntgenstrahlung empfindlich ist.

Diese Arbeit beschreibt die Bewegung von Signalelektronen vom Zeitpunkt ihrer Erzeugung bis zur Sammlung in den Speicherzellen der Pixelstruktur. Zur experimentellen Untersuchung von pnCCDs wurde ein Lochraster eingesetzt, das deren Oberfläche mit hoher räumlicher Auflösung abtastet. Mit Hilfe von numerischen Bauelementesimulationen stand ein Werkzeug zur Modellierung der elektrischen Bedingungen in pnCCDs zur Verfügung.

Durch die Kombination der durchgeführten Experimente und Simulationen konnte ein Modell für die Signalladungsdynamik im Energiebereich von 0.7 keV bis 5.5 keV erstellt werden. Im allgemeineren Sinne hat die vorliegende Arbeit mittels eines physikalisches Modells das Verständnis von pnCCDs erweitert. Die dazu entwickelten experimentellen und theoretischen Methoden können auf jeden Detektor angewendet werden, der auf einem vollständig verarmten Halbleitersubstrat aufbaut.

Abstract

Physics with X–rays spans from observing large scales in X–ray astronomy down to small scales in material structure analyses with synchrotron radiation. Both fields of research require imaging detectors featuring spectroscopic resolution for X–rays in an energy range of 0.1 keV to 20.0 keV. Originally driven by the need for an imaging spectrometer on ESA's X–ray astronomy satellite mission XMM-Newton, X–ray pnCCDs were developed at the semiconductor laboratory of the Max–Planck–Institute. The pnCCD is a pixel array detector made of silicon. It is sensitive over a wide band from near infrared– over optical– and UV–radiation up to X–rays.

This thesis describes the dynamics of signal electrons from the moment after their generation until their collection in the potential minima of the pixel structure. Experimentally, a pinhole array was used to scan the pnCCD surface with high spatial resolution. Numerical simulations were used as a tool for the modeling of the electrical conditions inside the pnCCD. The results predicted by the simulations were compared with the measurements.

Both, experiment and simulation, helped to establish a model for the signal charge dynamics in the energy range from 0.7 keV to 5.5 keV. More generally, the presented work has enhanced the understanding of the detector system on the basis of a physical model. The developed experimental and theoretical methods can be applied to any type of array detector which is based on the full depletion of a semiconductor substrate material.

Contents

Overview **1**

1 Introduction **3**
1.1 Motivation . . . 3
1.2 Basic semiconductor structures . . . 4
1.2.1 The pn-junction . . . 5
1.2.2 The MOS–capacitor . . . 7
1.3 X–ray photon detection in silicon . . . 14
1.4 Charge storage and shift in three phase CCDs . . . 16
1.5 pnCCD . . . 19
1.5.1 Full depletion of the detector volume . . . 19
1.5.2 Charge collection, storage and measurement in pnCCDs . . . 21
1.5.3 Readout electronics . . . 24
1.5.4 Applications for X–ray pnCCDs . . . 26

2 pnCCD in detail **31**
2.1 The pixel array of a pnCCD . . . 31
2.1.1 Structure and electric definition of a pixel . . . 31
2.1.2 The readout structure of a channel . . . 35
2.2 Electric potential in the bulk . . . 36
2.2.1 Drift and diffusion of electric charge . . . 38

3 The mesh experiment **45**
3.1 Function principle . . . 45
3.1.1 Energy range and spatial resolution . . . 47
3.2 Analysis of mesh measurement data . . . 49
3.2.1 Determination of the mesh geometry . . . 50
3.2.2 Reconstruction of the virtual pixel map . . . 55

4 Measurements **61**
4.1 Setup for the used pnCCDs . . . 61
4.1.1 The Rösti facility . . . 61
4.1.2 pnCCDs used for measurements . . . 63

4.1.3 mesh assembly . . . 64
4.2 Measurement program . . . 67
4.2.1 Back side illumination . . . 68
4.2.2 Front side illumination . . . 70
4.3 Standard analysis and calibration of data . . . 72
4.3.1 Noise and offset calibration . . . 73
4.3.2 Photon event detection . . . 75
4.3.3 Gain calibration and CTE correction . . . 76
4.3.4 Analysis output . . . 78

5 'Mesh' data analysis 81
5.1 Types of reconstructed pixel maps . . . 81
5.1.1 Event type maps . . . 82
5.1.2 Photon response maps . . . 85
5.2 Precision of the generated maps . . . 89
5.2.1 Geometrical mesh parameters . . . 89
5.2.2 Error function model of the charge collection function . . . 91
5.3 Analysis of the pixel response . . . 93
5.3.1 Location of event types . . . 94
5.3.2 Photon flux . . . 101
5.3.3 Charge collection . . . 108

6 Device simulations 115
6.1 Simulations of a pnCCD with 75 µm pixels . . . 118
6.1.1 Charge transfer direction . . . 119
6.1.2 Line direction . . . 122
6.2 Simulations of charge drift and diffusion . . . 124
6.2.1 Simulation principle . . . 124
6.2.2 Electron drift in the bulk . . . 128
6.2.3 Numeric simulations of the charge cloud expansion . . . 133

7 Comparison of device simulations and analysis results 137
7.1 Evaluation of ccf simulations . . . 137
7.1.1 75 µm pixel pnCCD . . . 138
7.1.2 51 µm pixel pnCCD . . . 139
7.1.3 Reconstruction of the photon conversion position . . . 144
7.2 Separation process of a charge cloud . . . 149
7.3 Photon absorption in the front-side structure . . . 152
7.3.1 Electric potential at the front side . . . 153
7.3.2 Best fit parameters for the absorption model . . . 159

Conclusion 163

List of figures i

Literature v

Overview

Physics with X–rays spans from observing large scales in X–ray astronomy down to small scales in material structure analyses with synchrotron radiation. Both fields of research require imaging detectors featuring spectroscopic resolution for X–rays in an energy range of 0.1 keV to 20.0 keV. Originally driven by the need for an imaging spectrometer on ESA's X–ray astronomy satellite mission XMM-Newton, X–ray pnCCDs were developed at the semiconductor laboratory of the Max–Planck–Institute (MPI-HLL). The pnCCD is a pixel array detector made of silicon. It is sensitive over a wide band from near infrared– over optical– and UV–radiation up to X–rays.

This thesis describes the dynamics of signal electrons from the moment after their generation until their collection in the potential minima of the pixel structure. Experimentally, a pinhole array was used to scan the pnCCD surface with high spatial resolution. Numerical simulations were used as a tool for the modeling of the electrical conditions inside the pnCCD. The results predicted by the simulations were compared with the measurements.

Both, experiment and simulation, helped to establish a model for the signal charge dynamics in the energy range from 0.7 keV to 5.5 keV. The benefits from this analysis approach are:

- Improvement of the spatial resolution of the detector. The conversion position of X–ray photons can be reconstructed from signal charge measurements. The accuracy of the reconstruction is only limited by the precision of a charge measurement.
- Better design capabilities for the definition of future pixel geometries. Pixel sizes can now be adjusted for the optimum ratio of the spatial resolution to the spectral resolution of the detector.
- Identification of insensitive regions in the detector volume. Insensitive regions with a volume as low as 0.2% of the total sensitive detector volume can be detected.

More generally, the presented work has enhanced the understanding of the detector system on the basis of a physical model. The developed experimental and theoretical methods can be applied to any type of array detector which is based on the full depletion of a semiconductor substrate material.

Chapter 1

Introduction

1.1 Motivation

The pnCCD is a semiconductor array detector which was developed for the detection of X–rays in the energy range from 0.1 keV to 20 keV [1]. It serves both as a spectrometer with a typical energy resolution of 140 eV at an energy of 5.9 keV and as an imaging array with pixel sizes from 36 µm to 150 µm.

Due to the photo effect, X–ray photons which are absorbed in silicon create an amount of electron hole pairs which is proportional to the photon energy. In short, the function principle of a pnCCD is to collect and measure the number of generated signal electrons in a pixel array. The amount of electrons in each pixel is determined by moving them pixel by pixel until they reach the readout node where a charge measurement is done. This way, the contents of each pixel are finally known as voltage values which are proportional to the number of signal electrons.

A pnCCD is sensitive over the complete thickness of its silicon substrate which ranges from 0.3 mm to 0.5 mm depending on the device. Charge storage and shift takes place close to the front side which carries the electrical contact structure of the pixel array. X–ray photons with an energy below 0.5 keV have a small penetration depth in silicon. In order to facilitate the detection of X–ray photons down to 0.1 keV, pnCCDs are illuminated from the back side which has a thin homogeneous entrance window. As a result, signal electrons are created close to the back side and drift over a distance of up to nearly the complete detector thickness before they reach the front side with the pixel structure.

Charge collection in a pnCCD begins with the separation of the initial electron hole cloud. Signal electrons drift along the gradient of the electric potential in the pnCCD. A signal electron cloud expands during the drift time before it is captured in the local potential minimum of a pixel. The drift speed and the speed of expansion of a signal charge cloud therefore determine the final charge distribution over the pixel array.

Due to its expansion during the drift time, a signal electron cloud may be split over up to four neighboring pixels of the array, causing so called ‘split events’. The amount of charge collected in neighboring pixels is primarily a function of the photon conversion

position and, to a lesser extend, a function of the photon energy.

In a X–ray imaging application of a pnCCD, the charge distribution in split events can be used to reconstruct the conversion position of X–ray photons. In this case and if the photons are vertically incident on the detector, the position resolution can be improved to a value below the size of a pixel. Therefore it is essential to determine the charge distribution in split events as a function of the photon conversion position.

A measurement with flat field illumination of the device delivers only imprecise information on the exact way the signal charge is collected in the pixel array. In order to get the signal charge distribution as a function of the X–ray photon conversion position, a measurement is required where the conversion positions of all detected photons are known. Scanning over a pixel with a narrow X–ray beam of a defined energy is the most direct way. This measurement has to be done at low X–ray intensities such that only one photon is detected in each readout cycle. The resulting measurement time is very long.

A much faster method was invented by H. Tsunemi et. al. and called the 'mesh method' [2]. They placed an opaque metal foil with a regular grid of holes over a CCD. This way, a virtual pixel scan which performs all scanning steps in parallel is performed. In order to relocate the hole positions relative to the pixel structure and to reconstruct the image of a scanned pixel, a matching analysis method was developed.

A different access to determine the charge distribution in split events is possible by creating a set of device simulations. The simulations are calculated for a set of separate photon conversion positions in the pixels of a pnCCD. Each simulation delivers the result of the final distribution of the signal electron cloud over neighboring pixels.

Both the mesh method and numerical device simulations of charge collection have been applied to device analyses in this thesis. The mesh method was adapted to the existing test facility in the MPI semiconductor laboratory. A new and extended mesh data analysis and pixel image reconstruction method was also developed. Device simulations were set up based on the design data of the pnCCDs used for the mesh measurements. The distribution of signal charge over neighboring pixels was determined for all possible photon conversion positions relative to the middle of a pixel. The simulations were evaluated by comparing them with the corresponding measurement results. This evaluation resulted in a detailed understanding of the electric potential values in a pnCCD and their influence on the signal charge collection process.

1.2 Basic semiconductor structures

The two main building blocks of pnCCDs are the pn–junction and the MOS–structure or 'MOS–capacitor'. In the following, these structures are discussed with an emphasis on the role they play in the functional principle of pnCCDs.

1.2.1 The pn-junction

One can think of a pn-junction as two contacting blocks of semiconductor material, one n-doped with positive space charges and electrons as majority carriers, one p-doped with negative space charges and holes as majority carriers. It is clear that in reality, the junction from p–type to n–type semiconductor is continuous, but for a basic understanding one can assume an abrupt junction. The following description is summarized from [3, 4, 5].

In the thermal equilibrium state, a region around the pn–junction is free of mobile electrons and holes. The existence of this region which is called the 'depletion region' can be motivated as follows: When the p– and the n–region are brought in contact, holes start to diffuse into the n–region and electrons start to diffuse into the p–region. At the junction of the p– and the n–region, the electrons and holes mix and neutralize each other. The space charges in the junction are therefore no longer screened and create an electric field. This electric field points from the n–region to the p–region. Thus, it moves electrons into the n–region and holes into the p–region and the junction region is depleted of free electrons and holes, see figure 1.1.

Due to the electron and hole concentration gradient at the borders of the depletion region, a diffusion current is induced which counteracts the depletion of the pn–junction by the drift current. The diffusion current moves electrons from the n–doped region and holes from the p–doped region back into the depleted junction region. The equilibrium condition is satisfied if the drift current which drives electrons and holes out of the junction is balanced by the diffusion current which has the opposite effect.

Integrating the electric field in the pn–junction yields a potential difference, the built in voltage V_{bi}. In the energy band model of a pn–junction, the potential difference is the difference of the Fermi levels in the p– and n–doped regions as shown in figure 1.1. In thermal equilibrium, no electric current flows through the pn–junction. Thus, the Fermi level must be constant in all regions of the structure. In order to achieve a constant Fermi level in the pn–junction, the electric potential difference of the p– and n–regions adjusts to the difference of the Fermi levels in the separated p– and n– regions. According to [3], V_{bi} is:

$$V_{\mathrm{bi}} = \frac{kT}{\mathrm{e}} \ln\left(\frac{N_{\mathrm{A}} N_{\mathrm{D}}}{n_{\mathrm{i}}^2}\right) \tag{1.1}$$

k is the Boltzmann constant, T is the temperature, e is the unit charge, n_{i} is the intrinsic carrier concentration, N_{A} is the concentration of acceptors in the p–region and N_{D} is the concentration of donors in the n–region. V_{bi} can be seen as a negative voltage of the p–region relative to the n–region. The width w_{d} of the depletion region is:

$$w_{\mathrm{d}} = w_{\mathrm{n}} + w_{\mathrm{p}} = \sqrt{\frac{-2\epsilon\epsilon_0 (V_{\mathrm{bi}} + V)}{\mathrm{e} \cdot (N_{\mathrm{A}} + N_{\mathrm{D}})}} \cdot \left[\sqrt{\frac{N_{\mathrm{A}}}{N_{\mathrm{D}}}} + \sqrt{\frac{N_{\mathrm{D}}}{N_{\mathrm{A}}}}\right] \tag{1.2}$$

where V_{bi} is measured in the p–region relative to the n–region and thus has a negative value. V is an external voltage applied to the p–region so that the effective voltage relative to the n–region is $V_{\mathrm{bi}} + V$. The parameter ϵ is the dielectric constant of the material, ϵ_0 is

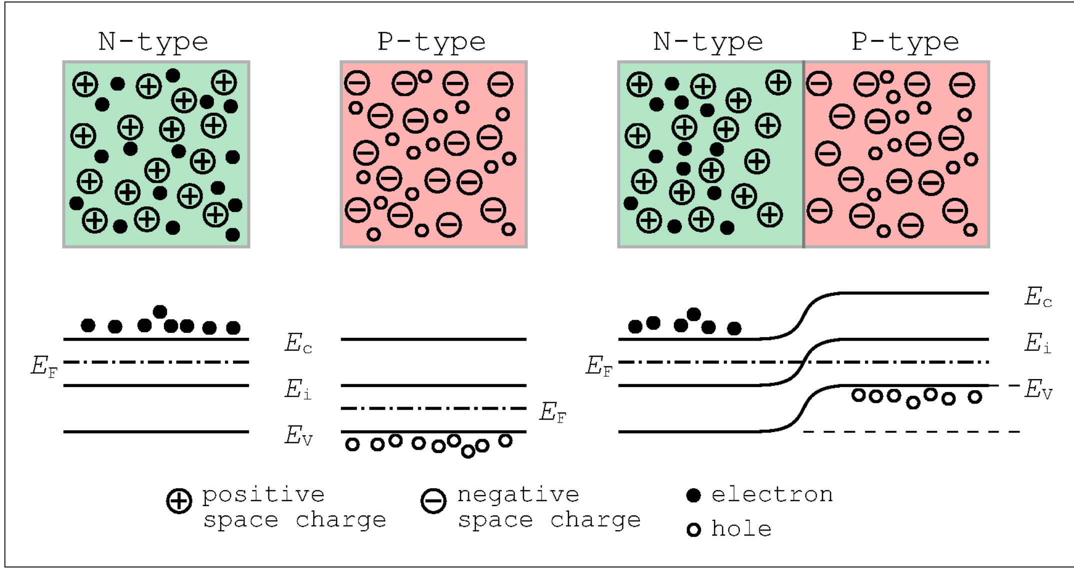

Figure 1.1: *Drawing of a pn-junction adapted from [3] and [4]. All energy levels refer to the potential energy of electrons. E_C and E_V are the energy levels of the conduction and the valence band. E_i is the intrinsic energy level, i.e. the Fermi level in silicon which is neither n– nor p–doped. E_F is the actual Fermi level which is above E_i for n–doped silicon and below E_i for p–doped silicon. In the case of thermal equilibrium when no external voltage is applied, the Fermi level E_F must be the same value in the whole junction region. The result is the voltage difference V_{bi} which builds up between the n– and the p–doped regions.*

the dielectric constant in vacuum, w_n is the depleted width in the n-region and w_p is the depleted width in the p-region.

If a negative voltage V is applied to the p-contact with respect to the n-contact, the width w_d increases. With appropriately low dopant concentrations, large regions of the pn-junction can be depleted. In the asymmetrical case $N_A \gg N_D$, the width w_n is much larger than w_p. In the pnCCD, p–contacts with a high dopant concentration are implanted on a weakly n–doped substrate to deplete the full width of the substrate.

Typical values for the dopant concentrations and thicknesses of the p– and n–doped regions in a pnCCD are $N_A = 10^{18}$ cm^{-3} and $d_p = 0.5$ µm for the p–region and $N_D = 10^{12}$ cm^{-3} and $d_n = 450$ µm for the n–region. The built in voltage in this case is $V_{bi} = -0.55$ V and the depletion depth without an external voltage is $w_p = 2.7 \cdot 10^{-5}$ µm in the p–region and $w_n = 27$ µm in the n–region. Applying a voltage of -156 V at the p–contact and 0 V at the n–contact depletes the whole n–region with a width of 450 µm while the depletion depth in the p–region is just $4.5 \cdot 10^{-4}$ µm.

1.2.1.1 The rectifying property of a pn–junction

A pn-junction only acts as a conductor if a positive voltage is applied to the p–contact. If a negative voltage is applied to the p–contact, the current flowing through the junction is practically zero. This rectifying property can be explained with the amount of electrons and holes that recombine in the depletion region.

If a positive voltage is applied to the p-contact with respect to the n-contact, the voltage sum $V_{\mathrm{bi}} + V$ approaches zero and w_{d} shrinks. If w_{d} is small enough, electrons from the n–doped region can recombine with holes from the p–doped region. The recombination rate and therefore also the current through the junction both depend exponentially on the voltage at the p–contact.

If a negative voltage is applied to the p–contact, the width of the depletion region increases and only a very small current, called the 'reverse bias current', flows through the junction. The processes that contribute to the reverse bias current are shown in figure 1.2. One source of this current are holes which are the minority charge carriers in the n–doped region and electrons which are the minority carriers in the p–doped region. The minority charge carrier concentration is given by $p_{\mathrm{n}} \approx n_{\mathrm{i}}^2/N_{\mathrm{D}}$ for holes in the n–region and $n_{\mathrm{p}} \approx n_{\mathrm{i}}^2/N_{\mathrm{A}}$ for electrons in the p–region. As soon as these holes and electrons reach the border of the depletion region, they see the electric field inside the depletion region and drift to the p–doped side (holes) and to the n–doped side (electrons).

Another source of the reverse bias current are electrons and holes which are generated inside the depletion region. These electrons and holes are emitted at impurities and defects in the crystal structure of silicon [3]. Impurities and crystal defects in silicon provide intermediate energy states between the valence and conduction band. The thermal energy of some electrons in the valence band is sufficient to reach these energy states. Electrons that reached the interstitial energy states can be further excited to reach the conduction band. Every electron emitted to the conduction band must leave a free hole in the valence band. Therefore the impurities and defects in the crystal structure which are located inside the depletion region act as centers for thermal emission of electrons and holes.

In the pn–structures employed in pnCCDs, the reverse bias current is dominated by the thermally generated electrons and holes which originate from the emission centers in the depletion region. Therefore the reverse bias current strongly depends on the temperature of the pn–junction. Lowering the device temperature by 8 ℃ reduces the reverse bias current by 50 %.

In the MPI–HLL, the leakage current of each produced pnCCD is measured for quality control purposes. A typical value for the reverse bias current measured in a fully depleted pn–structure with 450 µm thickness is $1 \cdot 10^{-9}$ A $\cdot$ cm^{-2} at a temperature of 300 K. A current of $1 \cdot 10^{-9}$ A $\cdot$ cm^{-2} is the equivalent of $6.24 \cdot 10^9$ electrons per second and cm^2.

1.2.2 The MOS–capacitor

A MOS-capacitor is a structure composed of a metal layer and an insulator (oxide) layer on semiconductor material substrate. MOS capacitors are the fundamental structures of

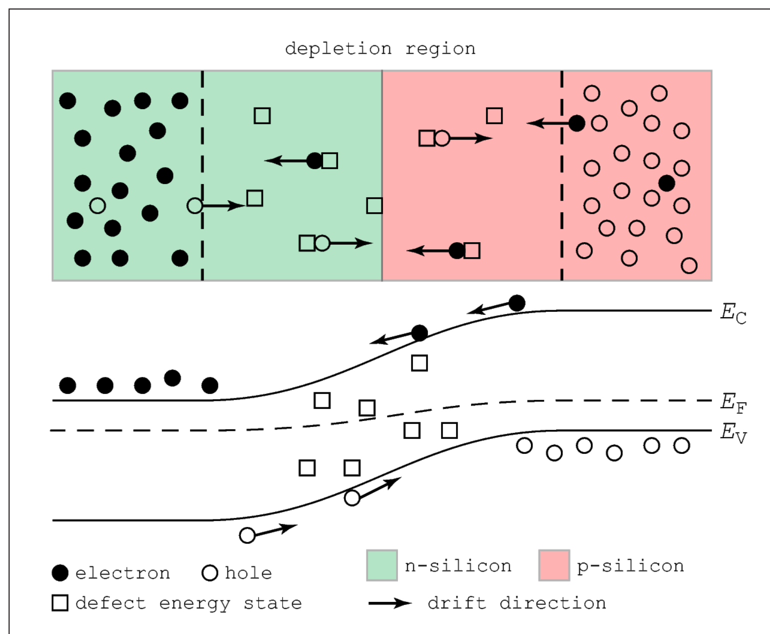

Figure 1.2: *Negatively biased pn–junction. Due to the negative p–contact voltage, the Fermi–level differs in the p– and n–doped regions and a current flows if free charge carriers enter the depletion region. Although the hole concentration in the n–doped region is very small, some holes reach the border of the depletion region by diffusion and start to drift to the p–doped side. The same process affects the small concentration of electrons in the p–doped region.*
The major part of the leakage current is caused by electrons and holes which are thermally emitted by crystal defects in the depletion zone. These defects provide energy states between the valence and the conduction band. Some electrons from the valence band have enough thermal energy to reach these defect energy states. If an electron is thermally excited to a defect energy state close to the conduction band, it can reach the conduction band by further excitation and drift to the n–doped region. Every electron that reaches the conduction band by thermal emission leaves a free hole in the valence band. Free holes which are emitted in the depletion region drift to the p–doped region. Cooling the pn–junction reduces the leakage current caused by thermally emitted electrons and holes.

MOS-CCDs but also a component of pnCCDs. The most common choice of materials is aluminum for the metal, silicon oxide for the insulator and silicon for the semiconductor. The semiconductor substrate is doped to be of either n– or p–type.

The following discussion is based on [3, 4, 5]. For the further understanding it is sufficient to discuss a structure consisting of aluminum, silicon oxide and n–doped silicon as shown in figure 1.3.

In the neutral state, the electric field in the oxide layer and the silicon is zero and the energy levels in the band diagram are flat, see the left part of figure 1.3. In order to achieve the neutral state, a voltage which is different from zero must be present between the metal

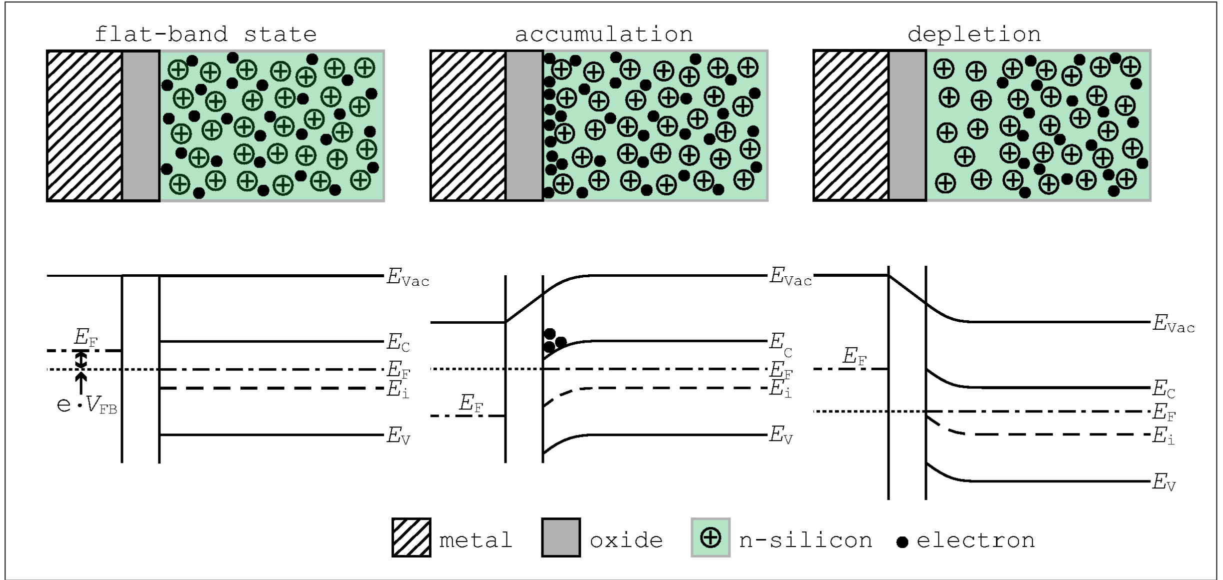

Figure 1.3: *Drawing of a MOS–capacitor on n–doped silicon adapted from [3] and [5]. In the flat–band state, no electric field is present. In the case of accumulation, the electron density directly at the silicon–oxide interface is much higher than in the bulk. If the MOS–capacitor is in depletion, the electron density up to the depth d_{depl} from the silicon–oxide interface is negligible compared to the rest of the bulk.*

E_{V} is the energy level of the valence band, E_{i} is the intrinsic Fermi level of undoped silicon, E_{F} is the Fermi level in the n–doped bulk material or metal and E_{C} is the energy level of the conduction band. Curved or sloped parts of the valence– or conduction band energy levels show the changes of the (electric) potential energy for electrons in silicon. Free electrons move to the region where they have the lowest potential energy.

and the silicon region. Since the neutral state is characterized by the flatness of the energy levels in the band diagram, this voltage difference is called the flat–band voltage V_{FB}.

The energy difference $-\mathrm{e} \cdot V_{\mathrm{FB}} = -\mathrm{e} \cdot \Phi_{\mathrm{m}} + \mathrm{e} \cdot \Phi_{\mathrm{Si}}$ is the difference of the electron work functions of a metal ($-\mathrm{e} \cdot \Phi_{\mathrm{m}}$) and n–type silicon ($-\mathrm{e} \cdot \Phi_{\mathrm{Si}}$). The electron work function $-\mathrm{e} \cdot \Phi$ is the amount of energy needed to move an electron from the Fermi level to the vacuum level just outside of a material.

For aluminum and weakly n–doped silicon, the electron work function difference $-\mathrm{e} \cdot V_{\mathrm{FB}}$ is 0.5 eV and the corresponding flat–band voltage is $V_{\mathrm{FB}} = -0.5$ V. In order to realize the flat–band state in the discussed structure, the flat–band voltage of -0.5 V must be applied to the aluminum contact while the silicon substrate is at 0 V.

If a voltage more positive than V_{FB} is applied to the aluminum contact with respect to the silicon, an electric field builds up in the oxide layer and in the silicon substrate near the oxide–silicon interface. The direction of the field points from the aluminum contact to the silicon substrate. Free electrons in the silicon are attracted to the oxide–silicon interface at $x = 0$ where they have the lowest potential energy, as shown in the middle section of figure

1.3. A thin layer with a strongly increased electron density builds up at the silicon–oxide interface. In this case, the MOS–structure is in the state of accumulation. The amount of charge in the electron layer is defined as the surface charge density $Q(x = 0)$ or $Q(0)$ at the silicon–oxide interface.

We are interested in the surface charge density and the electric potential at the silicon–oxide interface as a function of the aluminum contact voltage V_{Al}. With these values, the capacitance of the structure and the sheet resistance of the electron accumulation layer can be calculated. The capacitance of the MOS–structure is given by the series connection of the oxide capacitance and the silicon capacitance: $C_{\mathrm{MOS}} = (1/C_{\mathrm{ox}} + 1/C_{\mathrm{Si}})^{-1}$. The sheet resistance of the electron accumulation layer is $R_{\mathrm{acc}} = (\mathrm{e} \cdot \mu_{\mathrm{n}} \cdot Q(0))^{-1}$, where e is the elementary charge and μ_{n} is the electron mobility.

The surface charge density $Q(0)$ at the silicon oxide interface can be expressed as a function of the electric potential $\Psi(0)$ at the silicon–oxide interface with respect to the silicon bulk:

$$Q(0) \approx -\sqrt{2\epsilon_{\mathrm{Si}}\epsilon_0 \cdot N_{\mathrm{D}} kT e^{\frac{\mathrm{e}\Psi(0)}{kT}}} \tag{1.3}$$

ϵ_{Si} is the relative permittivity of silicon, ϵ_0 is the vacuum permittivity, N_{D} is the donor concentration in the n–type silicon bulk, k is the Boltzmann constant and T is the temperature of the structure. The thickness d_{acc} of the electron layer at the silicon–oxide interface is given by:

$$d_{\mathrm{acc}} \approx \frac{2\epsilon_{\mathrm{Si}}\epsilon_0 \cdot kT}{\mathrm{e}Q(0)} \tag{1.4}$$

The value of $\Psi(0)$ can be expressed as a function of the voltage drop V_{ox} across the oxide layer:

$$\Psi(0) = \frac{kT}{\mathrm{e}} \cdot \ln\left(\frac{V_{\mathrm{ox}}^2 C_{\mathrm{ox}}^2}{2\epsilon_{\mathrm{Si}}\epsilon_0 N_{\mathrm{D}} kT}\right) \tag{1.5}$$

C_{ox} is the capacitance per unit area of the oxide layer.

The voltage V_{Al} at the aluminum contact is measured with reference to the silicon bulk. It is the sum of the voltage drop V_{ox} across the oxide, the electric potential $\Psi(0)$ at the silicon–oxide interface and the flat–band voltage V_{FB}:

$$V_{\mathrm{Al}} = V_{\mathrm{ox}} + \Psi(0) + V_{\mathrm{FB}} \tag{1.6}$$

A MOS–structure with a flat–band voltage of −0.5 V is in accumulation if the aluminum contact voltage V_{Al} is larger than $V_{\mathrm{FB}} = -0.5$ V. With the equations 1.3 and 1.5, we can calculate the electric potential and the charge accumulated at the silicon–oxide interface for any given voltage $V_{\mathrm{Al}} > V_{\mathrm{FB}}$ at the aluminum contact.

Figure 1.4 shows the surface charge density, the electron layer thickness and the voltage drops across the oxide layer and the silicon bulk as a function of the aluminum contact voltage V_{Al}. The plotted values are calculated for a temperature of 300 K and for typical values of the oxide capacitance and the bulk donor concentration that occur in a pnCCD: $C_{\mathrm{ox}} = 8 \cdot 10^{-9}\ \mathrm{F} \cdot \mathrm{cm}^{-2}$ and $N_{\mathrm{D}} = 10^{12}\ \mathrm{cm}^{-3}$. In the plot on the left hand side of figure 1.4, one can see that the surface charge density at the silicon–oxide interface is practically

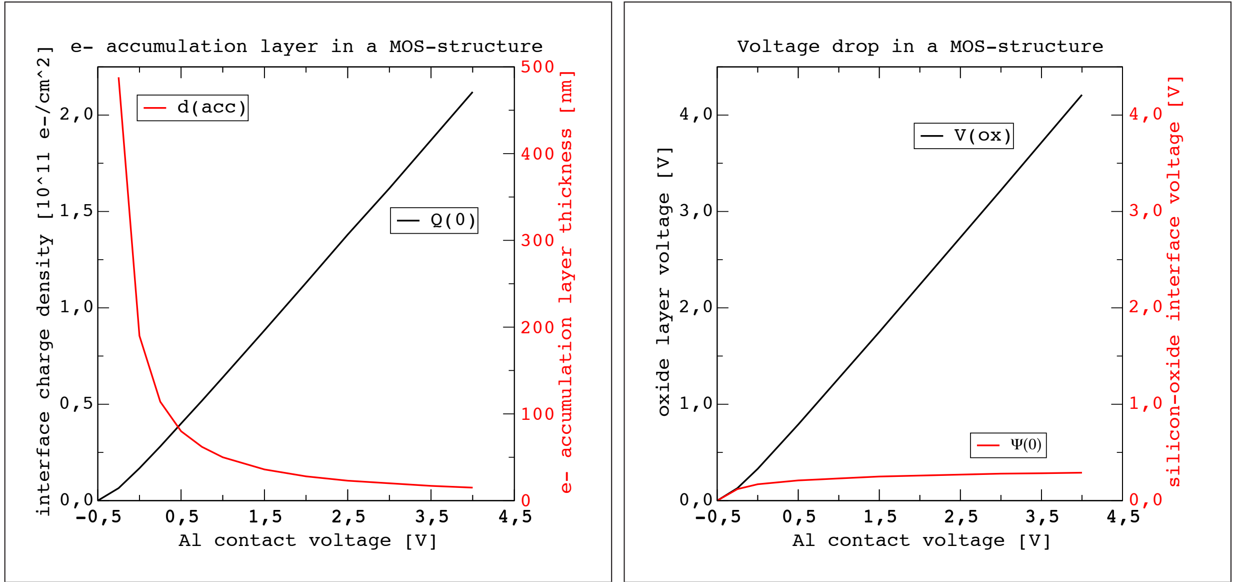

Figure 1.4: *In the left graph, the surface charge density at the silicon–oxide interface and the electron accumulation layer thickness is plotted as a function of the aluminum contact voltage. The right plot shows the drop across the oxide layer and the silicon bulk as a function of the aluminum contact voltage. All values are calculated for a temperature of* 300 K, *a donor concentration of* 10^{12} cm^{-3} *and an oxide capacitance of* $8 \cdot 10$ nF/cm^2. *The flat–band voltage* V_{FB} *is* -0.5 V, *so the structure is in accumulation for aluminum (gate) contact voltages larger than* -0.5 V *relative to the silicon bulk.*

a linear function of the voltage V_{Al} at the aluminum contact while the thickness of the charge layer quickly drops below a value of 100 nm if V_{Al} is increased. The plot on the right hand side shows that for voltages above $V_{\mathrm{Al}} = 0\ V$, raising the value of V_{Al} increases the voltage drop across the oxide layer while the voltage $\Psi(0)$ at the silicon–oxide interface remains nearly constant.

The ratio of the voltage drops over two capacitors connected in series is in inverse ratio to their capacitances. Therefore, the voltages V_{ox} and $\Psi(0)$ give the ratio of the oxide– and silicon capacitance as $C_{\mathrm{ox}}/C_{\mathrm{Si}} = \Psi(0)/V_{\mathrm{ox}}$. In combination with the results shown in figure 1.4 this means that in accumulation and for values of V_{Al} above 0 V, the MOS–structure can be approximated as a capacitor with the capacitance of the oxide layer C_{ox}.

The oxide capacitance per unit area C_{ox} and the oxide voltage V_{ox} give the surface charge density $Q(0)$ as $V_{\mathrm{ox}}/C_{\mathrm{ox}}$. $Q(0)$ determines the sheet resistance at the silicon oxide interface [4]. In the discussed structure with $N_{\mathrm{D}} = 10^{12}$ cm^{-3}, $C_{\mathrm{ox}} = 8 \cdot 10^{-9}$ F $\cdot$ cm^{-2} at a temperature of 300 K, the sheet resistance of the electron layer is $7.2 \cdot 10^4$ Ω/cm^2 at $V_{\mathrm{Al}} = 1$ V and $2.2 \cdot 10^4$ Ω/cm^2 at $V_{\mathrm{Al}} = 4$ V.

If V_{Al} is lower than V_{FB}, the resulting electric field in the MOS–structure points from the silicon substrate to the aluminum contact, see the right hand side of figure 1.3. Electrons near the silicon–oxide interface are pushed into the silicon bulk and the density of free

electrons becomes negligible compared to the rest of the silicon–bulk. Just like in the case of the pn–junction, the zone which is free from electrons is called the 'depletion region'. The depletion region extends from the silicon–oxide interface into the silicon–bulk up to a depth of d_{depl}. The depletion depth d_{depl} is a function of the square root of the voltage V_{Al} at the aluminum contact and of the inverse square root of the donor concentration N_{D}.

Decreasing V_{Al} more and more extends the depletion region until d_{depl} reaches an upper limit d_{max} at the threshold voltage $V_{\mathrm{Al}} = V_{\mathrm{T}}$. In this case, a layer of holes starts to build up at the silicon–oxide interface. The reason for the hole layer is that the negative electric potential $\Psi(0)$ at the silicon oxide interface decreases the energy difference between the valence band and the Fermi–level. Both the electron– and hole concentrations in a semiconductor are exponential functions of the distance from the Fermi level to the conduction band (electrons) and the distance from the valence band to the Fermi level (holes). If the Fermi level is closer to the valence band than to the conduction band, the density of holes is higher than the density of electrons.

If the voltage V_{T} of the aluminum contact is reached, the difference $E_{\mathrm{F}} - E_{\mathrm{V}}$ at the silicon oxide–interface is equal to the difference $E_{\mathrm{C}} - E_{\mathrm{F}}$ in the silicon bulk. Then, the hole density at the interface is equal to the electron density in the silicon bulk.

Any further decrease of V_{Al} results in the creation of more free holes that accumulate at the silicon–oxide interface. The holes compensate the decrease of V_{Al} by charging the oxide capacitance. Thus, both the voltage at the silicon–oxide interface and the depletion depth remain constant with a further decrease of V_{Al}.

In a conventional MOS–CCD, the depletion region is the sensitive detector volume, therefore d_{max} defines the maximum possible sensitive thickness of the silicon substrate. According to [3], d_{max} is given by:

$$d_{\mathrm{max}} = \sqrt{\frac{4\epsilon_{\mathrm{s}}\epsilon_0\Psi_{\mathrm{B}}}{\mathrm{e}N_{\mathrm{D}}}} \tag{1.7}$$

Ψ_{B} is the difference $(E_{\mathrm{F}} - E_{\mathrm{i}})/\mathrm{e}$ between the Fermi level of the used n–doped silicon substrate and the Fermi level of pure silicon, N_{D} is the concentration of donor ions and ϵ_{Si} and ϵ_0 are the permittivity values of silicon and free space. In n–doped silicon, Ψ_{B} is found from $\Psi_{\mathrm{B}} = kT/\mathrm{e}\ln(N_{\mathrm{D}}/n_{\mathrm{i}})$. In the example structure discussed before, with $N_{\mathrm{D}} = 10^{12}$ cm^{-3} at $T = 300$ K, the maximum depletion depth is 16.5 µm.

1.2.2.1 The effect of oxide charges in the MOS–structure

During the growth of a silicon oxide layer, crystal defects occur both in the oxide and at the silicon–oxide interface. At the silicon–oxide interface, the different lattice spacings of SiO_2 and silicon result in defects in the form of free silicon bonds [5]. Therefore the defect density at the silicon–oxide interface is much higher than in the oxide itself.

Crystal defects both result in fixed charge centers and in traps for electrons and holes [6]. The main part of the oxide charge is due to the fixed oxide charges which are predominantly positive. Most of the fixed oxide charge is located close to the SiO_2–silicon interface. Thus,

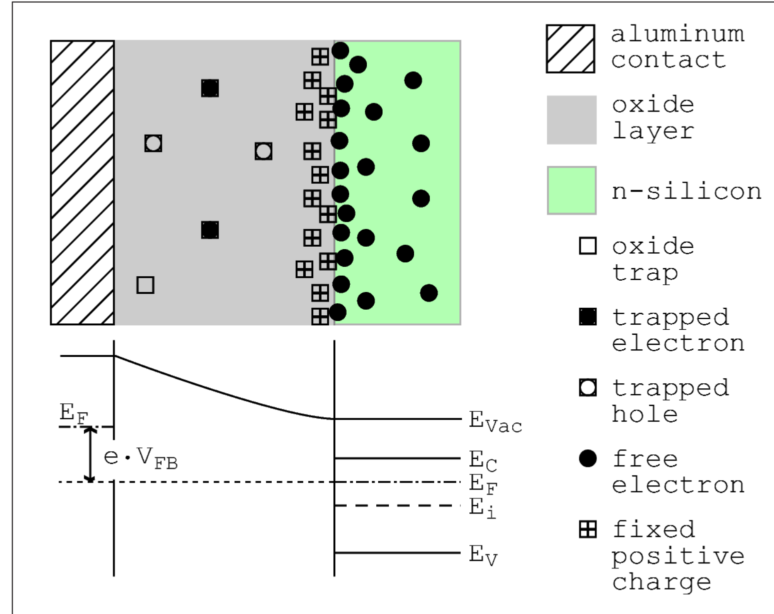

Figure 1.5: *Oxide charge in a MOS–capacitor. Charge in the bulk oxide is due to electrons or holes trapped at crystal defects in the oxide. The major part of the oxide charge is due to fixed oxide charge. Practically all of the fixed oxide charge is located in a charge layer at the silicon–oxide interface. This charge layer consists of positive charges and has a typical thickness of 20* nm. *The oxide charge creates an electric field in the oxide which results in a flat–band voltage change. This figure shows a nMOS–structure in the flat band state. Due to the positive oxide charge,* V_{FB} *is shifted to a more negative value.*

one can treat the fixed oxide charge as a positive layer of charge at the silicon–oxide interface to determine the resulting electric field in the oxide.

Measurements with test MOS–structures produced in the MPI semiconductor laboratory confirm the positive sign of the fixed oxide charge. These measurements show a typical charge density of $5 \cdot 10^{10}\ \mathrm{h}^{+} \cdot \mathrm{cm}^{-2}$ for silicon wafers with <100> crystal orientation and of $2 \cdot 10^{11}\ \mathrm{h}^{+} \cdot \mathrm{cm}^{-2}$ for wafers with $< 111 >$ crystal orientation. In the case of silicon with $< 111 >$ crystal orientation, the number density of silicon atoms at the wafer surface is larger. This also means a larger number of defects at the silicon–oxide interface and thus a larger measured fixed oxide charge density.

The fixed oxide charge layer creates an electric field which causes a voltage drop in the oxide. With the oxide capacitance C_{ox} and the surface charge density Q_{ox}, the voltage drop is found from $V(Q_{\mathrm{ox}}) = Q_{\mathrm{ox}}/C_{\mathrm{ox}}$. For a typical value of $C_{\mathrm{ox}} = 8 \cdot 10^{-9}\ \mathrm{F} \cdot \mathrm{cm}^{-2}$ of the oxide capacitance and the above mentioned surface charge densities of $5 \cdot 10^{10}\ \mathrm{h}^{+} \cdot \mathrm{cm}^{-2}$ and $2 \cdot 10^{11}\ \mathrm{h}^{+} \cdot \mathrm{cm}^{-2}$, the potential drop over the oxide is $V(Q_{\mathrm{ox}}) = 1.0\ V$ and $V(Q_{\mathrm{ox}}) = 4.0\ V$.

This potential drop can be compensated with the corresponding negative voltages of -1.0 V and -4.0 V at the aluminum contact. The flat band voltage in the nMOS–structure discussed here is thus shifted from -0.5 V to -1.5 V and -4.5 V respectively. If V_{Al} has a value of 0 V, the total voltage drop given by $V(Q_{\mathrm{ox}})$ and the flat band voltage V_{FB} drive

the MOS–structure in accumulation.

In order to find the value of the accumulation layer charge density with $V_{\mathrm{Al}} = 0$ V, one can use the results for a MOS–structure which is free of oxide charge. It makes no difference if $V(Q_{\mathrm{ox}})$ is caused by oxide charge or if it is applied to the aluminum contact.

The resulting electron accumulation layer density is shown in the left plot of figure 1.4. For $V_{\mathrm{Al}} = 1.0$ V, the surface charge density is $Q(0) = 5 \cdot 10^{10}$ $\mathrm{e}^- \cdot \mathrm{cm}^{-2}$. For $V_{\mathrm{Al}} = 4.0$ V, the surface charge density is $Q(0) = 2 \cdot 10^{11}$ $\mathrm{e}^- \cdot \mathrm{cm}^{-2}$. These values are equal to the respective fixed oxide charge densities. Thus, the positive fixed oxide charge layer is compensated by an electron accumulation layer with the same surface charge density.

1.3 X–ray photon detection in silicon

In silicon, the absorption of X–ray photons in the energy range up to 10 keV is dominated by the photo effect [7]. If an X-ray photon is absorbed, it completely transfers its energy to an electron in the L1, L2, L3 or K1 shell of a silicon atom. The electron is released from the shell, escapes the silicon atom and moves through the silicon bulk. Directly after the photoelectron is removed from the shell, it has a kinetic energy of $E_{\mathrm{kin}} = h\nu - E_{\mathrm{B}}$, where E_{B} is the binding energy of the electron [8].

In order to be absorbed due to the photo effect, the photon must have an energy above the electron binding energy of 99.4 eV of the L3 shell. The binding energies of electrons in the other shells involved in X-ray absorption processes are 99.8 eV (L2), 149.7 eV (L1) and 1839 eV (K1). At photon energies below the K–absorption edge of silicon (1840 eV), the internal photo effect is dominated by absorption in the L2 and L3 shells. At higher photon energies than the K–absorption edge, the internal photo effect is dominated by absorption in the K1 shell.

The absorption of the photon and the emission of the photoelectron leaves the silicon atom singly ionized. Since it has absorbed the binding energy of the photoelectron, the atom is also in an excited state. The excited and singly ionized atom immediately loses its potential energy in a relaxation process where electrons from the outer shells drop to the free state in the L or K shell. During this relaxation process either an Auger–electron or a fluorescence photon is emitted. The reabsorption of the fluorescence photon leads to the emission of a second photoelectron. Only a negligible amount of fluorescence photons can escape the silicon bulk.

The X–ray photon energy is therefore first converted into the kinetic energy of photo– and Auger–electrons. These electrons move through the silicon bulk and lose their energy in a number of inelastic coulomb collisions. Each collision involves two processes which consume the transferred energy: I. A valence band electron is moved into the conduction band and a hole is left in the valence band. Thus, a part of the collision energy is invested in the creation of an electron–hole pair. II. During the collision, the energetic electron transfers a part of its kinetic energy to a phonon. The creation of a phonon increases the thermal energy of the silicon bulk.

Finally, the absorbed X–ray photon energy is completely invested in the creation of

electron–hole pairs and into thermal energy. The mean energy ϵ needed to create one electron–hole pair by X–ray absorption in silicon is 3.65 eV at a photon energy of 1.4 keV and a temperature of 140 K [9]. No energy dependence of ϵ has been observed for photon energies between 1.4 keV and 10 keV. A photon with an energy of 5415 eV (Cr-Kα) creates 1484 electron–hole pairs on average.

Figure 1.6 shows three drawings that illustrate the steps from the generation of an electron–hole cloud due to the absorption of a X–ray photon to its separation by the drift field in a pnCCD.

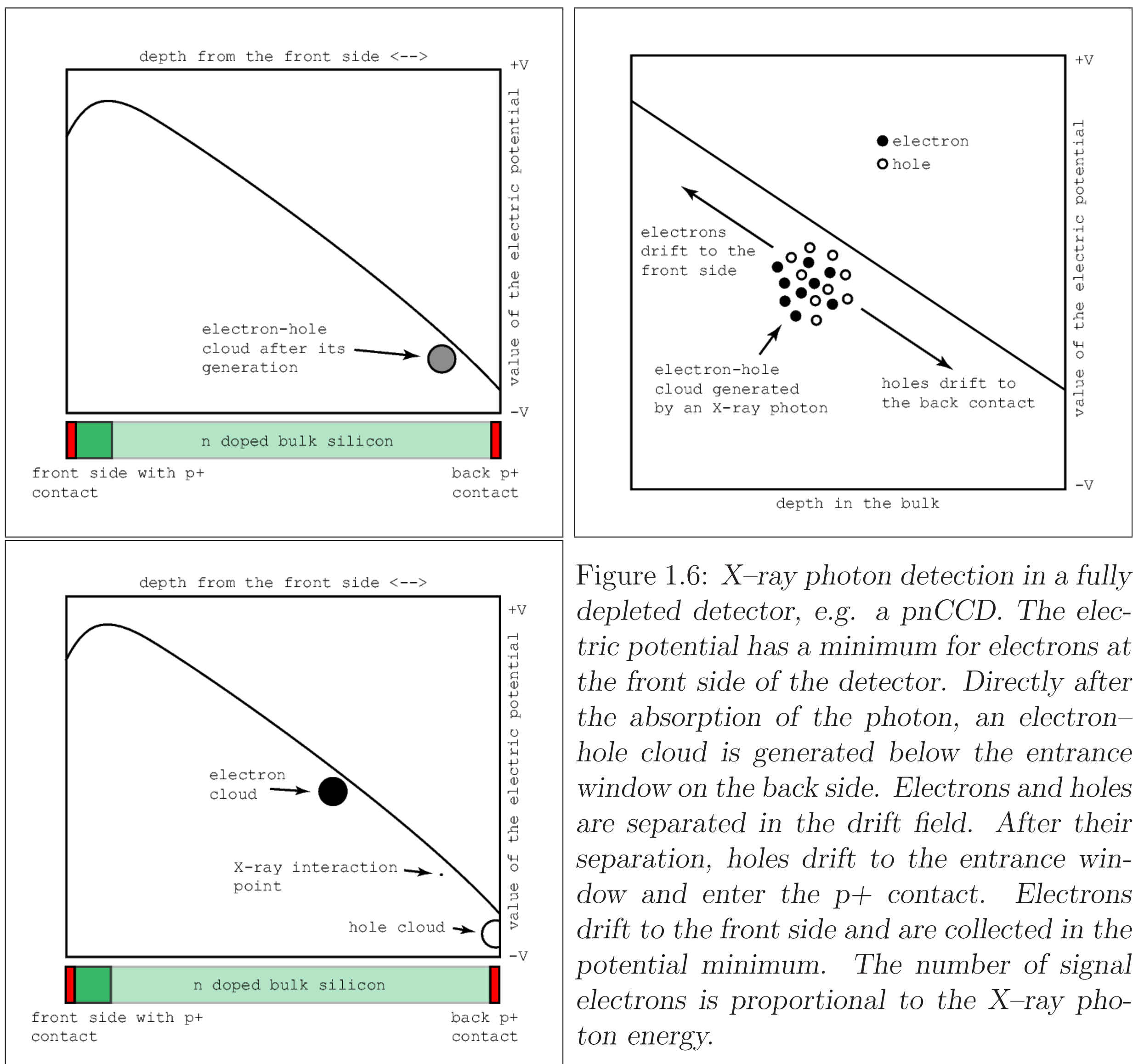

Figure 1.6: *X–ray photon detection in a fully depleted detector, e.g. a pnCCD. The electric potential has a minimum for electrons at the front side of the detector. Directly after the absorption of the photon, an electron–hole cloud is generated below the entrance window on the back side. Electrons and holes are separated in the drift field. After their separation, holes drift to the entrance window and enter the p+ contact. Electrons drift to the front side and are collected in the potential minimum. The number of signal electrons is proportional to the X–ray photon energy.*

X–ray photons with energies below 10 keV create charge clouds containing less than 3000 electron–hole pairs. The drift field in a pnCCD immediately separates electron–hole clouds with less than 3000 electron–hole pairs into two unipolar charge clouds which contain

exclusively electrons or holes. As soon as the electrons and holes are separated, the two charge clouds both expand due to diffusion and electrostatic repulsion (section 2.2.1).

The attenuation of X–rays in silicon follows an exponential law which is expressed by the following equation:

$$I(z) = I_0 \cdot \exp\left(\frac{-z}{z_{\text{att}}}\right) \tag{1.8}$$

Here, z is the path length in silicon and the length z_{att} is defined as the attenuation length. The incident intensity I_0 is reduced by a factor of 1/e if the path length is equal to z_{att}. Measurements of z_{att} in silicon and in the energy range from 30 eV to 30 keV are presented in [10]. At an energy of 90 eV which is the lower X–ray detection limit of current pnCCDs, the attenuation length z_{att} is 0.6 µm. At an energy of 1486 eV (Al–Kα) z_{att} is 7.9 µm and at 5415 eV (Cr–Kα, the largest photon energy used for measurements in this thesis) z_{att} is 22.6 µm.

The conversion of the photon energy E_{photon} in electron–hole pairs and thermal energy of the silicon bulk is a statistical process. Therefore, the number of created electron hole pairs is a Poisson distribution around the mean value of $n_{\text{e}} = E_{\text{photon}}/\epsilon$. The variance of the number of created electron–hole pairs is given by the Fano–theory:

$$\langle \Delta N^2 \rangle = F \cdot \frac{E_{\text{photon}}}{\epsilon} \tag{1.9}$$

F is the Fano–factor and ϵ is the mean energy needed to create an electron–hole pair [3]. The Fano–factor for silicon has a value of 0.13 at $h\nu = 1.5$ keV. F is independent of the temperature between 140 K and 300 K and constant for photon energies above 1.5 keV [9].

For a photon energy of 5415 eV and $\epsilon = 3.65$ eV, the variance ΔN is 13.9 electrons. At a given energy, ΔN determines the best possible energy resolution of a silicon detector. Consider a large number of measurements using photons with an energy of exactly 5415 eV. If the number of electron–hole pairs created by each photon is exactly measured, the resulting spectrum is a Gaussian with a fwhm of 119 eV.

After the generation of the electron hole pairs is completed, an electron–hole cloud is located where the X–ray photon was absorbed. Measurements presented and analyzed in [9] lead to the following expression for the initial radius of the electron–hole cloud:

$$R = R_0 + \beta \cdot E_{\text{X-ray}} \tag{1.10}$$

With $R_0 = 170$nm and $\beta = 0.023$nm/eV, both at a temperature of 140K. This means a typical radius of 295nm at a photon energy of 5415eV.

1.4 Charge storage and shift in three phase CCDs

CCDs or 'charge coupled devices' were first published as analog memory devices [11]. The general idea behind a CCD is to combine the storage of electric charge in separate cells with a serial readout of these cells. CCDs are semiconductor devices made of silicon, practically all CCDs use electrons as signal charge carriers.

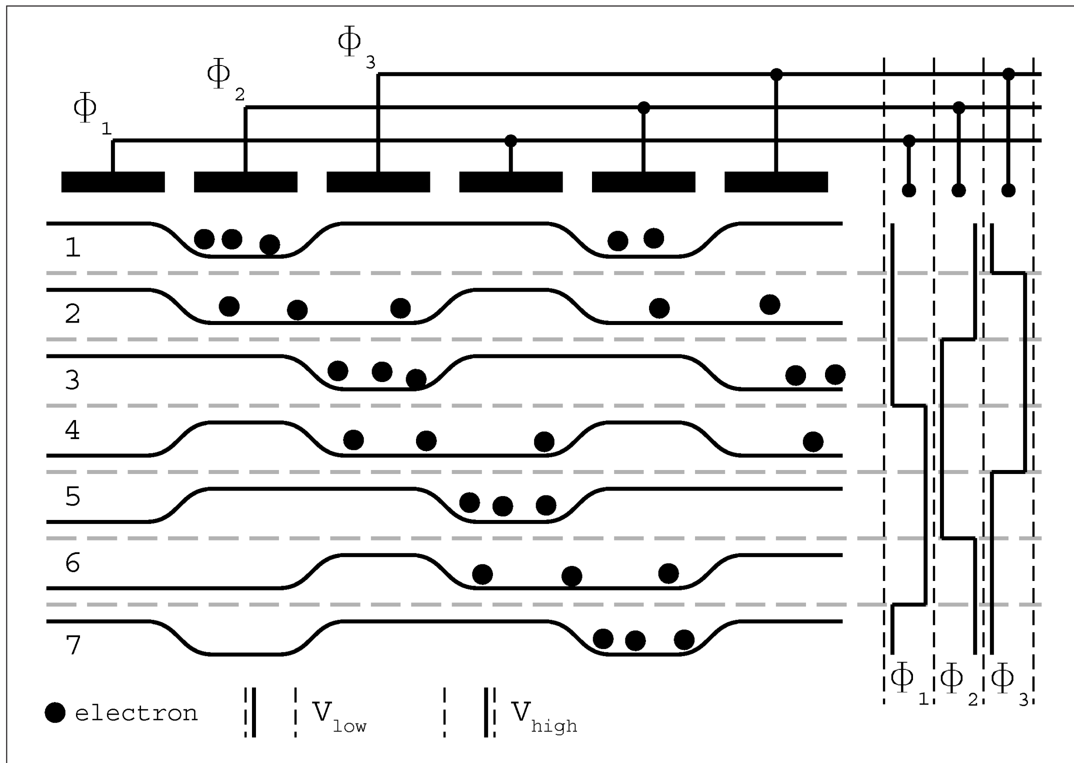

Figure 1.7: *Clocking scheme for a 3 phase 'n-channel' CCD. Electrons are stored below the register contacts with a positive voltage. In this case the middle contact Φ_2 is used as the storage register. The transfer of signal electrons from one cell to the next is done by periodically switching the register contacts between a positive and a negative voltage. On the right hand side, the switch timing diagram used for shifting the electrons to the right is shown.*

A CCD can be seen as a row of discrete potential minima for electrons which form the storage cells. The charge packets in the potential minima are simultaneously moved along the row without mixing them. A capacitor which is coupled to the gate of a transistor is placed at one end of the row. In order to measure the amount of charge in each cell, the charge packets are successively moved to the capacitor. The voltage change of the capacitor caused by the added charge of a cell is then amplified by the transistor.

Shifting the charge packets to the readout node is done by moving the potential minima along the row in the direction of the readout node. Since the signal electrons stay in their local potential minima, they are shifted to the readout node. The charge shift principle used in pnCCDs is called 'three phase shifting'. In a three phase CCD, each storage cell has three independent electric contacts or 'registers'. For the storage of electrons, either one or two of the registers have a positive voltage in order to form a local potential minimum for electrons. The remaining registers have a negative voltage and thus form a potential barrier to the neighboring pixels.

A row of storage cells is formed by repeating the basic cell structure. The three inde-

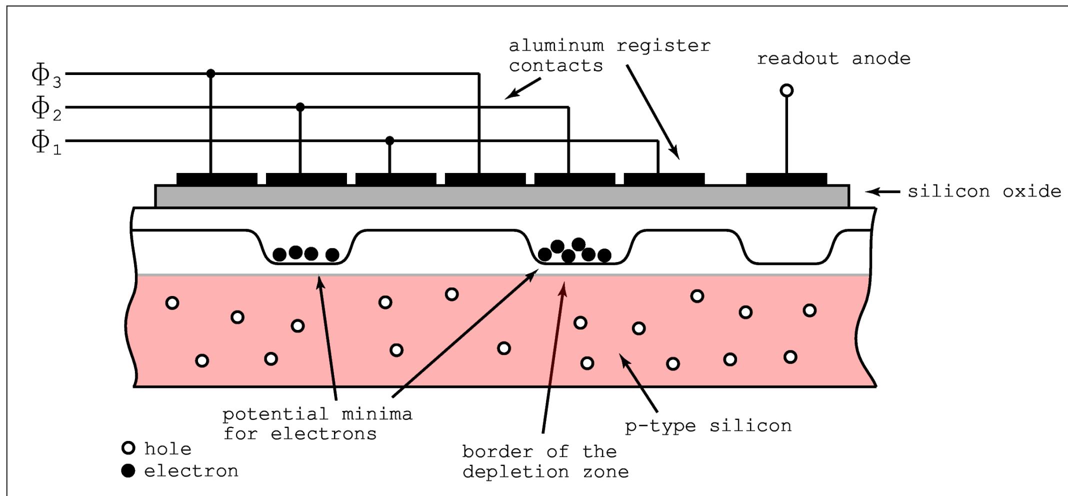

Figure 1.8: *Principle of a MOS–CCD on p-type silicon. Shown is a three phase CCD with storage of holes below the registers with phase Φ_2. Below the more negative storage registers, the depth of the depletion region is a bit higher but charge is stored directly below the silicon-oxide interface.*

pendent register contacts of each cell are connected to three different bus lines named Φ_1, Φ_2 and Φ_3. Figure 1.7 shows the charge shift principle of a three phase CCD and the connection of the register contacts.

All registers either have a negative (barrier) voltage V_{low} or a positive (storage) voltage V_{high}. In the case of storage below one register, shifting charge to right is begun by setting the voltage of the register Φ_3 from V_{low} to V_{high}. The electrons evenly distribute below Φ_2 and Φ_3. In the next step, the voltage of Φ_2 is set to V_{low} and the electrons below Φ_2 move to Φ_3. After this second step, the charge is moved by one register or one third of a pixel. Therefore six switching steps are required to move the charge by one pixel. The efficiency of the charge shifting process is parameterized with the **c**harge **t**ransfer **e**fficiency value 'CTE'. The CTE gives the relative amount of signal electrons which are transferred from one pixel to the next. A complementary value, the **c**harge **t**ransfer **i**nefficiency, the 'CTI', is defined as CTI $= 1 -$ CTE and gives the relative charge loss after a transfer of one pixel. Charge transfer losses are due defects in the silicon crystal grid. These defects provide energy states below the conduction band. Some of the signal electrons are trapped by the defect energy states which are located in the region of the transfer channel. The mean number of signal electrons trapped during the transfer of one pixel gives the charge transfer loss. Currently produced pnCCDs have a CTI as low as $1.0 \cdot 10^{-5}$.

The first CCD published in [11] uses a MOS–structure to realize the storage cells and the shift registers (figure 1.8). Each register contact consists of a small aluminized area with dimensions in the order of several µm. Positive voltages are applied to the registers Φ_1, Φ_2 and Φ_3 in order to deplete the p–doped substrate.

Electrons are used as signal charge carriers, they are collected in the vertical potential minimum at the silicon–oxide interface. The lateral storage minima for electrons are below

the Φ_2 contacts which have a higher voltage than Φ_1 and Φ_3. Since the signal electrons stay inside the depletion region at the silicon–oxide interface, they cannot recombine with holes. Therefore the signal electrons remain in the potential minima until they are shifted to the readout node.

1.5 pnCCD

The development of pnCCDs was motivated by the X–ray astronomy mission XMM–Newton. This mission needed a focal plane imaging spectrometer which is coupled to a Wolter–type X–ray telescope.

The silicon wafers which are used as the base material for the semiconductor detectors fabricated in the MPI–HLL have thicknesses from 280 µm to 450 µm. The upper energy limit of the Wolter–Telescope used on XMM–Newton is roughly 10 keV. X–ray photons with an energy of 10 keV have an attenuation length of 135 µm in silicon. In order to achieve the maximum possible sensitivity for X–rays with an energy of up to 10 keV, a pnCCD fabricated from the given base material must therefore be sensitive over the whole substrate thickness.

A pnCCD combines radiation sensitivity over the whole substrate thickness with the signal charge storage and readout principle of a CCD. The imaging array of a pnCCD is a parallel arrangement of linear CCDs (section 1.4), the basic semiconductor structure of a pnCCD is the pn–junction (section 1.2.1).

1.5.1 Full depletion of the detector volume

In pnCCDs, asymmetrically doped pn–junctions are used to deplete the weakly n–doped sensitive detector volume. These pn–junctions have a high acceptor concentration in the p–region and a low donor concentration in the n–region. In this case, the depletion width in the n–doped region is much larger than in the p–doped region (section 1.2.1).

Figure 1.9 shows a pnp–structure which consists of two pn–junctions with a common n–contact at the side [12]. The substrate is weakly n–doped (n-), the p–contacts at the top and the bottom are strongly p–doped (p+) and the n–contact at the side is strongly n–doped (n+). If the n+ contact is held at 0 V, the weakly n–doped substrate is fully depleted by the application of sufficiently negative voltages at the p+ contacts. This structure is the most simple implementation of a mechanism called 'sidewards depletion'. The pnp–structure is depleted from the side because all electrons in the n–substrate drift to the n+ contact which has the most positive voltage.

Throughout this thesis, the convention found in the literature to call the side with the small n+ doped side contact 'front–side' and the other one 'back–side' is used.

A simplified solution of the electric potential in the pnp–structure can be given. In this case, the p+ and n+ contacts are left out of the calculation and the built in voltage V_{bi} is neglected. The simplified solution is obtained by solving the Poisson equation with the

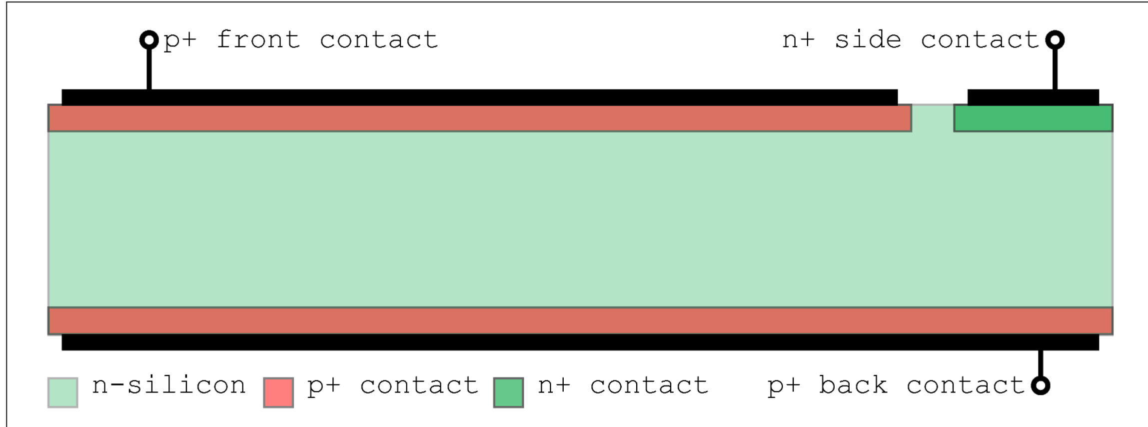

Figure 1.9: *Sidewards depletion structure with weakly n–doped bulk silicon and strongly doped double sided p+ contacts. The structure has two pn–junctions at the interface of the p+ contacts and the bulk. The common n–contact of the pn–junctions is the n+ side contact. Depletion of the n–doped bulk starts at the interfaces to the p+ contacts if the p+ contacts are at negative voltages and the n+ contact is at 0 V. With sufficiently negative p+ contact voltages the complete bulk can be depleted of free electrons. The vertical electric potential in the n–doped bulk is described by equation 1.12.*

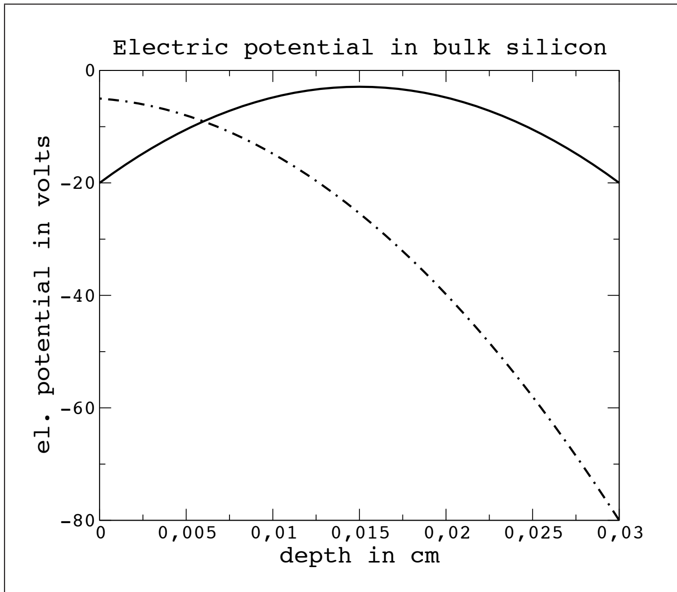

Figure 1.10: *Electric potential in a depleted pnp structure of 300µm thickness. The built in voltages of the front– and back p+ – n junctions are neglected, the front and back contact voltages are the values at the endpoints of the graph. As a result of the bulk donor concentration of* $1.0 \cdot 10^{12}$*, the potential has a parabolic form. Different front– and back contact voltages cause a linear term being added to the potential and at a given difference, the minimum for electrons lies close to one of the front– or back contacts.*

assumption that the weakly n–doped region is already fully depleted:

$$\frac{\partial^2 \varphi}{\partial z^2} = -\frac{\mathrm{e} \cdot N_\mathrm{D}}{\epsilon_0 \epsilon_\mathrm{Si}} \quad ; \quad 0 \leq z \leq d_\mathrm{s} \tag{1.11}$$

It delivers the electric potential φ as a function of the depth z. By definition, z has a value of 0 at the front side and d_s at the back side, d_s is the thickness of the weakly n–

doped region. N_D is the donor concentration, e is the elementary charge, ϵ_0 is the vacuum permittivity and ϵ_{Si} is the relative permittivity of silicon.

$$\varphi = -\frac{1}{2}\frac{e \cdot N_D}{\epsilon_{Si}\epsilon_0} z^2 + \left(\frac{1}{2}\frac{e \cdot N_D}{\epsilon_{Si}\epsilon_0} d_s + \frac{V_b - V_f}{d_s}\right) \cdot z + V_f \tag{1.12}$$

V_f and V_b are the front– and back contact voltages. The potential given by equation 1.12 has a maximum at:

$$z_{max} = \frac{1}{2} d_s + \frac{\epsilon_{Si}\epsilon_0}{e \cdot N_D} \frac{V_b - V_f}{d_s} \tag{1.13}$$

where z_{max} has a range from 0 to d_s. Both V_b and V_f have negative values. If the difference $V_b - V_f$ is larger than $-d_s^2 \cdot eN_D/(2\epsilon_{Si}\epsilon_0)$ and smaller than $d_s^2 \cdot eN_D/(2\epsilon_{Si}\epsilon_0)$, z_{max} is located inside of the pnp structure. If the difference $V_b - V_f$ is smaller than $-d_s^2 \cdot eN_D/(2\epsilon_{Si}\epsilon_0)$, the potential maximum z_{max} lies close to the front p+ contact.

Figure 1.10 shows solutions of equation 1.12 for a donor concentration of $1.0 \cdot 10^{12}$ with different front and back contact voltages.

1.5.2 Charge collection, storage and measurement in pnCCDs

Figure 1.11 shows the block diagram of a pnCCD. It has the same uniform back contact as the sidewards–depletion structure in figure 1.9. The front side p+ contact however is not uniform but structured into the separate register contacts. Three identical p+ registers form a storage cell. Each p+ register is connected to one of the three phases Φ_1, Φ_2 and Φ_3. MOS–structures define the electric potential on the surface regions between the p+ registers. The aluminum contacts of the MOS–gates are connected to the MOS–gate voltage V_{MOS}. The uniform p+ contact on the back side is connected to the back contact voltage V_b. In pnCCDs the n+ side contact is named the 'substrate contact' with the substrate voltage V_s.

Typical values of the contact voltages for a pnCCD with a substrate acceptor concentration of 10^{12} cm^{-3} are: $V_{high} = -15$ V for the storage registers, $V_{low} = -20$ V for the barrier registers, $V_{MOS} = 0$ V and $V_b = -200$ V. The substrate contact is always kept at $V_s = 0$ V. The vertical potential minimum is thus located at the front side close to the p+ register contacts.

A n–doped readout anode is placed next to the last register contact on the right hand side. The voltage of the readout anode is between V_s and V_{high}. Therefore the anode forms a local potential minimum and signal electrons drift into the readout anode as soon as they reach the neighboring shift register.

Since the n–doped silicon around the anode is depleted, the anode is insulated from all other contacts of the pnCCD. The readout anode thus acts as a capacitor which is charged by the signal electrons. A JFET which is integrated in the pnCCD structure is used as the first readout amplifier [13, 14]. The gate of the JFET is connected to the readout anode. The effective readout anode capacitance is the sum of the anode capacitance and the capacitance of the JFET gate.

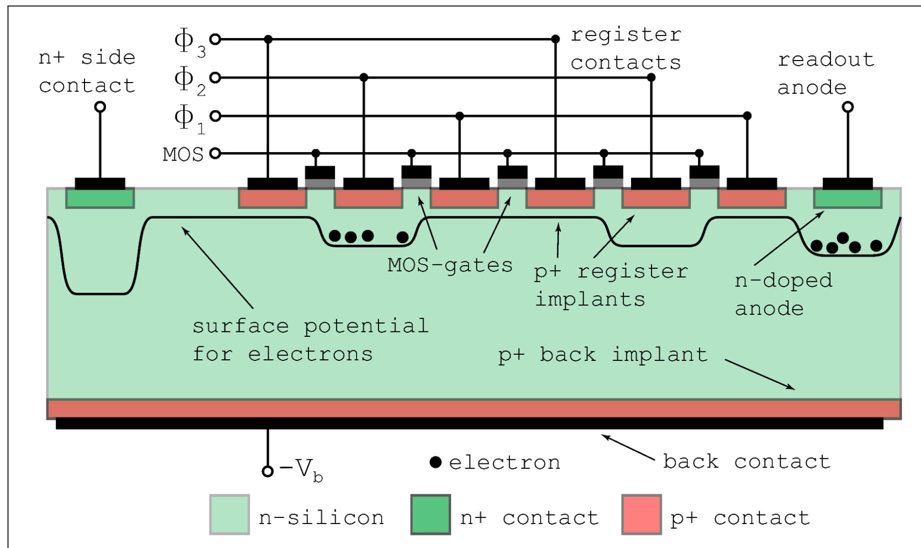

Figure 1.11: *Block diagram of a pnCCD with two pixels, the readout anode on the right hand side and the n+ substrate contact on the left hand side. The bulk is fully depleted due to the negative back contact and register voltages relative to the n+ substrate contact voltage of* 0 V*. Signal electrons collect in the potential minima below the p+ registers. The storage registers have a higher voltage than the barrier registers in order to form a lateral potential minimum for signal electrons.*
Electrons that reach the last register on the right hand side drift to the n–doped readout anode. The readout anode is a local potential minimum for electrons because it has a more positive voltage than the storage registers. Signal electrons cause a voltage change on the readout anode which is connected to the gate of a JFET in order to amplify the small anode signal.

The uniform back p+ contact of a pnCCD acts as the entrance window for radiation. X–ray photons that are absorbed in the depleted bulk create an electron–hole cloud. The electron–hole is separated into a hole cloud and an electron cloud by the electric field in the bulk. The storage region with the lowest electric potential for electrons lies close to the p+ registers while the back contact forms the global potential maximum for electrons. Therefore the electric field vector in the bulk points to the back side. Holes drift into the back p+ contact. Electrons drift to the front side where they stay in the local storage minima below the storage registers until they are shifted to the readout anode.

The pnCCD array consists of parallel linear pnCCDs which form the channels of the array, see figure 1.12. Each channel has the same number of storage cells and its own readout anode and first JFET transistor for the amplification of the signal. The number of channels is the 'x' dimension of the array. The number of storage cells in the channels is the 'y' dimension the array.

Signal electrons which are created in the bulk are collected in the storage cells on the register side of the array, see figure 1.13. The x–y coordinates of a storage cell correspond

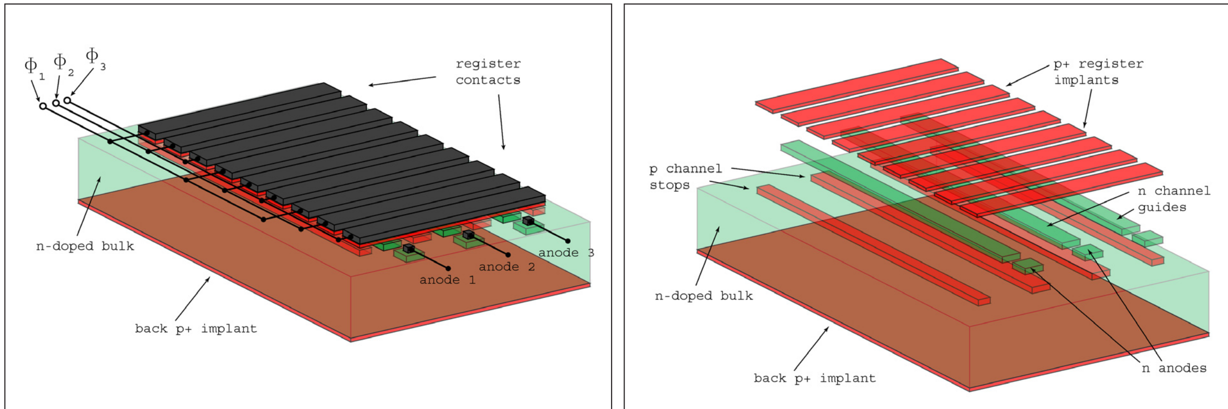

Figure 1.12: *Principle of a pnCCD array. The aluminum contacts of the register implants and the p+ register implants are common for all channels. The channels are defined by n–implants below the register contacts, the channel guides. P–implants placed between the n–channel guides serve as channel stops. The positive donor ions of the n–channel guides attract signal electrons while the negative acceptor ions of the p–channel stops push away the signal electrons. Therefore the channel guides form a lateral potential minimum along the channels while the channel stops form a potential barrier between the channels. Each channel has its own readout anode which is connected to the gate of a JFET.*

to the x–y coordinates of the photon absorption position. The amplitude of a signal is proportional to the number of signal electrons on the anode capacitance. Therfore the signal amplitude is proportional to the energy of the detected X–ray photon (section 1.3). Since pnCCDs are imaging detectors, the storage cells are called 'picture cells' or short 'pixels'.

1.5.2.1 Frame store CCDs

All currently fabricated pnCCDs which are designed for applications with a continuous photon flux can be operated in frame store mode. In frame store mode, the pixel array is divided in two halves. One half is the image area which is illuminated by the photon source. The other half serves as the storage area. Readout is done as follows: In the first step, the signal frame is quickly shifted from the image area into the storage area. In the second step, the signal frame is slowly shifted to the anodes for signal readout. This readout scheme is facilitated by separate register bus contacts for the image and storage areas. With the separate register contacts, the stored frame can be shifted to the readout nodes without moving the frame in the image area.

Operating a pnCCD in frame store mode reduces the 'dead time' between the integration periods. Photons that hit the CCD during the readout phase are detected, but the assignment of their row coordinates is incorrect. If a photon hits the middle of the array while one half of the signal frame has been read, the signal is added to the row with the greatest distance from the readout node. Photon events which occur during the readout

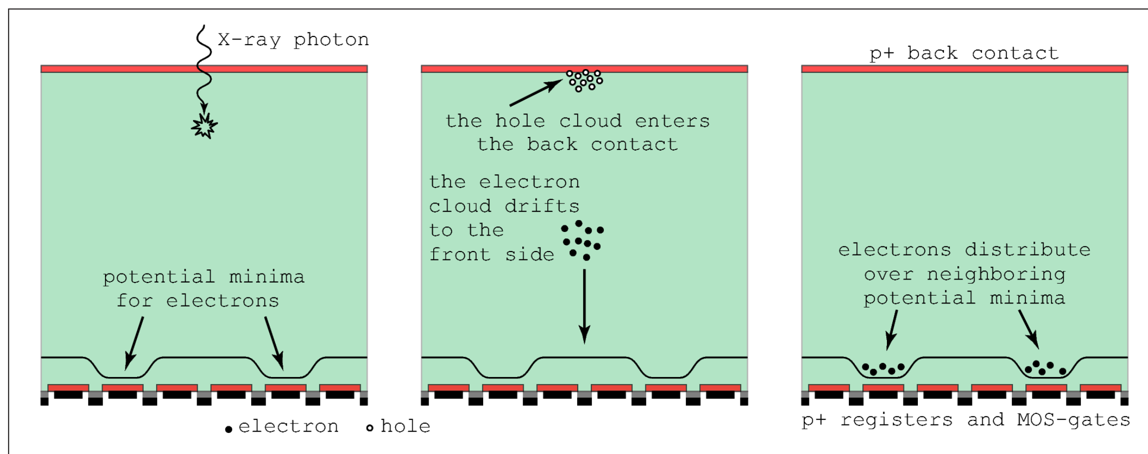

Figure 1.13: *Charge collection in a pnCCD. The vertical potential minimum for the signal electrons is at the register side. The lateral potential minima at the register side are below the storage registers. These potential minima define the middle of pixels, the pixel borders are between the two barrier registers. If a X–ray photon hits a pixel border, the signal electrons spread over the two neighboring potential minima.*

phase are called 'out of time events'. The largest frame store pnCCD currently fabricated is the 384 x 768 pixel detector for the eROSITA X–ray satellite instrument. Reading out a 384 x 384 pixel frame takes 10 ms while the transfer of the frame from the image to the storage area takes 200 µs. Compared to full frame operation of a 384 x 384 pixel pnCCD, this translates into a reduction of the dead time by a factor of 50 and a reduction of the number of out of time events by the same factor.

1.5.3 Readout electronics

Each channel of a pnCCD has a dedicated JFET or 'first–FET' which is located close to the readout anode. An aluminum contact layer connects the gate of the first–FET to the readout anode. In order to lower the impedance of the anode signal, the readout JEFTs are operated in source follower mode [14]. The current source which supplies the source current of the first–FET is integrated in a readout ASIC, named 'CAMEX'. The CAMEX ASIC has 64 to 132 identical readout channels which perform the parallel line by line readout of all pnCCD channels [15]. Large pnCCDs with more than 132 channels are read out with two or more CAMEX chips which are operated in parallel. Figure 1.18 shows a close view of a 128 channel CAMEX.

Each CAMEX channel begins with the current source for the first–FET on the pnCCD. The low impedance signal from the first–FET source is fed to a JFET amplifier for voltage amplification. A low pass filter which follows the JFET amplifier filters out high frequency noise. The sampling of the signal is done with an eight–fold correlated double sampling filter.

In the double sampling filter, the signal is sampled eight times and averaged both before

and after shifting the signal electrons on the readout anode. Sampling the signal several times and averaging the results acts as a low pass filter. Fluctuations of the signal due to high frequency noise are roughly reduced with the square root of the number of samples. The difference of the two averaged signals gives the final charge signal which is stored in a sample and hold circuit. Finally the signals stored in the sample and hold circuit are serialized with an output multiplexer and amplified by a output cable driver [16]. The digitization of the serialized signals is performed on an external ADC board.

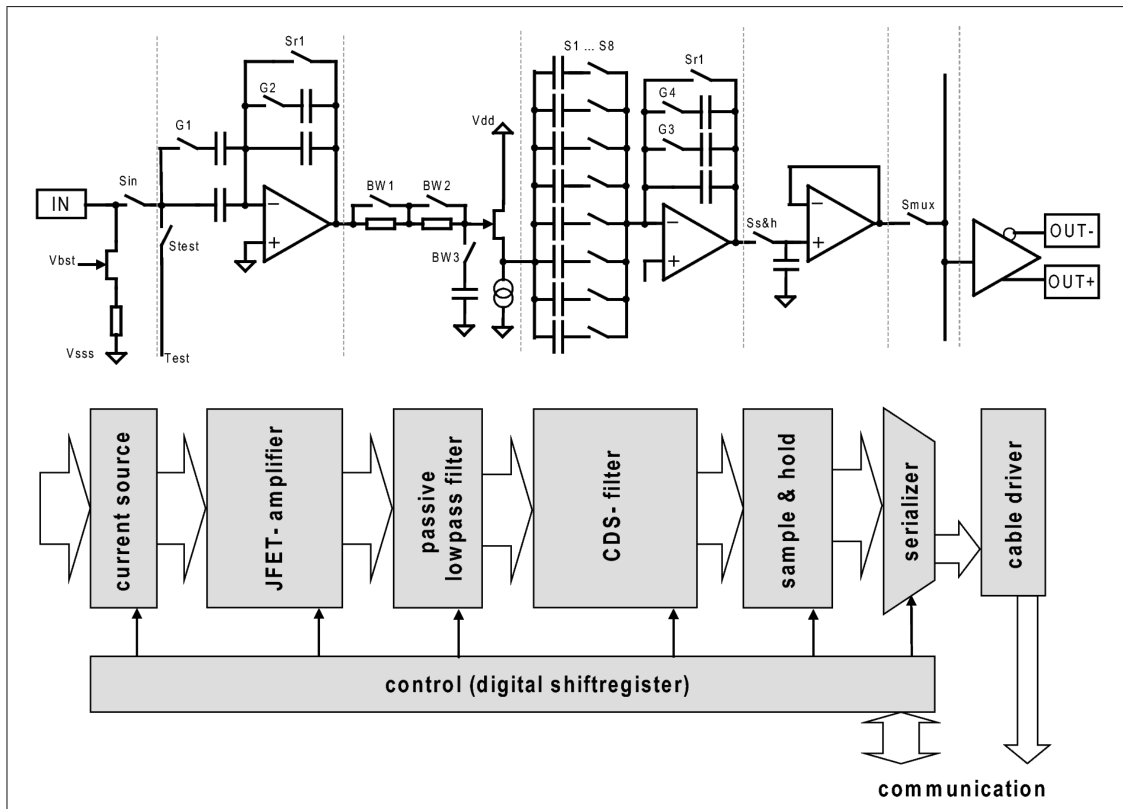

Figure 1.14: *Block diagram of one channel of the CAMEX readout ASIC with a programmable low pass filter and eight–fold correlated double sampling of the signal. The input of the channel is connected to the source of the readout JEFT on the pnCCD. All channels of the pnCCD have a dedicated CAMEX channel. For large CCDs, two or more CAMEX ASICs are operated in parallel. After filtering and sampling the signals of one line in the pnCCD frame, the signals are serialized and transferred to an external analog–to–digital converter (ADC).*

The most time consuming task of the readout process is the amplification and the sampling of the anode signals. Parallel readout of the pnCCD channels as performed with the CAMEX ASIC therefore enables fast readout cycles while maintaining low readout noise. Frame rates of 1 kHz and an ENC of 2.3 electrons have been realized with a 264x264 pixel pnCCD [17, 18].

1.5.4 Applications for X–ray pnCCDs

Since the realization of the first pnCCD type for the XMM-Newton X–ray satellite of the European Space Agency (ESA) in 1999, the development of pnCCDs has continued in order to provide these detectors for new applications. The 'XMM–type' pnCCD (figure 1.17) has a pixel size of 150 x 150 µm^2, 64 readout channels and 200 lines, resulting in an array size of 64 x 200 pixels. Due to the full sensitive thickness of 300 µm, the detection efficiency for 10 keV photons is 89 % while the low energy limit is at 0.5 keV. With a frame readout time of 4.6 ms and at a device temperature of -90 °C, the equivalent noise charge (ENC) of dark signals is 5 electrons. The energy resolution at an X–ray photon energy of 5.9 keV (Mn-Kα) is 150 eV. Twelve of these devices are arranged in a layout of 6 x 2 separate arrays in order to form the 6 x 6 cm^2 sized 384 x 400 pixel imaging spectrometer array of the EPIC–pn camera on XMM–Newton.

In the course of the development of new and improved pnCCDs, the original 'XMM–type' pnCCD has evolved into devices with smaller pixels down to a size of 51 x 36 µm^2, larger array sizes of up to 1024 x 512 pixels and a larger sensitive substrate thickness of 500 µm instead of 300 µm. As a result of the larger sensitive thickness of 500 µm, the detection efficiency at 10 keV is increased to 99.8 %. Improvements of the radiation entrance window have led to a lower insensitive thickness in order to realize an energy detection limit as low as 90 eV. At the same time, the dark signal noise has been lowered from 5 e$^-$ to 2 e$^-$ and a readout speed of 1000 frames s^{-1} have been realized with a 264 x 528 pixel frame store pnCCD detector [18].

In X–ray astronomy, the next application for pnCCDs after XMM is the X–ray satellite instrument eROSITA (extended Roentgen Survey with an Imaging Telescope Array) on the upcoming Russian new Spectrum–Roentgen–Gamma mission. The main scientific goal of eROSITA is to map the large scale structure of the universe with an all sky survey in the X–ray energy range from 0.2 keV to 10 keV [20, 21]. Observations of the hot intergalactic medium in 100,000 galaxy clusters and of the hot gas in filaments between the clusters will create a map of the mass distribution in the universe. Since this cluster survey will cover the redshift range from $z = 0$ to $z = 1.5$, the observation data facilitate a study of the evolution of the large scale structure of the universe. Cosmological models can be tested and improved with the studies, especially with respect to the nature of Dark Matter and Dark Energy.

In the X–ray energy band from 2 keV to 10 keV, eROSITA will try to detect all active galactic nuclei (AGN) in the local universe. This search includes those AGN which are obscured in the optical band by the matter in the accretion disk. X–ray observations of AGN facilitate the classification into obscured and unobscured AGN by the X–ray luminosity function even at high redshifts z and a measurement of the X–ray luminosity function of AGN. It has already been confirmed that the average luminosity of active galactic nuclei is a function of z [22] in the energy range from 0.5 keV to 2 keV. The space density of AGN with high luminosities has a peak at $z \sim 2$ while the space density of low luminosity AGN peaks at $z \sim 0.7$. Due to the extended upper energy limit of 10 keV, the AGN survey with eROSITA will deliver more precise results for the space density of AGN as a function of

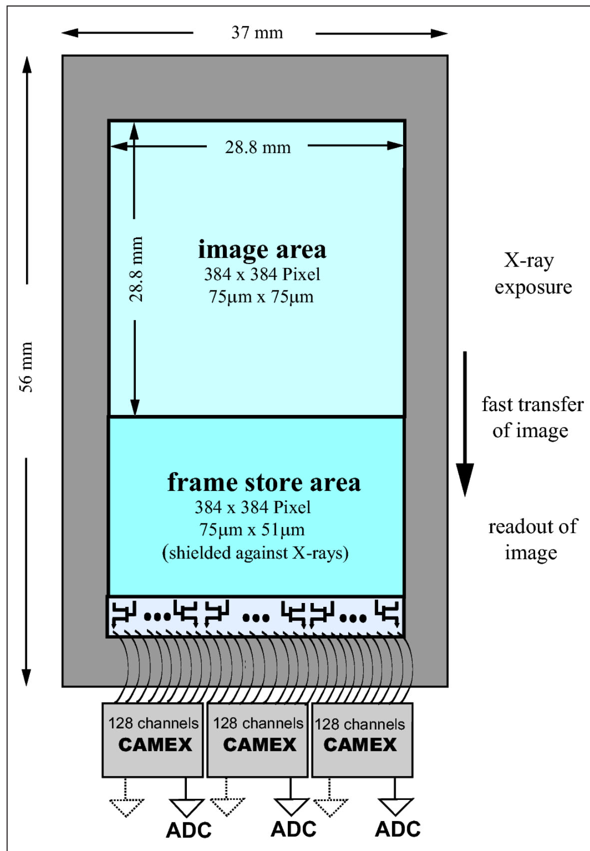

Figure 1.15: *Schematic of the frame store pnCCD which is used on the eROSITA experiment. The total size of the array is 384 x 768 pixels with a pixel size of 75 x 75 µm² in the image area and 75 x 51 µm² in the frame store area. Three 128 channel CAMEX ASICs facilitate the parallel readout of all 384 channels in 10 ms. The time needed to transfer a frame from the image to the frame store area is 200 µs. (Drawing by Norbert Meidinger, MPE [19])*

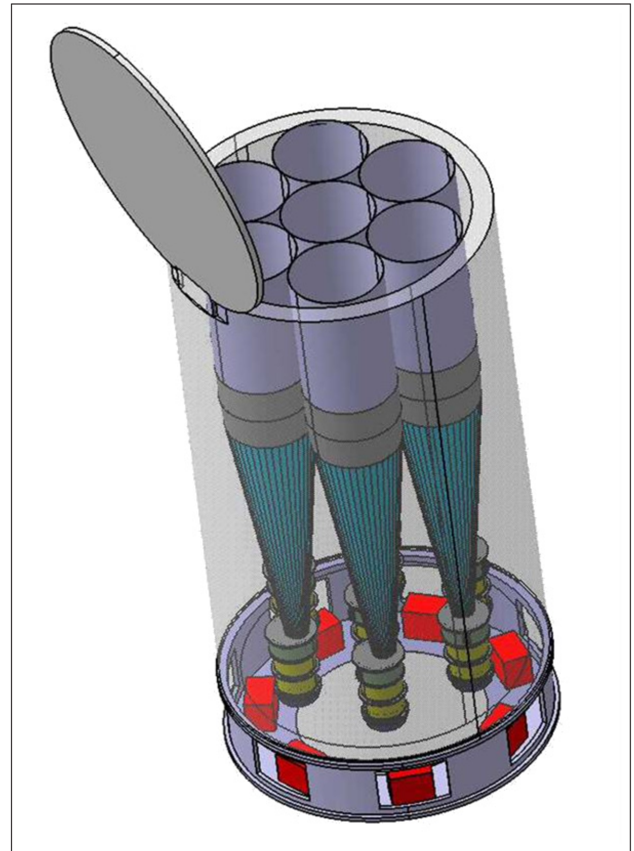

Figure 1.16: *Drawing of the eROSITA instrument. Seven Wolter type X–ray mirror telescopes with a focal length of 1.6 m are arranged in parallel. Each mirror module consists of 54 shells. The angular resolution of the telescopes is 15" on the optical axis. Each telescope has a separate camera module housing a 384 x 768 pixel frame store pnCCD with 75 x 75 µm² pixels in the image are, see figure 1.15. (Drawing by Peter Predehl, MPE [20])*

the luminosity in the local universe.

Figure 1.16 shows a drawing of the eROSITA instrument. It consists of seven Wolter-type X–ray mirror telescopes which are arranged in parallel in order to increase the total effective area in an energy range from 0.2 keV to 10 keV. Each mirror module consists of 54 gold coated mirror shells, has a focal length of 1600 mm and provides an angular resolution of 15 arc seconds or 0.12 mm in the focal plane. The eROSITA mission therefore requires a detector which works with high efficiency in the energy band from 0.2 keV to

10 keV and which matches the focal plane resolution of 0.1 mm of the X–ray optics. These requirements are ideally satisfied by the frame store pnCCD specifically designed for this purpose [19] (figure 1.15). It has an array size of 384 x 768 pixels with a size of 75 x 75 μm^2 in the image area and 75 x 51 μm^2 in the frame store area. The sensitive thickness is 450 µm which results in a detection efficiency close to 100 % in the energy range from 0.2 keV to 10 keV. At an operating temperature of -80 °Cand with a frame rate of 20 s^{-1}, the signal noise is 2 electrons ENC and the energy resolution is 139 eV at a photon energy of 5.9 keV (Mn–Kα). Figure 1.19 shows an early prototype of the eROSITA CCD which was used for a part of the measurements presented in this thesis.

Another new application for pnCCDs are material structure analysis experiments with synchrotron and free electron laser radiation. Currently the largest upcoming projects which use pnCCDs in free electron laser experiments are the LCLS (Linac Coherent Light Source) at SLAC in Menlo Park USA and the European XFEL (X–ray Free Electron Laser) facility in Hamburg, Germany. In these experiments, the scattering and diffraction of X–ray light at small structures with a size in the range of a few nanometers up to several hundred nanometers is studied. The analyzed structures can be clusters of atoms, single molecules or spherical particles e.g. made of polystyrene [23]. Depending on the structure size, X–ray light in the energy range from 90 eV ($\lambda = 13.8$ nm) up to 24 keV ($\lambda = 0.05$ nm) will be used, shorter wavelengths are required for smaller structures.

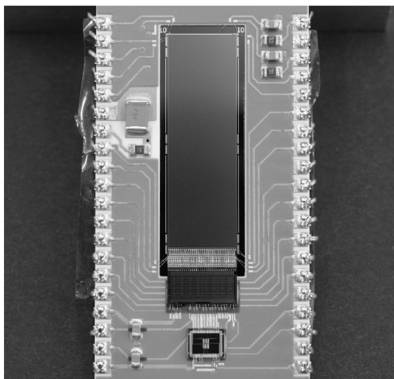

Figure 1.17: *An XMM-type pnCCD on its ceramic board. Below the large pnCCD are the 64 channel CAMEX readout ASIC and the TIMEX digital control ASIC.*

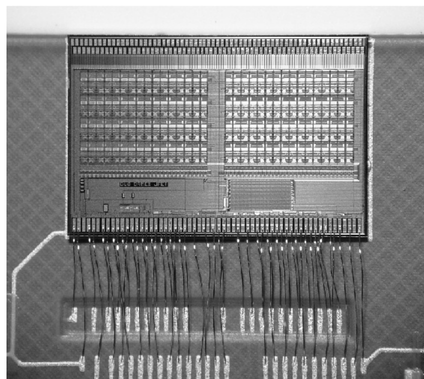

Figure 1.18: *New 128 channel CAMEX with bandwidth reduction and eight fold correlated double sampling. The readout and the digital control functionality has been integrated into a single ASIC.*

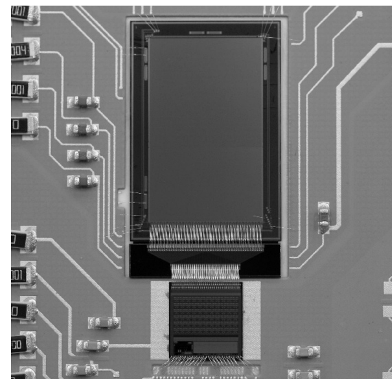

Figure 1.19: *A 128x250 pixel framestore pnCCD with 75x75 μm^2 pixels in the image area and 75x51 μm^2 pixels in the frame store area. The CAMEX readout ASIC is seen below.*

The X–ray light which is scattered at a particle in the X–ray beam creates a diffraction pattern which contains information on the structure of the particle. In order to reconstruct the structure information of the diffraction pattern, it must be recorded by an imaging detector which is sensitive in the given energy range from 0.3 keV to 24 keV. The timing

requirements follow from the pulse repetition rate of the X–ray beam which is in the range from 5 Hz to 250 Hz. Due to the high intensity range in the diffraction pattern, up to 10^3 photons can hit a pixel during the integration of one frame. Since the variance of the photon number N is given by Poisson statistics, the detector must be able to detect the number of photons with a precision of at least $N^{1/2}$ in the given dynamic range from 0 to 1000 photons per pixel while the photon energy ranges between 0.3 keV and 24 keV.

Specifically for the purpose of free electron laser experiments at LCLS, a pnCCD with 75 x 75 μm^2 pixels in a 512 x 1024 array has been designed and fabricated [19]. Two of these detectors a placed next to each other in the experimental setup in order to form a 1024 x 1024 pixel array with a side length of 7.7 cm. The dark signal noise is less than 25 electrons ENC at a frame rate of 250 Hz and an operating temperature of -20 ℃. A noise contribution of 25 e^- is smaller than the 82 e^- signal generated by a 0.3 keV photon. Thus, the detection precision of $N^{1/2}$ is achieved over the whole energy range. Due to the sensitive thickness of 450 µm, the detection efficiency is higher than 90 % from 0.3 keV to 11 keV and 20 % at 24 keV. This pnCCD is operated in full frame mode since there is no photon signal between X–ray pulses which a duration of a few femtoseconds. The images are read out in the 'dark time' after each pulse and before the next pulse arrives.

An even larger pnCCD with an array size of 1024 x 1024 pixels and identical specifications except for a slower frame rate of 125 Hz is projected for an upgrade of the LCLS pnCCD detector system. Four of these devices will be combined in a 2048 x 2048 pixel array. With a size of 7.7 x 7.7 cm^2, this will be the largest pnCCD array on a single chip after the 6 x 6 cm^2 XMM pnCCD array.

Chapter 2

pnCCD in detail

A closer look at the design principle and at the function of a pnCCD, as well as the electric potential in the pixel structure, is presented in this chapter. In the depleted silicon bulk volume of a pnCCD, three effects influence the motion of signal electrons:

For a study of the charge collection process in pnCCDs, it is essential to understand how the electric potential is determined by the device design and the voltages at the electrical contacts. The direction and the velocity of the motion of signal electrons in a pnCCD is controlled by the electric potential. In parallel to the motion in the electric field, electrons are subject to statistical motion because of their thermal energy. The statistical motion of electrons is the cause for the expansion of a charge cloud due to diffusion. The electric field caused by the signal electrons themselves causes them to repulse each other. The resulting expansion of an electron cloud acts in parallel with the expansion due to diffusion.

2.1 The pixel array of a pnCCD

Silicon wafers with a thickness from 280 µm to 450 µm are used as the base material for pnCCDs. The wafers are made of n–type silicon with a weak n–donor concentration in a range of $0.5 \cdot 10^{12}$ cm^{-3} to $1.0 \cdot 10^{12}$ cm^{-3}. A uniform n–doped layer with a thickness of 7 µm to 10 µm and a donor concentration of about 10^{14} cm^{-3} covers the side of the wafers which will later be the register side of a pnCCD. This layer is either realized by epitaxial growth of silicon with the required n–donor concentration or as a n–implant.

2.1.1 Structure and electric definition of a pixel

The pixel array of a pnCCD is formed by repeating the basic structure of a pixel in the vertical (charge transfer) and in the horizontal (channel or line) direction. Technically, the pixel array is realized as a set of ion implants, oxide layers and aluminum contacts, figure 2.1, 2.2, and 2.3. A thin, uniform p+ implant forms the back contact of the pnCCD. Each shift register consists of a p+ implant which has the form of a long strip. The p+ register implant strips run across the whole width of the pixel array perpendicular to the transfer

direction, see figure 2.2.

In order to realize the electrical contacts, all p+ implants are covered with aluminum layers. The width of the aluminum contacts on the p+ register implants is about half as much as the width of the p+ implants themselves, see figures 2.1 and 2.2. For X–ray applications, the back side p+ implant is normally covered with a homogeneous aluminum contact layer. This layer must be thin enough to prevent shielding of X–rays at the required low energy limit of the spectrum. If a pnCCD is designed for optical and uv applications, only the outer rim of the p+ back implant is covered with an aluminum layer.

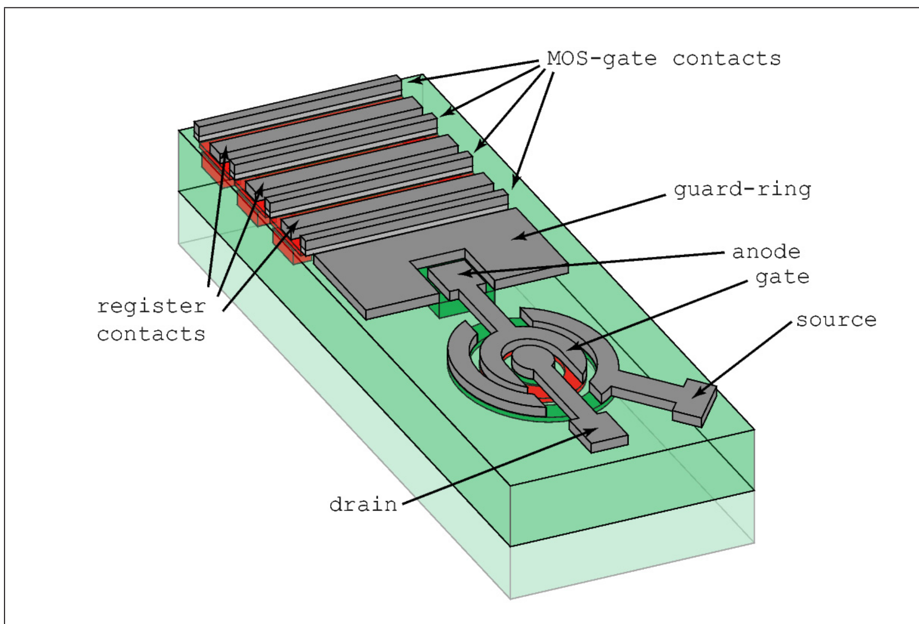

Figure 2.1: *The end of each pnCCD channel consists of an anode connected to a JFET transistor. These 'first FETs' have a common drain connection and are operated as source follower stages. A guard–ring contact at negative potential surrounds the anode and insulates the anodes and the pixel structure from the surrounding silicon substrate.*

The free regions between the p+ register implants are covered with silicon oxide and with aluminum contact strips on top of the silicon oxide layers, see figure 2.2. Together with the silicon bulk below, the silicon–oxide and the aluminum layers form MOS–structures (section 1.2.2). They are needed to define the electric potential on the silicon surfaces between the p+ contacts.

Both the n– and p–implants which define the channel structure of a pnCCD are located below the p+ registers, see figure 2.3. The p–implants define the borders between pixels of neighboring channels. The n–implants between two p–doped channel borders define the middle of a channel. These n–implants are called the 'channel guides'. Additional, smaller n–implants are centered in the middle of the channel guides and define the narrow transfer channel 'notches' along which signal electrons are shifted to the readout anode.

Typical contact voltages for the operation of a pnCCD with a thickness of 450 µm are -15 V for the storage registers, -20 V for the barrier registers, -200 V for the back contact and 0 V for both the MOS–gate contacts and the n+ side contact.

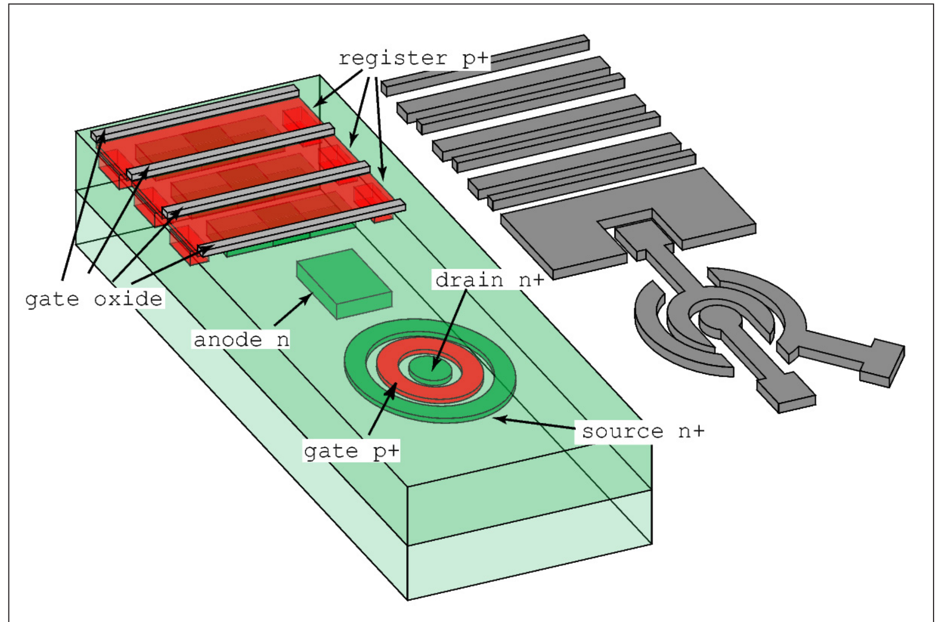

Figure 2.2: *Last pixel, anode and first FET as shown in fig. 2.1 with the aluminum contacts removed. The contact implants of the JFET and the p+ register implants together with the intermediate SiO_2 layers are visible. Between the JFET and the pixel structure is the anode n–implant.*

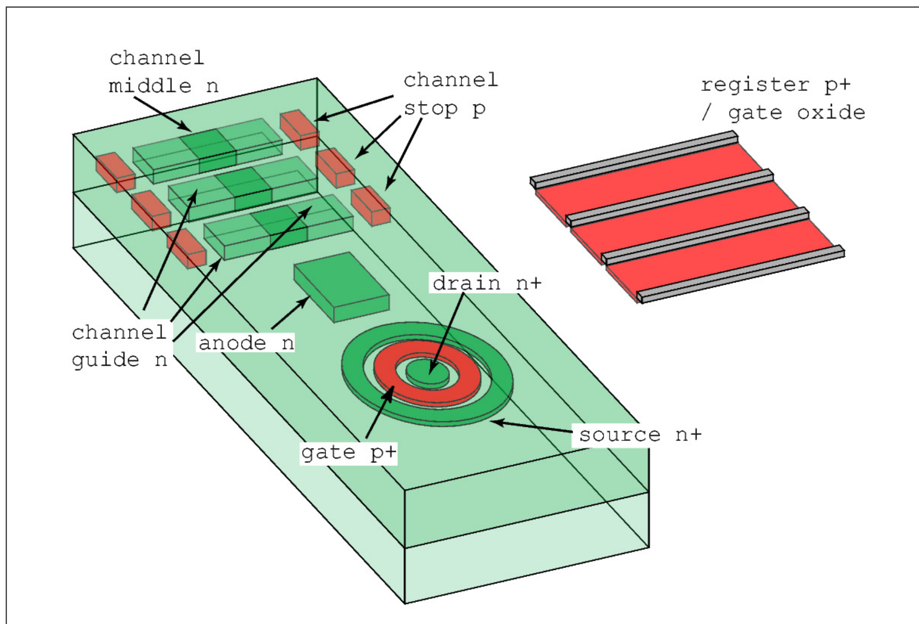

Figure 2.3: *Further removing the p+ register contacts and gate oxides shows the channel stop and channel guide implants. In the middle of the channel stops, the dopant concentration is increased to focus electrons to the middle of a channel.*

With these voltages, the front side of the pnCCD is depleted from the p+ registers and the rest of the bulk is depleted from the p+ back contact. Due to their high acceptor concentration, the p+ contacts are not depleted except a layer of 200 nm in the register implants and a layer of 5 nm in the back side implant (section 1.2.1 and equation 1.2). All implants on the front side are completely depleted except the p+ register contacts. Therefore, the electric potential in the depleted bulk is formed by the voltages at the p+ contacts and at the MOS–gates and by the space charges in the depleted n– and p– implants.

The uniform n–implant with a thickness of 7 µm to 10 µm on the register side creates a vertical potential minimum for electrons in a depth of roughly 7 µm, compare figure 2.4, 2.2 and 2.3. This potential minimum defines the storage depth for signal electrons in the vertical direction (section 2.2).

The positive space charge of depleted n–implants attracts electrons while the negative space charge of depleted p–implants pushes electrons away. In terms of the electric potential, n–implants form local potential minima for electrons and p–implants form local potential maxima for electrons. The potential minima for electrons are thus located below the channel notches.

In the charge transfer direction, the lateral electric potential is modulated by the voltages of the p+ register contacts and the voltages of the MOS–gates. The storage minima of the pixels are located below the register contacts with a more positive voltage e.g. -15 V if the barrier voltage is -20 V, figure 2.4. Signal charge can be stored below one or two of three registers. In the case of storage below two registers, the middle of the potential minimum lies below the MOS–gate between the two storage registers.

A voltage of 0 V is applied to the aluminum contacts of the MOS–gates. Therefore, they form local potential minima for electrons directly at the surface. In the storage depth of 7 µm however, the MOS–gates cause much smaller modulations of the electric potential than the p+ registers. This results from the small size of the MOS–gates relative to the p+ registers. Compared to the storage minima created by the p+ registers, the MOS–gates only cause small 'dips' in the electric potential (figure 2.4).

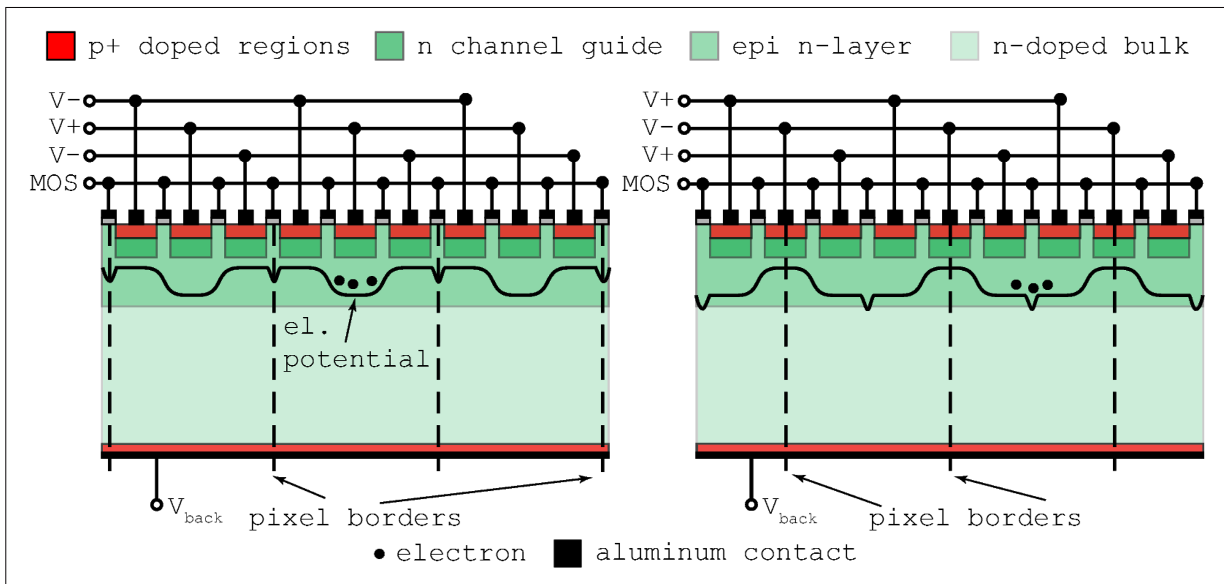

Figure 2.4: *Single– to the left and double–register storage to the right in a three phase pnCCD. The dashed lines show the pixel borders, V- is the voltage below non storage registers, V+ is the less negative voltage below storage registers and V_{back} the back contact voltage. Independent of the storage mode, a pixel always has the same total size of three registers.*

A qualitative view of the electric potential in three dimensions is obtained if the descriptions of the potential structure are combined for the vertical direction, the transfer direction and the line direction: In each pixel, the potential minimum for electrons is located in a depth of 7 µm to 10 µm below the one or two storage registers and in the middle of a channel at the n–doped notch implant.

Thus, the pixel structure is electrically defined by the external boundary conditions, i.e. the voltages at the electric contacts, and by the geometry and the ion concentrations of the implants on the register side.

2.1.1.1 The function of the MOS–gates

The MOS–gates between the p+ register contacts have two purposes: I. Electrons which are thermally generated by surface defects are attracted to the silicon–oxide interface. Therefore they cannot drift into the storage minima of the pixels and mix with the signal electrons. II. The insulation of the p+ registers is improved. The positive space charge of the depleted n–silicon between the p+ registers already creates a small potential barrier for holes. Keeping the surface potential near 0 V further increases this potential barrier. Parasitic hole currents between neighboring p+ registers are thus prevented even in the case of large register voltage differences, e.g. 10 V.

Defect states at the silicon surface act as generation centers for electrons. In the p+ contacts, these electrons recombine with holes. Below the MOS–gates, they form very thin conducting charge layers (section 1.2.2) if the electric potential at the silicon–oxide interface is more positive than in the surrounding silicon bulk. This condition is realized with a voltage of 0 V at the aluminum surface contacts of the MOS–gates. The equilibrium of the electron concentration is reached if the generation rate equals the rate of electrons which diffuse along the MOS–gates to regions with a lower concentration. In order to collect the generated electrons, the conducting electron layers below the MOS–gates are contacted with n+ implants at the sides of the pixel array. Aluminum layers on these n+ implants provide external electric connections. Due to the continuous electron generation, the expected voltage at the oxide–silicon interface is slightly below the n+ contact voltage of 0 V.

2.1.2 The readout structure of a channel

The readout node of each channel is realized as the combination of a n–doped contact and a n–channel JFET. Signal electrons are shifted out of the first pixel and into the anode. The anode is at a more positive potential than the storage minimum in the n–doped channel notch implants. Therefore, it forms a local potential minimum for the signal electrons.

An aluminum contact on top of the readout anode connects it with the p–doped gate of the circular n–channel JFET, figure 2.1. The JFET consists of a disk shaped n+ implant for the drain, a ring shaped p+ gate implant and a ring shaped n+ implant for the source (figure 2.3). Source, gate and drain are contacted with aluminum layers and insulated with oxide layers (the oxide layers are not shown in figures 2.1 to 2.3). The dopant concentration

in the source, gate and drain implants is so large that these regions are conducting. Thus, the aluminizations can be interrupted for short distances, e.g. the source aluminum contact which consists of two half ring shaped segments.

The conducting channel of the JFET is a circular n–doped region below the surface n+ and p+ contacts. In the operation mode used for the pnCCD, the drain is set to 4 V. In the XMM type CCD, the gate is biased to 0 V by a reset JFET switch. The more recent pnCCD designs use a MOS switch which is connected to a reset anode. The source–drain current is regulated by the external current source in the CAMEX readout ASIC (section 1.5.3). In the specific JFET design employed in a pnCCD, the JFET is operated in saturation mode where the n–channel is partly depleted near the drain due to the positive drain voltage relative to the gate.

Since the source–drain current is fixed by the current source, gate voltage changes force a modulation of the source potential. The source follows the gate voltage changes in order to keep the current at the regulated value. Electrons on the anode/gate capacitance cause a negative voltage drop which results in a source voltage drop of the same value [14]. The integrated JFET provides a transformation of the high impedance anode signal to a low impedance output signal. The output is further amplified, filtered and finally multiplexed to an ADC by the CAMEX readout ASIC (section 1.5.3).

2.2 Electric potential in the bulk

An approximation of the electric potential in a pnCCD can be given as an extension of the electric potential solution presented in section 1.5.1. There, the solution of the electric potential in a homogeneously n–doped and depleted silicon substrate is discussed. Equation 1.12 represents the electric potential in a structure with planar p+ contacts on both sides and a small n+ contact at the rim of the front side as shown in figure 1.9.

The only difference between the case discussed in section 1.5.1 and the structure presented here is the additional n–doped layer on the register side of the pnCCD substrate. This 'epi' or 'high–energy' n–layer is introduced in section 2.1.1. Its purpose is the definition of the storage depth of the signal electrons in the vertical direction, a few microns below the register side.

Here, the pnCCD bulk is simplified as the structure shown in figure 2.5. The Poisson equation can then be stated for the regions 1 and 2 as follows:

$$\frac{\partial^2 \varphi_1}{\partial z^2} = -\frac{\rho_1}{\epsilon_0 \epsilon_{\mathrm{Si}}} \quad ; \quad 0 \leq z \leq z_{\mathrm{epi}} \tag{2.1}$$

$$\frac{\partial^2 \varphi_2}{\partial z^2} = -\frac{\rho_2}{\epsilon_0 \epsilon_{\mathrm{Si}}} \quad ; \quad z_{\mathrm{epi}} \leq z \leq z_{\mathrm{b}} \tag{2.2}$$

$\rho_1 = -\mathrm{e} \cdot N_{\mathrm{D}}(1)$ is the space charge density in region 1, $\rho_2 = -\mathrm{e} \cdot N_{\mathrm{D}}(2)$ is the space charge density in region 2, ϵ_0 is the permittivity of vacuum, ϵ_{Si} is the relative permittivity of silicon, φ_1 and φ_2 are the values of the electric potential in region 1 and 2, z_{epi} is the thickness of region 1 (or the epi n–layer) and z_{b} is the thickness of the device. The following

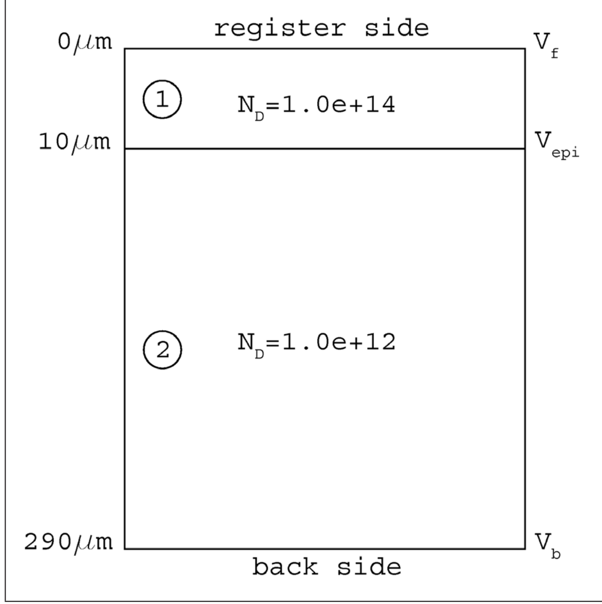

Figure 2.5: *Sketch of the region where the electric potential shown in equations 2.5 and 2.6 is defined. 280* µm *thick, weakly n–doped silicon substrate is covered by a 10 µm thick epitaxial silicon layer with a higher donor concentration. The epi–layer can be substituted by an implant of similar concentration. A high implantation energy deposits the donor ions in a depth of up to 10* µm. *The positive space charge in the epi– or high energy implant layer creates a potential minimum for electrons close to the front side. This potential minimum is located in in a depth of about 7* µm.

boundary conditions apply:

$$\varphi_1(z=0) = V_\mathrm{f} \quad ; \quad \varphi_2(z=z_\mathrm{b}) = V_\mathrm{b} \tag{2.3}$$

$$\frac{\partial\varphi_1(z=z_\mathrm{epi})}{\partial z} = \frac{\partial\varphi_2(z=z_\mathrm{epi})}{\partial z} \quad ; \quad \varphi_1(z=z_\mathrm{epi}) = \varphi_2(z=z_\mathrm{epi}) \tag{2.4}$$

In this case, $z = 0$ corresponds to the register contact side and z_b corresponds to the back p+ contact. V_f is the voltage at the front contact and V_b is the back contact voltage. The two parts of the solution are, with index 1 in the epi–layer and index 2 in the rest of the bulk:

$$\varphi_1(z) = -\frac{\rho_1}{2\epsilon}\cdot z^2 + \left[\frac{V_\mathrm{b}-V_\mathrm{f}}{z_\mathrm{b}} + \frac{\rho_2}{2\epsilon}\cdot z_\mathrm{b} - \left(\frac{\rho_2}{\epsilon}-\frac{\rho_1}{\epsilon}\right)\left(z_\mathrm{epi}-\frac{z_\mathrm{epi}^2}{2z_\mathrm{b}}\right)\right]\cdot z + V_\mathrm{f} \tag{2.5}$$

$$\begin{aligned}\varphi_2(z) &= -\frac{\rho_2}{2\epsilon}\cdot z^2 + \left[\frac{V_\mathrm{b}-V_\mathrm{f}}{z_\mathrm{b}} + \frac{\rho_2}{2\epsilon}\cdot z_\mathrm{b} + \left(\frac{\rho_2}{\epsilon}-\frac{\rho_1}{\epsilon}\right)\frac{z_\mathrm{epi}^2}{2z_\mathrm{b}}\right]\cdot z \\ &\quad - \left(\frac{\rho_2}{2\epsilon}-\frac{\rho_1}{2\epsilon}\right) z_\mathrm{epi}^2 + V_\mathrm{f}\end{aligned} \tag{2.6}$$

Figure 2.6 shows the electric potential in the structure shown in figure 2.5 as a function of the depth. The bulk donor concentration is 10^{12} cm^{-3} and the donor concentration in the epi layer is 10^{14} cm^{-3}. Two graphs are plotted, both with a front contact voltage of -15 V but with different back contact voltages of -100 V and -200 V. Differentiation of equation 2.5 and 2.6 delivers the depth z_max of the potential maximum. An appropriate choice of the bulk and epi–layer donor concentrations and contact voltages keeps z_max inside the epi layer near z_epi. Figure 2.7 shows the variation of the storage depth given by z_max as a function of the back contact voltage in the structure shown in figure 2.5. The front contact voltage is -15 V. Two graphs show the value of z_max both for donor concentrations of 10^{14} cm^{-3} and

of $5 \cdot 10^{13}$ cm^{-3} in the front side n–layer. With $V_\mathrm{f} = -15$ V and $V_\mathrm{b} = -100V$ the potential minimum for electrons lies in a depth of $z_\mathrm{max} = 9.3$ µm. If the back contact voltage is lowered to $V_\mathrm{b} = -200$ V, the potential minimum z_max for electrons moves from a depth of 9.3 µm to a depth of 7.0 µm. Although the absolute value of the back contact voltage has been doubled, the depth of the electric potential maximum still lies in the desired range from 7 µm to 10 µm.

In the case of a large amplitude of 10 V, the register voltage periodically changes between $V_\mathrm{high} = -10$ V and $V_\mathrm{low} = -20$ V. The corresponding results for z_max which are shown in figure 2.7 on the right hand side were obtained with a back contact voltage of -200 V. In the case of a donor concentration of 10^{14} cm^{-3} in the front side n–layer, z_max varies between 6.9 µm and 7.2 µm. This is a change of only 0.3 µm which means that the transfer channel for electrons is defined in a depth of 7 µm. Signal electrons are thus transferred in a depth of 7 µm over a wide range of register voltages. Both of the plots shown in figure 2.7 also show the variation of z_max for a donor concentration of $5 \cdot 10^{13}$ cm^{-3} in the front side n–layer. These results indicate that the value of z_max becomes more sensitive to variations of the back or front contact voltage if the donor concentration in the front side n–layer is decreased.

2.2.1 Drift and diffusion of electric charge

The basic principle of any semiconductor radiation detector design is the measurement of signal charge carriers generated by interacting photons. Here, we discuss the special case of X–ray photons in the energy range from $E_\mathrm{X-ray} = 0.1$ keV to $E_\mathrm{X-ray} = 10$ keV. The absorption process of photons in this energy range is discussed in section 1.3. After the absorption of an X–ray photon the generated electron hole pairs are located in a small spherical volume with a radius from 170 nm for $E_\mathrm{X-ray} = 0.1$ keV to 400 nm for $E_\mathrm{X-ray} =$ 10 keV. Near the radiation entrance window, the drift field is larger than 3000 V/cm. Electrons drift with a velocity of $v_\mathrm{e} = -\mu_\mathrm{n} \cdot \mathcal{E}$ where μ_n is the electron mobility and $\mathcal{E}$ is the drift field strength. At room temperature, the electron mobility in silicon is $\mu_\mathrm{n} = 1350\mathrm{cm}^2/\mathrm{Vs}$. The signal electrons thus leave an electron hole cloud with a diameter of 1 µm in $25 \cdot 10^{-12}$ s.

In a pnCCD, the hole cloud drifts to the back side and enters the p+ back contact. The electron cloud drifts to the front side and is collected in the storage cells of the pixel structure. During its drift to the register side, the signal electron cloud expands due to diffusion and electrostatic repulsion. Drift, diffusion and electrostatic repulsion of electron and hole clouds are described by the continuity equations for electrons and holes [3]:

$$\frac{\partial n}{\partial t} = \mu_\mathrm{n} \nabla n \cdot \vec{\mathcal{E}} + \mu_\mathrm{n} n \nabla \vec{\mathcal{E}} + D_\mathrm{n} \nabla^2 n \tag{2.7}$$

$$\frac{\partial p}{\partial t} = -\mu_\mathrm{p} \nabla p \cdot \vec{\mathcal{E}} - \mu_\mathrm{n} p \nabla \vec{\mathcal{E}} + D_\mathrm{p} \nabla^2 p \tag{2.8}$$

Where n and p are the electron and hole charge densities, μ_n and μ_p are the electron and hole mobility values, $\vec{\mathcal{E}}$ is the electric field vector, $D_\mathrm{n} = (kT/e) \cdot \mu_\mathrm{n}$ is the diffusion

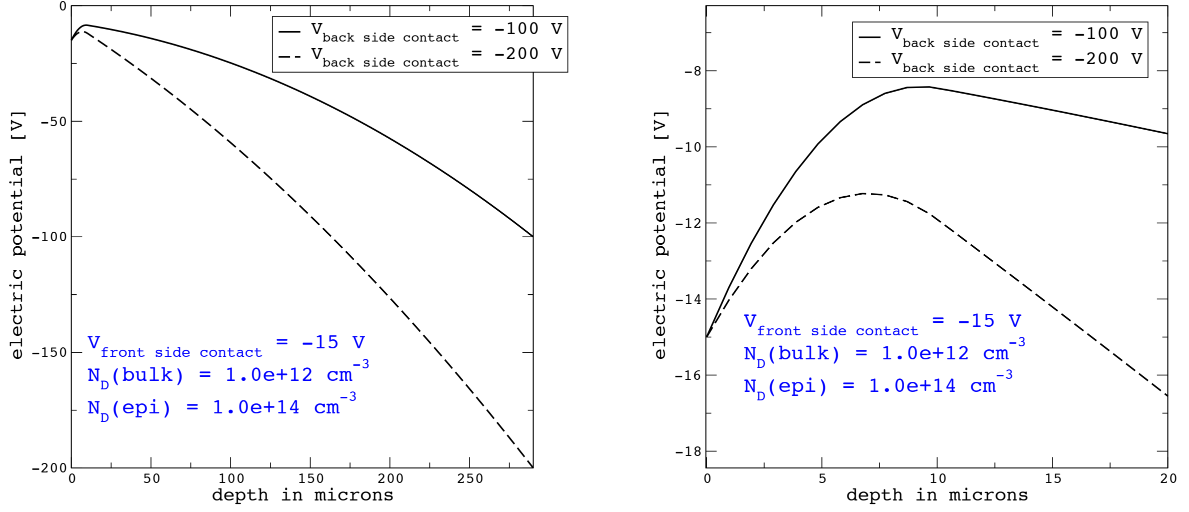

Figure 2.6: *Results of the electric potential solution given by the equations 2.5 and 2.6. The values are calculated for the geometry and the space charge densities of the structure shown in figure 2.5. The front contact at a depth of 0* µm *corresponds to a register contact in a pnCCD. In the plot on the right hand side, the electric potential is plotted up to a depth of 20* µm*. Although the value of the electric potential in the maximum changes by nearly 4* V*, the depth of the maximum only changes by about 3* µm*.*

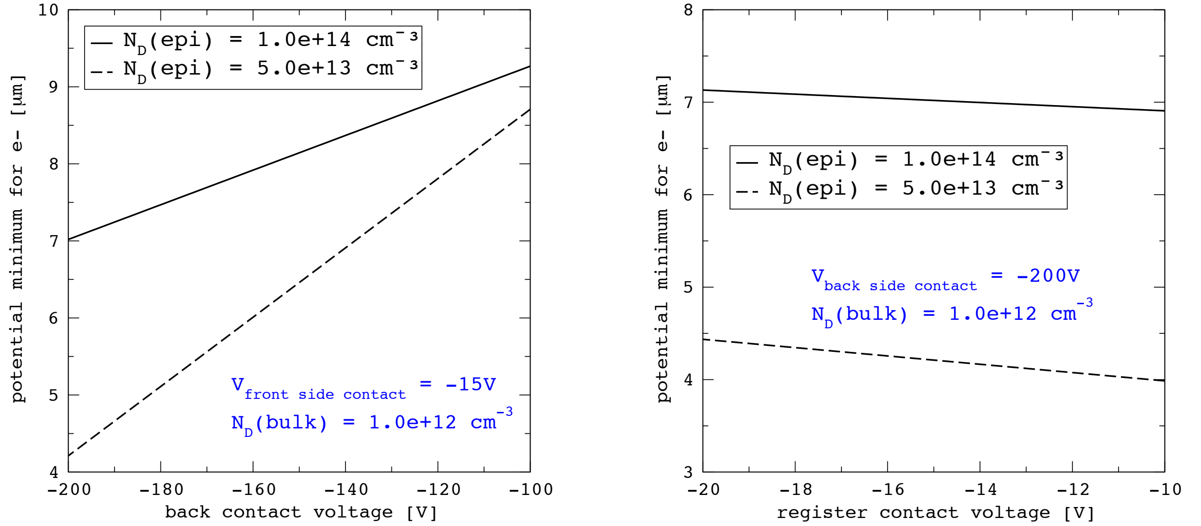

Figure 2.7: *Position variation of the potential minimum for electrons as a function of the contact voltages in the structure shown in figure 2.5. Electrons are in a potential minimum where the electric potential given by the equations 2.5 and 2.6 reaches its maximum value. On the left hand side, the position of the potential minimum for electrons is shown as a function of the back contact voltage. On the right hand side, the position of the potential minimum for electrons is shown as a function of the front side contact voltage. If the donor concentration in the epi–layer is decreased, the position of the potential maximum for electrons becomes more sensitive to changes of the contact voltages.*

coefficient for electrons, $D_{\rm p} = (kT/e) \cdot \mu_{\rm p}$ is the diffusion coefficient for holes and e is the elementary charge.

The mobility $\mu_{\rm n}$ of electrons in silicon depends on the temperature, the dopant concentration and also on the electric field [24]. Measurements and numeric simulations of the electron mobility as a function of the electric field strength are presented in [25, 26, 27]. As a general conclusion, the mobility does not depend on the electric field for field strengths below 4000 V/cm at a device temperature around 200 K or higher. The saturation value of the electron drift velocity is 10^7 cm/s. For field strengths below 4000 V/cm, the electron mobility can be calculated with the model presented in [28]. This mobility model considers both the temperature and the dopant concentration in silicon. It turns out that the low donor concentration of 10^{12} cm^{-3} and less in the bulk of a pnCCD has a negligible influence on the electron mobility. The temperature dependence of $\mu_{\rm n}$ is strong, close to room temperature it varies roughly with $(T/300\ \mathrm{K})^{-2.4}$. Compared to the value of $\mu_{\rm n} = 1350$ cm^2/Vs at room temperature, $\mu_{\rm n}$ has a value of 3612 cm^2/Vs at a device temperature of -80 °C or 193 K respectively.

For the further discussion, we restrict to the continuity equation 2.7 for electrons. In a homogeneous drift field, the charge distribution in an electron cloud is radially symmetric [3]. In order to find the charge distribution in an electron cloud, it is thus sufficient to look at one coordinate direction of equation 2.7. If the drift field $\vec{\mathcal{E}}$ is parallel to the x axis, the one dimensional simplification of equation 2.7 is given by:

$$\frac{\partial n}{\partial t} = \mu_{\rm n} \frac{\partial n}{\partial x} \cdot \vec{\mathcal{E}}_{\rm x} + \mu_{\rm n} n \frac{\partial \vec{\mathcal{E}}_{\rm x}}{\partial x} + D_{\rm n} \frac{\partial^2}{\partial x^2} n \tag{2.9}$$

Analytical solutions of this equation can be given if either electrostatic repulsion or diffusion is neglected [29]. The analytical solutions for the expansion of an electron cloud due to diffusion or electrostatic repulsion indicate which one is the stronger effect and give a first estimate of the charge cloud expansion speed.

2.2.1.1 Charge cloud expansion due to diffusion

If the electrostatic repulsion of the electrons in the charge cloud is neglected, equation 2.9 reduces to [3, 29]:

$$\frac{\partial n}{\partial t} = \mu_{\rm n} \frac{\partial n}{\partial x} \mathcal{E} + D_{\rm n} \frac{\partial^2}{\partial x^2} n \tag{2.10}$$

The solution is a Gaussian charge distribution which moves with a constant velocity along the x–axis:

$$n(x;t) = \frac{n_0 \sqrt{t_0}}{\sqrt{t + t_0}} \cdot e^{-(x + \mu_{\rm n} \mathcal{E} \cdot t)^2 / (4 D_{\rm n} \cdot (t + t_0))} \tag{2.11}$$

$n(x;t)$ is an expanding Gaussian charge cloud with $-\mu_{\rm n}\mathcal{E}$ as the drift velocity of its center. At the time t_0, the charge concentration in the center of the electron cloud is n_0. The sigma of the Gaussian is given by $\sigma_{\rm radius}(t) = \sqrt{2 D_{\rm n} \cdot (t + t_0)}$. It is both mathematically and physically correct to assume that the charge cloud expansion begins at the time $t_0 > 0$ with a sigma of $\sigma_{\rm radius}(t_0) = \sqrt{2 D_{\rm n} \cdot t_0}$. The total time of expansion is then $t_{\rm tot} = t + t_0$.

A physical peculiarity of charge cloud expansion due to diffusion is that $\sigma_{\mathrm{radius}}(t)$ does not depend on the total amount of charge. The reason for this property of the solution 2.11 becomes clear if equation 2.10 is divided by n. Then, the changes of n with time $\partial n/\partial t$ and with space $\partial n/\partial x$ are both normalized to the absolute value of the concentration n. Only the relative changes of n with time and space determine the (diffusion) expansion and motion of the charge cloud.

As an example, we calculate the expansion of an electron cloud at room temperature in silicon. In this case μ_{n} has a value of 1350 cm^2/Vs and sigma is given by $\sigma_{\mathrm{radius}}(t_{\mathrm{tot}}) = \sqrt{2 \cdot 0.0259\ \mathrm{V} \cdot 1350\ \mathrm{cm^2/Vs} \cdot t_{\mathrm{tot}}}$. After 1 ns sigma has a value of 2.6 µm, after 10 ns sigma has a value of 8.4 µm.

2.2.1.2 Charge cloud expansion due to electrostatic repulsion

If the diffusion of the charge carriers is neglected, the charge cloud expansion is only due to electrostatic repulsion. This case is analytically solved in ref. [29]. Integration of equation 2.7 in the spherical coordinates θ and ϕ while assuming that the external electric field is zero delivers an equation for the charge Q as a function of the radius r and the time t:

$$-\frac{\partial Q(r;t)}{\partial t} = Q(r;t)\frac{\partial Q(r;t)}{\partial r} \cdot \frac{1}{r^2} \cdot \frac{\mu_{\mathrm{n}}}{4\pi\epsilon} \tag{2.12}$$

Where $Q(r;t)$ is the amount of charge in the sphere with radius r and ϵ is short for $\epsilon_{\mathrm{Si}}\epsilon_0$. Equation 2.12 has the following solution:

$$Q(r;t) = \frac{r^3}{\frac{3\mu_{\mathrm{n}}}{4\pi\epsilon} \cdot t} \tag{2.13}$$

This is not yet the final solution since it does not consider the amount of charge in the electron cloud. The correct physical solution is found from the requirement that the total charge $Q_0 = N \cdot e$ is constant and that the charge is confined in a sphere with radius r_{max}:

$$Q(r_{\mathrm{max}};t) = N \cdot e = \frac{r_{\mathrm{max}}^3}{\frac{3\mu_{\mathrm{n}}}{4\pi\epsilon} \cdot t} \quad \Leftrightarrow \quad r_{\mathrm{max}} = \sqrt[3]{\frac{3\mu_{\mathrm{n}} \cdot Ne}{4\pi\epsilon} \cdot t} \tag{2.14}$$

Inside r_{max}, the charge density is constant so the charge cloud is like a 'ball' with uniform density.

In oder to compare the charge cloud expansion due to electrostatic repulsion with the expansion due to diffusion, the charge cloud size is calculated with equation 2.14 and the example values given in section 2.2.1.1 above. For the size comparison with the charge cloud radius r_{max}, the Gaussian charge cloud due to diffusion expansion is parameterized by the sigma radius $\sigma_{\mathrm{radius}}(t_{\mathrm{tot}})$. The amount of charge is assumed to be the equivalent of a 277 eV (C–Kα, 76 e$^-$) photon and of a 5415 eV (Cr–Kα, 1484 e$^-$) photon, the mobility is $\mu_{\mathrm{n}} = 1350$ cm^2/Vs at a temperature of 300 K. After 1 ns, the charge cloud radius r_{max} is 1.6 µm with 76 e$^-$ and 4.2 µm with 1484 e$^-$. After 10 ns, the charge cloud radius r_{max} is 3.3 µm with 76 e$^-$ and 9.0 µm with 1484 e$^-$.

A comparison with the results for diffusion expansion of $\sigma_{\text{radius}}(1 \text{ ns}) = 2.6$ µm and $\sigma_{\text{radius}}(10 \text{ ns}) = 8.4$ µm shows that for a photon energy of 277 eV, diffusion dominates the charge cloud expansion. For the higher photon energy of 5415 eV which is in the middle of the typical photon energy range of pnCCDs, electrostatic repulsion dominates the charge cloud expansion for an expansion time of 10 ns and less. Exact solutions which consider both diffusion and electrostatic repulsion for the charge cloud expansion are presented in section 6.2. The exact solutions are obtained from a numerical simulation of the charge cloud expansion with TeSCA.

2.2.1.3 Drift time equation in n–doped silicon

Here, the drift time equation of electrons is solved inside a uniformly doped silicon volume. This equation gives the drift distance of signal electrons inside the uniformly doped bulk of a pnCCD after a given time interval t. The drift velocity of an electron is given by $v = -\mu_{\text{n}} \cdot \mathcal{E}$. If the electric field depends on the coordinate x, v is also a function of x: $v(x) = -\mu_{\text{n}} \cdot \mathcal{E}(x)$. Then, the drift time along an infinitesimal path element dx is given as $dt = dx/v(x)$. Integration of dt yields the drift time between the points x_1 and x_2:

$$t = \int_{x_1}^{x_2} \frac{dx}{v(x)} \tag{2.15}$$

$v(x)$ is given as $v(x) = -\mu_{\text{n}} \cdot \mathcal{E}(x)$, $\mathcal{E}(x)$ in a pnCCD is known from the analytical solutions 2.5 and 2.6 or from a numerical simulation. Inside the bulk, without the influence of the front side registers and implants, $\mathcal{E}(x)$ is the linear electric field of a superposed parabolic and linear potential. Thus $\mathcal{E}(x)$ is given as $\mathcal{E}(x) = \mathcal{E}(x_0) + \mathcal{E}'(x_0) \cdot x$ where x is the distance from x_0 and $\mathcal{E}'(x_0)$ is the field derivative at x_0. Now x_1 and x_2 are defined as distances from x_0 and x_0 is the new coordinate origin. Insertion in 2.15 gives:

$$t = \int_{x_1}^{x_2} \frac{1}{-\mu_{\text{n}}(\mathcal{E}(x_0) + \mathcal{E}'(x_0) \cdot x)} dx \tag{2.16}$$

Replacing $u(x) = -\mu_{\text{n}}(\mathcal{E}(x_0) + \mathcal{E}'(x_0) \cdot x$ in the integral 2.16 gives the integral that has to be solved:

$$t = -\int_{(-\mu_{\text{n}}(\mathcal{E}(x_0)+\mathcal{E}'(x_0)\cdot x_1)}^{(-\mu_{\text{n}}(\mathcal{E}(x_0)+\mathcal{E}'(x_0)\cdot x_2)} \frac{1}{u} \frac{1}{\mathcal{E}'(x_0) \cdot \mu_{\text{n}}} du \tag{2.17}$$

The solution to 2.17 is:

$$t = \frac{-1}{\mathcal{E}'(x_0) \cdot \mu_{\text{n}}} \ln \left(\frac{\mathcal{E}(x_0) + \mathcal{E}'(x_0) x_2}{\mathcal{E}(x_0) + \mathcal{E}'(x_0) x_1} \right) \tag{2.18}$$

Setting $x_1 = 0$ and $x_2 = \Delta x(t)$ and rearranging the solution in 2.18 to obtain $\Delta x(t)$ finally results in:

$$\Delta x(t) = \frac{\mathcal{E}(x_0)}{\mathcal{E}'(x_0)} \left(\exp(-\mathcal{E}'(x_0) \mu_{\text{n}} t) - 1 \right) \tag{2.19}$$

The drift distance $\Delta x(t)$ is negative because electrons drift from the back side where x is positive to the front side where x is defined to be 0. The electric field derivative at the coordinate x_0 is given by $\mathcal{E}'(x_0) = \mathrm{e} \cdot N_\mathrm{D}(x_0)/(\epsilon_0 \epsilon_\mathrm{Si})$. $N_\mathrm{D}(x_0)$ is the donor concentration in the bulk at the position x_0, e is the elementary charge, $\epsilon_0\epsilon_\mathrm{Si}$ is the permittivity in silicon.

As an example, the drift time from the back side to the transfer channel is calculated for the charge cloud generated by a 5415 eV photon and the device discussed in section 6.1. 5415 eV X–rays have an attenuation length of 23 µm in silicon. The device thickness is 280 µm, so the drift starts in a depth of typically 257 µm from the front side. A typical operating temperature for this pnCCD is -80 °C or 193 K respectively. According to the mobility model given in [28, 24], the mobility in weakly n–doped silicon with $N_\mathrm{D} \leq 10^{12}$ cm^{-3} and at $T = 193$ K is $\mu_\mathrm{n} = 3612$ cm^2/Vs. The pnCCD discussed in section 6.1 has a bulk donor concentration of $0.75 \cdot 10^{12}$ cm^{-3}, the high energy n–implant on the front side can be approximated as a 10 µm thick layer with a donor concentration of $1.0 \cdot 10^{14}$ cm^{-3}. Inside the bulk, the electric field derivative is thus $\mathcal{E}'(x) = 115012$ Vcm^{-2}. With a front contact voltage of -15 V and a back contact voltage of -90 V, equation 2.6 delivers a field of $\mathcal{E}(x = 257\ \mu\mathrm{m}) = 4296$ V/cm in the start depth of 257 µm. The drift time t over a distance $\Delta x(t) = 247$ µm to a depth of 10 µm is $t = 2.6$ ns according to equation 2.19.

2.2.1.4 Combined drift and expansion of a charge cloud

The results from the preceding section 2.2.1.1, 2.2.1.2 and 2.2.1.3 can be combined in order to obtain the size of a signal electron cloud as it reaches the register side. Diffusion, electrostatic repulsion and drift of a charge cloud are then described by the three equations:

$$\sigma_\mathrm{radius}(t) = \sqrt{\frac{2kT}{e} \cdot \mu_\mathrm{n} \cdot t} \quad ; \quad r_\mathrm{max}(t) = \sqrt[3]{\frac{3 \cdot Ne}{4\pi\epsilon} \cdot \mu_\mathrm{n} \cdot t} \quad ;$$

$$t(\Delta x) = \frac{-1}{\mathcal{E}'(x_0) \cdot \mu_\mathrm{n}} \ln\left(\frac{\mathcal{E}(x_0) + \mathcal{E}'(x_0) \cdot \Delta x}{\mathcal{E}(x_0)}\right) \tag{2.20}$$

The last equation for $t(\Delta x)$ can be inserted in the equations for $\sigma_\mathrm{radius}(t)$ and $r_\mathrm{max}(t)$. This gives the charge cloud sigma or radius as a function of the (negative) drift distance Δx. The electron mobility μ_n is canceled out in this case and σ_radius or r_max are only a function of Δx and the electric field $\mathcal{E}(x_0)$ and its derivative $\mathcal{E}'(x_0)$.

Extending the calculation of the drift time of the previous section with the expansion of a charge cloud delivers an estimate of the signal charge cloud size directly before it is collected in the storage cells of the pixel structure. For a photon energy of 5415 eV or 1484 e$^-$ respectively, a temperature of 193 K and a mobility of 3612 cm^2/Vs, the following results are obtained: The value $\sigma_\mathrm{radius}(t = 2.6\ \mathrm{ns})$ due to diffusion expansion is 5.6 µm. Electrostatic repulsion leads to a radius $r_\mathrm{max}(t = 2.6\ \mathrm{ns}, E_\mathrm{X-ray} = 5415\ \mathrm{eV})$ of 8.0 µm. As already shown in the example in section 2.2.1.2, electrostatic repulsion dominates the expansion of a charge cloud with 1484 electrons if the expansion time is in the range of 2 ns.

Chapter 3

The mesh experiment

In a X–ray pixel scan, the output signal of a pixel and its neighbors is recorded together with the conversion position of each photon. The conversion position is controlled by the position of a narrow X–ray beam. The spatial resolution of the scan is determined by the size of the beam pencil and by the spacing of the scanning steps. The photon energy is determined by the used X–ray source, preferably a X–ray tube which emits the line spectrum of a specific target. With a X–ray pixel scan, a map which shows the signal pulse height recorded in the pixel as a function of the photon conversion position can be created for the given X–ray photon energy.

The mesh experiment is a method that facilitates a 'virtual' scan of the pixels of array detectors, e.g. pnCCDs. In this virtual pixel scan, all scanning steps are performed in parallel. Instead of scanning only one pixel of the detector, many pixels are used where each pixel delivers the data of one scanning step. The data of all pixels is then rearranged in the map of a single 'virtual' pixel. All pnCCD pixels have the same physical structure and therefore react in the same way to the conversion of a X–ray photon of a given energy at a given position. Thus, a virtual pixel scan of a pnCCD delivers a pixel map which is representative for the response of every pixel.

3.1 Function principle

The principle setup of a mesh-experiment is rather simple: A metal foil (the 'mesh') with holes aligned to a rectangular grid is placed close to the surface of a CCD with a rectangular pixel structure, figure 3.1. X–ray photons can only penetrate the mesh at the locations of the holes. In the simplest setup, the distance of the holes equals the pixel pitch. In any case the hole grid of the mesh is slightly tilted at a fixed angle of about $1°$ to $10°$ with respect to the pixel raster of the CCD. Every hole thus has a different position relative to the pixel below. The distribution of the relative hole positions can be seen in the 'coverage map' of a virtual pixel which shows for all holes the hole position relative to the pixel below. If the virtual pixel scan with a given array size and rotation angle of the mesh is correctly done, the relative hole positions are distributed over the whole area of the pixel

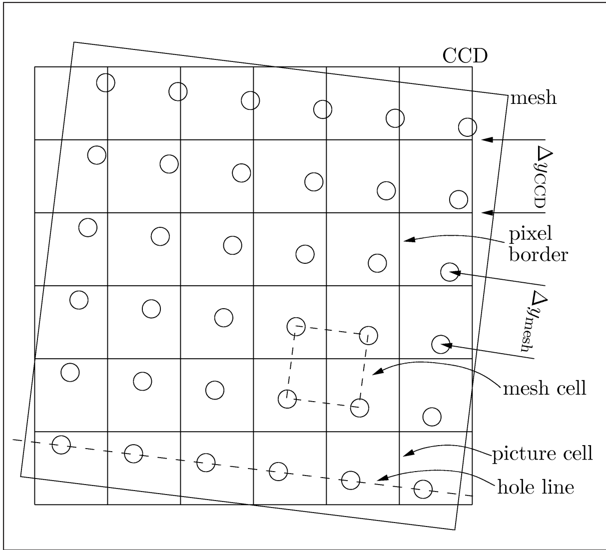

Figure 3.1: *Principle of the experiment. There are nearly vertical and nearly horizontal hole lines if the rotation angle is less than 45°.*

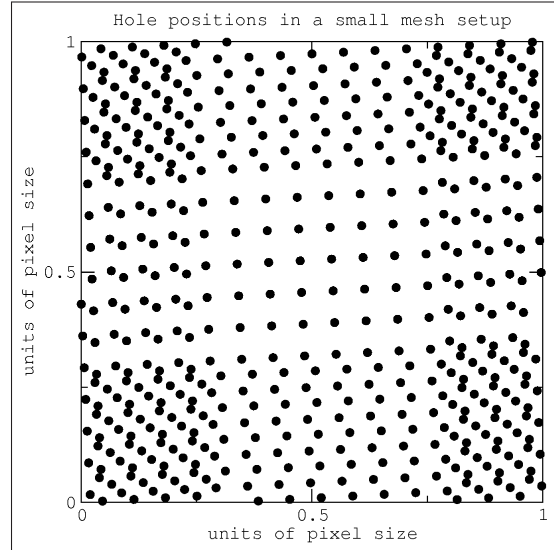

Figure 3.2: *Coverage map. This one is generated from a small frame area, one can see that some hole positions are close together.*

coverage map as shown in figure 3.2. Optical inspection of the coverage map map shows the occurring distances of neighboring hole positions. The best possible spatial resolution for a given sub–region of the coverage map is limited by the distances of neighboring holes in this region.

A variation of the 'single pitch' mesh experiment where the hole distance equals the pixel size is the 'multi pitch' experiment where the hole distance is an integer multiple of the pixel size. In the single pitch setup, a pixel may be covered by up to four holes, see the top row of figure 3.1 where each pixel is covered by two holes. If a pixel is covered by more than one hole, the photon conversion position is ambiguous. Photons detected in these pixels may not be associated to the hole they really passed through. The multi pitch setup has the advantage that each pixel is illuminated by maximally one mesh hole so that an ambiguity of the photon conversion position is impossible.

For the special case of the single pitch experiment, a data analysis method which avoids ambiguities of the photon conversion position was developed. This analysis makes use of the signal charge distribution over neighboring pixels. Ambiguities of the conversion position only occur if holes are located near the border or the corner of a pixel. The signal charge created by a photon incident on a pixel border or corner is distributed over the pixels facing the border or the corner. Therefore, the conversion position of a photon can be estimated to be near the border or the corner of the pixels which show a photon signal. The estimated conversion position can then be correlated with the closest hole position in order to find the exact conversion position of the photon.

In [2] the basic and first version of the mesh experiment is described, this publication

also introduces the name 'mesh-experiment'. Different realizations with the same basic principle are shown in [30] and [31].

3.1.1 Energy range and spatial resolution

The upper limit of the usable energy range in a mesh experiment setup is given by the X–ray energy at which the metal foil of the mesh becomes transparent. The spatial resolution is determined by the hole size and by the diffraction of X–ray radiation at the mesh holes.

The metal foil used for the mesh becomes more transparent for X-ray photons of higher energies. Depending on the material, thickness and geometry of the mesh, there is a threshold energy when the transmission due to the material thickness is equal to the pure geometric transmission defined by the diameter and distance of the holes. In this case, half of the incoming photons do not pass through the mesh holes and have an unknown conversion position. The transmission due to the hole geometry is:

$$I_{\text{geom}} = \frac{\pi \cdot r_{\text{h}}^2}{l_{\text{h}}^2} \cdot I_0 \tag{3.1}$$

where r_{h} is the mesh hole radius, l_{h} is the hole distance and I_0 is the incoming intensity. According to [32], page 988, the transmission due to absorption in the mesh material is:

$$I_{\text{transm}} = I_0 \cdot \exp(-\frac{4\pi\beta}{\lambda} \cdot w) = I_0 \cdot \exp(-2r_0\lambda N f_2 \cdot w) \tag{3.2}$$

where I_0 is the intensity of the incoming radiation, w is the material thickness, $4\pi\beta/\lambda$ is the linear absorption coefficient with $\beta = (r_0 \cdot \lambda^2 \cdot N f_2)/(2\pi)$, r_0 is the classical electron radius of $2.82 \cdot 10^{-15}$ m, λ is the wavelength, N is the number density of atoms and f_2 is the imaginary part of the atomic scattering factor.

Large values of the ratio $I_{\text{geom}}/I_{\text{transm}}$ indicate that most of the incoming photons pass through the mesh holes. A gold mesh with $r_{\text{h}} = 2.5$µm, $l_{\text{h}} = 150$µm and $w = 10$µm was used for all measurements. The geometric transmission is $I_{\text{geom}} = 8.7 \cdot 10^{-4}$ for this mesh geometry. Results for $I_{\text{geom}}/I_{\text{transm}}$ using the transmission values from [33] and [34] are shown in table 3.1. The table shows the effect of the increasing transparency of the gold

X-ray line	Fe-Lα	Cu-Lα	Al-Kα	W-Mα	Ti-Kα	Cr-Kα
energy in eV	705	930	1487	1775	4510	5415
I_{transm}	0.0	0.0	$1.25 \cdot 10^{-19}$	$6.74 \cdot 10^{-13}$	$3.77 \cdot 10^{-8}$	$1.67 \cdot 10^{-5}$
ratio $I_{\text{geom}}/I_{\text{transm}}$	$> 10^{16}$	$> 10^{16}$	$6.98 \cdot 10^{15}$	$1.29 \cdot 10^{9}$	$2.31 \cdot 10^{4}$	52.3

Table 3.1: *Ratio of geometrical transmission to transmission through a gold foil with a thickness of 10µm for the used X-ray energies.*

foil with an increasing X-ray energy. At 5415eV, 2% of the photons pass through the gold foil rather than through the mesh holes. A photon energy of 6404eV (Fe-Kα) was used to

investigate the effect of photons passing through the gold foil. Then the ratio $I_{\text{geom}}/I_{\text{transm}}$ is 1.17 and about half of the incoming photons pass directly through the gold foil. It was decided that it is still acceptable if 2% of all photons reaching the detector have an unknown conversion position. A ratio $I_{\text{geom}}/I_{\text{transm}} = 1.17$ at 6.4 keV however means that 46% of all detected photons passed through the gold foil instead of the mesh holes. In this case, the mesh becomes ineffective as a position filter for photons. The maximum photon energy used for the measurements is thus 5.4 keV (Cr-Kα).

Diffraction at the mesh holes was evaluated with the numerical calculation method described in [35]. The size of the illuminated spots on the sensor is a function of the wavelength, the hole radius and the distance from the hole to the sensor. The distance of 4 m between the radiation source and the hole is large compared to the hole radius. Thus the diffraction theory of Fresnel with the approximation that the source is at an infinite distance can be used.

Quantitatively, the validity of the Fresnel approximation with a source at infinity is demonstrated by the values of $u = 2\pi a^2/\lambda z$, the configuration parameter of Fresnel diffraction theory where a is the hole radius, λ is the wavelength and z is he distance mesh to pnCCD surface [35]. If u is close to zero, diffraction is described by the theory of Fraunhofer ([32], page 357). If u is larger than 100, diffraction effects become negligible. In our setup, u has values from 2.19 (C-Kα 277eV, a=2.5µm z=4mm) to 85.8 (Cr-Kα 5415eV a=2.5µm z=2mm).

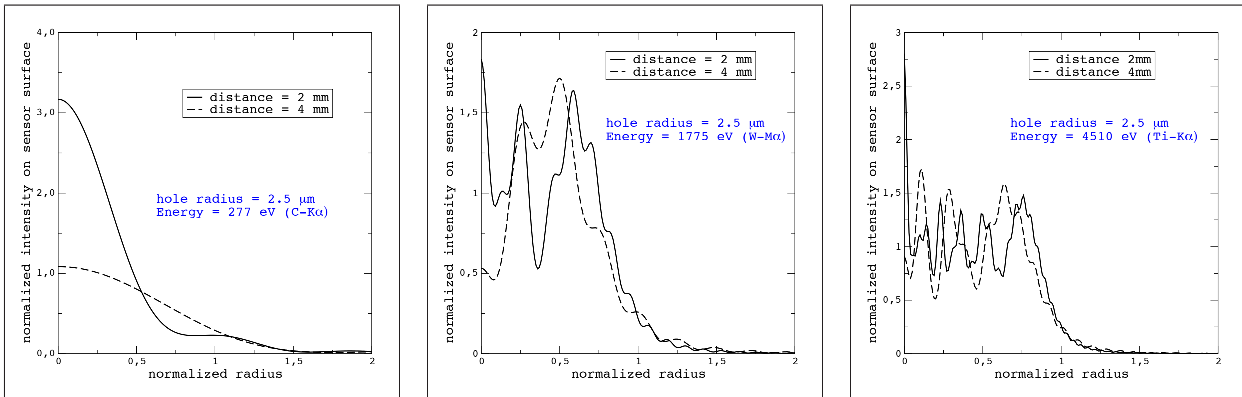

Figure 3.3: *Fresnel diffraction at the mesh holes. From left to right for photon energies of 277 eV, 1775 eV and 4510 eV. The plots show the radial intensity function on the sensor plane. An intensity value of 1.0 is equal to the incoming intensity at the mesh.*

A distance of 2mm to 4mm between mesh and pnCCD was chosen as a compromise in order to prevent mechanical damage of the sensor while the size of the illuminated spots at an energy of 0.7 keV is still close to the hole diameter of 5 µm. Results of the calculations are shown in figures 3.3. For higher energies and/or shorter distances z, the flux is more concentrated in the circular area with the normalized hole radius 1.0. Integration of the flux distribution for different values of u gives the following results: With C-Kα 277eV photons and 4mm distance of the 5µm hole to the pnCCD, 62% of the flux is concentrated into the

geometrical image of the hole on the sensor plane and 81% of the flux is concentrated in a circular area with $2 \cdot r_{\text{hole}}$. 94% of the flux is concentrated into the geometrical image of the hole for a photon energy of 5415eV/Cr-Kα and a distance z of 2mm. An increase of the effective hole diameter due to diffraction therefore occurs only for a photon energy of 277 eV and at a hole to sensor distance of 4 mm. In order to avoid a reduction of the spatial resolution due to diffraction at the mesh holes, the lowest energy used for the mesh measurements presented here is 705 eV (Fe–Lα). With a distance of 2 mm to 4 mm between to the pnCCD entrance window, a gold mesh with 5 µm hole diameter, a hole distance of 150 µm and a thickness of 10 µm mesh can be used in an energy range from 705 eV / Fe–Lα to 5415 eV / Cr–Kα while the spatial resolution is only limited by the hole diameter.

3.2 Analysis of mesh measurement data

Every data set obtained in a mesh measurement is used both for the reconstruction of the mesh position and for the creation of the virtual pixel scan provided by the mesh method. The reconstruction of the mesh position from the measurement data itself is more precise than a direct mechanical measurement of the setup geometry which has a precision of roughly 1 µm. Maps of the virtual pixel can be created as soon as the mesh geometry and thus the position of every hole is known.

Several methods for the mesh data reconstruction are shown in [2], [36], [37] and [38]. Detailed information on how to reconstruct the mesh geometry and on the generation of the representative pixel maps is given there. These methods indirectly find the setup geometry with a minimization of the variance of a reconstructed pixel image [39] or with a minimization method similar to pattern recognition [37].

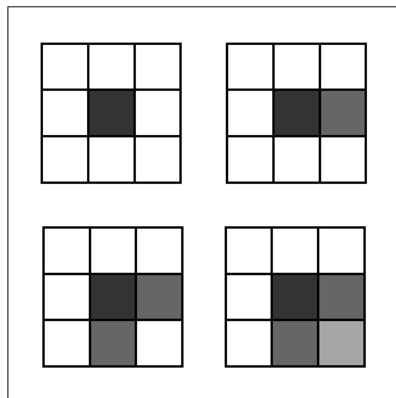

Figure 3.4: *Topologies of valid photon event patterns. Split patterns shown here may be rotated in steps of 90° to form other valid patterns. Dark gray shades indicate higher signal ratios.*

The orientation of the mesh is however directly derivable from the data of a mesh measurement if the hole distance is an integer multiple of the pixel size. This condition is

fulfilled for the used gold mesh with 150 µm hole distance and pnCCDs with a pixel size of 150 µm, 75 µm and 51 µm. A new method which is based on analytical calculations for the determination of the mesh orientation was therefore developed and implemented as a software together with a dedicated method for the reconstruction of virtual pixel maps.

In order to understand the reconstruction method for the mesh position, one has to recall that in an X-ray pnCCD, the signal charge generated by absorbed X-ray photons can be distributed over neighboring pixels. If a X–ray photon hits the detector near a pixel border, the signal charge reaches the pixels which face the sides of the pixel border. If a photon hits a pixel near one of its corners, the signal charge is distributed over three or four pixels near the conversion position. The possible topologies of signal charge distribution are grouped by the number of pixels which show a signal. In pnCCDs with pixel sizes between 51 µm and 150 µm, charge splitting over up to four pixels is observed and X-ray events are grouped in singles, doubles, triples and quadruples, see figure 3.4.

3.2.1 Determination of the mesh geometry

X–ray pixel events are detected and grouped in singles, doubles, triples and quadruples by the data analysis software. The software then creates maps of the detector array which show the number of detected events for each pixel. In a further analysis step, one can create array maps which show the relative abundance of a specific event type for each pixel, e.g. single pixel events. Maps which show the relative abundance of singles, doubles and triples + quadruples in a mesh measurement are shown in figure 3.5 for a 150 x 150 µm^2 pixel pnCCD and a measurement energy of 4510 eV (Ti–Kα).

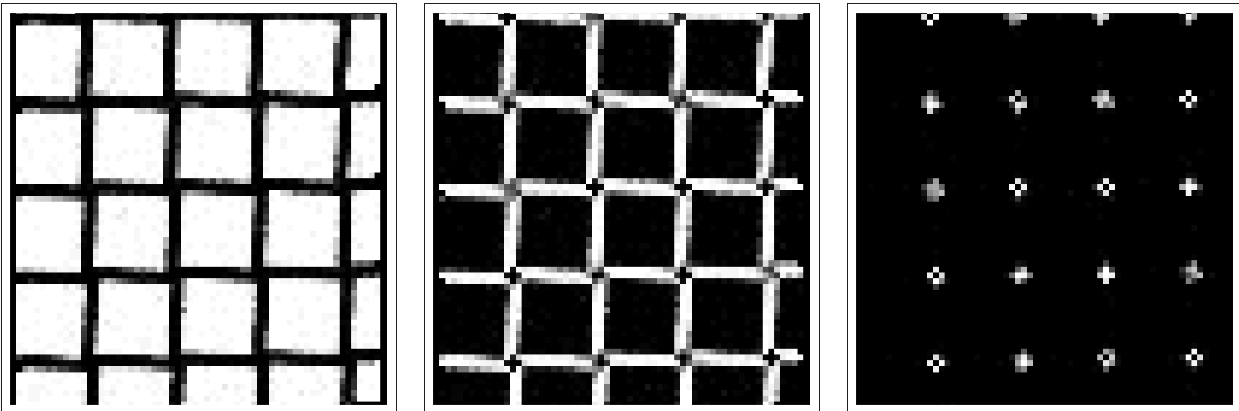

Figure 3.5: *Moiré patterns generated from mesh data taken with a 150µm pixel pnCCD and a mesh with a hole distance of 150µm. The patterns show where a specific event type occurs with the ratio $N_{\mathrm{event\,type}}/N_{\mathrm{all\,events}}$, this ratio has a value between 0 (black) and 1 (white). From left to right: single events, double events and triple + quadruple events.*

Due to the systematically varying hole positions relative to the pixels below, the maps show moiré patterns of dark and bright areas. Pixels where the relative hole position is close to the pixel middle appear as white areas in a map which shows the relative abundance

of single events. Pixels where the relative hole position is close to the border appear as white areas in a map which shows the relative abundance of double events.

Geometrically, the moiré patterns for single and double event maps can be parameterized as line systems. An important property of these line systems is that the lines can be grouped in nearly horizontal and nearly vertical lines. Each group of lines can be described by three parameters: offset to the coordinate origin, line to line distance and angle with the coordinate axes. This makes six parameters in total which fully describe the geometry of the observed moiré pattern.

The line direction of the pixel array is defined as the x–axis, the column or channel direction of the array is defined as the y–axis. Therefore, the orientation of the rectangular hole grid on the mesh can also be defined with six parameters: offset to the coordinate origin, line to line distance and angle with the coordinate axes of the nearly vertical and nearly horizontal lines which run through the centers of the mesh holes. Since the mesh is tilted by less than 10° relative to the detector array, nearly vertical hole lines have an angle of less than 10° with the y–axis and nearly horizontal hole lines have an angle of less than 10° with the x–axis. The six geometry parameters of the moiré line system correspond to the six geometry parameters of the mesh hole grid.

The determination of the mesh geometry with the moiré method is split into two parts. I. The parameters of the moiré lines are extracted from a moiré image generated with the data of the mesh measurement. This is done with a least squares fit of a line model to the moiré pattern map. Each line of the fit model is defined as a Gaussian profile. Fitting the Gaussian line profiles to the moiré pattern lines delivers the coordinates of the geometrical lines which run through the middle of the moiré lines. II. The six moiré line system parameters are transformed into the six geometry parameters of the mesh. This can be done with an analytical calculation. Only the sense of rotation of the mesh has to be determined directly at the measurement setup.

3.2.1.1 Transformation of the line system parameters

Each of the two line directions is defined by a unit vector, the offset, and the distance of the lines. The calculations are done in pixel coordinates since the hole positions on the pixel matrix are needed. The line pattern is defined by 'x' and 'y' lines as shown in figures 3.6 and 3.7. 'x' and 'y' lines are named after the axis intersections chosen for their offset and distance definition:

$$\mathbf{x}_{\text{moiré}} = x \cdot \vec{x}_{\text{u}} + \mathbf{x}_{\text{k}} \quad ; \quad \mathbf{y}_{\text{moiré}} = y \cdot \vec{y}_{\text{u}} + \mathbf{y}_{\text{l}} \tag{3.3}$$

with:

$$\begin{aligned} \vec{x}_{\text{u}} = \cos(\vartheta_{\text{x}}) \cdot \vec{e}_{\text{x}} + \sin(\vartheta_{\text{x}}) \cdot \vec{e}_{\text{y}} \quad &; \quad \vec{y}_{\text{u}} = \sin(\vartheta_{\text{y}}) \cdot \vec{e}_{\text{x}} + \cos(\vartheta_{\text{y}}) \cdot \vec{e}_{\text{y}} \\ \mathbf{x}_{\text{k}} = (x_0 + k \cdot \Delta\tilde{x}_{\text{moiré}} \, , \, 0) \quad &; \quad \mathbf{y}_{\text{l}} = (0 \, , \, y_0 + l \cdot \Delta\tilde{y}_{\text{moiré}}) \end{aligned} \tag{3.4}$$

where $\mathbf{x}_{\text{moiré}}$ is a coordinate on a 'x' line and $\mathbf{y}_{\text{moiré}}$ is a coordinate on a 'y' line. $\Delta\tilde{x}_{\text{moiré}}$ and $\Delta\tilde{y}_{\text{moiré}}$ are the distances between two lines on the x and y axes. x_0 and y_0 are the origins of

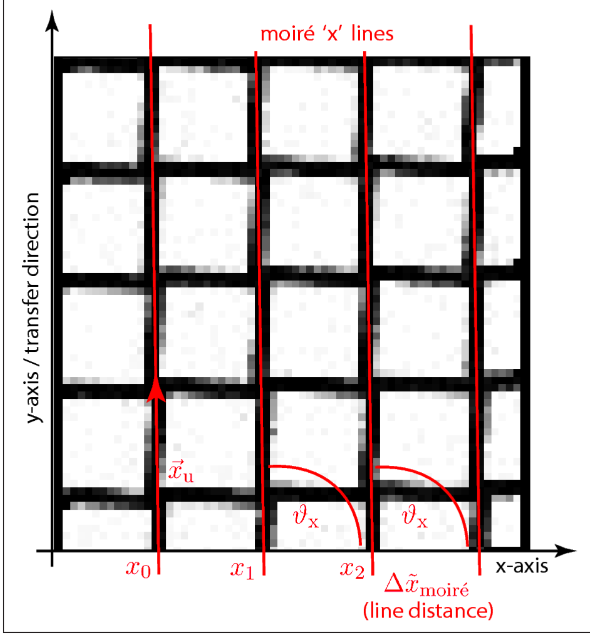

Figure 3.6: *Vector description of a vertical 'x' moiré line group. x_0 is the offset coordinate of the line group.*

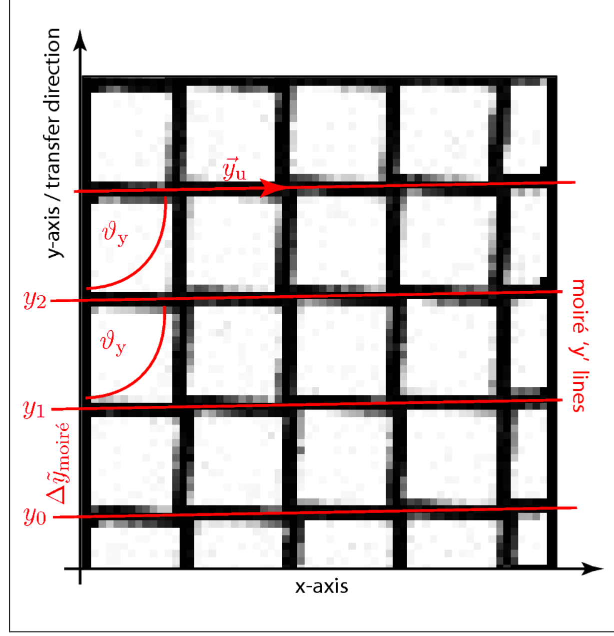

Figure 3.7: *Vector description of a horizontal 'y' moiré line group. Note that the line angle is defined relative to the y-axis.*

the 'x' and 'y' line groups and ϑ_x and ϑ_y are the angles between a line and the corresponding coordinate axis. With x_0, $\Delta\tilde{x}_{moiré}$, ϑ_x, y_0, $\Delta\tilde{y}_{moiré}$, ϑ_y and the sense of rotation of the mesh, the moiré line system is completely defined. The transformation to the hole line parameters is discussed for the x–axis (the pixel row direction) and the corresponding hole lines which are slightly tilted to the x–axis. Figure 3.8 illustrates the geometry for counterclockwise rotation of the mesh. It is convenient to normalize all distances to the pixel side lengths Δx_{CCD} and Δy_{CCD} for the following calculations. In figure 3.8 the two horizontal lines correspond to pixel borders and the two tilted lines correspond to hole lines. Points a and b are intersections of pixel borders and hole lines, the vector from a to b gives the direction of a 'x' moiré line which is nearly vertical. In order to find the angle ϑ_x of the 'x' line, we look at the triangle $a\ b\ c$. $\vec{ab}$ has the y component $\Delta y_{CCD} = 1$ and $\vec{ab}$ is also given by $\vec{ac} + \vec{cb}$. Using the above requirement that $\vec{ab} = \vec{ac} + \vec{cb}$ has a y component of 1, we get:

$$\vec{ab} = \begin{pmatrix} -\Delta y_{mesh} \cdot \sin(\varphi_x) + \xi_x \cdot \cos(\varphi_x) \\ \Delta y_{mesh} \cdot \cos(\varphi_x) + \xi_x \cdot \sin(\varphi_x) \end{pmatrix} \tag{3.5}$$

with $\vec{ab}_y = \Delta y_{CCD} = 1$. The value ξ_x is found by:

$$1 = \Delta y_{mesh} \cdot \cos(\varphi_x) + \xi_x \cdot \sin(\varphi_x) \quad \Leftrightarrow \quad \xi_x = \frac{1 - \Delta y_{mesh} \cdot \cos(\varphi_x)}{\sin(\varphi_x)} \tag{3.6}$$

Now, $\vec{ab}_x$ is given by:

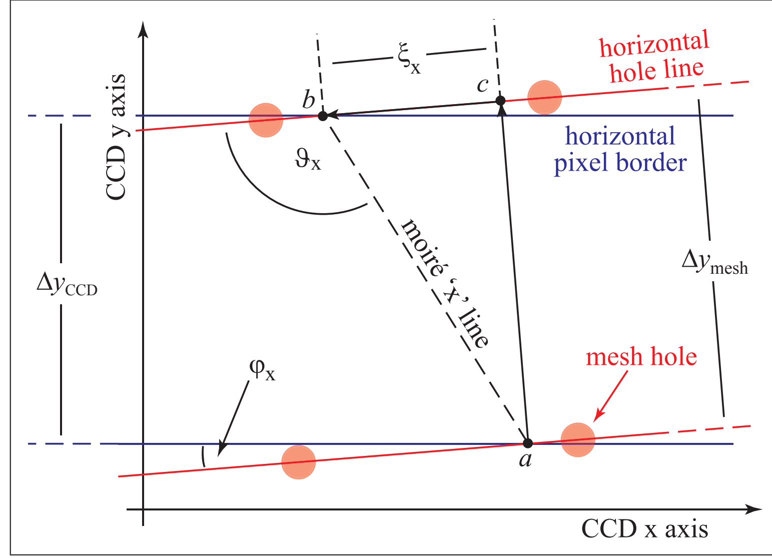

Figure 3.8: *Angle of an 'x' line group with the x axis. A line of the group runs through the points a and b.*

$$\begin{aligned} \vec{ab}_{\mathrm{x}} &= -\Delta y_{\mathrm{mesh}} \cdot \sin(\varphi_{\mathrm{x}}) + \xi_x \cdot \cos(\varphi_{\mathrm{x}}) \\ &= -\Delta y_{\mathrm{mesh}} \cdot \sin(\varphi_{\mathrm{x}}) + (1 - \Delta y_{\mathrm{mesh}} \cdot \cos(\varphi_{\mathrm{x}})) \cdot \cot(\varphi_{\mathrm{x}}) \end{aligned} \tag{3.7}$$

$\vec{ab}_{\mathrm{x}}/\Delta y_{\mathrm{CCD}}$ is equivalent to $\cot(\vartheta_{\mathrm{x}})$, thus it follows:

$$\begin{aligned} \cot(\vartheta_{\mathrm{x}}) &= -\Delta y_{\mathrm{mesh}} \cdot \sin(\varphi_{\mathrm{x}}) + (1 - \Delta y_{\mathrm{mesh}} \cdot \cos(\varphi_{\mathrm{x}})) \cdot \cot(\varphi_{\mathrm{x}}) \\ \Leftrightarrow \Delta y_{\mathrm{mesh}} &= \frac{\cot(\varphi_{\mathrm{x}}) - \cot(\vartheta_{\mathrm{x}})}{\cos(\varphi_{\mathrm{x}}) \cot(\varphi_{\mathrm{x}}) + \sin(\varphi_{\mathrm{x}})} \end{aligned} \tag{3.8}$$

Δy_{mesh} is the distance of two nearly horizontal hole lines. The angle φ_{x} is still unknown but can be found as shown in figure 3.9. Using the triangles $a\ b\ c$ and $d\ b\ c$, φ_{x} is found from:

$$\tan(\varphi_{\mathrm{x}}) = \frac{\Delta y_{\mathrm{CCD}}}{\Delta \tilde{x}_{\mathrm{moire}} + \cot(\vartheta_{\mathrm{x}}) \cdot \Delta y_{\mathrm{CCD}}} \tag{3.9}$$

Similarly, for the horizontal moiré lines follows:

$$\Delta x_{mesh} = \frac{\cot(\varphi_{\mathrm{y}}) - \cot(\vartheta_{\mathrm{y}})}{\cos(\varphi_{\mathrm{y}}) \cot(\varphi_{\mathrm{y}}) + \sin(\varphi_{\mathrm{y}})} \tag{3.10}$$

$$\tan(\varphi_{\mathrm{y}}) = \frac{\Delta x_{\mathrm{CCD}}}{\Delta \tilde{y}_{\mathrm{moire}} + \cot(\vartheta_{\mathrm{y}}) \cdot \Delta x_{\mathrm{CCD}}} \tag{3.11}$$

The last step is to find the offset of the mesh relative to the pixel matrix since by now only the angle and the distance of nearly horizontal and vertical hole lines are known. If the position of one hole is known, the known parameters define the position of all other

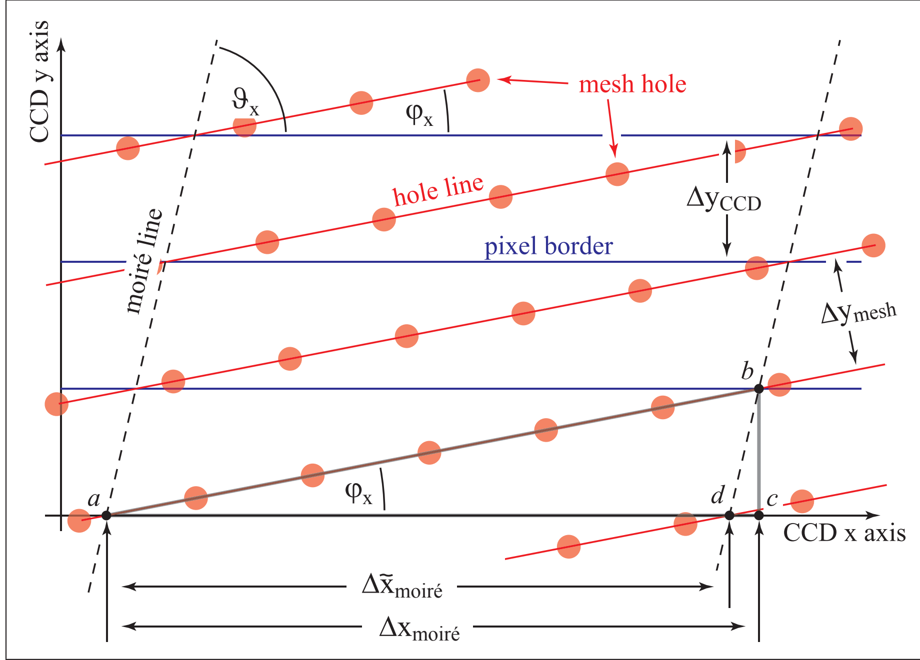

Figure 3.9: *Alignment angle between mesh and CCD coordinate system. Horizontal solid lines denote borders between two pixels, lines of mesh holes are denoted by tilted solid lines and moiré lines are denoted by tilted dashed lines.*

holes. Therefore only the method to find the first known hole position will be described as illustrated by figure 3.10. We start from points $\mathbf{p}_x$ and $\mathbf{p}_y$. $\mathbf{p}_x$ lies at the crossing of a moiré 'x' line with a horizontal pixel boundary, $\mathbf{p}_y$ lies at the crossing of a moiré 'y' line with a vertical pixel boundary. Starting from these points, one follows $\vec{u}_{mesh(x)}$ from $\mathbf{p}_x$ and $\vec{u}_{mesh(y)}$ from $\mathbf{p}_y$. This way, a nearly horizontal and nearly vertical hole line is defined. By definition, their intersection at $\mathbf{p}_h$ is a mesh hole position. For the two lines we have the following mathematical expressions:

$$\begin{aligned} \mathbf{x}_{mesh} &= \mathbf{p}_x + \chi_{off} \cdot \vec{u}_{mesh(x)} \\ \Leftrightarrow \mathbf{x}_{mesh} &= \mathbf{p}_x + \chi_{off} \cdot (\cos(\varphi_x), \sin(\varphi_x)) \end{aligned} \tag{3.12}$$

$$\begin{aligned} \mathbf{y}_{mesh} &= \mathbf{p}_y + \gamma_{off} \cdot \vec{u}_{mesh(y)} \\ \Leftrightarrow \mathbf{y}_{mesh} &= \mathbf{p}_y + \gamma_{off} \cdot (-\sin(\varphi_y), \cos(\varphi_y)) \end{aligned} \tag{3.13}$$

Their point of intersection is found from the requirement that $\mathbf{x}_{mesh}$ and $\mathbf{y}_{mesh}$ are identically equal:

$$\mathbf{p}_x + \chi_{off} \cdot \vec{u}_{mesh(x)} = \mathbf{p}_y + \gamma_{off} \cdot \vec{u}_{mesh(y)}$$

$$\Leftrightarrow \begin{pmatrix} p_x^x \\ p_x^y \end{pmatrix} + \chi_{off} \cdot \begin{pmatrix} \cos(\varphi_x) \\ \sin(\varphi_x) \end{pmatrix} = \begin{pmatrix} p_y^x \\ p_y^y \end{pmatrix} + \gamma_{off} \cdot \begin{pmatrix} -\sin(\varphi_y) \\ \cos(\varphi_y) \end{pmatrix}$$

$$\Leftrightarrow \left\langle \begin{aligned} p_x^x + \chi_{off} \cdot \cos(\varphi_x) &= p_y^x - \gamma_{off} \cdot \sin(\varphi_y) \\ p_x^y + \chi_{off} \cdot \sin(\varphi_x) &= p_y^y + \gamma_{off} \cdot \cos(\varphi_y) \end{aligned} \right\rangle \tag{3.14}$$

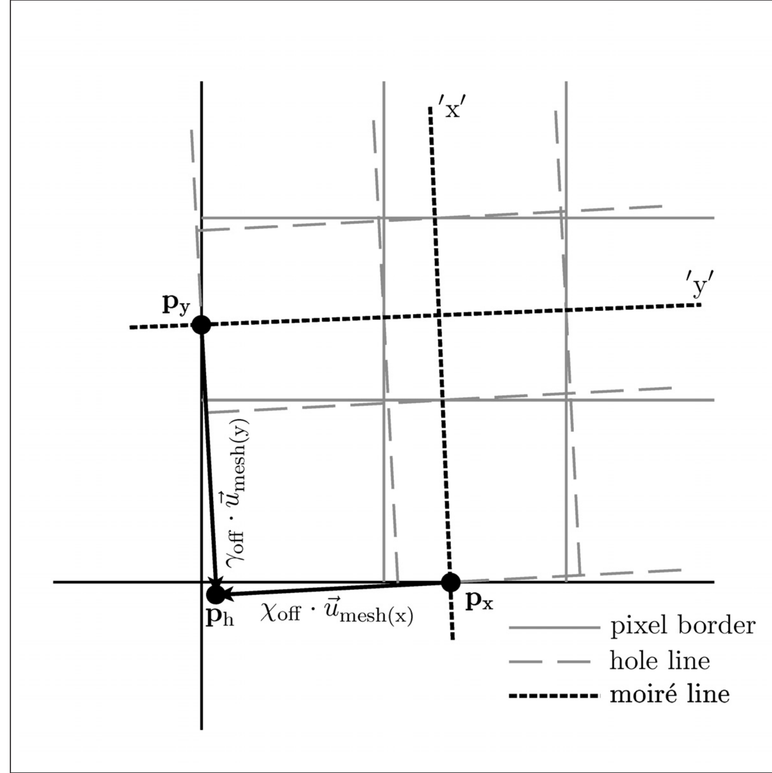

Figure 3.10: *Finding the absolute position of a mesh–hole from the parameters of a moiré pattern and the moiré lines in a frame. Hole lines are abstracted from the hole grid of the mesh so that mesh hole positions are defined by line intersections. An intersection of a hole line with a pixel border is indicated by the intersection of a moiré line with a pixel border.*

Solving for χ_{off} and γ_{off} delivers:

$$\chi_{\text{off}} = \frac{\mathbf{p}_{\text{y}}^{\text{y}} - \mathbf{p}_{\text{x}}^{\text{y}} + (\mathbf{p}_{\text{y}}^{\text{x}} - \mathbf{p}_{\text{x}}^{\text{x}}) \cdot \cot(\varphi_{\text{y}})}{\sin(\varphi_{\text{x}}) + \cos(\varphi_{\text{x}}) \cot(\varphi_{\text{y}})} \quad (3.15)$$

$$\gamma_{\text{off}} = \frac{\mathbf{p}_{\text{y}}^{\text{x}} - \mathbf{p}_{\text{x}}^{\text{x}} + (\mathbf{p}_{\text{x}}^{\text{y}} - \mathbf{p}_{\text{y}}^{\text{y}}) \cdot \cot(\varphi_{\text{x}})}{\sin(\varphi_{\text{y}}) + \cos(\varphi_{\text{y}}) \cot(\varphi_{\text{x}})} \quad (3.16)$$

Inserting χ_{off} or γ_{off} in equation 3.12 or 3.13 delivers the position of one mesh–hole $\mathbf{p}_{\text{h}}$ which defines the needed offset coordinates relative to the CCD.

3.2.2 Reconstruction of the virtual pixel map

Once the mesh geometry parameters are known, each hole position is known in pixel coordinates. The measurement data from all pixels which are located near a mesh hole is rearranged into the map of the virtual pixel. The map which describes the distribution of the signal charge over neighboring pixels is called the 'charge map'. It covers an area of

three by three pixels, since it also shows the amount of charge that is collected if a photon is converted outside of the pixel border.

The function which is shown by the 'charge map' is the '**c**harge **c**ollection **f**unction', in short 'ccf', which gives the charge collection efficiency as a function of the photon conversion position. It is generally defined as:

$$ccf = f(l_{\text{pixel}}(x), l_{\text{pixel}}(y), T, U_{\text{bc}}, U_{\text{storage}}, U_{\text{barrier}}, n(e^-), x_\gamma, y_\gamma) \quad ; \quad 0 \leq ccf \leq 1; \quad (3.17)$$

With $l_{\text{pixel}}(x)$ and $l_{\text{pixel}}(y)$ being the pixel sizes in row and column direction, T the temperature of the device, U_{bc} the back contact voltage, U_{storage} and U_{barrier} the voltages of the storage and barrier registers respectively, $n(e^-)$ the number of generated signal electrons, x_γ and y_γ the x and y coordinates of the photon conversion position. The normalized ccf has a value of 1.0 where 100 % of the signal charge generated by a photon is collected, i.e. where single events occur.

Maps which show the relative abundance of a specific event type are called 'single map', 'double map', 'triple map' or 'quad map'. These maps only show the area of one pixel since the coordinates of X–ray events are only defined for hole positions inside of the pixel borders. It is however convenient to stitch 9 event type maps of a pixel into a three by three pixel map in order visualize the distribution of event types in the detector array.

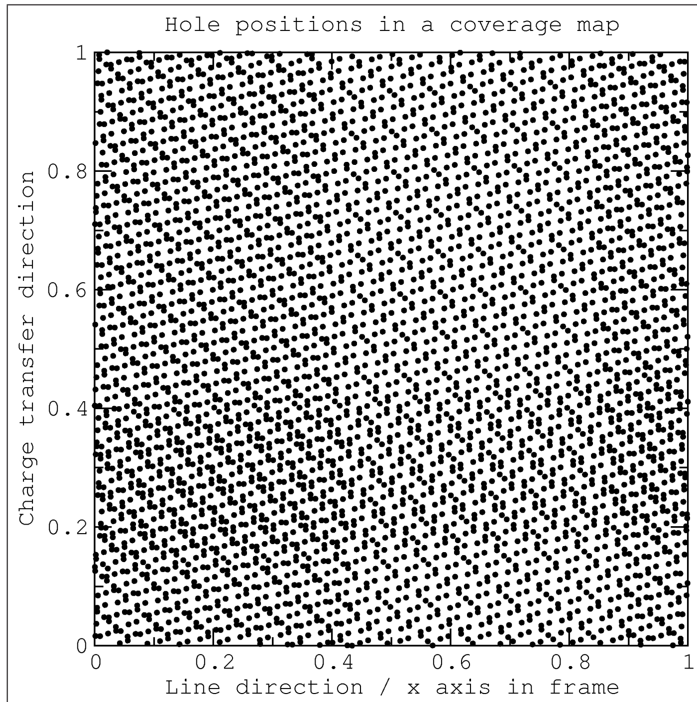

Figure 3.11: *Coverage map for all occurring hole positions of a measurement. The positions of hole centers relative to the pixel below each hole are displayed. It is clearly visible that the hole positions do not lie on a rectangular grid.*

The occurring hole positions relative to the pixels below the holes are displayed in a 'coverage map' of the experiment. A look at the coverage map for a given measurement shows that hole positions in the representative pixel do not lie on a rectangular grid, see figure 3.11. An irregular distribution of map values at the given hole positions cannot be

displayed as computer graphics. In order to create a regular virtual pixel map with data points on a rectangular grid, an approach with two reconstruction steps was chosen: I. The pixel map for a specific physical quantity e.g. the abundance of single pixel events is computed for the positions of the (irregular) coverage map. II. The resultant irregular pixel map is either used to fill a two-dimensional histogram or it is interpolated to a quadratic grid. Interpolation to a quadratic grid allows for finer resolution of the final map and therefore the extraction of all information contained in the measurement.

The reconstruction of the pixel response into a irregular virtual pixel map can be seen as a transformation from data values in frame coordinates to data values in pixel map coordinates. This transformation is defined by the coverage map of the relative hole positions inside of a pixel and the absolute hole positions in frame coordinates, figure 3.12. The data values, e.g. the values of the charge collection function ccf, used in the transformation are computed for each hole position in the pixel array.

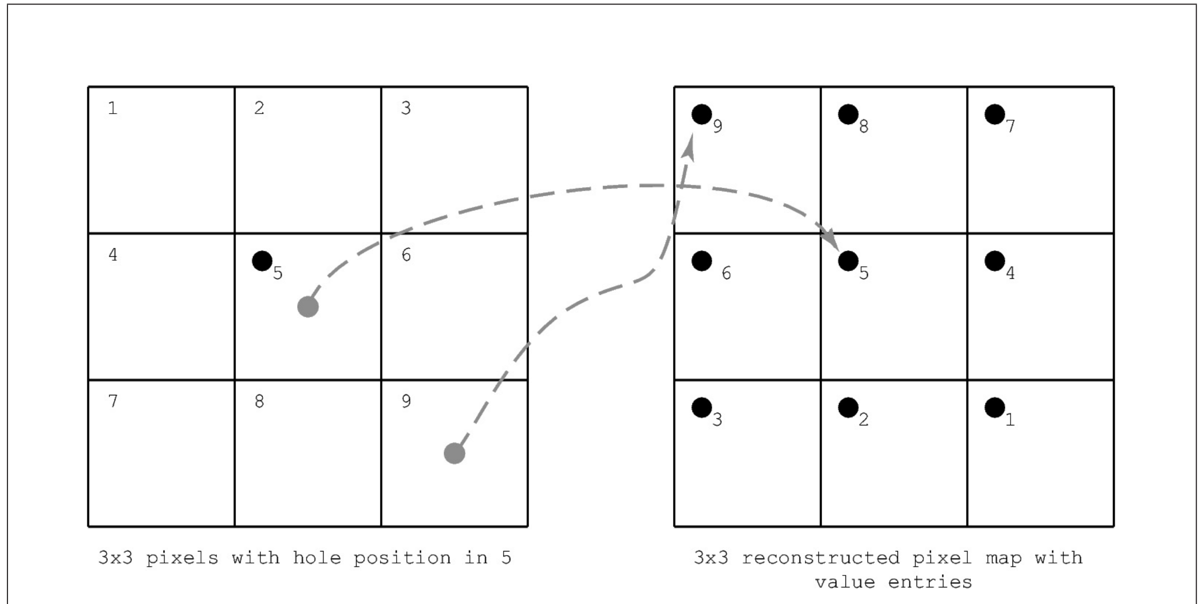

Figure 3.12: *Reconstruction of a pixel map from X-ray event data. On the left hand side, 3 x 3 pixels in the CCD frame with the position of a mesh hole are shown. To the right hand side is a virtual map of 3 x 3 pixels, e.g. of the ccf, equation 3.17. It shows the data points at the corresponding hole positions of the coverage map in each of the nine pixels. The assignment of pixel data values in frame coordinates to the map positions is symbolized by the gray lines.*

A simple regular map of the representative pixel can be generated by filling a two dimensional histogram. Each histogram bin is defined by a coordinate range $n_{\mathrm{bin(x)}}/N_{\mathrm{bins(x)}} - n_{\mathrm{bin+1(x)}}/N_{\mathrm{bins(x)}}$; $n_{\mathrm{bin(y)}}/N_{\mathrm{bins(y)}} - n_{\mathrm{bin+1(y)}}/N_{\mathrm{bins(y)}}$. Each bin value is computed as the average value of the entries. A histogram map is problematic for finer binning in the x and the y direction. Depending on the distribution of hole positions, some bins will not be filled and must be set to zero. In this case the resultant regular pixel map is difficult

to interprete since data values are missing at some coordinates.

An interpolation of the irregular pixel map values gives a result for every map coordinate and can be used to create regular virtual pixel maps with a finer resolution than two–dimensional histograms. A simple method for local, two dimensional interpolation was thus developed and implemented for this thesis. Figure 3.13 shows the first step of the interpolation method, the selection of data points around the coordinate of the interpolation value. If the hole positions around the interpolated point are selected, the simplest

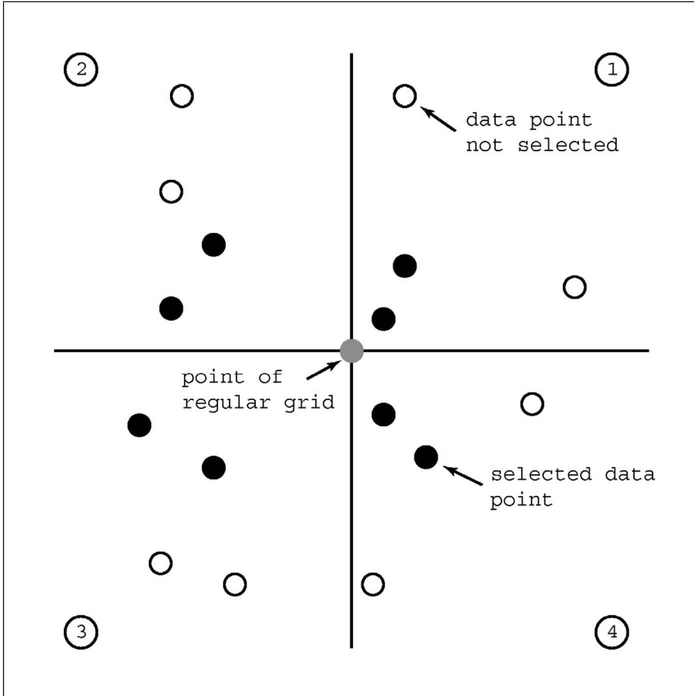

Figure 3.13: *Selection of hole positions in the irregular pixel map for local interpolation. In each quadrant 1 to 4 around the position of the desired interpolation value, at least one data point/hole position is selected. The distance to the interpolated point is used as the selection criterion. For each quadrant, the hole positions closest to the interpolated point are chosen.*

method to find the interpolated value is to compute the average of the given values, similar to the histogram method but with the advantage that for every interpolation coordinate enough surrounding data points can be found. A more sophisticated method involves fitting a plane to the surface defined by the hole coordinates and data values. This problem is solved by a linear least squares fit as explained in [40] p. 258. A plane in three dimensions is defined as:

$$z = \mathrm{u} + x \cdot \mathrm{v} + y \cdot \mathrm{w} \tag{3.18}$$

With z the value and the coordinates x and y. For each data point z_j, this equation is:

$$z_\mathrm{j} = \mathrm{u} + x_\mathrm{j} \cdot \mathrm{v} + y_\mathrm{j} \cdot \mathrm{w} \tag{3.19}$$

The general linear least squares problem to be solved is:

$$\boldsymbol{\eta} + \mathbf{a}_0 + \mathbf{A}\vec{x} \approx 0 \tag{3.20}$$

with $\boldsymbol{\eta}$ being the vector of function values, $\mathbf{a}_0$ and $\mathbf{A}$ the vector and Matrix of measurement values and $\vec{x}$ the vector of variables in demand. In our case $\boldsymbol{\eta}= \vec{z}$, $\vec{x} = (\mathrm{u};\mathrm{v};\mathrm{w})$, $\mathbf{a}_0 = \vec{0}$

and $\mathbf{A} = (1; \mathrm{x_j}; \mathrm{y_j})_\mathrm{i}$. We can therefore write:

$$\begin{pmatrix} z_1 \\ \vdots \\ z_\mathrm{n} \end{pmatrix} + \begin{pmatrix} 1 & x_1 & y_1 \\ \vdots & \vdots & \vdots \\ 1 & x_\mathrm{n} & y_\mathrm{n} \end{pmatrix} \cdot \begin{pmatrix} \mathrm{u} \\ \mathrm{v} \\ \mathrm{w} \end{pmatrix} \approx 0 \tag{3.21}$$

In the ideal case, the problem could be solved by $\vec{x} = \mathbf{A}^{-1} \cdot \boldsymbol{\eta}$. In our case it is practically always solved by employing a singular value analysis, see [40] p. 500 which delivers the best least squares fit solution $(\mathrm{u}; \mathrm{v}; \mathrm{w})$. Finally, the value at the interpolation position on the regular grid is found by inserting its x,y coordinates in equation 3.18.

Chapter 4

Measurements

Each data set recorded for a mesh experiment with a given X–ray energy and a given set of device operation parameters consists of a pair of separate measurements. The first measurement is performed with a flat illumination of the detector array. It is used to calibrate the signal output of each pixel for a given X–ray energy so that a given amount of signal charge generates the same signal pulse height for every pixel. The second measurement is performed with the mesh mounted in front of the pixel array. This measurement delivers the data for both the position determination of the mesh and the construction of the virtual pixel maps.

4.1 Setup for the used pnCCDs

The electrical and mechanical components used for the mesh measurements except the mesh assembly itself are parts of the standard test setup for pnCCDs. A standard flat field measurement with the 5.9 keV (Mn–Kα) and 6.5 keV (Mn–Kβ) lines of of a Fe55 source was used for a first performance evaluation of the four pnCCDs which were finally selected for the mesh experiment. For the pairs of flat field and mesh measurements, the X–ray tube of the test setup was employed as the radiation source for the used X–ray emission lines from 705 eV (Fe–Lα) up to 6.4 keV (Fe–Kα). The mesh assembly was either mounted directly on the ceramic carrier board of the pnCCD or on the cooling mask of the CCD test setup.

4.1.1 The Rösti facility

The standard test setup for pnCCDs at the MPI–HLL is the 'Rösti' test facility, an evacuated beam line consisting of an X–ray tube and a vacuum test chamber. A pipe connecting the X–ray tube and measurement chamber keeps the sensor and the anode target at a distance of 4 meters to ensure even illumination of the sensor. An exchangeable flange in the test chamber holds the electronics and the mechanical mounting components necessary to operate the used pnCCD.

A vacuum with a pressure below $1.0 \cdot 10^{-6}$ mbar is present in the complete beam line in order to prevent the absorption of the X–rays in air and the formation of a condensation ice layer on the cooled pnCCD. In a distance of 4 meters from the source in air at normal pressure, the flux of a 6.4 keV (Fe-Kα) X–ray beam is reduced by a factor of more than 1000. Lower energy X–ray radiation as used for the mesh experiments discussed here is absorbed to an even greater extent. All used pnCCDs were cooled below -80 ℃ in order to reduce leakage current. At normal pressure, freezing cannot be avoided at this temperature even in dried air. It would lead to short circuits between the electrodes and thus a destruction of the device.

A sketch of the setup in the Rösti facility is shown in figure 4.1. Even illumination of the mesh was checked by measurements with flat field illumination, the same measurements were also used to investigate the spectrum from the X–ray tube. Anode targets of carbon, aluminum, iron, tungsten, chromium and copper were used to generate fluorescence line spectra from 277 eV to 5415 eV. In order to concentrate the total photon flux in a narrow energy band, X–ray energies other than the needed emission line are suppressed with filters. Low energy spectra of the 277 eV C–Kα line and the 705 eV Fe–Lα line were filtered with a light absorption filter which is identical to the one used in the EPIC–pn camera on XMM–Newton. Emission line spectra with high energies were filtered with thin foils made of the same material as the anode target. These filters reduce the intensity of the radiation except for narrow energy bands below the K–, L– or M– absorption edges of the filter / anode material.

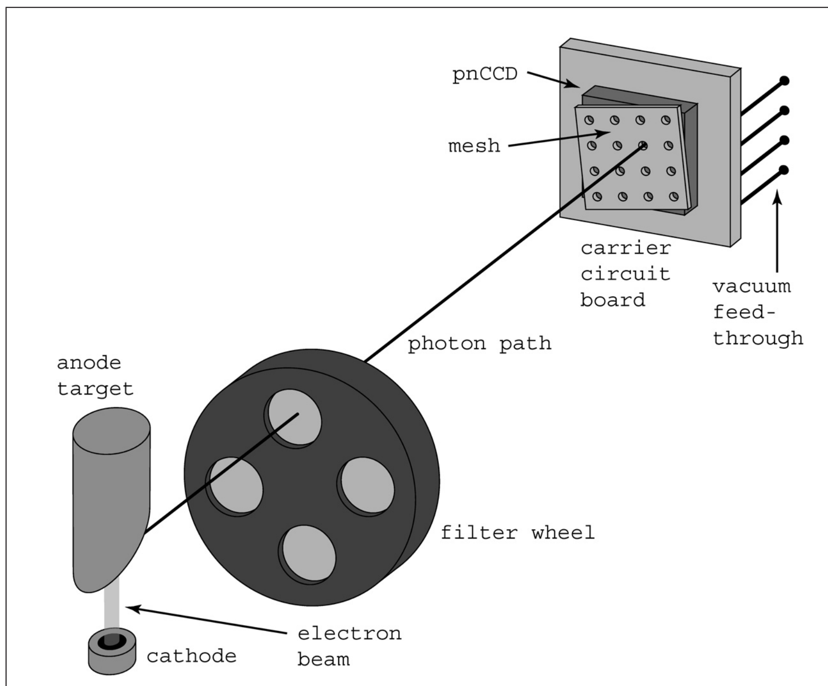

Figure 4.1: *Principle of the experiment in the Rösti facility. The mesh is evenly illuminated by the X-ray source. A photon path from the anode target through a mesh hole and onto the pnCCD is shown. Filters are used to suppress the bremsstrahlung continuum of the X–ray spectrum and block infrared and visual radiation from the detector. The anode target can be exchanged to generate different X–ray emission lines.*

A view of the Rösti facility in the lab is shown in figures 4.2 and 4.3. The mounting flange and the test chamber can be seen in figures 4.4, 4.5, 4.6 and 4.8. During measurements of

the electronic noise and the signal offset, the device is shielded from radiation with a shutter inside the measurement chamber. A manipulator arm in the measurement chamber carries a Fe55 source which allows for measurements with the 5894eV Mn-Kα and 6490eV Mn-Kβ lines without using the X–ray tube. Figure 4.5 shows the open measurement chamber with the CCD flange and cooling mask, the shutter and the Fe55 source on the manipulator arm. All functional tests and first performance qualification measurements of pnCCDs are done with the Fe55 source. Figure 4.4 shows the exchangeable vacuum flange for frame–store pnCCDs with pixel size of 75µm and 51µm. It carries the inner circuit board with the sockets for the ceramic carrier circuit board of the CAMEX readout chip and the pnCCD and the outer circuit board. The outer circuit board carries buffers for the output signals of up to four CAMEX–ASICs and buffers for the incoming digital clocking signals of the CAMEX and the pnCCD. For each type of ceramic CCD carrier board with different pin layouts, a separate flange is assembled with the matching circuit boards and cooling mask. The flanges can be exchanged in order to accommodate different types of pnCCDs.

4.1.2 pnCCDs used for measurements

Four different pnCCDs with three different pixel sizes of 150 µm, 75 µm and 51 µm were used for the mesh measurements. Using devices with different pixel sizes provides insight into the influence of the pixel size on the charge collection process in pnCCDs. One of the 75 µm pixel CCDs was reverse mounted with the register side facing towards the mesh and the X–ray tube. The reverse mounted and front side illuminated pnCCD was used to study the absorption of X–ray photons in the contact–, oxide– and implanted silicon layers at the front side of the device. The pnCCDs used for the mesh measurements are from three successive production runs which is reflected in the improved noise performance and better charge transfer efficiency of the newer devices, see table 4.1.

Since the mesh method requires a uniform response of all pixels in the frame, the uniformity of the performance of all pixels is the main selection criterion for a specific device. In a flat field measurement, the uniformity of the array is judged by the following criteria: • Uniformity of the pixel noise and pixel signal offset map. Excessive noise or an excessively large signal offset of a pixel indicate an increased leakage current which alters the signal output of a pixel. • Uniformity of the photon count map of a measurement. Variations in the photon count / intensity map above the variations due to Poisson statistics indicates non uniformities in the thickness of the insensitive p+ doped layer in the entrance window. This would affect mainly low energy X–ray photons with a short penetration depth in silicon. • Variations in the photon count maps which only show a specific split event type, e.g. double split events. Variations above the range expected due to Poisson statistics indicate non uniformities of the distribution of split events over the pixel array. The mesh method however requires that the relative occurrence of different split event types is the same for all pixels.

In order to find out which kind of array non uniformities occur, data sets from different pnCCDs and measurements with different X–ray energies from 1.5 keV to 8.0 keV were evaluated. The outcome of these evaluations showed that only a few devices have pixels

or pixel groups with excessive noise or signal offset values. If these pixels or groups of pixels are masked out in the analysis, the remaining part of the array is homogeneous with respect to the detection efficiency and the split statistics. None of the evaluated pnCCDs showed variations of the detection efficiency or the split statistics which were above the detection threshold. The selection of devices for the mesh measurements could therefore concentrate on the following properties:

- Good noise performance of the device. Both leakage current and readout noise should be as low as possible to facilitate detection of small signals, i.e. small signals in split events where the signal charge is distributed over more than one pixel. The sum of readout noise and leakage noise is lower than 6.6 electrons ENC for all used pnCCDs.
- Low charge transfer losses / good charge transfer efficiency (section 1.4). The charge transfer loss or inefficiency (CTI) was compared to other pnCCDs of the same design. A charge transfer loss that is at least as low or lower than the average for a given device type was required for the used CCDs. A high charge transfer inefficiency degrades the signal of the pixels depending on their distance from the readout anodes. Generally the CTI should be better than $500 \cdot 10^{-6}$/pixel which results in a signal loss of less than 10% after charge transfer over 200 pixels.

Table 4.1 shows the characteristic technical parameters of the used pnCCDs. It also shows the basic performance parameters for the operating conditions realized in the mesh measurements. With the succession of the pnCCD production runs, the CAMEX readout ASIC evolved towards a design allowing for higher readout speed and lower readout noise at the same time. The principle of the CAMEX design is described in [18, 16].

As a result of the combined improvements of the pnCCDs and CAMEX readout chips, the total noise σ could be reduced by a factor of 2.9 relative to the oldest used device, pnCCD C09_08_10. In addition, the CTI was lowered by a factor of 17. A value of the CTI below $16.5 \cdot 10^{-6}$ means that signal degradation after 528 transfers through the image and the framestore area as in pnCCD C11_11_85 is less than 1%. Improvements of the total noise σ and the CTI lead to a fwhm of the Ti-Kα 4510eV line below 120 eV for single events, close to the Fano limit in silicon [41] of 102.5eV at this energy.

4.1.3 mesh assembly

The mesh is a gold foil with a thickness of 10 µm and a size of 13x18 mm^2 supplied by Optnics Precision Co., Ltd.. It is structured as a rectangular hole grid with a hole diameter of 5 µm and a hole distance of 150 µm. Optnics states a tolerance of 1 µm for the diameter of the holes and the hole distance. The exact hole distance is derived by the mesh data analysis, see chapter 3.2, so systematic tolerances of this parameter have no negative effect on the analysis precision.

For the first measurements with the XMM–type pnCCD, the mesh was mounted in a rigid stainless steel frame. Clamps were glued on the ceramic carrier board of the device in order to hold the frame with the mesh, see fig. 4.7. In the experiments with the other three

pnCCD type	V9 XMM–type	V10 framestore #1
device id	C09_08_10	C10_19_01
pixel size [image/frame store]	150x150µm^2	75x75µm^2/75x51µm^2
geometry	64 channels, 200 rows	128 channels, 125 rows imaging area
substrate thickness	290µm	280µm
illumination	back side	back side
CAMEX version	CMX 64B	CMX 132
measurement temperature [°C]	-148	-80
frame readout time [ms]	4.6 / 200 lines	5.6 / 250 lines
integration time [ms]	360	300
noise σ [e^-]	6.6	5.5
CTI [$1.0 \cdot 10^{-6}$] at 4510eV	282	16.5
Ti-Kα 4510eV fwhm [eV]	154.5 (single evts.)	119.2 (single evts.)

pnCCD type	V10 framestore #2	V11 framestore
device id	C10_19_16	C11_11_85
pixel size [image/frame store]	75x75µm^2/75x51µm^2	51x51µm^2/51x51µm^2
geometry	128 channels, 125 rows imaging area	264 channels, 264 rows imaging area
substrate thickness	280µm	450µm
illumination	front side	back side
CAMEX version	CMX 128D	CMX 132F
measurement temperature [°C]	-120	-93
frame readout time [ms]	5.6 / 250 lines	8.0 / 528 lines
integration time [ms]	200	200
noise σ [e^-]	3.7	2.3
CTI [$1.0 \cdot 10^{-6}$] at 4510eV	13.4	11.6
Ti-Kα 4510eV fwhm [eV]	117.8 (single evts.)	117.1 (single evts.)

Table 4.1: *Basic parameters of the pnCCDs used for mesh measurements. The V9 to V11 designation gives the production generation of the device. Devices of version V9 and V10 are made on 4 inch wafers; V10 with 280 µm thickness, V9 devices are made on wafers with an additional epi layer and 290 µm thickness. The devices from production V11 came available in 2005 and are made on 6 inch wafers of 450 µm thickness. Note that the noise and CTI performance is improved for successive device generations.*

CCDs, the mesh assembly was mounted on the larger cooling mask as shown in figures 4.6 and 4.9. This method has the advantage that the ceramic board of the pnCCD is not modified which means less danger to damage the sensitive device. In all setups, the mesh is cooled down together with the pnCCD.

A comparison of figures 4.6 and 4.8 shows that the setups for front– and back side illumination are very similar. For the reverse mounted CCD with front side illumination, a

Figure 4.2: *A view of the Rösti test facility. The X–ray tube not visible here has various anode targets mounted on a wheel which can be operated from outside the vacuum. During measurements and when the pnCCD is cooled, the evacuated volume is kept at pressures below* $1.0{\cdot}10^{-6}$ *mbar. At higher pressures, residual gases could condense on the entrance window and affect the device performance by absorbing low energy X–rays.*

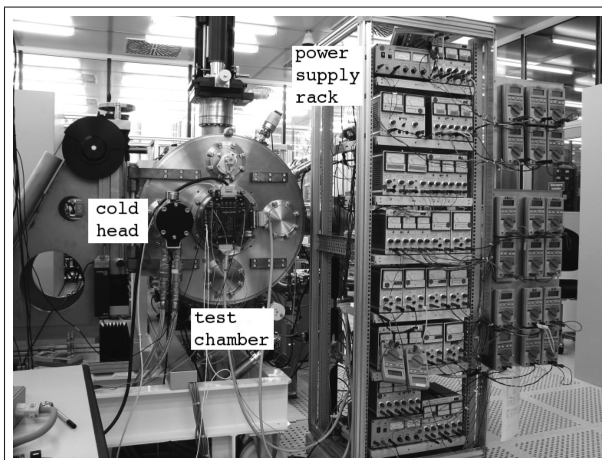

Figure 4.3: *The measurement chamber with a power supply rack. In the middle of the round chamber door, the outer circuit board can be seen, the cold head is on the left and the shutter assembly on the top part of the door. The multimeters to the right of the power supply rack are used to control the supply currents and voltages. A manipulator arm for an Fe55 X–ray source is mounted on top of the measurement chamber.*

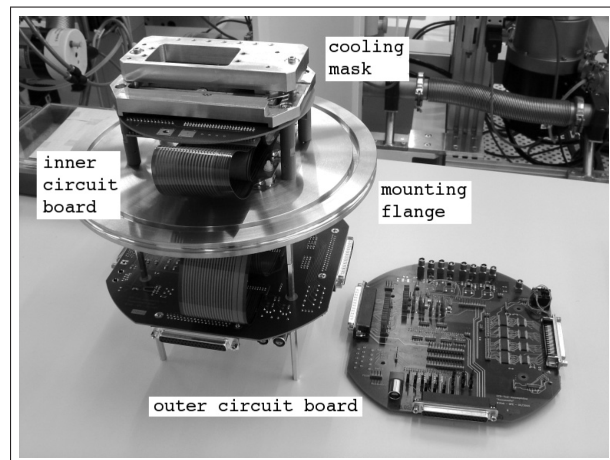

Figure 4.4: *A vacuum flange with the inner and outer circuit boards and the cooling mask for operation of 75 µm and 51 µm pixel frame–store pnCCDs. The cooling mask is made of copper but gold plated to prevent corrosion, the ceramic carrier board of the pnCCD is clamped between the two parts of the cooling mask. In the measurement chamber, the cooling mask is connected to the cold head by copper wires.*

ceramic board with reversed pins and an inner circuit board with reversed connector sockets was used. No modifications to the electronics or other mechanical parts than the upper

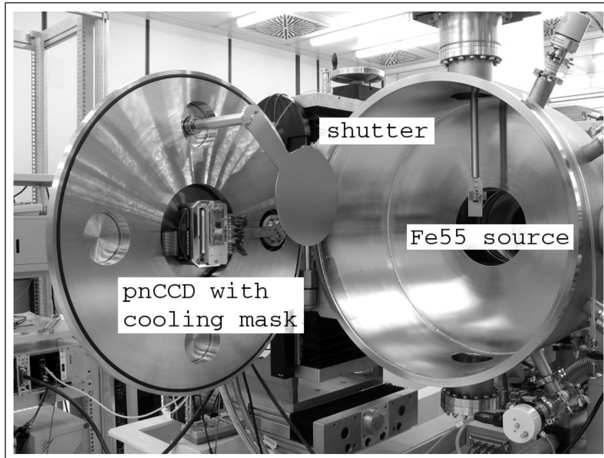

Figure 4.5: *The measurement chamber of the Rösti facility with mounted V10 pnCCD and mesh. X–rays enter the chamber through the hole behind the Fe55 source which can be moved out of the beam with a manipulator. the shutter in front of the pnCCD blocks X–rays from the Fe55 source or the X–ray tube.*

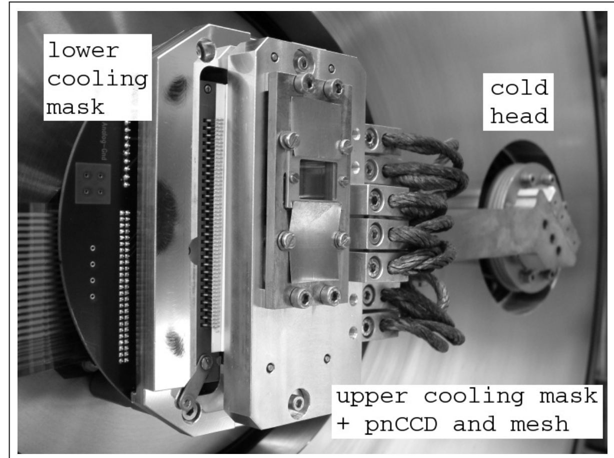

Figure 4.6: *A closeup view of the cooling mask for V10 and V11 pnCCDs complete with V10 pnCCD mounted for front side illumination and mesh assembly. The mesh holder is made of stainless steel, it is cooled down together with the pnCCD. Heat is conducted to the cold head via the copper wires and a cold finger.*

cooling mask were needed. The mesh assembly could be reused without modifications which reduced the time needed for the completion of the front side illumination setup.

Stainless steel was chosen as the material for all mesh assemblies. It has the advantage of being resistant to corrosion and thus prevents pollution of the vacuum. Another advantage of stainless steel is that its thermal expansion coefficient value of $17.3 \cdot 10^{-6}$ K^{-1} is close to $14.2 \cdot 10^{-6}$ K^{-1}, the thermal expansion coefficient of gold [42]. The difference of $3.1 \cdot 10^{-6}$ K^{-1} results in compressing the mounted mesh by 8.4 µm along its longer side when cooling down from 300 K to 150 K. This amount of length compression causes only a small deformation in the lateral and vertical direction of the mesh in its frame, negative effects on the measurement precision were not observed.

4.2 Measurement program

The measurement program carried out for this thesis addresses the three main questions which should be answered with the mesh experiment: I. How does the electric potential inside of a pnCCD influence the collection of signal charge, especially with respect to the different pixel sizes? II. What is the influence of the amount of signal electrons in the charge cloud on the final charge distribution? III. Which information on the structure of the shift registers can be extracted from measurements with a special setup for front side illumination? In order to provide the necessary data sets, measurements with back side

Figure 4.7: *The XMM-type pnCCD with the mesh mounted directly on the ceramic board.*

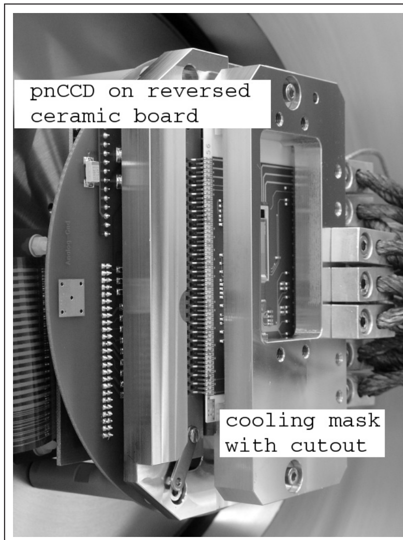

Figure 4.8: *V10 framestore pnCCD mounted on reversed ceramic board for front side illumination.*

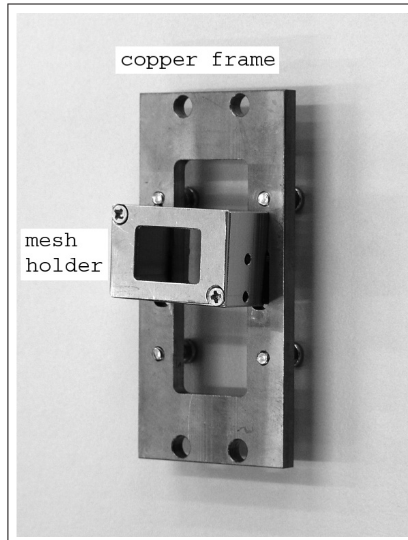

Figure 4.9: *The mesh assembly which is mounted on the cooling mask of the V10 and V11 framestore pnCCDs.*

illumination at different X–ray energies as well as measurements with front side illumination were performed.

4.2.1 Back side illumination

Back side illumination is the default operation mode of pnCCDs. The radiation entrance window on the back side is highly optimized towards a very low insensitive thickness in order to prevent the absorption of low energy X–rays. If charge collection in the pixel structure is studied however, the used X–ray energies should not be to small. Low energy X–ray photons produce a small amount of signal electrons. The measurement precision of the charge distribution in split events depends on the ratio of the electronic noise to the total amount of signal charge. The minimum X–ray energy used for measurements with back side illumination is therefore 930 eV (Cu–Lα).

The X–ray line energies of 930eV (Cu–Lα), 1486 eV (Al–Kα), 1775 eV (W–Mα), 4510 eV (Ti–Kα) and 5415eV/Cr-Kα were used to study the energy dependence of charge collection. These energies result in attenuation lengths from 2.2µm to 22.6µm in silicon and 255 to 1484 electron–hole pairs in the signal electron cloud. Compared to the total wafer thickness of 280µm to 450µm and the correspondingly long drift distance before charge collection in the pixel structure, the difference of the penetration depth of 20.4µm is small. A more significant effect should result from the electrostatic repulsion which is stronger for larger numbers of signal electrons[1], see section 2.2.1.2.

[1] Electrons and holes are quickly separated in the drift field of the bulk. After the separation, electrostatic

operation mode → C09_08_10	single register storage, voltage set a) T = -148°C	double register storage, voltage set a) T = -148°C	single register storage, voltage set b) T = -148°C
X–ray line ↓			
Cu-Lα 930eV	flatfield+mesh	flatfield+mesh	flatfield+mesh
Al-Kα 1487eV	flatfield+mesh	flatfield+mesh	flatfield+mesh
Ti-Kα 4510eV	flatfield+mesh	flatfield+mesh	flatfield+mesh

Table 4.2: *Measurements with the V9 XMM–type pnCCD C09_08_10. Both flatfield and mesh measurements were done for each configuration.*

C09_08_10	voltage set a)	voltage set b)
back contact	-170V	-180V
Phi_{123}	-15V	-10V
ΔPhi_{123}	-5V	-10V
MOS–gates	0V	-10V

Table 4.3: *Operating voltages of pnCCD C09_08_10. Single register storage is below Phi2, double register storage is below Phi2 and Phi3. The barrier register voltage is given by* $Phi_{123} + \Delta Phi_{123}$.

After the first measurement run, it was considered more sensible to concentrate on a few X–ray lines in order to perform a smaller number of longer measurements with better photon statistics. 1775eV/W-Mα and 4510eV/Ti-Kα have nearly the same attenuation length in silicon with 13.0µm (W-Mα) and 13.5µm (Ti-Kα). Due to the different number of generated signal electrons which are generated in the same depth, the observed effects on the signal charge distribution must be a result of the different strength of electrostatic repulsion. With the appropriate data analysis, one can thus isolate the influence of electrostatic repulsion on charge collection.

A question which is of interest for the mesh experiment as a measurement method is the maximum X–ray line energy where the effect of photons which penetrate the gold foil can still be neglected. As stated before, at large X–ray energies, the ratio of the signal charge to the equivalent noise charge is higher and the measurement precision of split events is increased. At the same time, more X–ray photons with undefined conversion positions penetrate the gold foil at higher energies. These photons cause a degradation of the effective measurement precision. This effect should appear visibly in the reconstructed pixel images at a sufficiently large X–ray energy (chapter 3.1.1). It was finally confirmed by measurements that 5415eV (Cr-Kα) is the highest usable X–ray line energy with the given mesh.

repulsion takes effect.

operation mode → C10_19_01	single register storage, voltage set a) T = -80℃	double register storage, voltage set a) T = -80℃	single register storage, voltage set b) T = -80℃	single register storage, voltage set a) T = -120℃
X–ray line ↓				
W-Mα 1775eV	flatfield+mesh	flatfield+mesh	flatfield+mesh	flatfield+mesh
Ti-Kα 4510eV	flatfield+mesh	flatfield+mesh	flatfield+mesh	flatfield+mesh
Cr-Kα 5415eV	flatfield+mesh			
Fe-Kα 6404eV	flatfield+mesh			
Cu-Kα 8040eV	flatfield+mesh			

operation mode → C10_19_01	double register storage, voltage set a) T = -120℃	single register storage, voltage set c) T = -80℃		
X–ray line ↓				
W-Mα 1775eV	flatfield+mesh	flatfield+mesh		
Ti-Kα 4510eV	flatfield+mesh	flatfield+mesh		

Table 4.4: *Measurements with the V10 frame store pnCCD C10_19_01. Both flatfield and mesh measurements were done for each configuration. Measurements with Cr-Kα, Fe-Kα and Cu-Kα X–ray lines were done to find the maximum energy usable for mesh measurements with the available mesh.*

C10_19_01	voltage set a)	voltage set b)	voltage set c)
back contact	-90V	-140V	-90V
Phi_{123}	-15V	-15V	-15V
ΔPhi_{123}	-6V	-5V	-6V
Phi_{456}	-15V	-15V	-15V
ΔPhi_{456}	-6V	-5V	-6V
MOS–gates	0V	0V	-10V

Table 4.5: *Operating voltages of the frame store pnCCD C10_19_01. The image and frame store areas have separate register contacts: Phi1, Phi2 and Phi3 in the image area and Phi4, Phi5 and Phi6 in the frame store area. Single register storage is below Phi2 and Phi5, double register storage is below Phi2 + Phi3 and Phi5 + Phi6. The barrier register voltage is given by $Phi_{123} + \Delta Phi_{123}$ and $Phi_{456} + \Delta Phi_{456}$.*

4.2.2 Front side illumination

For front side illumination a special setup including a pnCCD mounted on a reversed ceramic board was needed, see figure 4.8. As reverse mounted devices are not usable in the standard setup for back side illumination, only a few pnCCDs were available for mounting on the reversed ceramic board. For the first test, the frame store pnCCD C10_19_16 which

operation mode → C11_11_85	single register storage voltage set a) T = -90°C	double register storage voltage set a) T = -90°C	single register storage voltage set b) T = -90°C
X–ray line ↓			
C-Kα 277eV	flatfield+mesh	flatfield+mesh	flatfield+mesh
W-Mα 1775eV	flatfield+mesh	flatfield+mesh	flatfield+mesh
Ti-Kα 4510eV	flatfield+mesh	flatfield+mesh	flatfield+mesh
Cr-Kα 5415eV	flatfield+mesh	flatfield+mesh	flatfield+mesh

Table 4.6: *Measurements with the V11 frame store pnCCD C11_11_85. Both flatfield and mesh measurements were done for each configuration.*

C11_11_85	voltage set a)	voltage set b)
back contact	-250V	-180V
Phi_{123}	-15V	-15V
ΔPhi_{123}	-4V	-4V
Phi_{456}	-15V	-15V
ΔPhi_{456}	-4V	-4V
MOS–gates	0V	0V

Table 4.7: *Operating voltages of the frame store pnCCD C11_11_85. The image and frame store areas have separate register contacts: Phi1, Phi2 and Phi3 in the image area and Phi4, Phi5 and Phi6 in the frame store area. Single register storage is below Phi2 and Phi5, double register storage is below Phi2 + Phi3 and Phi5 + Phi6. The barrier register voltage is given by Phi_{123} + ΔPhi_{123} and Phi_{456} + ΔPhi_{456}.*

is from the same wafer as pnCCD C10_19_01, was selected. Since both devices are of the same design, the intention behind this choice was to compare measurements with front– and back side illumination of a physically comparable device.

Flatfield measurements with C10_19_16 showed that it has 12 channels with a total noise more than twice as high as the average noise. The amount of rejected pixels is thus below 20%. Since the performance of the rest of the frame area is completely unaffected by these noisy channels, CCD C10_19_16 was considered acceptable for mesh measurements. A range of X–ray line energies from 277eV (C–Kα) to 5415eV (Cr–Kα) was used to study photon absorption in the register structure. Since the complete production process is controlled, the dimensions and thicknesses of structures on the front side are well known. With this information it was possible to identify insensitive regions of the silicon bulk below the front side structure. These parts of the bulk are seen in the numerical device simulations as regions where generated signal electrons cannot drift into the potential minimum of a pixel.

operation mode → C10_19_16	single register storage voltage set a) T = -120°C	double register storage voltage set a) T = -120°C	single register storage voltage set b) T = -120°C
X–ray line ↓			
C-Kα 277eV	flatfield+mesh	flatfield+mesh	
Fe-Lα 705eV	flatfield+mesh	flatfield+mesh	
Cu-Lα 930eV	flatfield+mesh	flatfield+mesh	flatfield+mesh
Al-Kα 1487eV	flatfield+mesh	flatfield+mesh	flatfield+mesh
W-Mα 1775eV	flatfield+mesh	flatfield+mesh	
Ti-Kα 4510eV	flatfield+mesh	flatfield+mesh	
Cr-Kα 5415eV	flatfield+mesh	flatfield+mesh	

Table 4.8: *Measurements with the V10 frame store pnCCD C10_19_16. Both flatfield and mesh measurements were done for each configuration.*

C10_19_16	voltage set a)	voltage set b)
back contact	-90V	-140V
Phi_{123}	-17V	-20V
ΔPhi_{123}	-8V	-4V
Phi_{456}	-17V	-17V
ΔPhi_{456}	-8V	-8V
MOS–gates	0V	0V

Table 4.9: *Operating voltages of the frame store pnCCD C10_19_16. The image and frame store areas have separate register contacts: Phi1, Phi2 and Phi3 in the image area and Phi4, Phi5 and Phi6 in the frame store area. Single register storage is below Phi2 and Phi5, double register storage is below Phi2 + Phi3 and Phi5 + Phi6. The barrier register voltage is given by* $Phi_{123} + \Delta Phi_{123}$ *and* $Phi_{456} + \Delta Phi_{456}$.

4.3 Standard analysis and calibration of data

Together with the development of the first pnCCD array detectors for the EPIC–PN camera on XMM–NEWTON [43], a standard analysis procedure for frame data was developed. It is discussed with reference to the data analysis for the XMM EPIC–PN camera in [44, 45, 46]. The methods described there are very similar to the frame data analysis originally developed for the first array pnCCDs in the MPI–HLL. This analysis for lab measurements is used to determine the performance of every newly fabricated and mounted device. Besides the performance analysis, the standard analysis provides an energy calibration of the detector system and extracts the X–ray event data from the signal frames. The extracted and calibrated event data can be used by further analysis programs, e.g. the mesh analysis.

The pixel signal data is read from the pnCCD readout electronics in the form of pixel signal data frames with the geometry of the physical device. The readout rate of the frames can be freely chosen, but it is typically 20 frames per second and can reach speeds of 1000

frames per second [18]. In mesh measurements, the mesh attenuates the photon flux by a factor of 1150, section 3.1.1. Low frame rates with integration times from 200ms to 360ms are therefore used in order to collect roughly 1 X–ray photon event per 200 pixels in each frame, table 4.1.

4.3.1 Noise and offset calibration

Even without a photon hit, each pixel in each data frame has a signal level above zero. It can be divided into three separate contributions. These are the constant pixel offset $\Delta U_{\mathrm{off}}(x, y)$, the time variable pixel offset $\Delta U_{\mathrm{cmm}}(y, t)$ which has the same value for all pixels with the same line index y and the pixel noise (signal variance) $\sigma_{\mathrm{U}}(x, y)$. The constant offset of a pixel and the time variable offset of a pixel–line, which is called 'common mode', are determined and subtracted from the signal. The remaining signal is the noise contribution of the pixel. It is given as an approximate Gauss distribution around zero after subtracting the pixel offset $\Delta U_{\mathrm{off}}(x, y)$ and the common mode value $\Delta U_{\mathrm{cmm}}(y, t)$. The signal fluctuation due to the noise determines the smallest detectable photon signal. Noise is directly measured in **a**nalog **d**igital **u**nits 'adu'. For better comparability of different devices and different gain settings it is converted to the **E**quivalent **N**oise **C**harge, the amount of signal electrons that would generate the same signal as the noise sigma value.

Photon signals must be rejected from the offset and noise calculations to avoid them modifying the result. This is possible for low photon count rates. It was considered safer to begin all measurements with a set of 200 dark frames for the offset and noise calculation. The common mode offset of each frame data line is calculated for all data, including the photon signal frames.

In its simplest form, the constant signal offset is given as the average of each pixel signal value of the dark frame data set. The standard analysis used for lab measurements ignores the signals that emerge from MIP events. MIPs are 'minimum ionizing particles', mainly secondary particles from cosmic radiation penetrating the atmosphere. MIPs are excluded from the offset and noise calculation by rejecting the three largest signal values of each pixel in the dark frame set.

The line common mode algorithm calculates the common mode offset as the median of the pixel signals in a line of the frame. Using the median of the pixel signals proved to be a successful method to minimize the influence of photon signals on the result [47, 48].

A map of an uncorrected signal frame from the frame store pnCCD C10_19_01 with 128x250 pixels is shown in figure 4.12. It shows a number of dots on the blue background, these are pixels with X–ray events. Figures 4.11 and 4.10 show the results of the offset and noise determination from dark frames taken with the same device. Fig. 4.11 shows the offset variations are dominated by the differences of the channels. This means that pixel offset variations are mainly due to the different offset levels of the first FETs and following amplifier stages in the CAMEX readout ASIC. An increased offset of individual pixels indicates an increased leakage current and therefore also an increased noise in these pixels. CCD C10_19_01 does not have any noisy pixels as seen in fig. 4.10. The noise map shows only two channels with an increased noise level. These channels have a noise value

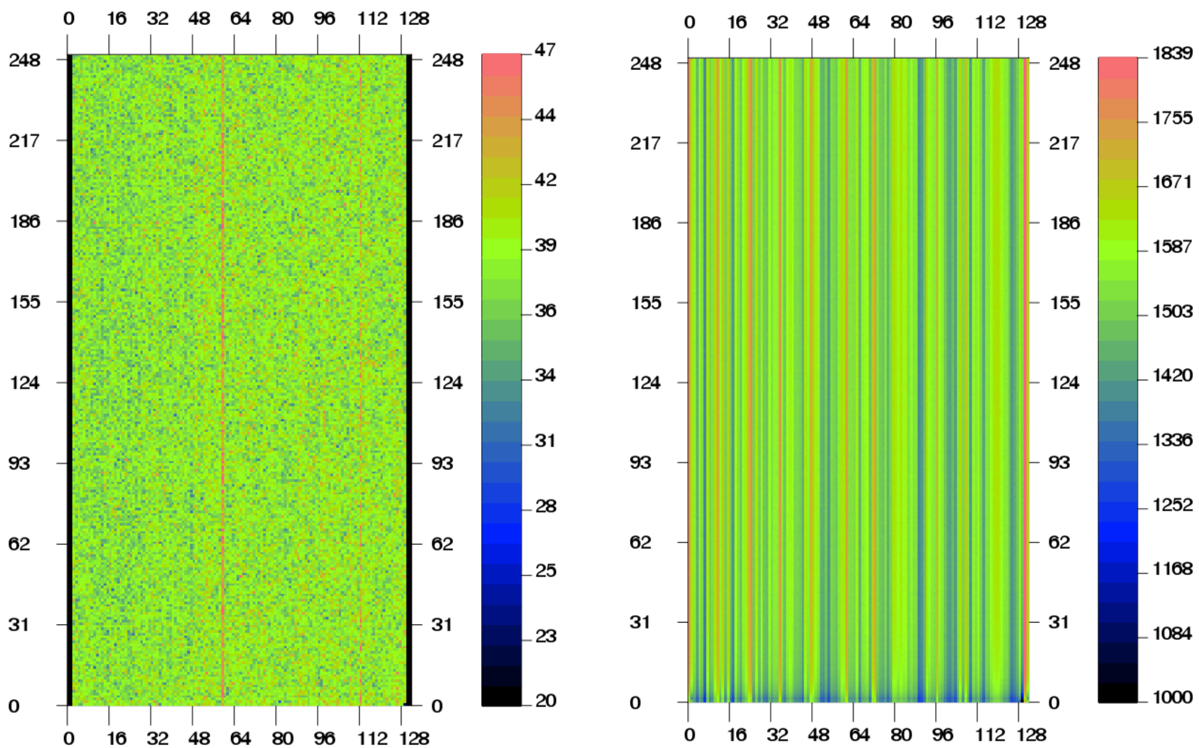

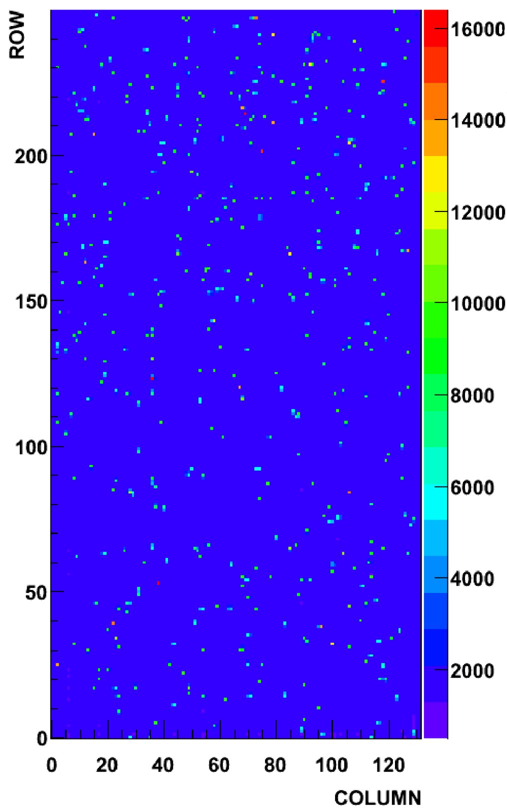

Figure 4.10: *(top left) Noise map with a scale in adu. Since the used CAMEX chip has 132 channels while the CCD has 128 channels, two channels on each side of the frame are empty. Two channels have a slightly increased noise. However, the noise value of these channels is below twice the average noise, so they do not need to be rejected from the analysis.*

Figure 4.11: *(top right) Offset map of the same device, the scale is in adu. The offset variations are in the range of 1600 adu. This variation is smaller than the pulse height of a signal which is created by a Ti-Kα photon.*

Figure 4.12: *(bottom left) Uncorrected signal frame. The bright or red dots are X–ray events of Ti-Kα (4510 eV) photons. The maximum possible adu value is 16384 (14 bits).*

which is below twice the average noise σ value of the whole device and do not need to be rejected from the data analysis.

4.3.2 Photon event detection

All X–ray measurements with pnCCDs aim at the detection of individual photon events. The signal amplitude which is proportional to the number of measured signal electrons is thus proportional to the photon energy. If two photons hit the same pixel or two neighboring pixels, the signal electrons are mixed and the energy of the individual photons cannot be reconstructed. In order to avoid this situation, also called 'photon pileup', all calibration and mesh measurements were done at photon rates of no more than 1 photon per 200 pixels of a frame. In measurements with a monochromatic X–ray line though, photon pileup can be easily identified. Adding the signal charge of two or three photons causes additional lines in the spectrum with twice or three times the primary line energy.

Photon events are detected as signals above the noise level of a pixel. First, the constant offset of each pixel is subtracted from the pixel signal of a frame. Then the common mode offset is determined for each line and subtracted from the pixel signal which remains after the offset correction. After the offset and the common mode correction, the remaining pixel signal is the sum of noise and a possible photon signal. This signal is compared to a threshold defined by the noise sigma value σ_{ENC} of the pixel multiplied with a constant factor. Factors between 4 and 8 are normally chosen for the event detection in order to reject the noise signal extremes and keep even small photon signals. As discussed in section 2.2.1, the signal electron cloud expands during its drift to the register side and can thus be split over neighboring pixels. The pixels which contain enough electrons generate a signal above the noise threshold and are thus selected for the photon event detection. Signals of neighboring pixels which are above the threshold are combined into a signal pattern. If a signal pattern consists of more than one pixel, its topology is compared to a set of allowed topologies. Only patterns with no more than four pixels are accepted. After the topology analysis, the signal pulse heights of the accepted patterns are summed up in order to obtain the total pulse height of the pattern.

The definition of valid and invalid split event pattern topologies is based on two assumptions. I. During drift to the front side, signal charge is distributed over an area that is smaller than a pixel $\longrightarrow$ The maximum pattern size is four pixels in an area of 2x2 pixels. II. Signal charge is distributed in a Gaussian charge cloud that is split at the pixel borders $\longrightarrow$ In a triple event the highest signal pixel is at the corner. In a quad event the highest and lowest signal pixels are on a diagonal. Double split patterns where the two pixels are on a diagonal do not occur. Triple patterns with three pixels in a line do not occur.

Figures 4.13 to 4.16 show the corresponding topologies of valid photon event patterns. Pixel signals are displayed as bar charts, bars with dark gray shades indicate signals above the event threshold. Rotating the valid topologies shown in figures 4.14 to 4.16 in 90°steps creates other valid topologies. Figures 4.17 and 4.18 show examples of invalid topologies.

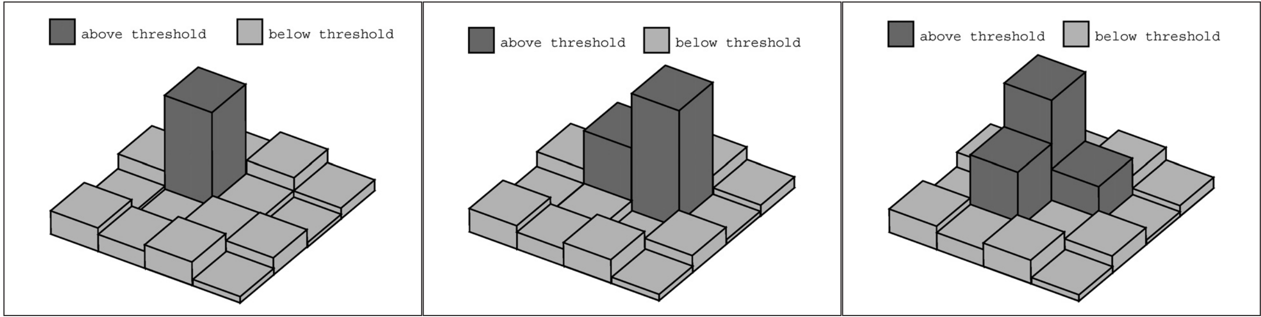

Figure 4.13: *Single pixel event 'single'*

Figure 4.14: *Double pixel event 'double'*

Figure 4.15: *Triple pixel event 'triple'*

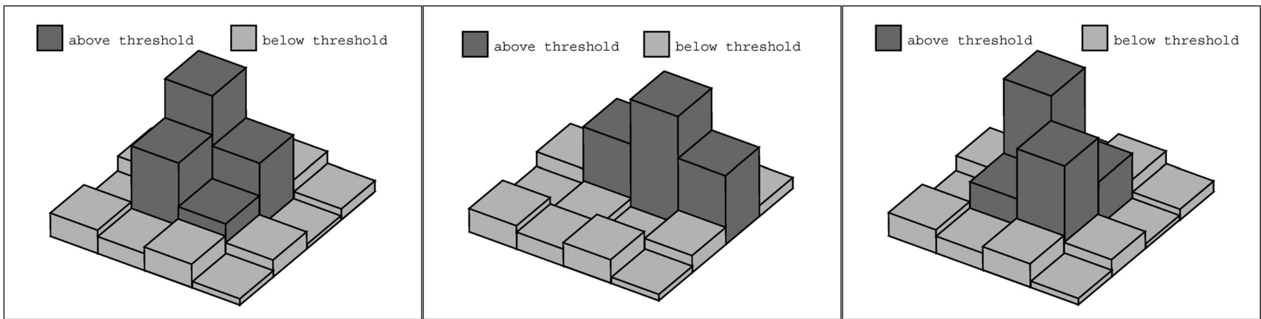

Figure 4.16: *Quad pixel event 'quad'*

Figure 4.17: *Invalid triple pixel event*

Figure 4.18: *Invalid quad pixel event*

4.3.3 Gain calibration and CTE correction

The signal pattern analysis extracts the photon signals from the raw data frames of a measurement. In order to convert the total signal pulse height of a signal pattern from ADC units (adu) to a photon energy value in eV, the signal conversion factor $g_{\mathrm{CCD}}(n)\,[\mathrm{eV/adu}]$ is needed where n is the channel index. The value of $g_{\mathrm{CCD}}(n)\,[\mathrm{eV/adu}]$ slightly differs for each channel since the amplification factor of each CCD first–FET plus CAMEX readout channel varies slightly around the specified mean value. Gain variations of the readout channels are compensated with a relative correction factor $g(n)$ factor for each channel. The signal value in units of eV is calculated with $U_{\mathrm{eV}} = U_{\mathrm{adu}} \cdot g(n) \cdot g_{\mathrm{CCD}}\,[\mathrm{eV/adu}]$ where $g_{\mathrm{CCD}}\,[\mathrm{eV/adu}]$ is the average signal conversion factor of all channels.

Directly after the signal electrons are collected, the total amount of electrons in all pixels of a pattern is proportional to the photon energy. After a given number of transfers towards the readout anode however, a small loss of signal charge is observed, section 1.4. Charge loss is corrected for by multiplying the signal pulse height of a pixel with the factor $1/(1-\mathrm{CTI})^n$ where CTI is the relative charge loss for a shift of one pixel and n is the number of transfers. Charge transfer loss causes an uncertainty of the signal pulse height since it is a statistical process. The result is a noise contribution to the signal and therefore a decrease of the energy resolution. Charge transfer loss noise cannot be corrected for by

the CTI correction. In addition to Fano noise [41] and electronic noise, the CTI value is one of the performance parameters which determine the energy resolution of a pnCCD [49].

For the gain calibration and the CTI correction, a flat field measurement of a spectrum with a defined X–ray emission line energy is needed. The relative gain correction factors and the CTI values are calculated separately for each readout channel. Therefore only single events and double split events where both contributing pixels have the same channel index are chosen for the correction. The gain calibration first determines the peak position of the ADC value spectrum for each channel. All peak positions of the channels are then averaged in order to obtain the mean value $U_{\mathrm{adu}}(\mathrm{peak, mean})$ of the peak position. The relative correction factor for each channel is calculated as $g(n) = U_{\mathrm{adu}}(\mathrm{peak, mean})/U_{\mathrm{adu}}(\mathrm{peak, n})$ where $U_{\mathrm{adu}}(\mathrm{peak, n})$ is the spectrum peak position of the channel with the index n. The average conversion factor g_{CCD} [eV/adu] is calculated as g_{CCD} [eV/adu] $= E_{\mathrm{peak}}$ [eV]$/U_{\mathrm{adu}}(\mathrm{peak, mean})$ where E_{peak} [eV] is the energy of the X–ray emission line.

The charge transfer efficiency $\mathrm{CTE} = 1 - \mathrm{CTI}$ is determined separately for each channel. The CTE determination begins with the creation of a scatter plot which shows for each pixel of a channel the pulse height distribution of the photon events as a function of the line index. Only single events and double split events with a split orientation along the channel are selected. Thus, all pixel signals in the selected single and double events have the same channel index. The CTI value for the best transfer loss correction is determined with a least squares fit of the function $(1 - \mathrm{CTI})^n = \mathrm{CTE}^n$ to the scatter plot. It is generally more convenient to use the CTI value instead of the CTE since the typical transfer efficiency of a pnCCD is around 0.999985 giving a CTI of $15 \cdot 10^{-6}$.

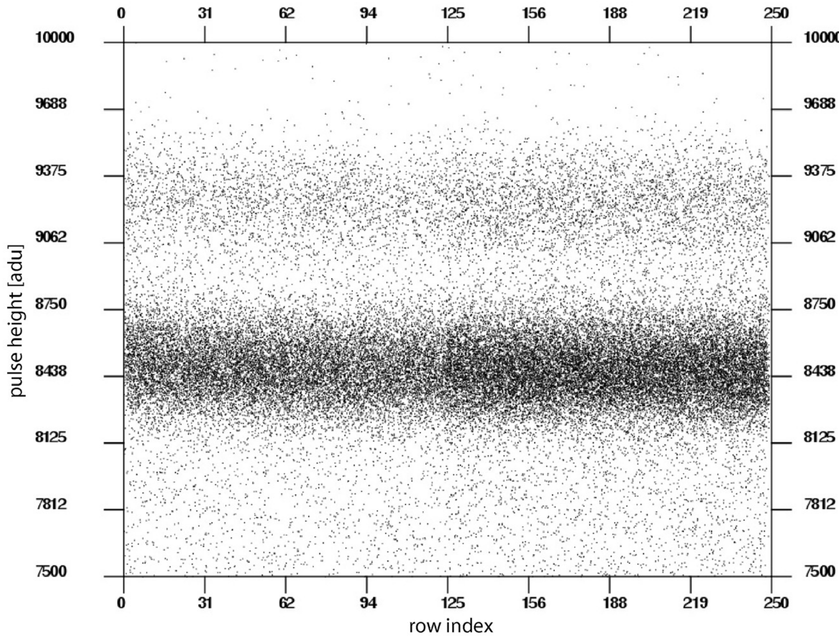

Figure 4.19: *Row scatter plot of a Ti-Kα spectrum, recorded with the frame store pnCCD C10_19_01. Row 0 is at the readout node, the frame store area ends at row 124. Rows 125 to 250 are in the image area. A dot is shown for each X–ray event. In the frame store area the, event density is lower due to the the smaller pixel size of 51x75 µm² vs. 75x75 µm² in the image area.*

4.3.4 Analysis output

After the gain calibration factors and the CTE correction values are determined, the energy calibration for each pixel is finished. Combining the individual pulse heights of split event partners delivers the correct energy of the detected photon within the limits of the Fano–noise and the electronic noise of the detector. The quality of the energy calibration can be tested when the fwhm of a X–ray line in a measured energy spectrum is compared to the theoretical fwhm which results from addition of the Fano–noise and the measured electronic noise of the detector. CCD C11_11_85 (table 4.1) has an electronic noise of 2.3 e^- ENC and the measured fwhm of the 4510 eV Ti–Kα line is 117.1 eV for a spectrum which is created from single event signals. If noise due to charge transfer losses is neglected, the smallest possible fwhm of 110.8 eV is given by the addition of the squares of the Fano noise of 109 eV and the electronic noise equivalent of 19.8 eV. The good quality of the energy calibration is demonstrated by the difference between the measured fwhm and the smallest possible fwhm which is only 6.3 eV or 5.7 %. A 4510 eV (Ti–Kα) spectrum measured with the pnCCD C10_19_01 is shown in fig. 4.20.

The energy calibrated X–ray event data which is extracted from the raw signal frame data of a measurement is written to a file. For each event, the corrected energy, the multiplicity and the center of gravity coordinate is recorded together with the coordinates and the corrected pulse heights of all pixel signals which contribute to the event pattern. The center of gravity coordinate is calculated as $x_{\text{cgrv}} = \sum_{n=1}^{n=n(\text{split})} x \cdot U_{\text{eV}} / \sum_{n=1}^{n=n(\text{split})} U_{\text{eV}}; y_{\text{cgrv}} = \sum y \cdot U_{\text{eV}} / \sum U_{\text{eV}}$ where U_{eV} is the pulse height of a pixel signal, x and y are the line and column coordinates of the pixel and $n(\text{split})$ is the multiplicity of the split event. Photon event files are used as the input of the mesh data analysis, the center of gravity coordinates of the event patterns provide a first, rough estimate of the photon conversion positions.

Figures 4.21 and 4.22 show maps where the Ti–Kα photon count rate is plotted for each pixel of the image area of a 75 x 75 µm^2 pixel frame store pnCCD. The assignment of a photon detection to a pixel coordinate is given by the center of gravity coordinate of the resulting event pattern. Figure 4.21 shows the homogeneous illumination by the distant X–ray source. The remaining count rate fluctuations are due to Poisson statistics. At the edges, the count rate drops to zero since pixel events at the edges were rejected from the analysis.

Figure 4.22 shows a regular moiré pattern with regions where only one out of four pixels is illuminated by the mesh. The pattern is due to the geometry of a mesh setup with a pixel side length of 75 µm and a hole distance of 150 µm in the column (x) and the row (y) coordinate directions. Since the mesh has a rotation angle of 2.5° relative to the pixel array, the position of a hole relative to the pixel below gradually varies over the frame area, see section 3.1. In the regions of the map where the hole positions lie in the middle of pixels, mostly single events occur and one out of four pixels is illuminated. In the regions of the map where the hole positions lie at the rim or at the corner of a pixel, the count rate is lower and every pixel or one out of two pixels is illuminated. The lower count rate results from the distribution of the photons which pass through the hole over up to four neighboring pixels.

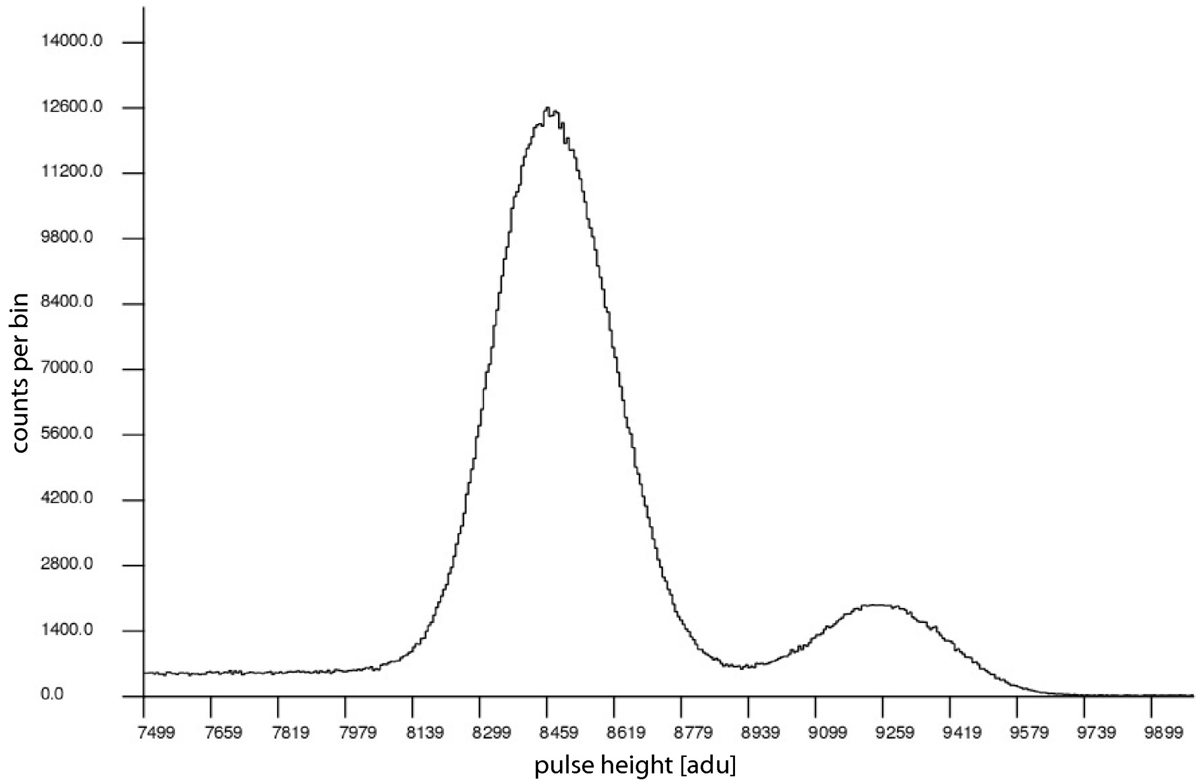

Figure 4.20: *Corrected spectrum of a 4510eV Ti-Kα line, measured with the pnCCD C10_19_01. The gain and CTE correction results in well separated Ti-Kα (4510eV) and Ti-Kβ (4932eV) peaks. The energy calibration can be performed with the pulse height of the Ti-Kα peak as the reference for the gain conversion eV/adu.*

The gain calibration factors and the CTE correction values of each channel are written to a separate calibration file if the analyzed measurement was performed with flat field illumination. Any data set with uncalibrated pixel event data can be corrected with an external calibration file. The calibration however is only correct if the data sets were recorded with the same X–ray spectrum and flux, pnCCD, integration time and the same operation parameters.

In a mesh measurement the pixels are not evenly illuminated. Some pixels show neither single events nor double split patterns where both pixel signals have the same column index. Therefore the energy and the CTE calibration delivers incorrect results for mesh measurement data. A measurement with flat field illumination of all pixels is thus performed in order to provide the energy calibration data of each mesh measurement.

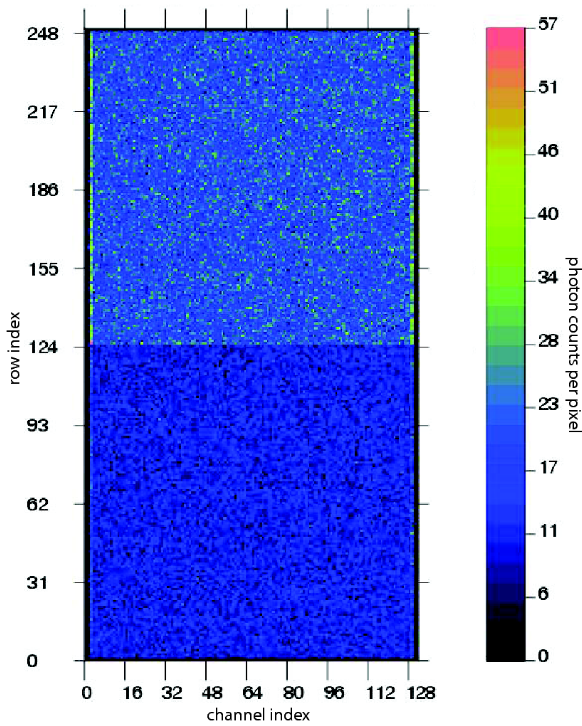

Figure 4.21: *Event count map of a Ti-Kα measurement with flat field illumination. In the image area of the pnCCD C10_19_01, the pixel size is 75x75 µm, in the frame store area (the lower part of the frame), the pixel size is 75x51 µm. Due to the smaller pixel size, the event count rate per pixel is smaller in the frame store area. The count rate value for each pixel is given by the sum of single– to quad event patterns which were detected at a given pixel index in all data frames of the measurement.*

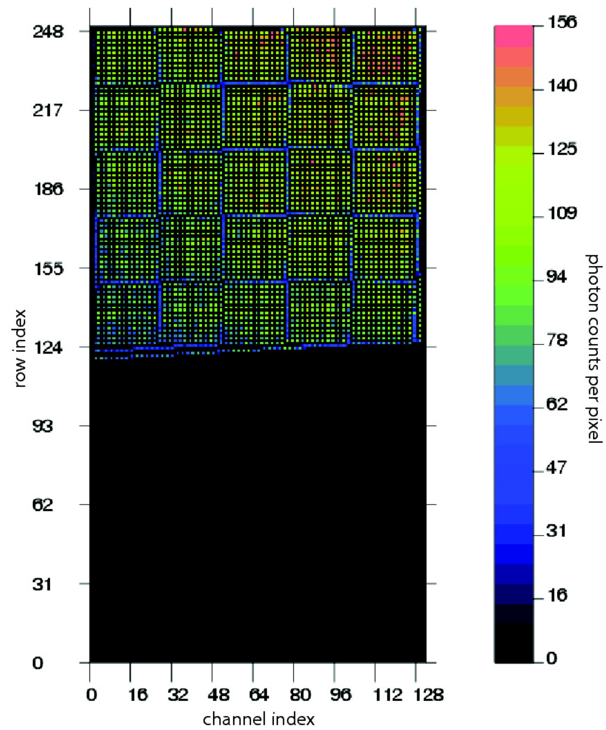

Figure 4.22: *Event count map of a Ti-Kα measurement with illumination through the mesh. The mesh covers the image area in the upper half of the CCD, the mesh angle is 2.5°. Event pattern types from singles to quads were used to calculate the count rate values of the pixels. The hole distance is twice the pixel side length. Thus, every second pixel in a line or row shows a signal except where holes are located at the borders of a pixel. In this case, the events are distributed over neighboring pixels.*

Chapter 5

'Mesh' data analysis

The 'mesh' data analysis works on the photon event data which is provided by the standard data analysis described in section 4.3. Its purpose is to provide a microscopic view of the signal charge distribution for any given photon conversion position in the pixel array. The conversion positions of the photons are controlled by the known mesh hole positions. The charge distribution is given by the signal pulse heights of the individual pixels in an event pattern. The position information of the mesh holes and the signal charge distribution information of the photon event patterns is combined by the mesh analysis. Maps of a reconstructed, virtual pixel which is representative for all pixels of the detector array are created as the final analysis output.

5.1 Types of reconstructed pixel maps

In a reconstructed pixel map, every data point represents a function value at a given photon conversion position. The data values are first calculated for every hole position of the irregular pixel coverage map and then interpolated to a regular grid of 100 x 100 data points per pixel (section 3.2.2, figures 3.11 and 3.12). A high resolution of the interpolated maps facilitates one to transfer all information that is contained in the irregular maps into the interpolated, regular virtual pixel maps.

Reconstructed pixel maps provide insight into two aspects of the function principle and of the physical structure of pnCCDs: I. The majority of signal electrons generated by photons with an energy of up to 6 keV drifts over nearly the whole thickness of the device. How is the signal charge distributed over the pixel structure after its drift to the front side? II. Signal electrons which are generated close to the MOS–gates do not reach the storage cells of the pixels and signal electrons which are generated in the undepleted parts of the p+ register contacts recombine with holes. What is the effective insensitive thickness of these regions?

In order to facilitate a qualitative and quantitative analysis of these effects, the reconstructed pixel maps must provide a representation of the signal charge distribution and the relative sensitivity of different regions within a pixel. These requirements translate in a

set of six maps of the reconstructed pixel response. They are generated from the detected valid single to quad events. The x– and y–coordinates of all reconstructed pixel maps are normalized to the size of the pixels of the analyzed pnCCD.

5.1.1 Event type maps

All pixel maps shown for the illustration of the different map types below are generated from Monte–Carlo simulation[50, 51] data of a setup with a pnCCD and a mesh. In a Monte–Carlo simulation of mesh data, the charge distribution is known for each photon conversion position, so that a consistency check of the mesh analysis results is possible. A pnCCD with a pixel size of 75 x 75 µm^2 and a substrate thickness of 450 µm was simulated. The simulated X–ray line was Ti-Kα with a photon energy of 4510 eV. The mesh has a hole distance of 150 µm on a rectangular grid and a hole diameter of 5 µm, exactly as the mesh employed for all measurements. The simulation makes the simplified assumption that the charge cloud is separated at the pixel borders in depth of 10 µm from the register side. Only the expansion due to diffusion is considered. The back contact voltage and the temperature were adjusted to values that result in a sigma value of 8 µm of the Gaussian charge cloud.

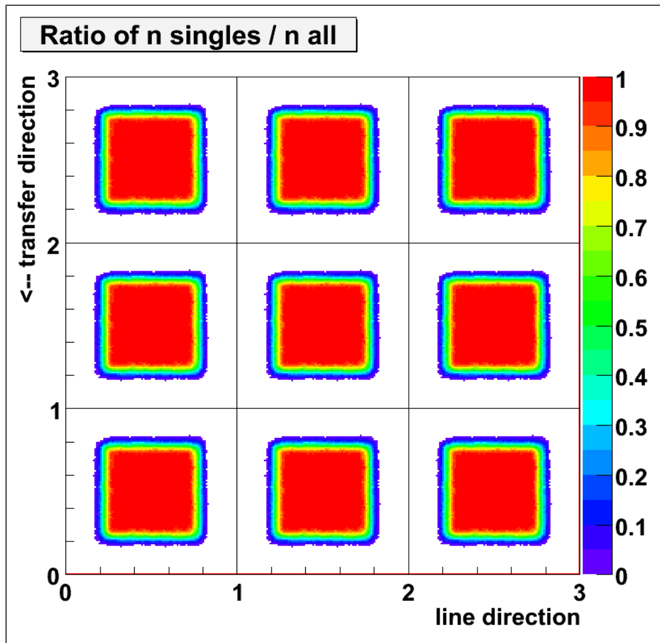

Figure 5.1: *'single map' reconstructed from Monte–Carlo simulation data of a 75 µm pixel pnCCD. Single events occur if a photon is absorbed in the middle of a pixel. The gradual drop of the single event ratio to zero is due to the finite hole size and the signal noise which influences the detection of a split event if the smaller split partner is at the detection threshold. Therefore, both single and split events occur at hole positions near the border of the region where single events occur. The map is generated by repeating the reconstructed 'single map' for one pixel in a 3 by 3 pixel pattern.*

5.1.1.1 'single map'

A single event occurs when a X–ray photon is absorbed near the middle of a pnCCD pixel and if the charge cloud is smaller than the pixel size before it reaches the storage cell. In a single map, the ratio $n_{\text{singles}}/n_{\text{all}}$ is plotted for every photon conversion position in a pixel, where n_{singles} is the number of single events detected at a given conversion position and n_{all}

is the total number of events (including singles) with multiplicities of up to four detected at the same given position.

It thus shows the probability for the collection of the complete signal charge in one pixel if an X–ray photon hits a pixel at a given position. Since the number of detected single events is normalized to the total event rate n_{all}, the result is less prone to statistical or systematic variations of the count rate in different regions of the reconstructed pixel, see section 5.1.2.1.

Figure 5.1 shows a single map reconstructed from the above mentioned Monte–Carlo simulation data. The original single map has a size of one pixel but the plotted map is tiled from nine identical single maps. The tiled three by three pixel map contains the same information as the original single map. In a three by three pixel map however, the width of the region at the pixel borders where only split events occur can be directly compared to the size of the region where only single events occur. The gradual transition from the region with $n_{\mathrm{singles}}/n_{\mathrm{all}} = 1$ to the region with $n_{\mathrm{singles}}/n_{\mathrm{all}} = 0$ is caused by the finite hole size and the signal noise contribution. Due to the finite hole size, the photons which pass through a hole have slightly different conversion positions. If a hole lies at the border of the region where single events occur, a small difference of the photon conversion position decides whether the photon event is a single or a split event. For these hole positions, a mix of single and split events is detected. A similar effect is caused by the signal noise. If a small amount of signal charge reaches the neighboring pixel, the statistically varying electronic noise contribution can move the resulting signal pulse height over the event detection threshold. Finally, the signal charge distribution is a statistical process such that the charge split ratio slightly varies for a number of photons which hit the pixel at the same position. As a result, at a given photon conversion position at the border of the region where only single events occur, both single and split events may be detected.

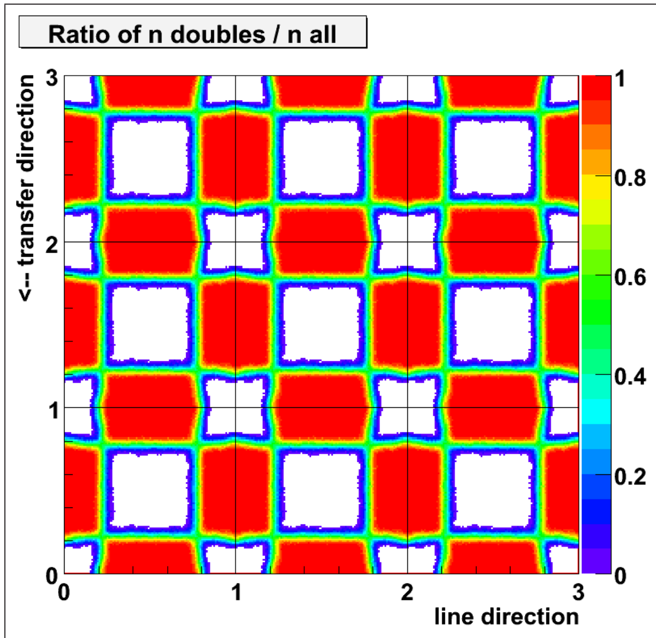

Figure 5.2: *This plot of a 'double map' covers an area of three by three pixels where each pixel is the identical double map of the reconstructed pixel. The map is reconstructed from simulation data with a pixel size of 75 µm. Double events occur near the pixel borders in the red regions of the map, but not in the corners of a pixel. A three by three pixel map is easier to interpret since the regions where double events occur are not interrupted at the pixel borders. Note the yellow, green, and blue transition regions where double events occur with less than 100% probability due to the finite hole size and signal noise.*

5.1.1.2 'double map'

Double events occur if a photon hits a pixel border. The region where double events occur has the width of the gap between the regions where only single events occur.

Similar to the single map, the ratio $n_{\text{doubles}}/n_{\text{all}}$ is plotted. Here, n_{doubles} is the number of detected double split events at a given photon conversion position and n_{all} is the number of all events with a multiplicity of up to four which are detected at the given position. Figure 5.2 shows the double map reconstructed from the Monte–Carlo simulation data described above. The reasons for the gradual transition from $n_{\text{doubles}}/n_{\text{all}} = 1$ to $n_{\text{doubles}}/n_{\text{all}} = 0$ are the same as discussed for the same effect in the single map.

The advantage of having a tiled three by three pixel map now becomes obvious. Since X–ray photons cause double events if they hit the border of a pixel, the width of the areas where double events occur is directly visible only in maps which cover at least two by two pixels.

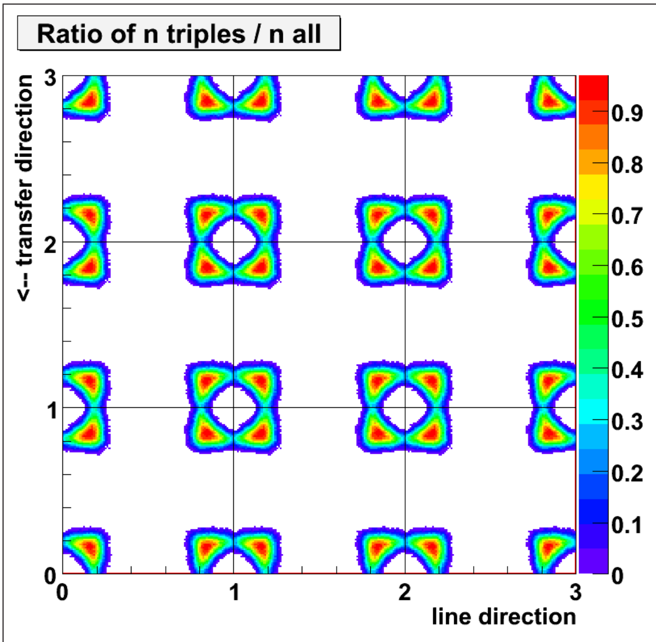

Figure 5.3: *'triple map' of 75* µm *pixel simulation data. The map shows the ratio* $n_{\text{triples}}/n_{\text{all}}$. *Triples occur near the corner of a pixel when the main part of signal charge is distributed over three pixels as shown in figure 4.15. For the simulation data shown in this reconstruction, a model is used where a Gaussian charge cloud is split at the pixel borders. This is indicated by the symmetric location of the regions where triples occur around pixel corners. Directly on the pixel borders either doubles or quadruples occur.*

5.1.1.3 'triple map'

In section 4.3.2, the topology of a triple event is illustrated in figure 4.15. Triple events are generated by photons hitting a pixel near a corner, but not directly on a corner. This is illustrated by figure 5.3 which shows a triple map which displays the ratio $n_{\text{triples}}/n_{\text{all}}$, for the Monte–Carlo simulation data set of a pnCCD with 75 µm pixels.

5.1.1.4 'quad map'

Quad maps show the ratio $n_{\text{quads}}/n_{\text{all}}$ for each photon conversion position in the reconstructed virtual pixel. Figure 5.4 shows a quad map generated from the Monte–Carlo

simulation data used for the single– to triple maps. As expected, quad events are caused by photons which hit a pixel close to its corner.

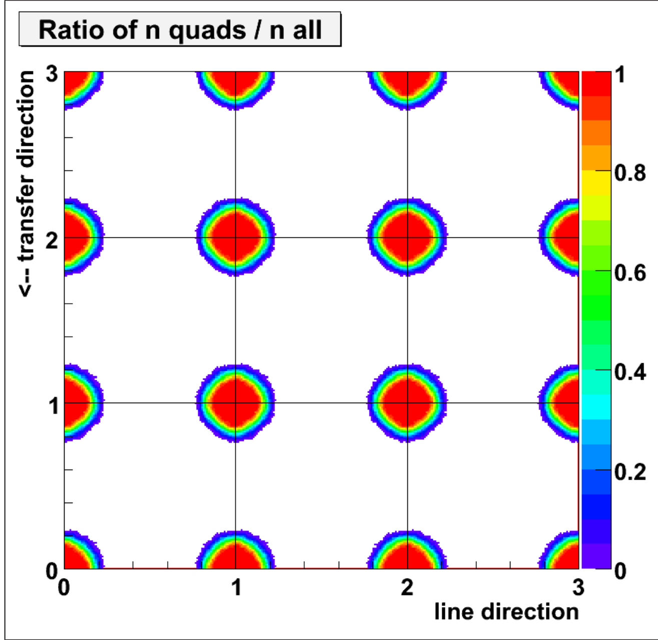

Figure 5.4: 'quad map' which displays the ratio $n_{\text{quads}}/n_{\text{all}}$ for monte–carlo simulation data of a 75 µm pixel pnCCD. Quad events are caused by photons which hit the pixel closer to the corner than photons generating triple events. Triples and quads are also referred to as corner events. The size of the round region where quads occur is influenced by the threshold used for the event detection and by the charge cloud size before separation. A higher threshold will shrink the region where quads occur while a larger charge cloud size causes an expansion of this region.

As all other event maps, the quad map mainly serves the purpose of checking the general expectations of charge splitting in the pixel structure and the success of the pixel reconstruction. A failed reconstruction of the geometrical mesh parameters will cause distorted or irregular event maps where e.g. single events are distributed over the whole reconstructed pixel map and not only in its center. A higher event detection threshold will increase the number of singles and thus the size of the region where $n_{\text{singles}}/n_{\text{all}}$ is close to 1.0. Event maps therefore give qualitative information on the charge distribution process in the pixel structure. Asymmetries of the charge distribution as a function of the photon conversion position however are directly visible in the event maps.

5.1.2 Photon response maps

The maps shown in the following two sections are reconstructed from the same Monte–Carlo simulation data set that was used for the event maps shown in section 5.1.1. Photon response maps are used for the quantitative analysis of the mesh data. The count map shows the relative X–ray photon absorption factor of different regions in the register structure. The charge map shows the distribution of signal charge over the pixel structure.

5.1.2.1 'count map'

The irregular 'count map' shows the absolute number of detected X–ray photons for each hole position in the coverage map. In the regular map discussed here, the count values at the hole positions in the coverage map are interpolated to a regular grid with the method

described in section 3.2.2. Identical to the event maps, the count map originally covers one pixel. In order to facilitate the interpretation of the map values at the pixel borders, it is tiled into a three by three pixel map.

Back side illuminated pnCCDs have a uniform detection efficiency for X–ray photons over all pixels in the frame area. A count map which is reconstructed from a mesh measurement with back side illumination shows the X–ray photon event count rate as a function of the photon conversion position in a pixel. The detection efficiency is expected to be homogeneous not only over the pixel array but also inside of a pixel. The photon count map of the reconstructed pixel should therefore only show statistical variations of the photon count rate. Figure 5.5 shows a count map reconstructed from Monte–Carlo simulation data. The simulation modeled a pnCCD with back side illumination and homogeneous sensitivity both over the frame area and inside of each pixel. In the shown count map, a systematic drop of the count rate appears in the corners of the reconstructed pixel. This effect is an analysis artifact which results from the method of event pattern selection described in section 4.3.2. It is discussed in detail in section 5.3.2.1.

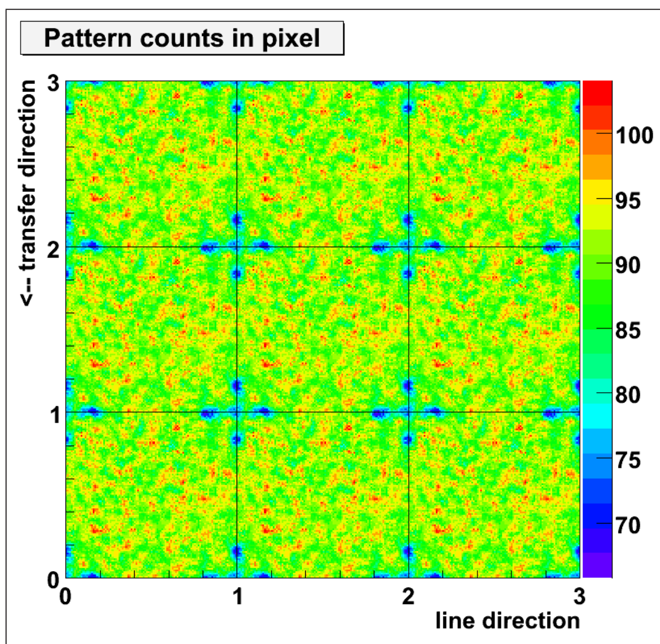

Figure 5.5: *The 'count map' displays the number of detected X-ray photons for each hole position. Like the 'single map', it is generated by arranging the count map for one pixel in a 3x3 pattern. Note the statistical variations of the count rate over the map area and the drop of the count rate in the corners of the pixels. Since this map is created from simulation data, the count rate drop in the corners is an analysis artifact. These artifacts have to be considered in the analysis of measurements with front side illumination.*

For mesh measurements with front side illumination, the count map is used to calculate the relative differences of the count rate in different regions of the register structure. Due to the errors of the count rate values in the corners of the reconstructed pixel, these regions must be skipped from the count rate analysis. Relative count rate differences directly give the relative differences of the photon absorption in different parts of the pixel, e.g. at the register contacts and at the MOS–gates. In the analysis presented in sections 5.3.1.4 and 7.3, count maps are used to evaluate the absorption of low energy photons in the register structure.

5.1.2.2 'charge map'

The charge map displayed in figure 5.6 shows the 'charge collection function' which is defined both inside of the central pixel in a region covering three by three pixels and in the surrounding eight pixels. For each photon conversion position in the three by three pixel map, the 'charge collection function' gives the amount of charge collected in the central pixel relative to the total amount of signal charge generated by a photon with a given energy. Drawing 5.7 shows a graphic description of the values of the charge collection function plotted in the charge map.

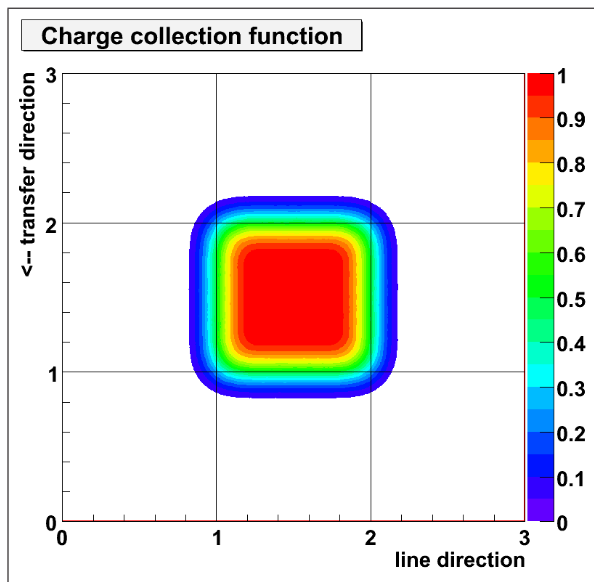

Figure 5.6: *This 'charge map' of 75 µm pixel simulation data shows the efficiency of signal charge collection for the reconstructed pixel. In the center of the pixel 100% of the signal charge is collected, the collection efficiency drops to 0% far outside the pixel borders.*

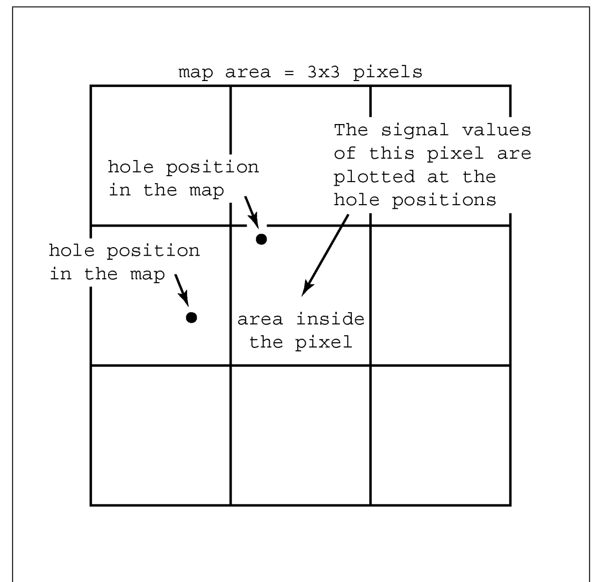

Figure 5.7: *Interpretation of values in a charge map with an area of 3x3 pixels. Each map point gives the relative amount of signal charge that reaches the central pixel when a photon is absorbed at the given map position.*

For each X–ray photon event, the value of the charge collection in the three by three pixel map is calculated in the following way: The hole position at which the event was detected in the pixel array is located in the three by three pixel map which shows nine reconstructed virtual pixels. The relative pulse height of the central pixel in the map is calculated by dividing the signal pulse height which is detected in the central pixel into the total pulse height of the photon event pattern. Since the signal pulse height in each pixel of the pattern is proportional to the amount of signal charge, the map value gives the relative amount of signal charge detected in the central pixel. If the pulse height of the central pixel is equal to the total pulse height of the pattern, i.e. in the case of a single pattern, the map value is 1.0. If the pulse height of the central pixel is one half of the total pattern pulse height, i.e. in the case of a symmetric double split event, the map value is

0.5. If the pulse height of the central pixel is zero, i.e. in the case of a hole position at the outer border of the three by three pixel region, the map value is zero. The charge map therefore displays the relative amount of charge which is collected in the central pixel as the function of any given photon conversion position inside of an area of three by three pixels. The final value of the charge collection function at a given hole position is the average of the individual values calculated for all event patterns detected at the hole position. The charge map values at the hole positions in the virtual pixel coverage map are interpolated to a regular grid with the method discussed in section 3.2.2.

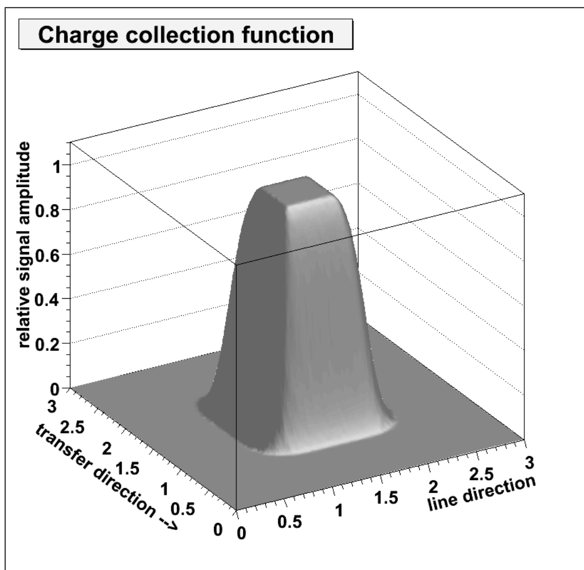

Figure 5.8: *The charge collection function displayed in map 5.6 as a surface plot. The flat area in the middle of the map is the region of the reconstructed pixel where single events occur.*

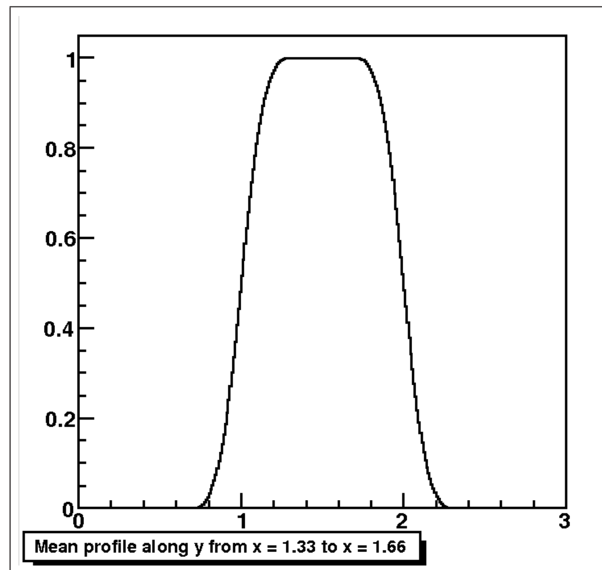

Figure 5.9: *A profile of the charge collection function in the charge transfer direction (the y coordinate). Each value is averaged from x = 1.33 to x = 1.66 where x is the row coordinate.*

Further representations of the charge collection function are shown in figures 5.8 and 5.9. Plot 5.8 shows that the charge collection function has the form of a hill with a plateau in the middle pixel of the map. The model for the charge distribution employed in the Monte–Carlo simulation assumes expansion of the charge cloud due to diffusion during the drift time before collection in the pixel structure. A longer drift time or a higher temperature causes a larger charge cloud and therefore a less steep slope at the sides of the charge collection function 'hill'. In the following sections, the relation between this slope and the size of the charge cloud will be used to parameterize the charge cloud size. In chapter 7, the measured charge cloud size is compared with the results of numerical simulations of signal charge collection.

5.2 Precision of the generated maps

The complete mesh analysis of a pnCCD consists of the mesh measurement, the standard analysis, the mesh analysis, the creation of reconstructed pixel maps and their final interpretation. Statistical errors due to the limited number of detected photons and due to electronic noise originate in the measurement and propagate through all steps of the analysis chain. Due to the complexity of this analysis process, it is reasonable to use simulation data with known input parameters and compare the analysis results with the input values of the simulation [51] instead of a stepwise error analysis.

The 75 µm pixel pnCCD data set which is used to illustrate the types of reconstructed pixel maps in sections 5.1.1 and 5.1.2 belongs to a simulation data set created for the error analysis of the mesh position reconstruction and the charge map generation. Monte–Carlo data sets of a pnCCD with a pixel size of 51 µm were created in order to find out if the reconstruction precision changes with the pixel size. An X–ray line energy of 4510 eV (Ti–Kα) was chosen for all simulations.

In the first step, the values of the mesh angle and the hole distance for both vertical and horizontal hole lines were compared to the input parameters. Finally a charge map was generated from the simulation data and compared to the input of the physical simulation model.

5.2.1 Geometrical mesh parameters

The mesh angle was varied from 2.2° to 2.8° in 0.1° steps for both the 75 µm pixel and 51 µm pixel simulations resulting in a total number of 14 data sets. The mesh parameters were set to the values specified for the mesh which was used in all measurements. The hole diameter is 5.0µm and the hole distance is 150 µm. In the Monte–Carlo simulation, the final signal charge distribution for each detected photon is obtained from the width and the center position of a Gaussian charge cloud. After it has reached a depth of 10 µm from the front side of the simulated pnCCD, the charge cloud is split at the borders of the pixels. Therefore, the amount of charge in a pixel is given by the integral of the charge density over the area of the pixel.

A mean value of 7.97 µm (σ) for the width of the Gaussian charge cloud resulted from a back contact voltage of -150 V, a detector thickness of 450 µm, a separation depth of 10 µm from the front side and a device temperature of 300 K. This value of σ is close to the values which were found with the analysis of mesh data obtained with the used 75 µm pixel and 51 µm pixel pnCCDs at an energy of 4510 eV (Ti–Kα). The exact charge cloud size for each photon event slightly depends on the actual absorption depth which follows an exponential distribution, section 1.3. Since the absorption length of Ti–Kα photons is 13 µm, the variation of the absorption depth is small compared to the total drift distance of typically 427 µm. The electronic noise added to the signals is 6.0 e^- ENC in the case of both simulated pnCCDs. This noise value is higher than the noise of the pnCCDs with 75 µm and 51 µm which were used for the mesh measurements, see table 4.1. Since electronic noise causes a degradation of the signal measurement precision, it also causes a

degradation of the reconstruction precision. The signal noise value in the simulations is thus overestimated in order to obtain an upper limit of the mesh reconstruction error.

input angle	horizontal angle error	vertical angle error	horizontal dist. error	vertical dist. error	max. pos. error
2.2°	$(-4.3 \cdot 10^{-3})°$	$(-6.3 \cdot 10^{-3})°$	$-3.0 \cdot 10^{-3}$ µm	0.0 µm	2.0 µm
2.3°	$(-2.0 \cdot 10^{-4})°$	$(-4.8 \cdot 10^{-3})°$	$8.25 \cdot 10^{-3}$ µm	$-3.75 \cdot 10^{-3}$ µm	1.1 µm
2.4°	$(-5.0 \cdot 10^{-3})°$	$(4.8 \cdot 10^{-3})°$	$-7.5 \cdot 10^{-4}$ µm	$-9.75 \cdot 10^{-3}$ µm	2.3 µm
2.5°	$(5.1 \cdot 10^{-3})°$	$(-2.0 \cdot 10^{-3})°$	$4.5 \cdot 10^{-3}$ µm	$3.0 \cdot 10^{-3}$ µm	1.7 µm
2.6°	$(-4.2 \cdot 10^{-3})°$	$(-1.0 \cdot 10^{-4})°$	$-3.75 \cdot 10^{-3}$ µm	$4.5 \cdot 10^{-3}$ µm	1.2 µm
2.7°	$(-2.3 \cdot 10^{-3})°$	$(-4.0 \cdot 10^{-3})°$	$3.75 \cdot 10^{-3}$ µm	$3.75 \cdot 10^{-3}$ µm	1.5 µm
2.8°	$(-5.6 \cdot 10^{-3})°$	$(6.2 \cdot 10^{-3})°$	$7.5 \cdot 10^{-4}$ µm	$3.75 \cdot 10^{-3}$ µm	2.3 µm
mean err. →	$(-2.4 \cdot 10^{-3})°$	$(-8.9 \cdot 10^{-4})°$	$1.4 \cdot 10^{-3}$ µm	$2.0 \cdot 10^{-4}$ µm	0.7 µm
variance →	$(3.7 \cdot 10^{-3})°$	$(4.8 \cdot 10^{-3})°$	$4.3 \cdot 10^{-3}$ µm	$5.3 \cdot 10^{-3}$ µm	2.0 µm

Table 5.1: *Results of the mesh position reconstruction for simulation data of a 75x75 µm^2 pixel pnCCD with 128x128 pixels. The simulated line energy is 4510 eV. For each line of the table, the maximum possible position error of a hole position is shown in the last column. The maximum systematic deviation from the input values is given by the mean error in the second last line, the expected error is the value of the variance in the last line. The maximum error of the hole position is smaller than the hole radius and does therefore not reduce the spatial resolution of the virtual pixel scan.*

input angle	horizontal angle error	vertical angle error	horizontal dist. error	vertical dist. error	max. pos. error
2.2°	$(-9.4 \cdot 10^{-5})°$	$(-4.3 \cdot 10^{-4})°$	$-9.75 \cdot 10^{-4}$ µm	$5.25 \cdot 10^{-4}$ µm	0.2 µm
2.3°	$(3.3 \cdot 10^{-4})°$	$(-4.3 \cdot 10^{-4})°$	$8.1 \cdot 10^{-3}$ µm	$-9.75 \cdot 10^{-4}$ µm	0.7 µm
2.4°	$(-4.1 \cdot 10^{-4})°$	$(3.2 \cdot 10^{-4})°$	$-2.6 \cdot 10^{-3}$ µm	$5.25 \cdot 10^{-4}$ µm	0.3 µm
2.5°	$(-1.3 \cdot 10^{-5})°$	$(-5.3 \cdot 10^{-4})°$	$3.53 \cdot 10^{-3}$ µm	$5.03 \cdot 10^{-3}$ µm	0.6 µm
2.6°	$(5.7 \cdot 10^{-4})°$	$(2.2 \cdot 10^{-4})°$	$5.25 \cdot 10^{-4}$ µm	$5.25 \cdot 10^{-4}$ µm	0.2 µm
2.7°	$(2.9 \cdot 10^{-4})°$	$(-6.2 \cdot 10^{-4})°$	$-9.75 \cdot 10^{-4}$ µm	$5.25 \cdot 10^{-4}$ µm	0.3 µm
2.8°	$(-2.6 \cdot 10^{-4})°$	$(-9.6 \cdot 10^{-4})°$	$2.03 \cdot 10^{-3}$ µm	$3.53 \cdot 10^{-3}$ µm	0.6 µm
mean err. →	$(5.9 \cdot 10^{-5})°$	$(-3.5 \cdot 10^{-4})°$	$1.4 \cdot 10^{-3}$ µm	$1.4 \cdot 10^{-3}$ µm	0.25 µm
variance →	$(3.5 \cdot 10^{-4})°$	$(4.6 \cdot 10^{-4})°$	$3.6 \cdot 10^{-3}$ µm	$2.1 \cdot 10^{-3}$ µm	0.5 µm

Table 5.2: *Results of the mesh position reconstruction for simulation data of a 51x51 µm^2 pixel pnCCD with 192x192 pixels. The total simulation area of the device is thus the same as in table 5.1. The simulated line energy is 4510 eV. Compared to the results of the 75* µm *pixel simulation in table 5.1, the reconstruction accuracy is improved by a factor of more than two. As in the case of the 75* µm *pixel simulation, the maximum position error is smaller than the hole radius and thus not detrimental to the accuracy of the reconstructed pixel maps.*

Tables 5.1 and 5.2 show the results of the mesh position reconstruction analysis. A

estimation of the upper limit of the geometrical position reconstruction error of the mesh holes was obtained with the relation which is illustrated in figure 5.10:

$$\begin{aligned}\Delta s_{\max} = &\tan(|\Delta\varphi_{\mathrm{x}}|)\cdot\Delta x_{\mathrm{mesh}}\cdot n_{\mathrm{holes}}(x)\\ &+\tan(|\Delta\varphi_{\mathrm{y}}|)\cdot\Delta y_{\mathrm{mesh}}\cdot n_{\mathrm{holes}}(y)\\ &+|\Delta\Delta x_{\mathrm{mesh}}|\cdot n_{\mathrm{holes}}(x)\\ &+|\Delta\Delta y_{\mathrm{mesh}}|\cdot n_{\mathrm{holes}}(y)\end{aligned} \tag{5.1}$$

where x and y are the horizontal and vertical hole line directions respectively, $\Delta\varphi_{\mathrm{x}}$ and $\Delta\varphi_{\mathrm{y}}$ are the errors of the hole line angles, $\Delta\Delta x_{\mathrm{mesh}}$ and $\Delta\Delta y_{\mathrm{mesh}}$ are the hole distance errors, Δx_{mesh} and Δy_{mesh} are the hole distances and $n_{\mathrm{holes}}(x)$ and $n_{\mathrm{holes}}(y)$ are the numbers of mesh holes along each side of the mesh. Section 3.2.1 discusses the mesh geometry and the mesh position parameters.

Summing up the results of tables 5.1 and 5.2 shows that the hole position error is smaller in the case of the smaller pixel size of 51 µm. The maximum hole position error is 2.3 µm for 75 µm pixels and 0.7 µm for 51 µm pixels. A position error of 2.3 µm is slightly below the hole radius and therefore acceptable. It must be kept in mind that 2.3 µm is the upper limit of the position errors in table 5.1 and that equation 5.1 represents a worst case combination of the individual parameter errors which are shown in the tables 5.1 and 5.2. Therefore it is safe to say that the position reconstruction is precise enough even in the worst case. The average of the hole position errors of table 5.1 is 1 µm which is uncritical since it is smaller than the hole radius.

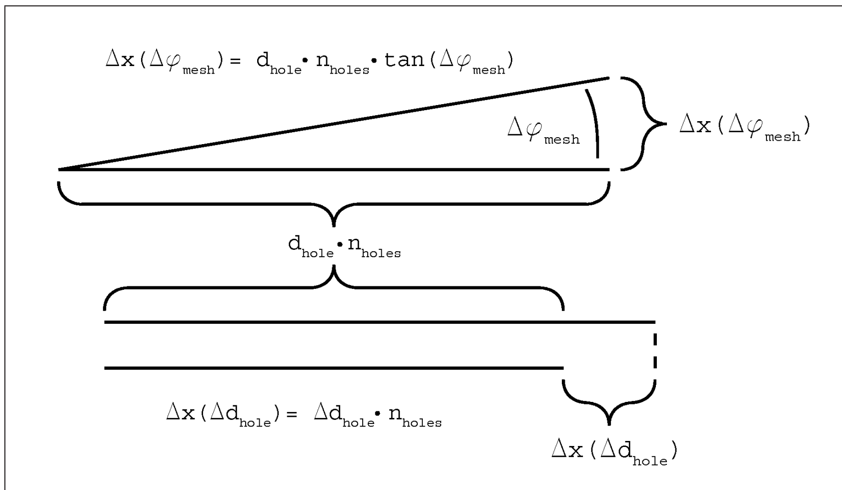

Figure 5.10: *Geometrical estimate of the maximum hole position error due to errors of the reconstructed mesh angle and the hole distance, compare equation 5.1. The position errors due to the two mesh angle– and two hole distance–errors are added to get the worst case of linear addition.*

5.2.2 Error function model of the charge collection function

During the mesh data analysis for all studied pnCCDs, it turned out that nearly all results for the charge collection function reconstructed from mesh measurements can be parame-

terized with a two dimensional error function of the following form:

$$\mathrm{ccf}_{\mathrm{mod}}(x;y;\sigma_{\mathrm{x}};\sigma_{\mathrm{y}};x_0;x_1;y_0;y_1) = \frac{1}{4}\cdot(\mathrm{erf}(x;\sigma_{\mathrm{x}};x_0)-\mathrm{erf}(x;\sigma_{\mathrm{x}};x_1)) \cdot(\mathrm{erf}(y;\sigma_{\mathrm{y}};y_0)-\mathrm{erf}(y;\sigma_{\mathrm{y}};y_1)) \quad (5.2)$$

where the error function $\mathrm{erf}(x,\sigma,x_0)$ is defined as:

$$\mathrm{erf}(x;\sigma;x_0) = \frac{2}{\sqrt{\pi}}\cdot\int_0^{(x-x_0)/(\sqrt{2}\sigma)} e^{-t^2}dt \quad (5.3)$$

σ_x and σ_y parameterize the size of the Gaussian charge cloud, x_0 and y_0 have the value 1.0, x_1 and y_1 have the value 2.0. Equation 5.2 also describes the charge collection function model of the Monte–Carlo simulation program which was used for the evaluation of the mesh position reconstruction. In the simulation, it has the form $\mathrm{ccf} = \mathrm{ccf}_{\mathrm{mod}}(x;y;\sigma_{\mathrm{mean}};\sigma_{\mathrm{mean}};1.0;2.0;1.0;2.0)$ where σ_{mean} results from the average σ of all collected charge clouds generated by the simulated X–ray photons.

Table 5.3 lists the charge cloud sigma values which were obtained with fits of the ccf model defined by equation 5.2 to the reconstructed charge collection functions. The relative error of σ is below 1% in both coordinate directions. The errors are mainly systematic, but not significant due to their small values. Note that the fit results of σ_{x} and σ_{y} include the convolution of the charge collection function with the form of the 5µm large mesh holes. Despite the fact that the hole size of 5 µm is in the order of the charge cloud σ, it has a negligible effect on the results for σ_{x} and σ_{y}. Figures 5.11and 5.12 show the difference of the reconstructed charge collection function and the best fit model as defined in equation 5.2.

	75 µm pixel		51 µm pixel	
mesh angle	σ_{x} error	σ_{y} error	σ_{x} error	σ_{y} error
2.2°	0.05 µm / 0.6%	0.03 µm / 0.4%	-0.03 µm / -0.4%	-0.04 µm / -0.5%
2.3°	0.04 µm / 0.5%	0.03 µm / 0.4%	-0.05 µm / -0.6%	-0.04 µm / -0.5%
2.4°	0.04 µm / 0.5%	0.03 µm / 0.4%	-0.03 µm / -0.4%	-0.02 µm / -0.3%
2.5°	0.03 µm / 0.4%	0.04 µm / 0.5%	-0.04 µm / -0.5%	-0.03 µm / -0.4%
2.6°	0.05 µm / 0.6%	0.03 µm / 0.4%	-0.04 µm / -0.5%	-0.04 µm / -0.5%
2.7°	0.06 µm / 0.8%	0.05 µm / 0.6%	-0.04 µm / -0.5%	-0.02 µm / -0.3%
2.8°	0.06 µm / 0.8%	0.06 µm / 0.8%	-0.03 µm / -0.4%	-0.03 µm / -0.4%
mean err. →	0.05 µm / 0.6%	0.04 µm / 0.5%	-0.04 µm / -0.5%	-0.03 µm / -0.4%
variance →	0.01 µm / 0.1%	0.01 µm / 0.1%	0.01 µm / 0.1%	0.01 µm / 0.1%

Table 5.3: *Results of pixel reconstruction from Monte–Carlo simulation data. The data sets are the same as in section 5.2.1. The input sigma value from the simulation model is chosen to be 7.97 µm for all data sets. This sigma value is near the mean of the results for experimental data which are shown in the tables 5.6 and 5.8. Note that the errors of* σ_{x} *and* σ_{y} *are smaller than 1% in all cases and can thus be neglected.*

As expected, the biggest deviations between the fit model and data are found at the slopes where the charge collection function has values between 0 and 1. Near the center of the pixel, the small split signals of neighboring pixels are rejected by the signal threshold. This results in a too large value of the collection efficiency, see the middle part of figs. 5.11 and 5.12. Where the reconstructed charge collection function drops to zero, the values are too small compared to the fit model because the correspondingly small signals of the center pixel are below the threshold and are rejected.

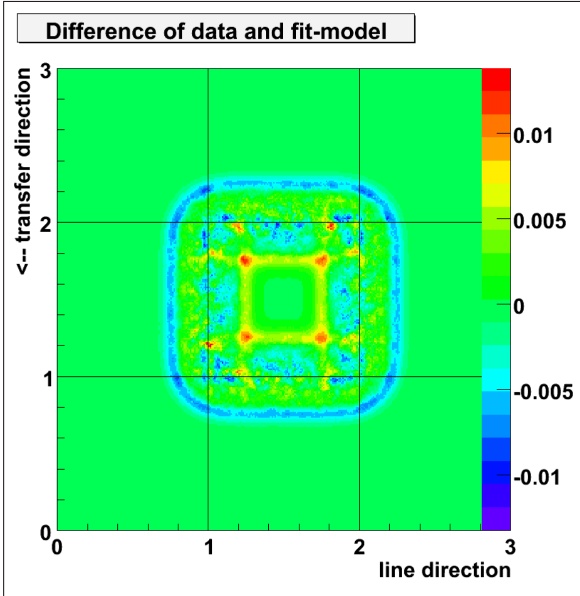

Figure 5.11: *Map of the difference after subtracting the fit model result from the input data of the reconstructed charge collection function. The charge collection function is reconstructed from a simulated data set of a simulated device with 75x75 μm² pixels.*

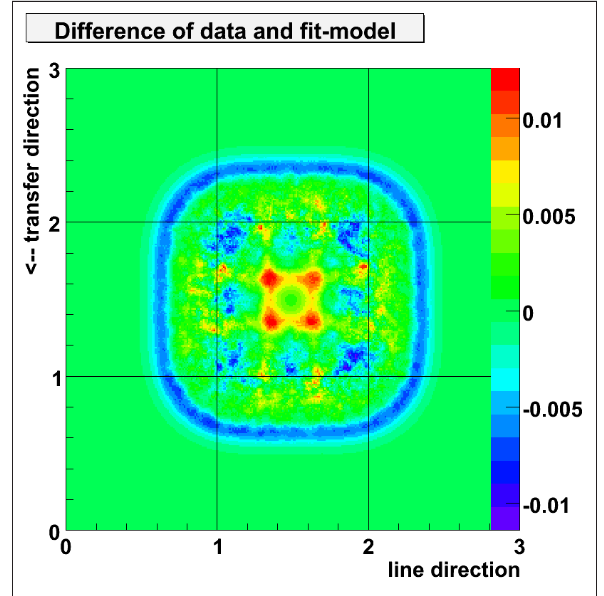

Figure 5.12: *The difference between the reconstructed ccf and the ccf fit–model for data of a simulated pnCCD with 51x51 μm² pixels. The maximum deviation between the fitted ccf model and the reconstructed ccf is less than* 1.5%.

The errors of the charge collection function reconstruction from simulated data sets are below 1% for σ_x and σ_y and below 1.5% for the ccf amplitude values. These errors are so small that they are negligible in the quantitative analysis of the charge collection function.

5.3 Analysis of the pixel response

Event maps facilitate a qualitative analysis of the charge collection function and therefore the information needed for a general understanding of the charge collection process. The quantitative data analysis is done with the photon count maps and the maps of the charge collection function.

5.3.1 Location of event types

The event maps which are defined and discussed in section 5.1.1 represent the model of charge collection which is implemented in the Monte–Carlo simulation software for pnCCDs. The types of X–ray photon events from single to quadruple split events which are observed in flat field X–ray measurements with pnCCDs are explained with the assumption that a Gaussian signal electron cloud is split at the pixel borders. In a flat field measurement however, the regions where specific split event types occur in a pixel are not visible and the correctness of the assumed charge collection model cannot be proven.

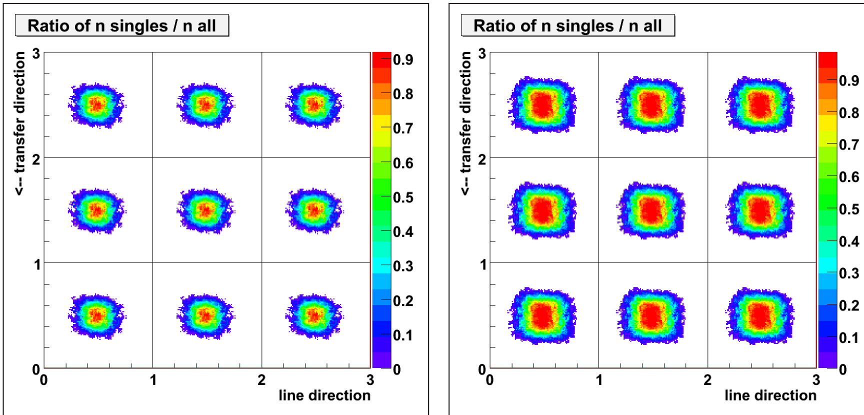

Figure 5.13: *Single maps reconstructed from mesh data processed with an event threshold of $8\sigma_{\rm noise}$ (left) and $16\sigma_{\rm noise}$ (right). The region where single events occur grows with an increasing event threshold.*

Mesh measurements with a given set of different X–ray energies provide the data which is needed to create the event maps which give a qualitative representation of the charge collection process in pnCCDs. The interpretation of event maps must consider the effect of the applied signal threshold for X–ray events. Figure 5.13 demonstrates that a different event threshold changes the relative abundance of the detected event types for given data set. The charge distribution information contained in the original data set is the same for both maps. A higher event threshold however leads to the rejection of split pattern members with small signal amplitudes and thus increases the relative number of single events which is plotted in a single map. The analysis of event maps therefore focuses on the general location of specific event types, not on the absolute size of the region where they occur.

5.3.1.1 150µm pixel XMM–type pnCCD

Here the interest is focused on the measurements listed in table 4.2 with voltage set a), table 4.3 because of the larger number of collected photons compared to the measurements with voltage set b). The best signal to noise ratio for the split event detection is obtained with the highest used X–ray energy of 4510 eV (Ti-Kα), so event maps created from Ti–Kα measurements are shown here. A signal threshold of $4 \cdot \sigma_{\rm noise}$ was applied which results in a signal threshold of $26.4e^-$ or $26.4e^-/1236e^- = 2.1\%$ of the X–ray line energy. The single to quad event maps are shown in figure 5.14.

The fact that in the 150 µm pixel XMM pnCCD most of the detected events are single events is reflected in the appearance of the virtual pixel map where most of the pixel area is covered by the region where only single events occur. In the case of double register storage, the region where single events occur with a probability of 1.0 is a square and split events occur only at the pixel borders. The regions in the pixel where photons cause quadruple split events are centered on the corners of the pixel and triple events are detected in regions which surround the corners. The topology of the event maps obtained with double register storage corresponds to the model of a Gaussian charge cloud which is split at the pixel borders, see the top row of figure 5.14.

The event maps have a very different topology for the measurement with single register storage. Less single events occur and the map area where they are detected shrinks and loses its quadratic shape. The regions where triple and quad events are detected are elongated along the charge transfer direction. Double events occur mostly at the horizontal pixel borders, especially near the channel stops at the vertical pixel borders. In terms of the model where a charge cloud is splitted at the pixel borders, the effective charge cloud size increases with increasing drift time. A longer drift time thus results in more split events. In the case discussed here, the drift time is anisotropic over the pixel area. This is indicated by the event maps which show that near the pixel corners, split events occur in regions which are elongated in the charge transfer direction.

5.3.1.2 75µm pixel frame store pnCCD

The frame store pnCCD with 75 x 75 µm^2 pixels which is discussed here has pixels which cover one quarter of the area compared to the pixels of the previously discussed XMM–type CCD. This means that the charge cloud size is roughly twice as large relative to the pixel size. The maps shown in figure 5.15 are reconstructed from measurements with the 4510 eV Ti–Kα emission line. An event threshold value of $8\sigma_{\text{noise}}$ was chosen for the event selection. It results in an effective event threshold of $44e^-$ or $44e^-/1236e^- = 3.6\%$ of the line energy, compare table 4.1. The operating voltages are listed in voltage set b) of table 4.5 for single register storage and voltage set a) of table 4.5 for double register storage. The top row of event maps shows the case of single register storage, the bottom row the case of double register storage.

A comparison with the results for the 150µm pixel device confirms the expectation that the region where single events occur is smaller. Due to the larger charge cloud relative to the pixel size, more split events occur. A more subtle difference is visible between the upper row and the lower row of the event maps. During the measurement with single register storage which is represented in the maps of the top row, a more negative back contact voltage was applied. Therefore the drift time from the generation of signal charge to its final distribution over the pixel structure is shorter. This results in a shorter time span for the expansion of the signal charge cloud and a smaller signal charge cloud size. The effect that more split events occur if the device is operated in single register storage mode with the same operating voltages is also observed with the discussed 75 µm pixel pnCCD. This effect can be compensated with a more negative back contact voltage. In

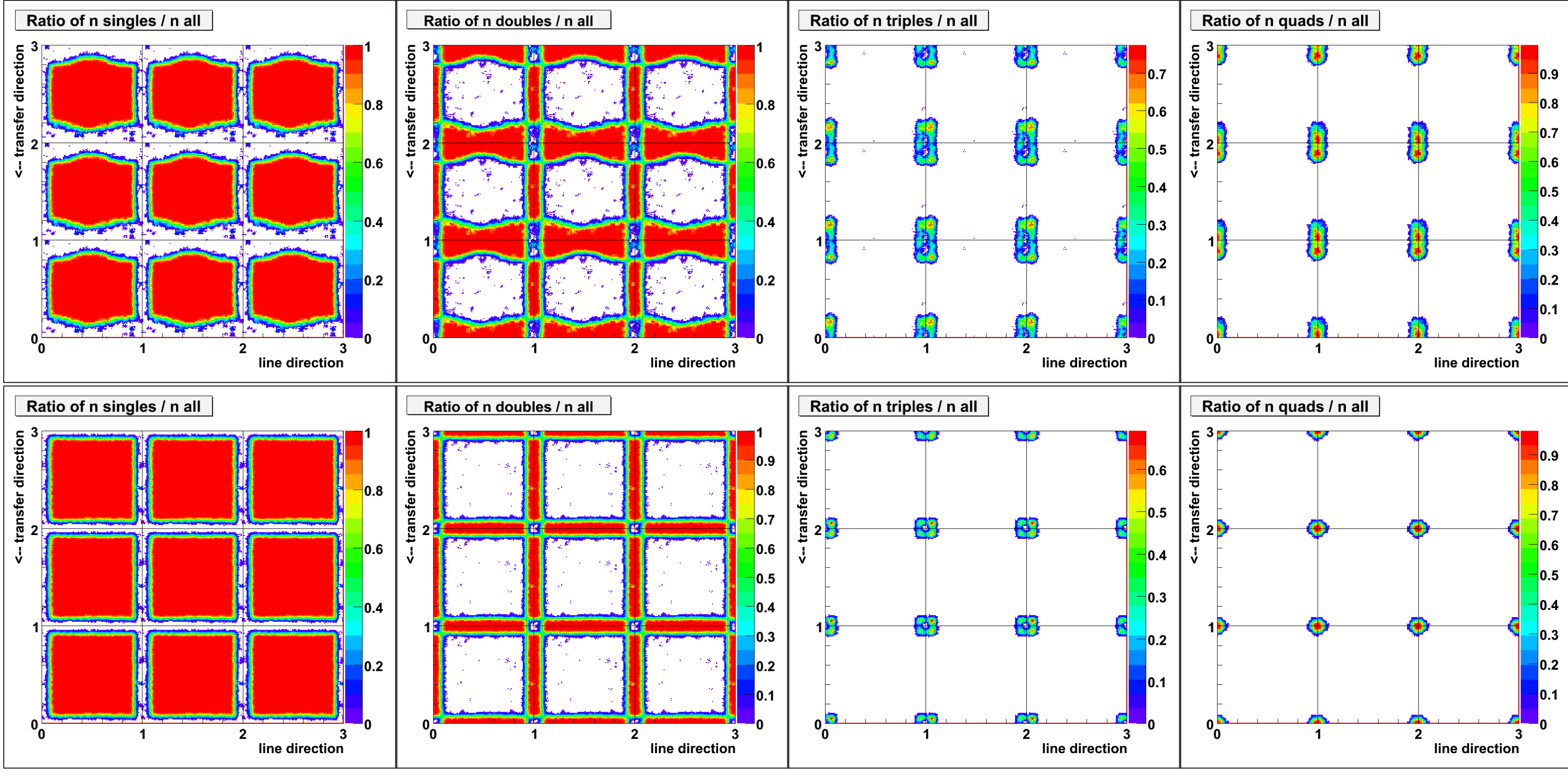

Figure 5.14: *Event maps reconstructed from two data sets taken with the XMM–type pnCCD C09_08_10. The X–ray line used is Ti-Kα (4510 eV) and the entrance window (back side) of the pnCCD was illuminated . In the top row reconstructed event maps are shown for data taken with single register storage. In the bottom row the same maps are shown for data taken with double register storage. Note the asymmetric event distribution with single register storage. In this storage mode, the width of the regions where singles and doubles occur is different for the middle and the borders of the pixel in channel direction. With double register storage the event distribution is practically the same in the line– and the charge transfer direction.*

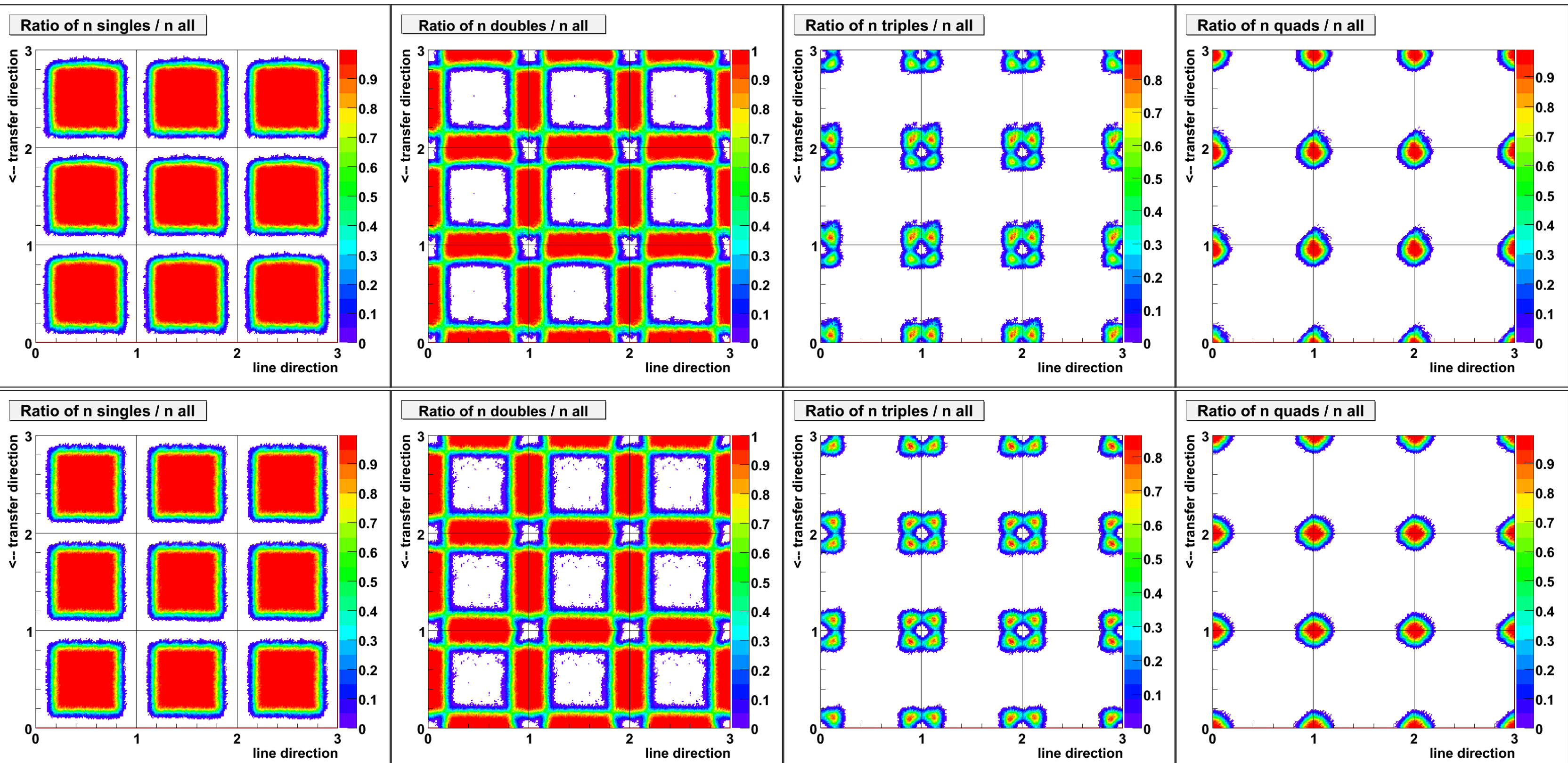

Figure 5.15: *Event maps reconstructed from two data sets taken with the frame store pnCCD C10_19_01. The used X–ray line is Ti-Kα (4510 eV), the back side of the device was illuminated. In the top row reconstructed event maps are shown for data taken with single register storage. In the bottom row the same maps are shown for data taken with double register storage. Compared to fig. 5.14 the difference of the event maps for single– and double register storage has become so small that it is hard to detect. Obviously changing the storage mode has less influence on the event distribution in this specific device.*

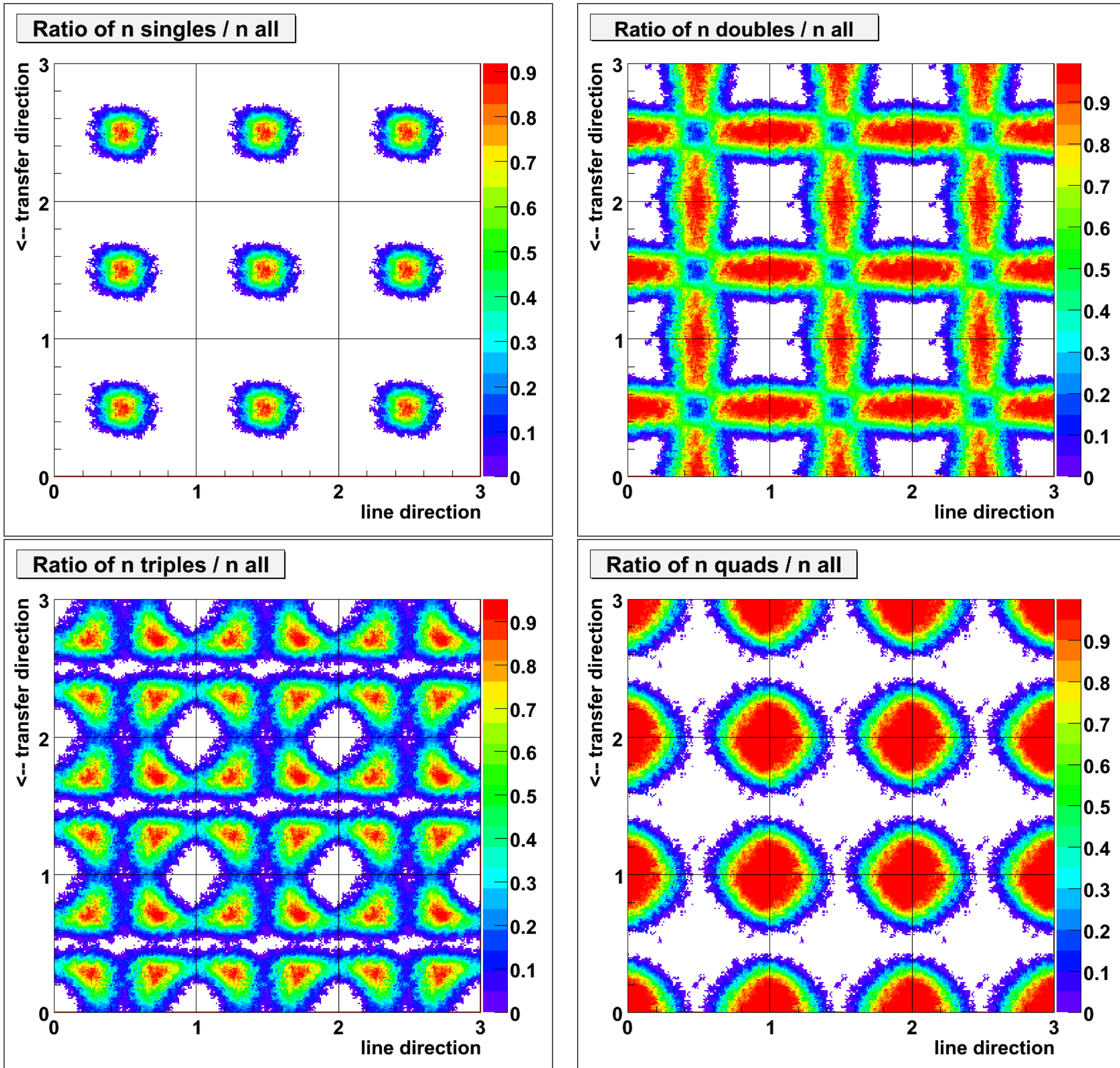

Figure 5.16: *Event maps reconstructed from a data set taken with the frame store pnCCD C11_11_85 at 4510 eV (Ti-Kα). The pnCCD was operated in single register storage mode and illuminated on the back side. A comparison with figures 5.14 and 5.15 demonstrates the effect of moving to smaller pixel sizes. Relative to the pixel size, the signal charge cloud size before charge collection gets larger, and thus less singles and more split events occur.*

the event maps of the top row, the area where single events occur is larger and the areas where split events occur are smaller than in the event maps shown in the bottom row.

The event maps of the top row of figure 5.15 are reconstructed from a data set recorded

with single register storage, the event maps in the bottom row are reconstructed from a data set recorded double register storage. In difference to the event maps in figure 5.14 a change of the storage mode of the 75 µm pixel CCD has a smaller influence on the topology of the event maps. This is obviously a result of the larger signal charge cloud size relative to the pixel size and the more similar structure of the electric potential in the bulk for the different storage modes. Identical to the 150 µm pixel data, the most regular event maps where single events occur in a square area and quadruple events occur directly on the pixel corners are observed with double register storage.

5.3.1.3 51µm pixel frame store pnCCD

Only event maps for the operation with single register storage of a 51 µm pixel pnCCD are displayed in figure 5.16. Differences in the map topology between single– and double register storage mode are no longer visible in the event maps which are reconstructed from measurements with the 51 µm pixel frame store pnCCD. Figure 5.16 shows event maps which represent the single register storage measurement with a line energy of 4510 eV in table 4.6 and the voltage set a) in table 4.7. An event detection threshold of $8 \cdot \sigma_{\text{noise}}$ was used. It results in a threshold of $18.4e^-$ or $18.4e^-/1236e^- = 1.5\%$ of the used 4510 eV (Ti-Kα) line.

The event maps in figure 5.16 confirm the observation that the pixel size of a pnCCD directly influences the ratio of single events to split events. The smaller the pixel size, the larger the total number of split events relative to the total number of split events. This observation is explained with the previously discussed charge split model. It is based on the assumption that the signal charge cloud expands during its drift from the back side to the register side and is split at the pixel borders in a short distance from the register side.

5.3.1.4 Front side illumination of a 75µm pixel pnCCD

In the case of front side illumination, the signal charge is generated close to the storage cells. The drift time of a signal charge cloud before its collection in the pixels is much shorter compared to the case of back side illumination. The pnCCD C10_19_16 which was used for the measurements with front side illumination is of the same design as C10_19_01. Reconstructed event maps for two measurements with a X–ray line energy of 4510 eV and with single and double register storage are shown in figure 5.17. In the top row the event maps for single register storage are shown, the event maps for double register storage are shown in the bottom row. The measurements are listed in table 4.8, voltage set b) of table 4.9 was used.

In conformity with the expectation of a much shorter drift time and hence a smaller size of the signal charge cloud, the area where single events occur occupies most of the reconstructed pixel. Due to the signal charge generation close to the cells, variations of the drift field strength at the front side cause significantly different drift times for signal charge clouds generated in different regions of the pixel. In the double event map in the top row of figure 5.17 which represent the measurement with single register storage, the width

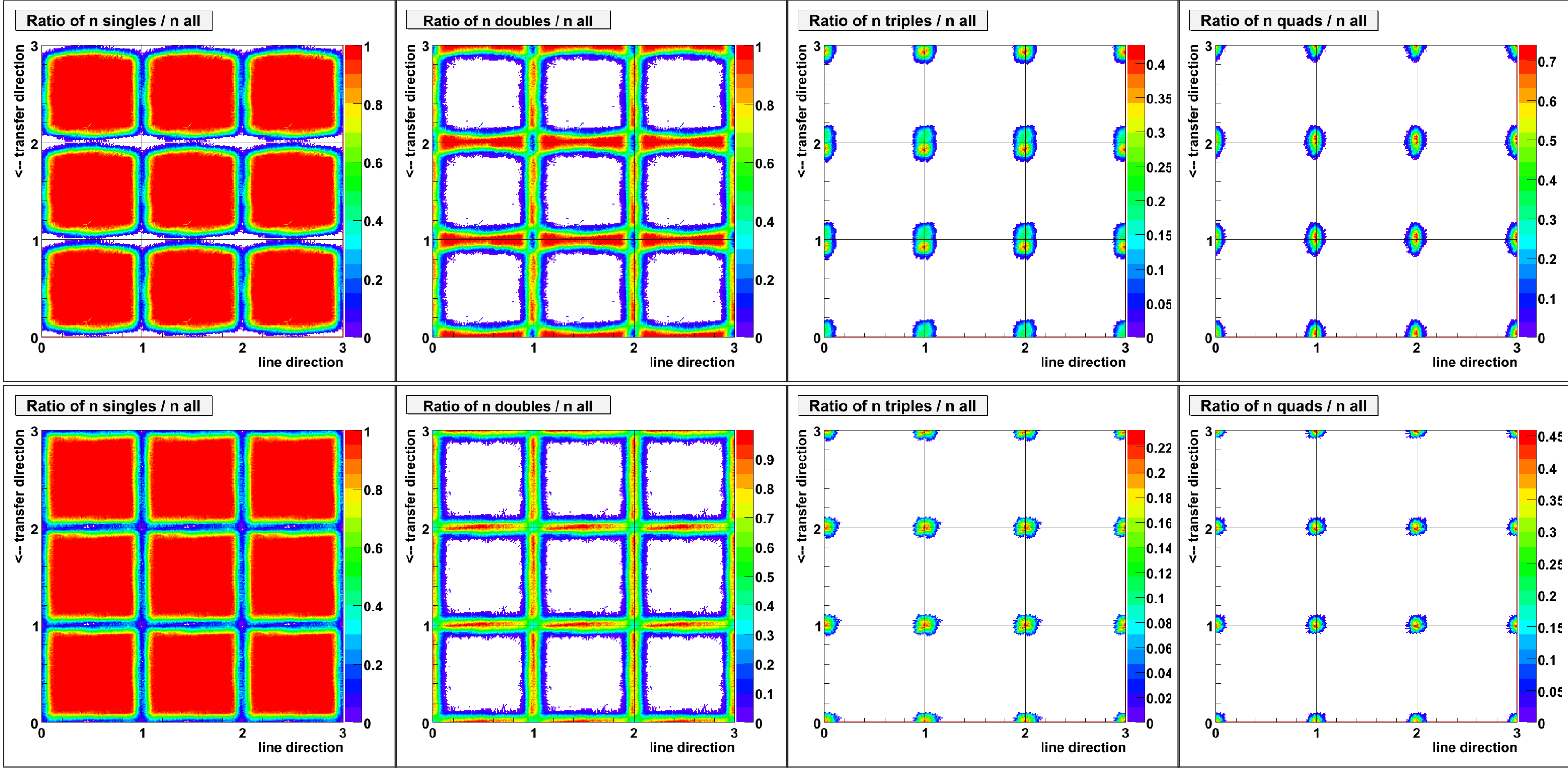

Figure 5.17: *Event maps reconstructed from two data sets taken with the frame store pnCCD C10_19_16. The X–ray line used is Ti-Kα (4510 eV) and the front side of the pnCCD was illuminated . In the top row reconstructed event maps are shown for data taken with single register storage. In the bottom row the same maps are shown for data taken with double register storage. If the register side is illuminated, the drift time of the signal charge to the potential minima is very short compared to back side illumination. Therefore the signal electron clouds have less time for expansion and more single events occur. In single register storage mode, the region where single events occur has no regular, rectangular shape due to the irregular form of the electric potential barriers between the pixels.*

of the regions where the double events occur is larger near the pixel corners than in the middle of the pixel borders. Obviously the drift field is weaker at the pixel corners so that signal charge clouds have more time for expansion than in the middle of the pixel borders. The double event map for double register storage in comparison shows that double events occur in regions which have a constant width and which are more concentrated at the pixel borders. This indicates that in the case of double register storage, a signal charge cloud which is generated at a pixel corner has the same drift time as a signal charge cloud which is generated near the middle of a pixel border.

5.3.2 Photon flux

Count rate maps are the representation of all X–ray events detected in a mesh measurement. They show the number of detected photons for each hole position as explained in section 5.1.2.1. If the sensitivity in the pixels is uniform, the reconstructed count map only shows statistical variations of the detected number of photons. Back side illuminated pnCCDs have a uniform photon detection efficiency in the pixels because of the uniform radiation entrance window. If a pnCCD is illuminated from the front side, the reconstructed count rate map of a pixel is not uniform. It directly shows the variation of the transmission for photons of the used X–ray emission line energy in different surface structures of the pixel.

5.3.2.1 Count maps with back side illumination

Figures 5.18 to 5.20 show count maps reconstructed from data sets recorded with back side illuminated devices at an X–ray energy of 4510 eV (Ti-Kα). To the right hand side of each count map, a profile plot along the charge transfer direction is shown. It is averaged over a width of $0.133 \cdot l_{\text{pixel}}$ where l_{pixel} is the pixel side length and centered on a vertical line with an x–coordinate of 1.0. Figure 5.18 shows a count rate drop of 33% in the pixel corners where triples and quadruples occur (compare the maps in figure 5.14). Figure 5.19 shows a smaller count rate drop of 11% in the pixel corners where triples and quads occur (compare figure 5.15). In figure 5.20 the count rate variations in the reconstructed pixel have an irregular structure without a smaller count rate value in the pixel corners. In the case of the 51 µm pixel pnCCD, the expected homogeneous sensitivity of the pixels is confirmed by the count map.

Count maps reconstructed from data of measurements with different X–ray lines from 1487 eV (Al–Kα) to 5415 eV (Cr-Kα) also show a count rate drop in the pixel corners for pixel sizes of 150 µm and of 75 µm but not for a pixel size of 51 µm. The cause of the observed count rate drop in the pixel corners is an analysis effect which results from the event pattern selection. It is defined as 'event pattern pileup'[1] since it occurs if two neighboring event patterns overlap and form an 'invalid' pattern which consists of at least four pixels. Since the signal charge of the two photons is mixed in the overlapping region, the invalid pattern cannot be divided into two valid patterns. Pileup patterns are therefore

[1] This is different from the effect of photon pileup where two photons hit the same pixel in the same data frame and form a valid event pattern with the combined signal pulse height of both photons.

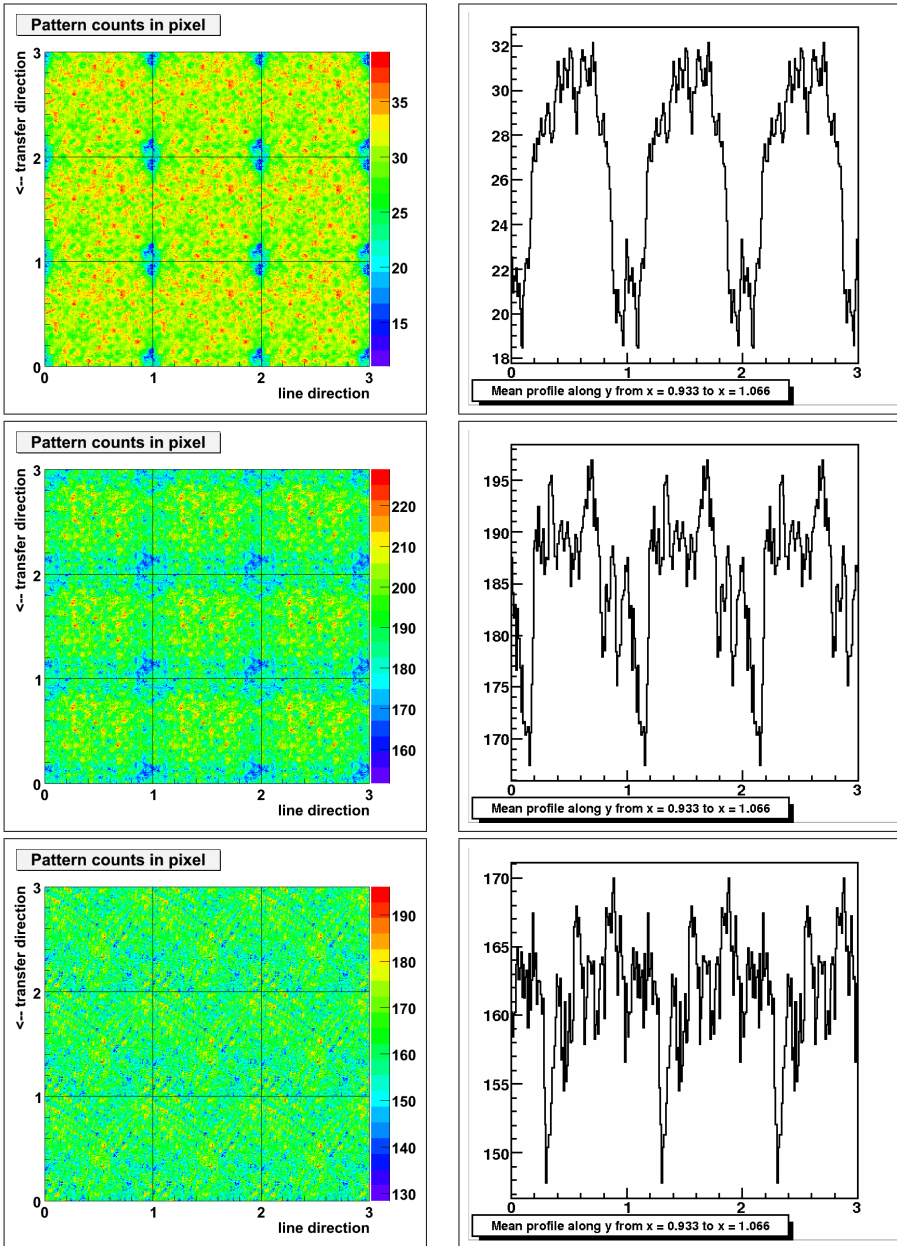

Figure 5.18: *Count map of a Ti-Kα measurement with a 150 µm pixel XMM–type pnCCD and single register storage. The count rate drops in the regions where triples and quads occur.*

Figure 5.19: *As above, but measured with a 75 µm pixel frame store pnCCD. The lower count rate around the pixel borders indicates that split events are rejected by the standard data analysis.*

Figure 5.20: *As in the top row, but a 51 µm pixel frame store pnCCD was used. Different to the previous measurements, there is no systematic count rate drop around the pixel borders.*

rejected from the analysis. Figure 5.21 explains how event pattern pileup occurs. If the mesh hole distance is equal to the pixel size, pattern pileup occurs for all hole positions. If the mesh hole distance is twice the pixel size, pattern pileup only occurs if neighboring mesh holes have positions near the corners and the borders of a pixel.

The distribution of the detected photons over the mesh holes is a statistical process. The more photons are detected in each data frame of a mesh measurement, the higher is the probability that two photons pass through neighboring mesh holes and generate a pileup pattern. A large photon flux thus results in better statics for the same measurement time but also in more pattern pileup. The only way to avoid pattern pileup is a mesh

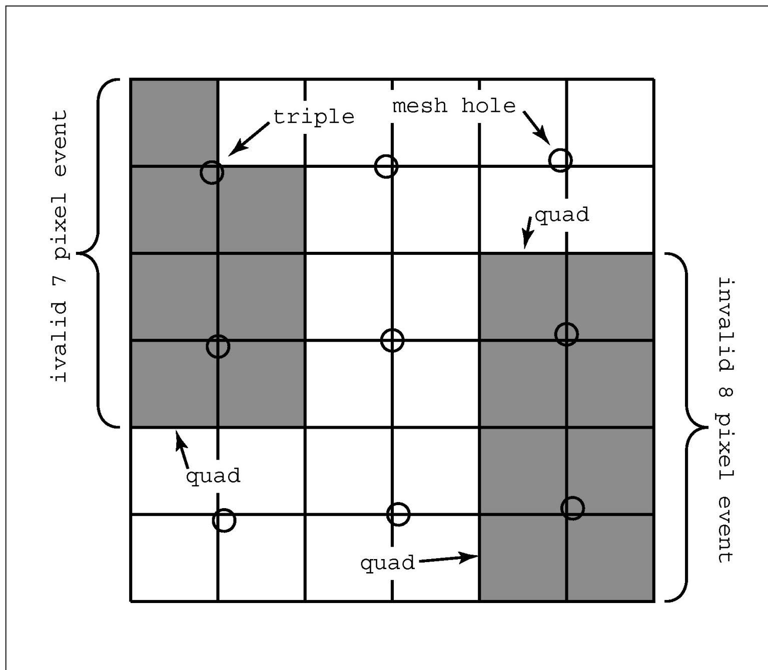

Figure 5.21: *Photons which pass through neighboring holes in the same signal frame integration period form combined patterns. These patterns are rejected by the standard analysis software because of the lost energy information of the individual photons. As a result of the rejection of combined patterns, the count map of a reconstructed pixel shows a lower count rate in regions where split events occur. If the hole distance is three times the pixel size this effect does not occur.*

measurement setup where the hole distance is three times the pixel size. Future mesh measurements will therefore be performed with a triple pitch mesh or at low count rates of 10 photons or less in a region of 128x128 pixels.

Event pattern pileup does not directly affect the reconstruction of event maps and charge maps. The values in these maps are normalized to the number of the photons detected at each hole position, compare section 5.1. A reduced count rate at hole positions near the pixel corners means that the number of events which contribute to the calculation of a map value is smaller. This is no problem if the initial requirement is satisfied that at least ten or more valid events are detected at each mesh hole position. In the measurements with the 75 µm pixel pnCCD and back side illumination, the photon flux and the measurement time were increased compared to the previous mesh measurements with the 150 µm pixel CCD. The rejection of photon events by pattern pileup in the pixel corners is compensated by the increased total number of detected photons. Figure 5.19 shows that more than 150 valid photon events are detected at each mesh hole even in the pixel corners.

5.3.2.2 Count maps with front side illumination

Figure 5.22 shows count maps which are reconstructed from measurements with double register storage and profiles of the count rate along the charge transfer direction. The profile plots below each count map are averaged over the width of one pixel. Red regions indicate areas with a high count rate and a correspondingly high transmission of photons through the register side. Generally, the higher the X–ray energy, the lower the effect of photon absorption in the register structure. The y coordinate direction of the count maps corresponds to the charge transfer direction of the pnCCD. The pixel borders with the y

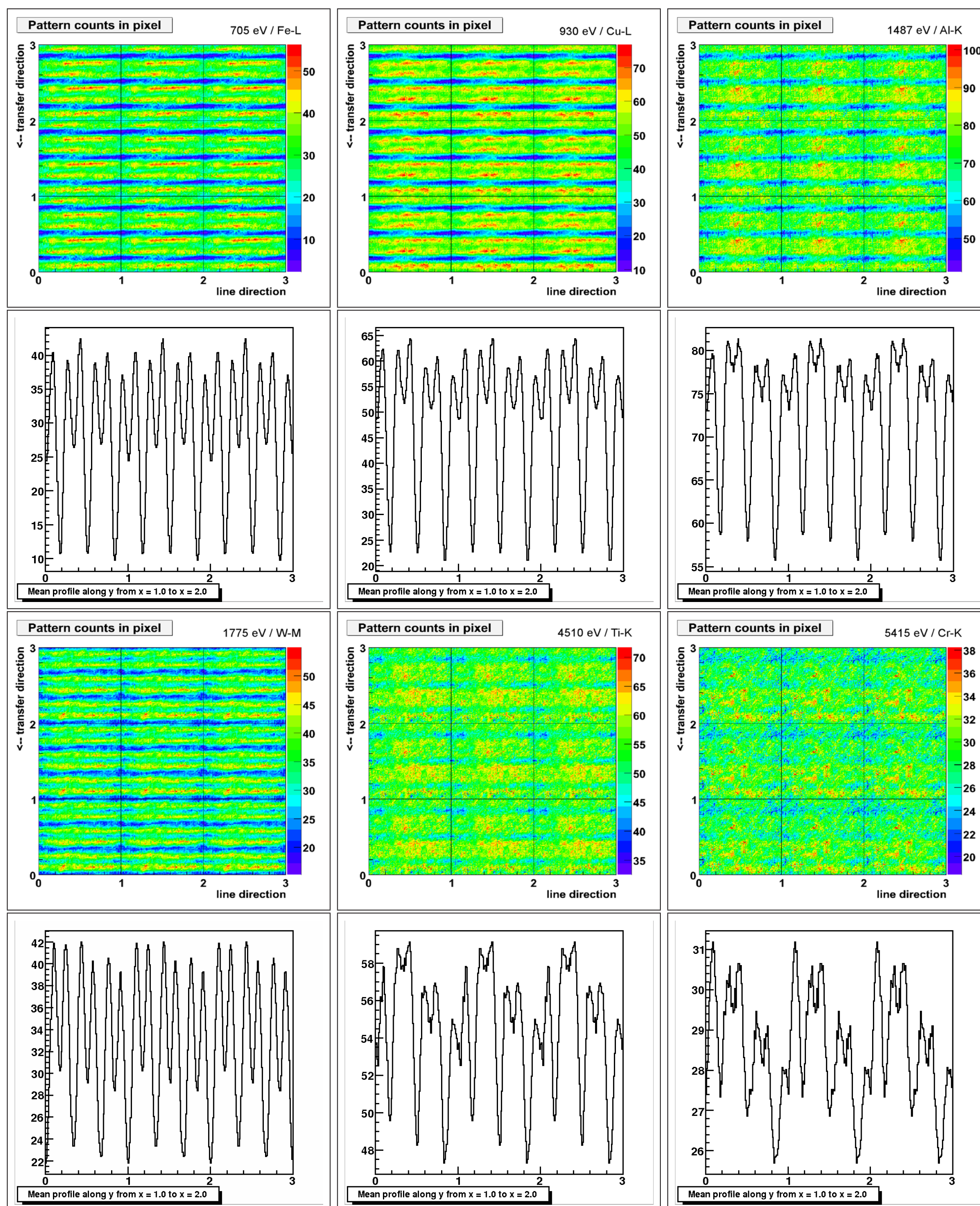

Figure 5.22: *Count maps reconstructed from data measured with a front side illuminated 75x75 µm² pixel pnCCD in double register storage mode. From top left to the lower right for X-ray photons of Fe–L (705 eV), Cu–L (930 eV), Al–Kα (1487 eV), W–M (1775 eV), Ti–Kα (4510 eV) and Cr–Kα (5415 eV). Below each count map, the averaged profile of a cut along the transfer direction is shown. The profile is averaged over the width of one pixel.*

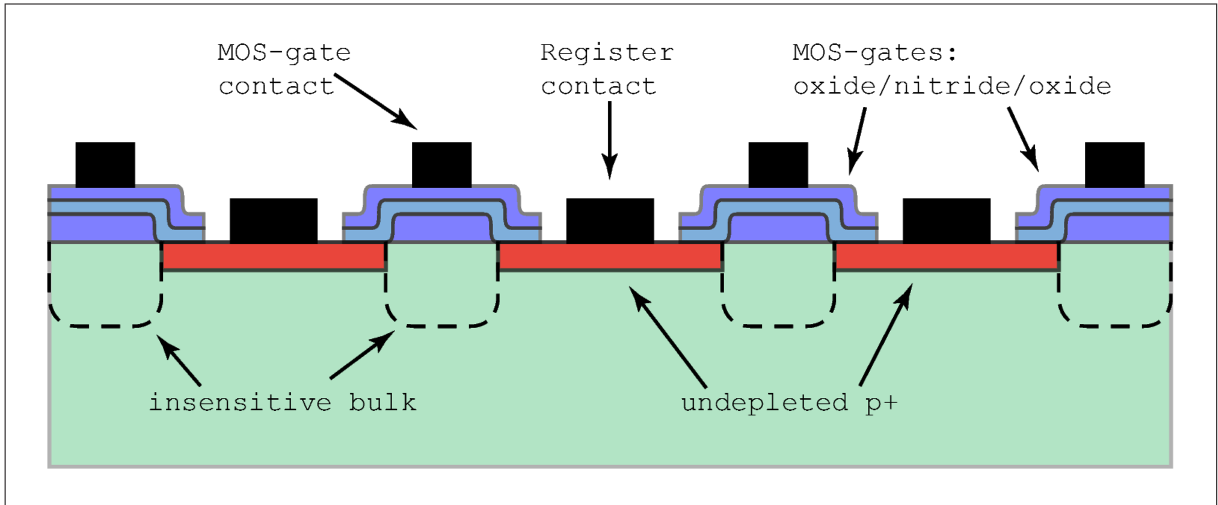

Figure 5.23: *Cut through a pixel of the 75µm pixel pnCCD used for mesh measurements with front side illumination. The cut shows three register contacts and four MOS–gates. In the layout, a pixel is defined by three register contacts which are separated by MOS–gates, see chapter 2.1.1. Analysis of the count maps for different X–ray energies from 705 eV (Fe-Lα) to 4510 eV (Ti-Kα) shows that below the MOS–gates regions of insensitive bulk silicon must exist.*

coordinates 0, 1, 2 and 3 are identical to the middle of the barrier registers. The pixel centers with the y coordinates 0.5, 1.5 and 2.5 are identical to the middle of the MOS–gates between two storage registers.

Figure 5.23 shows a cut along the charge transfer direction of the studied 75 µm pixel pnCCD C10_19_16 (table 4.1). The thickness and geometry of each surface layer is known, so the absorption for X–ray photons of a given energy can be calculated. For each coordinate along the transfer direction, the total absorption of X–ray photons is given by the combined absorption of all layers which cover the silicon bulk. A qualitative interpretation of the absorption structures in the count maps of figure 5.22 is summarized below:

Fe–Lα 705 eV — The aluminum register contacts are visible as green/blue lines between two red stripes where the bulk silicon is not covered. At the register contacts, the count rate drops to about two thirds of the peak count rate. An even stronger drop of the count rate is observed at the MOS–gates. This cannot be explained by the MOS–gate structure alone which consists of aluminum, nitride and oxide layers.

Cu–Lα 930 eV — Compared to the Fe-Lα measurement, the absorption topology is the same but the count rate drops compared to the count rate peaks are smaller, about 20% at the register contacts. At the MOS–gates a higher drop of the photon count rate than at the register contacts is observed. In similarity to the Fe-Lα measurement the count rate drop is stronger than expected for photon absorption in the MOS–gate surface structure.

Al–Kα 1487 eV — Here the register contacts absorb a small amount of radiation since the Al-Kα line is just below the K–absorption edge of aluminum. The MOS–gates show a strong effect of photon absorption which confirms the previously made observation that this effect is stronger than absorption by the aluminum, nitride and oxide layers of the MOS–gate alone.

W–Mα 1775 eV — This is the only measurement where the X–ray absorption at the p+ register contacts is stronger than at the MOS–gates. Three effects have to be considered at this photon energy. I. 1775 eV is just above the K–absorption edge of aluminum, so the absorption of W-Mα photons in aluminum is very strong. II. 1775 eV is below the K–absorption edge of silicon, so W-Mα photons have a long absorption length of 13 µm in silicon. III. The hole diameter of 5 µm is larger than the width of the aluminum contact strips on the MOS–gates, but smaller than the aluminum p+ register contact strip width. Therefore the strongest absorption is observed at the p+ register contacts, while the contrast for the detection of insensitive regions in the silicon a few µm below the register structure is lower.

Ti–Kα 4510 eV — At this photon energy, the absorption in the aluminum contacts and the oxide and nitride layers of the MOS–gates is not very strong. As a consequence the count rate profile in the transfer direction is not very pronounced. In contrast to the weak absorption in the aluminum register contacts layers, the MOS–gates are visible as regions with stronger absorption.

Cr–Kα 5415 eV — Cr-Kα photons have an absorption length of 20µm in silicon and the absorption in the surface layers of the register structure in close to being negligible. At this energy, the MOS–gates are the only structures which are visible as a drop in the count rate map and its profile. The small drop of the count rate means that the depth of the insensitive regions is much smaller than the absorption length of 23 µm. Most of the incident photons pass through the insensitive regions before they are absorbed in the silicon substrate.

The observed absorption structure can be partly explained with the known thicknesses and geometry of the oxide–, nitride– and aluminum layers that form the register structure. It is also known that at the p+ contacts, the silicon substrate is not depleted to a depth of about 0.4µm. Up to this depth no drift field exists and the generated signal electrons recombine with the free holes in the p+ region. X–ray photons which are absorbed in the undepleted part of the p+ register contacts are thus not detected. A quantitative analysis of the front side illumination data is described in detail in section 7.3.

Even without a quantitative analysis, a qualitative understanding of the count maps in figure 5.22 is possible if the surface structures in figure 5.23 are considered. The strong absorption at the MOS–gates is due to the electric potential in the regions below the MOS–gates which is discussed in section 6.1. Signal electrons which are generated directly below the MOS–gates do not drift into the storage cells but to the silicon–oxide interface at the surface. The result is a count rate drop between the register contacts since the

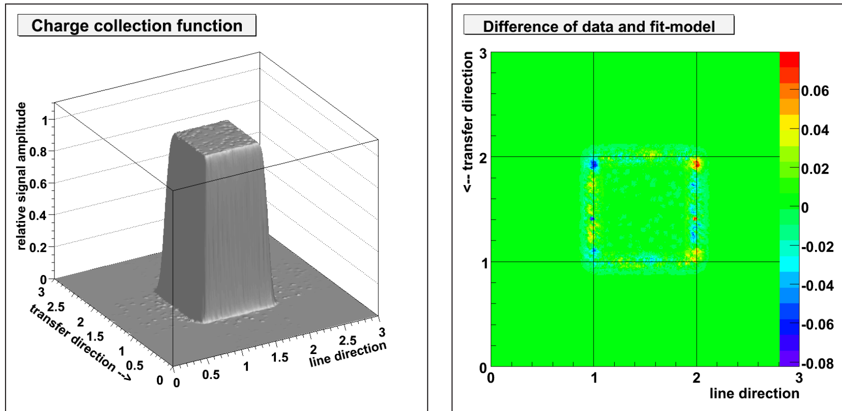

Figure 5.24: *Charge collection function, left, and its difference to the best–fit model, right, of the 150 µm pixel XMM–type pnCCD. The measurement was done with two register storage at an energy of 4510 eV.*

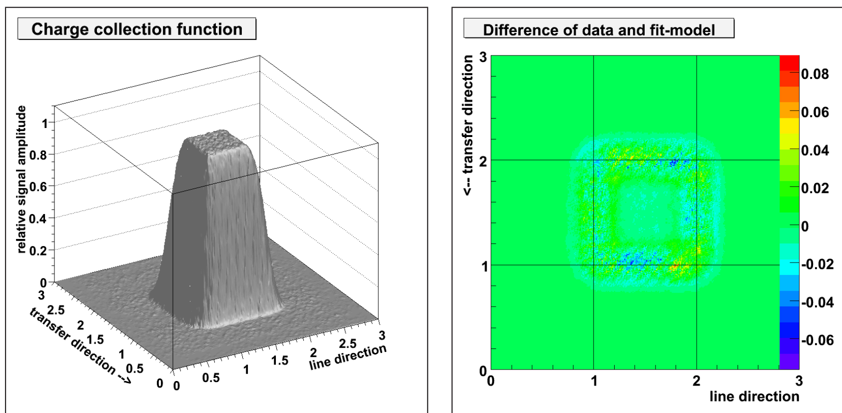

Figure 5.25: *Charge collection function, left, and its difference to the best–fit model, right, of the 75 µm pixel frame store pnCCD. The measurement was done with double register storage at an energy of 4510 eV.*

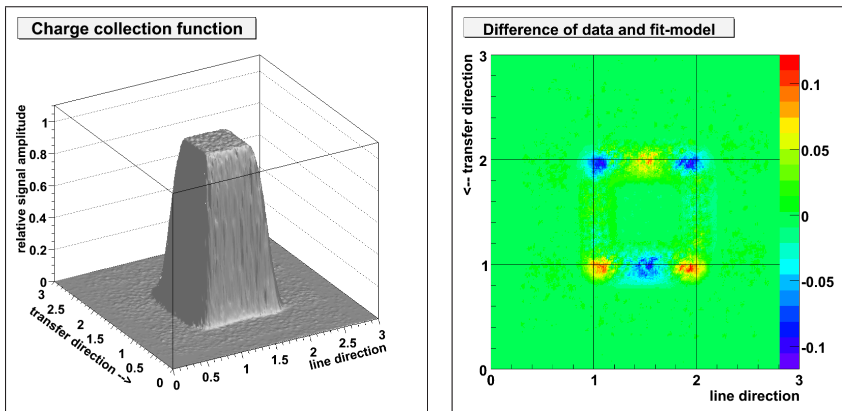

Figure 5.26: *Charge collection function, left, and its difference to the best–fit model, right, of the 75 µm pixel frame store pnCCD. The measurement was done with single register storage at an energy of 4510 eV.*

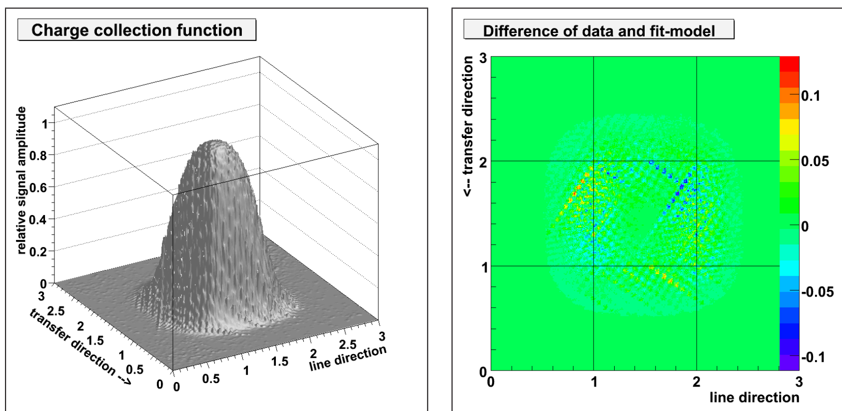

Figure 5.27: *Charge collection function, left, and its difference to the best–fit model, right, of the 51 µm pixel frame store pnCCD. The measurement was done with single register storage at an energy of 4510 eV.*

photons which are absorbed below the MOS–gates do not create photon signal events. At higher X–ray energies of 4510 eV and 5415 eV, the mean penetration depth of the incident photons is larger. Most of the signal charge is thus created in a depth which is beyond the insensitive region at the silicon–oxide surface and the count rate drop at the MOS–gates is smaller.

The analysis of count maps with back side illumination in section 5.3.2.1 showed that count maps do not give correct results in the regions where split events occur. However, due to the short drift distance of signal charge in the case of front side illumination, only a small fraction of the detected photon events are split events. The maps in figure 5.17 show that the split events only occur in narrow regions around the pixel borders. The largest part of the count maps is thus not affected by the rejection of split events due to pattern pileup and can be used for a quantitative analysis.

X–ray energy	storage mode	event threshold	σ_{line}	σ_{transfer}	max. deviation
Temperature 125K, V_{back} = -170V, mesh angle 4° $\longrightarrow$					
Cu-Lα 930 eV	double register	10.4% of 930 eV	5.89 µm	5.50 µm	+8% / -8%
Al-Kα 1487 eV	double register	6.5% of 1487 eV	6.20 µm	5.86 µm	+8% / -8%
Ti-Kα 4510 eV	double register	2.1% of 4510 eV	6.72 µm	6.38 µm	+6% / -8%
Temperature 125K, V_{back} = -170V, mesh angle 4° $\longrightarrow$					
Cu-Lα 930 eV	single register	10.4% of 930 eV	5.91 µm	17.86 µm	+30% / -30%
Al-Kα 1487 eV	single register	6.5% of 1487 eV	6.22 µm	18.35 µm	+30% / -30%
Ti-Kα 4510 eV	single register	2.1% of 4510 eV	6.74 µm	18.89 µm	+30% / -30%

Table 5.5: *Results of fitting the reconstructed charge collection function 'ccf' measured with the back illuminated 150 µm pixel pnCCD C09_08_10. Two storage modes were used for measurements with each energy. The maximum deviation is the biggest difference between the measurement and best fit ccf–model. Note the high values of this difference for the measurements with single register storage. These results cannot be represented properly with the error function fit–model.*

5.3.3 Charge collection

The error function model of the charge collection function is first introduced in section 5.2.2, equation 5.3. It describes the integration of the charge density in a Gaussian charge cloud over the area of the reconstructed pixel. For any given photon conversion position, $ccf_{\text{mod}}(x; y; ...)$ gives the relative amount of signal charge which reaches the storage cell of the reconstructed pixel in the middle of the charge map. The values of σ_{x} and σ_{y} in the line and the charge transfer direction respectively parameterize the size of the charge cloud. Each charge collection function which is reconstructed from the mesh measurements was fitted with the error function hill model of the ccf. The map of the difference values between the best fit model and the measurement allows for an evaluation of the validity of the fit. If no systematic differences between the charge map data and the fit model are found, the assumption that a Gaussian signal charge cloud is split at the pixel borders is

correct. The best fit values of σ_x and σ_y describe the average size and the form of a signal electron cloud directly before its separation and collection in the storage cells of the pixels.

5.3.3.1 Results with back side illumination

The tables 5.5, 5.6, 5.8, and 5.9 show the results of parameterizing the measured charge collection functions with σ_x and σ_y. Separate columns list the maximum difference values between the measured ccf and the best fit model. Large differences between the data and the best fit either indicate reconstruction errors or that the fit model is inappropriate for the given charge map data.

In a qualitative interpretation of the ccf fit results, σ_x and σ_y are compared for different measurement conditions and also for different devices. The maps of the differences between the fit and the data are evaluated in order to find systematic errors of the fit model. The qualitative interpretation of the fit results shows if the values of $\sigma_\mathrm{x} = \sigma_\mathrm{line}$ and $\sigma_\mathrm{y} = \sigma_\mathrm{transfer}$ change as expected if the back contact voltage, the storage mode, or the device temperature is changed. Based on the physics of the drift and the expansion of a charge cloud which is discussed n section 2.2.1 and the expected structure of the electric potential inside the device, the following assumptions are made:

I. Changing the back contact voltage	With a change of the back contacts to lower, i.e. more negative values, the strength of the electric drift field $\mathcal{E}_\mathrm{drift}$ in the bulk region increases. This increases the drift velocity $\mu_\mathrm{n} \cdot \mathcal{E}_\mathrm{drift}$ and therefore reduces the drift time before collection of the charge cloud. A shorter drift time consequentially means a smaller charge cloud size which is reflected in smaller values of σ_line and σ_transfer in the charge collection function $\mathrm{ccf}(\sigma_\mathrm{line}, \sigma_\mathrm{transfer}, ...)$.
II. Changing the device temperature	Variations of the device temperature result both in a change of the charge carrier mobility and the thermal mean energy of the charge carriers. In section 2.2.1.4, equation 2.20, it was shown that changes of the mobility have no influence on the charge cloud expansion after a given drift distance if the drift velocity is proportional to the drift field strength. The device temperature can thus only influence the charge cloud sigma by the mean thermal energy of the signal electrons. At lower temperatures the speed of diffusion decreases, so that the measured charge cloud size will be smaller, see equation 2.11.

III. Changing the storage mode

If the storage mode is changed between single and double register storage, the width of the potential barrier between two pixels changes in the charge transfer direction. The barrier is wider in the case of single register storage where two registers are at a more negative potential. A signal electron cloud which arrives at a pixel border therefore sees a larger region which is at the same electric potential and thus a smaller lateral drift field at the front side. Due to the smaller lateral drift field, the separation of the charge cloud at the pixel border takes longer than for double register storage. Therefore a larger value of σ_{transfer} is expected in the case of single register storage.

Assumption 'I.' is confirmed by the measurements with different values of V_{back} in tables 5.6 and 5.8. Comparing the results for σ_{line} and σ_{transfer} shows that a more negative back contact voltage directly leads to smaller values of σ_{line} and σ_{transfer}. All observed changes of the charge cloud size are far above the reconstruction errors studied in section 5.2.2.

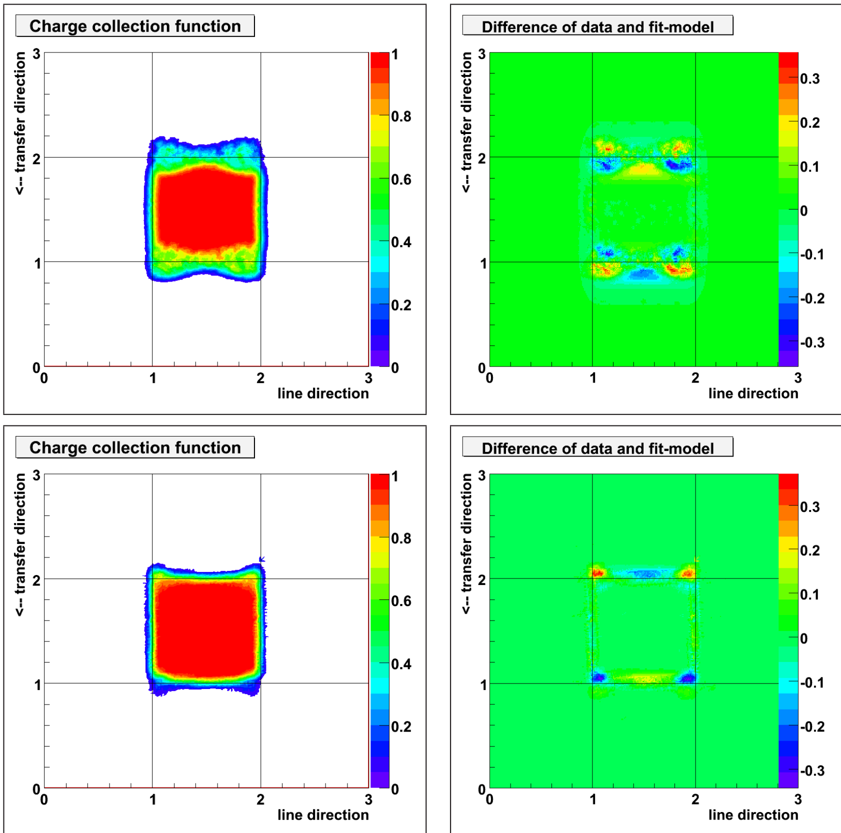

Figure 5.28: *Charge collection function, left, and its difference to the best–fit model, right, of the 150 µm pixel XMM–type pnCCD. The measurement was done with single register storage at an energy of 4510 eV.*

Figure 5.29: *Charge collection function, left, and its difference to the best–fit model, right, of the 75 µm pixel frame store pnCCD. The measurement was done with double register storage at an energy of 930 eV.*

Measurements with different device temperatures were only performed with pnCCD C10_19_01. The temperature effect can be studied with the results shown in table 5.6. If the temperature is lowered from 193 K to 153 K, the values of σ_{line} and σ_{transfer} are systematically lower. This observation confirms the correctness of the second assumption.

X–ray energy	storage mode	event threshold	σ_{line}	σ_{transfer}	max. deviation
Temperature 193K, V_{back} = -90V, mesh angle 4° ⟶					
W-Mα 1775 eV	single register	6.8% of 1775 eV	6.96 µm	7.18 µm	+8% / -8%
W-Mα 1775 eV	double register	6.8% of 1775 eV	6.91 µm	6.70 µm	+8% / -10%
Ti-Kα 4510 eV	single register	3.6% of 4510 eV	7.54 µm	7.83 µm	+8% / -6%
Ti-Kα 4510 eV	double register	3.6% of 4510 eV	7.49 µm	7.27 µm	+8% / -6%
Temperature 193K, V_{back} = -140V, mesh angle 4° ⟶					
W-Mα 1775 eV	single register	6.8% of 1775 eV	6.11 µm	6.66 µm	+15% / -10%
Ti-Kα 4510 eV	single register	3.6% of 4510 eV	6.58 µm	7.19 µm	+10% / -10%
Temperature 153K, V_{back} = -90V, mesh angle 4° ⟶					
W-Mα 1775 eV	single register	6.5% of 1775 eV	6.77 µm	6.90 µm	+10% / -10%
W-Mα 1775 eV	double register	6.5% of 1775 eV	6.72 µm	6.47 µm	+10% / -10%
Ti-Kα 4510 eV	single register	3.4% of 4510 eV	7.36 µm	7.48 µm	+8% / -8%
Ti-Kα 4510 eV	double register	3.4% of 4510 eV	7.32 µm	7.02 µm	+8% / -6%
Temperature 153K, V_{back} = -140V, mesh angle 4° ⟶					
W-Mα 1775 eV	single register	6.5% of 1775 eV	5.96 µm	6.32 µm	+10% / -10%
Ti-Kα 4510 eV	single register	3.4% of 4510 eV	6.45 µm	6.86 µm	+10% / -10%
Temperature 193K, V_{back} = -85V, mesh angle 2.5° ⟶					
W-Mα 1775 eV	single register	6.8% of 1775 eV	7.04 µm	7.24 µm	+10% / -10%
Temperature 193K, V_{back} = -90V, mesh angle 2.5° ⟶					
W-Mα 1775 eV	single register	6.8% of 1775 eV	6.90 µm	7.11 µm	+10% / -10%
W-Mα 1775 eV	double register	6.8% of 1775 eV	6.87 µm	6.66 µm	+8% / -6%
Ti-Kα 4510 eV	single register	3.6% of 4510 eV	7.46 µm	7.77 µm	+8% / -8%
Ti-Kα 4510 eV	double register	3.6% of 4510 eV	7.40 µm	7.12 µm	+10% / -10%
As before but twice the amount of collected photons ⟶					
Ti-Kα 4510 eV	single register	3.6% of 4510 eV	7.42 µm	7.71 µm	+6% / -6%
Temperature 193K, V_{back} = -90V, V_{MOS} = -10V, mesh angle 2.5° ⟶					
W-Mα 1775 eV	single register	6.8% of 1775 eV	6.92 µm	6.88 µm	+10% / -10%
Ti-Kα 4510 eV	single register	3.6% of 4510 eV	7.50 µm	7.45 µm	+10% / -10%
Temperature 193K, V_{back} = -90V, mesh angle 2.5° ⟶					
Cr-Kα 5415 eV	single register	3.3% of 5415 eV	7.52 µm	7.76 µm	+6% / -6%
Fe-Kα 6404 eV	single register	3.8% of 6404 eV	7.59 µm	7.85 µm	+4% / -6%

Table 5.6: *Fit results of ccf data reconstructed from data sets taken with the back illuminated 75 µm pixel frame store pnCCD C10_19_01. Variations of both the device temperature and storage mode were done in combination with the different used energies. In comparison to table 5.5, the maximum deviations between the data and the best fit model are smaller for single register storage.*

Changing the storage mode from single– to double register storage leads to a smaller value of σ_{transfer} as predicted by the third assumption. However, the value of σ_{line} also decreases if double register storage is used, but to a much smaller degree near the detection limit of 1% of the charge cloud sigma.

In the case of the measurements which were performed with single register storage and

X–ray energy	storage mode	event threshold	σ_{line}	$\sigma_{transfer}$	max. deviation
Temperature 180K, V_{back} = -250V, mesh angle 1.5° ⟶					
C-Kα 277 eV	single register	13.2% of 277 eV	8.30 µm	7.93 µm	+10% / -10%
W-Mα 1775 eV	single register	3.8% of 1775 eV	8.80 µm	8.53 µm	+10% / -10%
Ti-Kα 4510 eV	single register	1.5% of 4510 eV	9.24 µm	9.03 µm	+10% / -10%
Cr-Kα 5415 eV	single register	1.2% of 5415 eV	9.27 µm	9.05 µm	+10% / -10%
Temperature 180K, V_{back} = -250V, mesh angle 1.5° ⟶					
C-Kα 277 eV	double register	13.2% of 277 eV	8.29 µm	7.78 µm	+10% / -10%
W-Mα 1775 eV	double register	3.8% of 1775 eV	8.81 µm	8.43 µm	+10% / -10%
Ti-Kα 4510 eV	double register	1.5% of 4510 eV	9.26 µm	8.94 µm	+8% / -8%
Cr-Kα 5415 eV	double register	1.2% of 5415 eV	9.27 µm	8.98 µm	+10% / -10%
Temperature 180K, V_{back} = -180V, mesh angle 1.5° ⟶					
C-Kα 277 eV	single register	13.2% of 277 eV	9.77 µm	8.85 µm	+10% / -15%
W-Mα 1775 eV	single register	3.8% of 1775 eV	10.21 µm	9.59 µm	+10% / -10%
Ti-Kα 4510 eV	single register	1.5% of 4510 eV	10.70 µm	10.10 µm	+10% / -10%
Cr-Kα 5415 eV	single register	1.2% of 5415 eV	10.71 µm	10.21 µm	+10% / -10%

Table 5.8: *A third set of measurements with back side illumination of a pnCCD employed the 51 µm pixel frame store pnCCD C11_11_85. Now the difference between the reconstructed ccf and its best–fit model does not depend on the storage mode anymore. The measurement series with a more positive back contact voltage shows larger σ values as expected from a longer drift time.*

with CCDs which have 75 µm and 150 µm pixels, the charge collection functions have systematic deviations from the fit model. This effect is visible in figure 5.26 and in figure 5.28. Both of the figures show the maps of the difference $ccf_{data} - ccf_{mod}$ at an X–ray energy of 4510 eV (Ti-Kα). Figure 5.27 only shows a periodic ripple of the reconstructed ccf which results from a small deformation of the mesh, but no systematic deviation of the reconstructed ccf from the fit model is visible. These observations show that the error function model, eq. 5.2, is less and less valid with increasing pixel size and with charge storage below a single register. In the case of the CCD with 150 µm pixels, the fit to data deviations reach a value of 30%. Except for one measurement with a maximum deviation of 15%, the fit to data deviation for the single register storage measurements with 75 µm pixel size is 10% and less. If the pixel size is 75 µm or smaller, the error function model is thus a good approximation to the measured charge collection function for both double– and single register storage.

As a conclusion, we can state that the previously made assumptions I. to III. are confirmed. The erf hill model defined by equation 5.2 is appropriate for all evaluated pixel sizes in the case of storage below two registers. In the case of pixel sizes of up to 75 µm, the erf hill model can also be applied to reconstructed charge collection functions for single register storage.

5.3.3.2 Results with front side illumination

X–ray energy	storage mode	event threshold	σ_{line}	σ_{transfer}	max. deviation
Temperature 151K, V_{back} = -90V, mesh angle 2.5° $\longrightarrow$					
Fe-Lα 705 eV	single register	7.9% of 705 eV	2.80 µm	3.96 µm	+40% / -30%
Cu-Lα 930 eV	single register	6.0% of 930 eV	2.80 µm	3.98 µm	+30% / -30%
Al-Kα 1487 eV	single register	3.7% of 1487 eV	2.89 µm	4.01 µm	+20% / -20%
W-Mα 1775 eV	single register	3.1% of 1775 eV	3.01 µm	4.16 µm	+20% / -20%
Ti-Kα 4510 eV	single register	1.8% of 4510 eV	3.16 µm	4.40 µm	+20% / -20%
Cr-Kα 5415 eV	single register	1.5% of 5415 eV	3.34 µm	4.47 µm	+15% / -20%
Temperature 151K, V_{back} = -90V, mesh angle 2.5° $\longrightarrow$					
Fe-Lα 705 eV	double register	7.9% of 705 eV	2.54 µm	2.68 µm	+20% / -20%
Cu-Lα 930 eV	double register	6.0% of 930 eV	2.68 µm	2.62 µm	+15% / -20%
Al-Kα 1487 eV	double register	3.7% of 1487 eV	2.71 µm	2.77 µm	+15% / -15%
W-Mα 1775 eV	double register	3.1% of 1775 eV	2.94 µm	2.69 µm	+15% / -15%
Ti-Kα 4510 eV	double register	1.9% of 4510 eV	2.99 µm	3.01 µm	+15% / -15%
Cr-Kα 5415 eV	double register	1.6% of 5415 eV	3.28 µm	3.15 µm	+15% / -10%

Table 5.9: *Fit results of charge collection functions which were reconstructed from front side illumination measurements with the 75 µm pixel frame store pnCCD C10_19_16. The smaller σ values are a direct result of the short drift time of the signal electron clouds which are generated at the front side close to the storage minima of the electric potential. Strong deviations between the reconstructed ccf and best–fit models show that the erf–hill approximation fails to describe the ccf, especially in the case of single register storage.*

The fit results of the charge collection functions which were reconstructed from measurements with front side illumination are shown in table 5.9. Compared to the case of back side illumination, the drift time of signal electrons to the storage cells is short if the photons are absorbed close to the register side. The penetration depth of photons of a given energy varies around their mean penetration depth. Since the decay of the radiation intensity is an exponential function (section 1.3), the number density of the absorbed photons is an exponential function of the same form. Thus, the signal electrons are generated in different depths from the register side. The drift time of each charge cloud and accordingly its size before the separation at the pixel borders depends on the generation depth. However, the error function fit model of the charge collection function assumes that the signal charge drift time is similar for all detected photons. This condition is not satisfied in the case of front side illumination. Larger deviations between the best fit models and the data are expected compared to the results with back side illumination. Table 5.9 lists a fit to data deviation which is at least 15%. In the case of single register storage, the fit to data deviation reaches values of 30% to 40%. Similar to the single register storage measurements with back side illumination, the largest deviations between the data and the best fit model occur in the corners of the reconstructed pixel. The resulting values of σ_{line} and σ_{transfer} are much smaller than in the case of back side illumination. This is

the result of the short drift time of the electrons which are generated close to the register side. The error function model of the charge collection function is thus only valid for back side illumination of pnCCDs. The closest approximation of the error function model to the measured ccf with back side illumination is obtained if a pnCCD is operated in double register storage mode.

Chapter 6

Device simulations

Numerical simulations of pnCCDs deliver a solution of both the electric potential and the motion of electrons and holes in a sub volume of the device. The device model is based on the design data of the simulated pnCCD which includes the contacts and oxide layers on the surface and the ion implants in the bulk. The simulation region is discretized into a set of grid points. Each point in the grid represents a small volume element of the simulation region. The time interval is discretized into a set of time steps. A time dependent solution

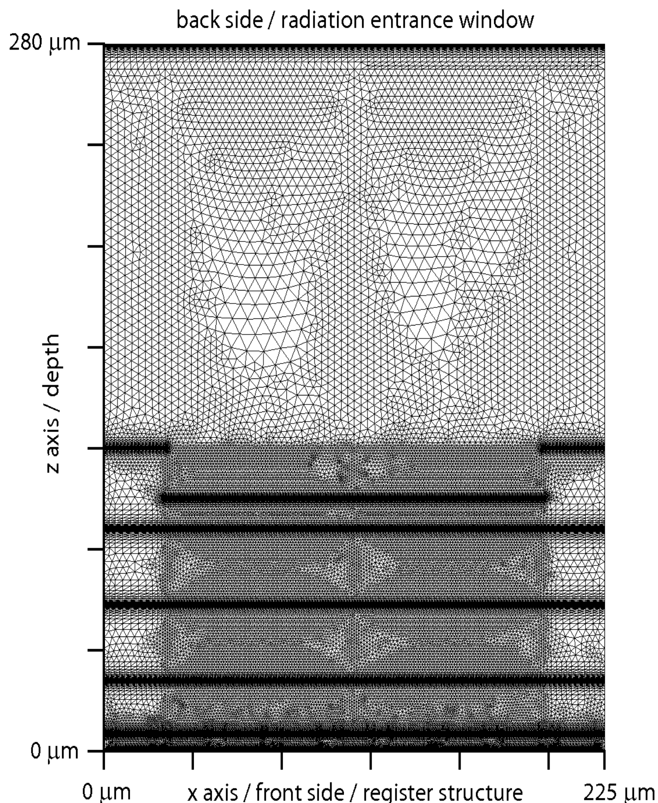

Figure 6.1: *Triangular grid for a simulation region covering three pixels as shown in fig. 6.2. This region is for a 75 µm pixel pnCCD. Dark regions have a high grid density, so individual triangles are not visible. The grid needs to be dense where either physical parameters like the dopant concentration or the electric potential vary on small length scales or where structure sizes are small. This is the case for the register side and the back contact, but generally not for the bulk. An exception are regions of the bulk where the drift of signal charges is investigated. Here, a region with higher grid density is placed below the front side to a depth of 120 µm. The side length of the largest triangles is about 4 µm, the size of the smallest 0.2 µm at the MOS–gates, register– and back contacts.*

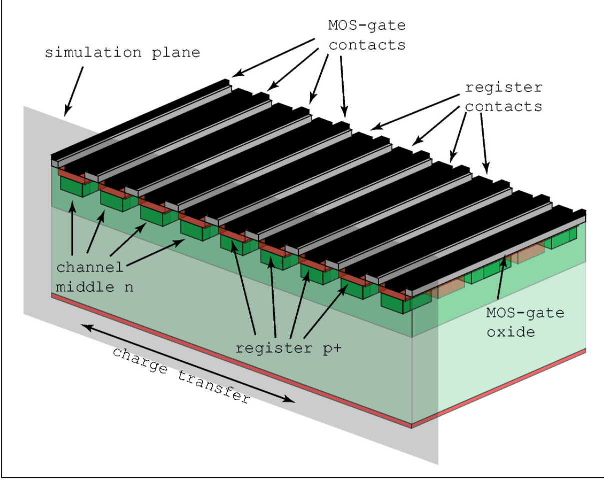

Figure 6.2: *Cut through the middle of a channel guide along the charge transfer direction. Again, the simulated region is the side facing to the front left, reaching to the back contact. It covers nine registers resulting in a total size of three pixels. This region is symmetrical to the middle register.*

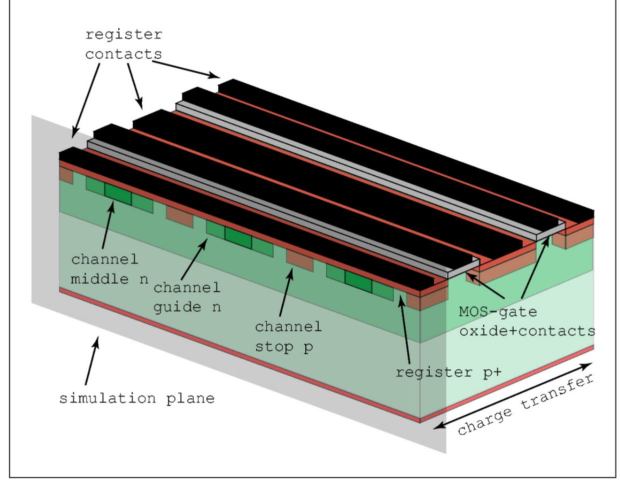

Figure 6.3: *Cut through the middle of a register contact along the line direction of the pixel array. The simulated region is the side facing to the front left. This structure has a width of three pixels. It is symmetrical to the channel guide of the pixel in the middle.*

of the Poisson equation and the continuity equations for electrons and holes is calculated for a given time interval [24]:

$$-\mathrm{div}(\mathrm{grad}\,\varphi) = \frac{\mathrm{e}}{\epsilon_{\mathrm{Si}}\epsilon_0} \cdot (N_{\mathrm{D}} - N_{\mathrm{A}} + N_{\mathrm{p}} - N_{\mathrm{n}}) \tag{6.1}$$

$$\mathrm{e} \cdot \frac{\partial N_{\mathrm{n}}}{\partial t} - \mathrm{div} J_{\mathrm{n}} = \mathrm{e} \cdot (G_{\mathrm{n}} - R_{\mathrm{n}}) \tag{6.2}$$

$$\mathrm{e} \cdot \frac{\partial N_{\mathrm{p}}}{\partial t} + \mathrm{div} J_{\mathrm{p}} = \mathrm{e} \cdot (G_{\mathrm{p}} - R_{\mathrm{p}}) \tag{6.3}$$

Here e is the unit charge , $\epsilon_{\mathrm{Si}}\epsilon_0$ is the permittivity of silicon, N_{n} is the electron density, N_{p} is the hole density, N_{D} is the donor concentration and the N_{A} is the acceptor concentration. J_{n} is the electron current density, J_{p} is the hole current density, G_{n} and R_{n} are the electron generation and recombination rates and G_{p} and R_{p} are the hole generation and recombination rates. The solution of the equations 6.1, 6.2 and 6.3 gives the values of the electric potential and the charge carrier densities at all grid points at each time step.

All device simulations presented in this thesis were done with the 'TeSCA' software [52]. TeSCA solves the equations 6.1, 6.2 and 6.2 with the finite element method on a two dimensional triangular Delaunay grid. An example of a grid employed in a TeSCA simulation is shown in figure 6.1. The bottom side of the simulation region with $z = 0$ is the front side of the device, the top side with $z = d$ is the back side of the device, d is the substrate thickness.

The pixel array of a pnCCD is formed by repeating the basic pixel structure in both the charge transfer and the line direction (section 2.1.1). A device simulation of a region which covers three by three pixels is therefore sufficient to understand the function of the whole array. In order to understand the electric potential and the drift of signal charge in three dimensions, two different two–dimensional TeSCA simulations are needed. One of them represents a cut along the charge transfer direction, figure 6.2. The other one represents a cut along the line direction, perpendicular to the charge transfer direction, figure 6.3. The width of each structure is three pixels, the depth is equal to the device thickness of 280 µm or 450 µm.

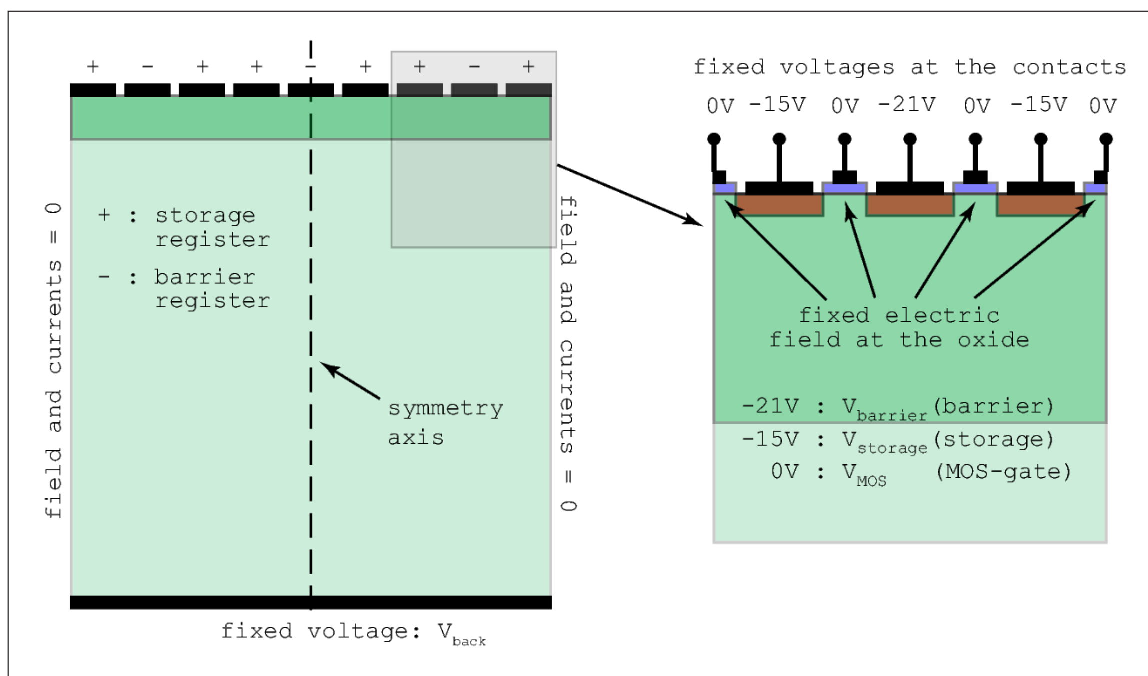

Figure 6.4: *Boundary conditions for an example of a two–dimensional simulation region which is as deep as the real device but only three pixels wide. A boundary with a metal contact is defined by the applied external voltage. MOS–contacts are treated similarly with the inclusion of effects due to the oxide. For boundaries with an interface to the vacuum or bulk silicon, symmetry conditions are applied. Note that a vertical symmetry axis is defined in the middle of the region and that the contact voltages need to be symmetric to this axis.*

Applying the correct boundary conditions at the borders of the simulation regions guarantees that the solutions of the electric potential are valid [24]. The boundary conditions applied by TeSCA ensure that the electric potential in the simulation region is a subset of the periodic potential function of the pixel array. Figure 6.4 shows a cut along the charge transfer direction with the boundary conditions applied by TeSCA.

At the p+ back and register contacts the boundary condition is the contact voltage. At the MOS–gates, the electric field in the oxide created by the aluminum contact voltage and

by the oxide charges defines the electric field at the silicon–oxide interface. At interfaces to bulk silicon or vacuum, TeSCA assumes that the normal vector components of the electric field and of the electron– and hole current densities are zero. A global condition which needs to be satisfied in the simulation region is the symmetry of the electric potential to the middle z–axis. Therefore, the simulation region itself and thus all surface structures, implants and the contact voltages at the registers must be symmetric to the middle z–axis.

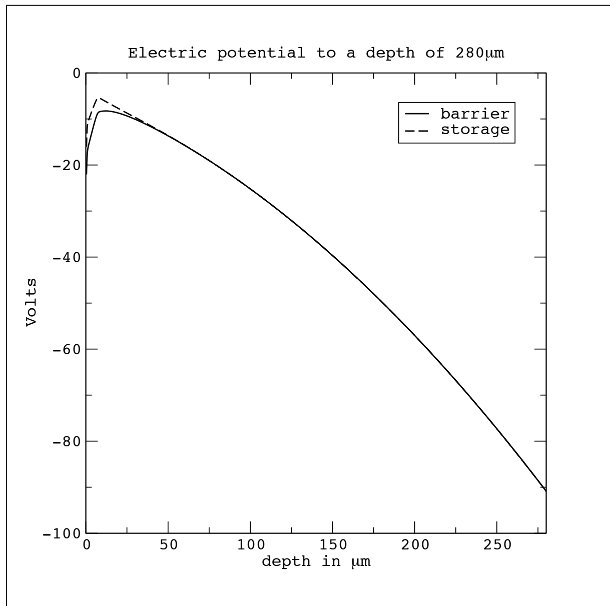

Figure 6.5: *Electric potential in the bulk of a 75 µm pixel pnCCD with storage below two of three registers. Two cuts through the two–dimensional simulation region are shown. One in the middle of a storage register and one in the middle of a barrier register. Both cuts go vertically from the register– to the back side.*

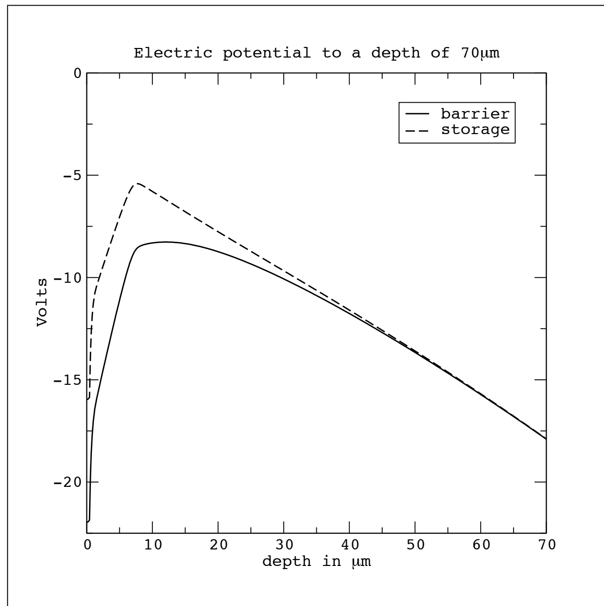

Figure 6.6: *A detail of figure 6.5. The minimum for electrons which forms the transfer channel is in a depth of 8 µm to 10 µm relatively independent of the register contact voltage. In a depth of about 50 µm, the difference of the potential due to the different register contact voltages vanishes.*

6.1 Simulations of a pnCCD with 75 µm pixels

During the integration phase of a signal frame, the voltages of the back contact, the register contact and the MOS–gate contacts remain fixed. A CCD simulation with the constant contact voltages which are applied in the integration phase provides insight into the structure of the electric potential inside of the device. It facilitates us to study the electric potential modulations caused by the storage and barrier registers and by the channel guide and channel stop implants (section 2.1.1). In the following discussion, the location and depth of the potential maximum where signal electrons are stored will be examined. An-

other part of the discussion focuses on the region below the MOS–gates. The MOS–gates define the electric potential at the surfaces between the register contacts (section 2.1.1.1).

All results shown here were obtained from the simulation of a pnCCD with 75 x 75 µm^2 pixels and a substrate thickness of 280 µm. The n–layer on the front side is a high energy implant which reaches into a depth of 7 µm. The layout of the simulation region as well as the acceptor and the donor concentrations of the implants are reproduced from the design data of the pnCCD. The following contact voltage values were applied during the operation of the device: A back contact voltage V_{back} of -90 V, a storage register voltage V_{store} of -15 V, a barrier register voltage V_{barr} of -21 V and a MOS-gate voltage V_{mos} of 0 V. These voltages, as well as storage below one or two registers were reproduced in the device simulations.

Figures 6.5 and 6.6 show the vertical function of the electric potential below a storage and a barrier register. Comparing figures 6.5 and 6.6 with figure 2.6 shows the differences between an analytical calculation and a numerical simulation. Inside the bulk, the parabolic form of the electric potential is correctly given by the analytical calculation. In a distance of less than 50 µm from the front side however, the modulation of the electric potential due to the p+ register contact voltages and the n channel guide implants can be seen. Figure 6.6 shows that the lateral barrier height between two storage maxima is 3.6 V along the charge transfer direction if the signal charge is stored below two registers. In a depth of 50 µm from the register contacts, the lateral barrier height is only 0.012 V. At room temperature, the thermal mean energy of an electron is 0.026 eV. Therefore, an electron can easily pass the lateral pixel barrier of 0.012 V in a depth of 50 µm by thermal motion, but not the 3.6 V barrier in the storage depth of 7 µm.

6.1.1 Charge transfer direction

Figures 6.7, 6.8, 6.9 and 6.10 all show a region with a width of 75 µm (1 pixel) and a depth of 30 µm from the register side. The charge transfer channel is located in a depth of 7 µm and is characterized by a local maximum of the electric potential in the vertical direction, compare figures 6.5 and 6.6.

The MOS–gates are identified by local maxima of the electric potential at the register side. Compared to the register contacts at -21 V and -15 V, the MOS–gates are more positive with a voltage of 0 V. The electric potential around the MOS–gates is plotted in figures 6.11, 6.12, 6.13 and 6.14. Both surface plots show a region with a width of 20 µm in the transfer direction and a depth of 30 µm. The MOS–gate is located in the middle of the x axis, the p+ registers are located to the left and to the right of the MOS–gate. Both contour plots show a region which is 6 µm wide and 10 µm deep, the MOS–gate is located in the middle of the x axis.

Below the MOS–gates, the electric potential has a saddle point. Between two p+ register contacts, the saddle point is the maximum of a lateral potential barrier for holes. Between the transfer channel and the silicon–oxide interface, the saddle point is the maximum of a vertical potential barrier for electrons. The height of the potential barriers depends on the potential at the saddle point below the MOS–gates, see the contour plots 6.12 and 6.14.

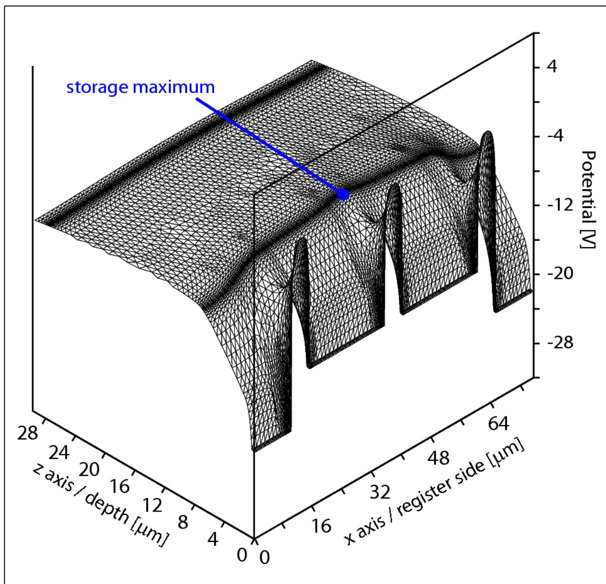

Figure 6.7: *Electric potential below two storage registers in a 75 µm pixel pnCCD. The MOS–gates are at 0V.*

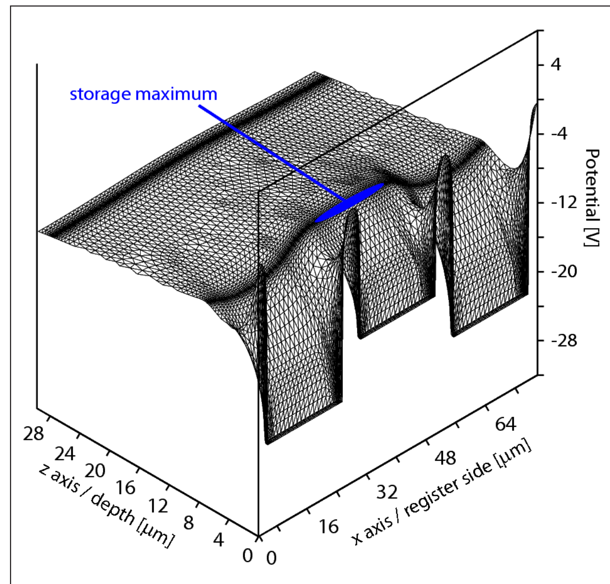

Figure 6.8: *Electric potential below the storage register in a 75 µm pixel pnCCD. The MOS–gates are at 0V.*

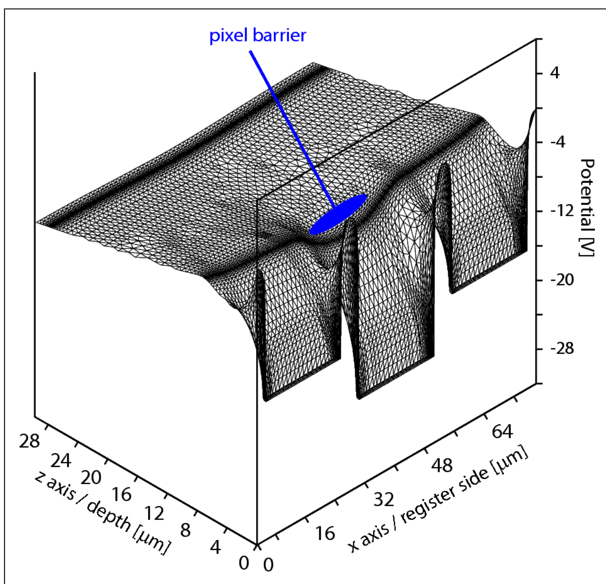

Figure 6.9: *Electric potential below the barrier register in a 75 µm pixel pnCCD. The two more positive registers are at storage potential. The MOS–gates are at the peaks of the potential at the register side.*

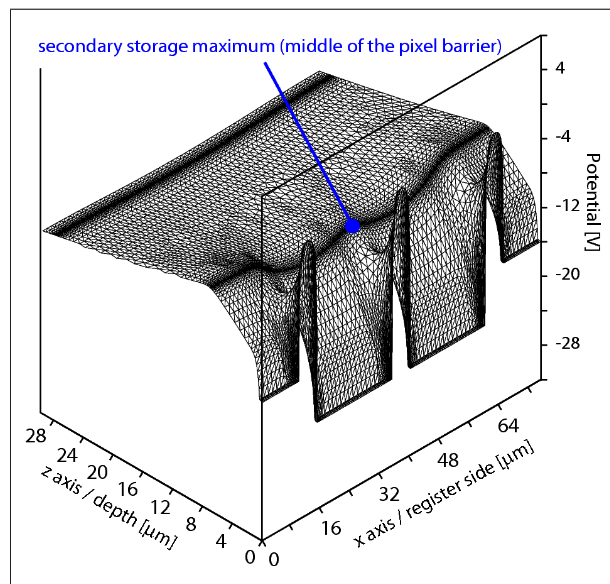

Figure 6.10: *Electric potential below two barrier registers in a 75 µm pixel pnCCD. A secondary storage maximum is located below the MOS–gate in the middle of the potential barrier.*

The potential difference present between the saddle point and the storage register is 7.5 V. This potential barrier prevents any hole current from the storage to the barrier registers. The potential difference between the storage maximum and the saddle point is 1.4 V. For an electron this means a potential barrier of 1.4 eV to the MOS–gate. This barrier is 50 times higher than the thermal mean energy of 0.026 eV of electrons at room temperature. Thus, signal electrons cannot escape the storage minimum by thermal motion. Electrons at the silicon–oxide interface of the MOS–gates see an even higher barrier of 6 V to 7.6 V to the charge transfer channel and thus can never reach the transfer channel.

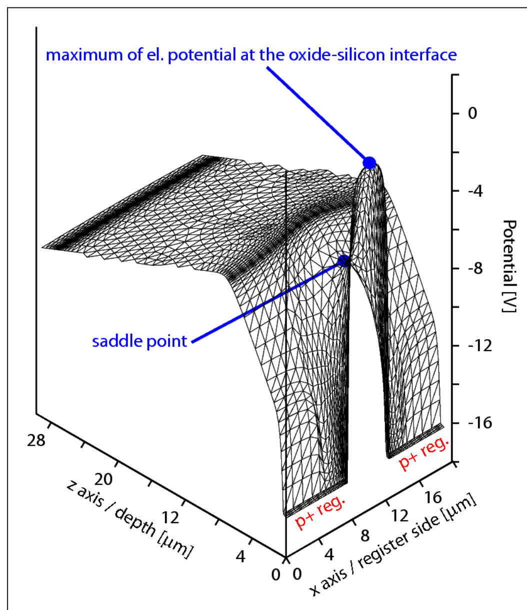

Figure 6.11: *Electric potential at a MOS–gate between two storage registers. Electrons at the MOS–gate cannot get into the bulk due to its strongly positive potential.*

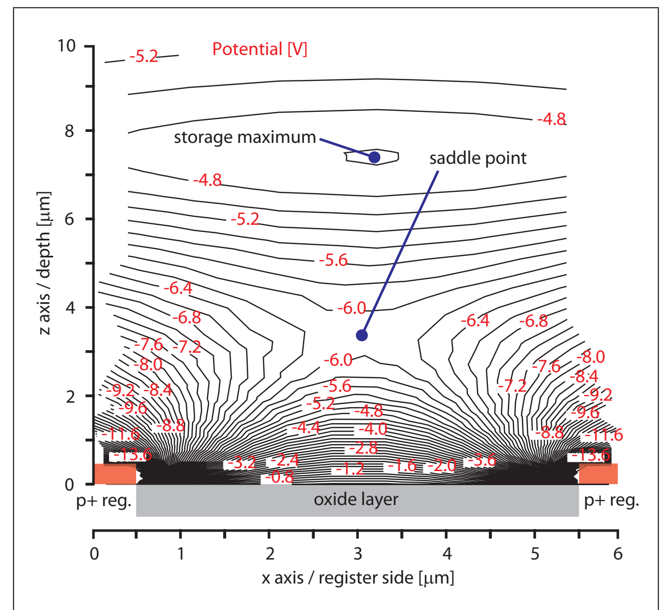

Figure 6.12: *Electric potential at a MOS–gate between two storage registers shown as a contour plot. The region is 6 µm wide and 10 µm deep.*

The storage maximum in a depth of 7 µm is clearly seen in figure 6.7 which shows the case of storage below two registers. Figure 6.8 shows the storage maximum below one storage register for the case of single register storage. In both plots, the middle of the barrier to the neighboring pixels is located at the ends of the x axis in the plots. The potential barrier height between two storage maxima along the transfer direction changes with the used storage mode. In the case of the applied register voltages of -21V and -15V, the barrier height is 3.6 V for storage below two registers and 2.8 V for storage below one register.

Compared to these barrier heights, the 1.4 V potential barrier to the MOS–gate is 2.2 V to 1.4 V smaller respectively. The effective potential depth of a storage cell is therefore the height of the smallest barrier: 1.4 V. Signal electrons arriving from the back side entrance window however do not see the vertical barrier to the MOS–gates but the lateral barrier between two registers. The mean lateral drift field strength from a pixel barrier to a storage

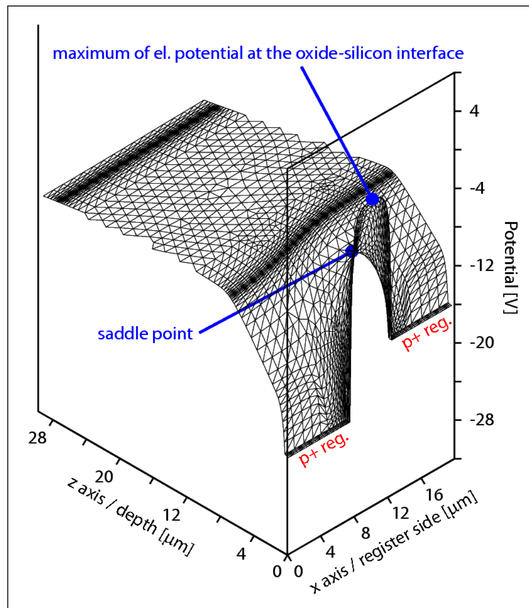

Figure 6.13: *Plot of the electric potential around a MOS–gate between a storage register on the right hand side and a barrier register on the left hand side.*

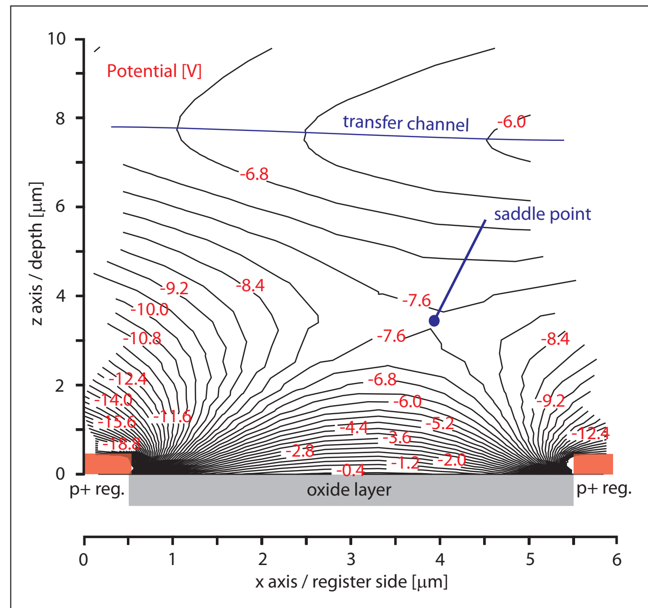

Figure 6.14: *Contour plot of the electric potential at a MOS–gate between a storage and a barrier register covering a region 6 µm wide and 10 µm deep.*

cell is given by the barrier height of 3.6 V or 2.8 V divided by the lateral distance of 37.5 µm from the barrier to the storage cell. In the case of double register storage, the mean lateral drift field is 960 V/cm, in the case of single register storage the mean lateral drift field is 750 V/cm.

A secondary storage maximum appears between the barrier registers in single register storage mode. It is caused by the positive MOS–gate between the barrier registers, see figure 6.10. The vertical barrier height to the MOS–gate is 1.4 V and the lateral barrier height to the neighboring pixel storage cells is 0.8 V. An electron therefore sees a barrier of 0.8 eV to the two neighboring storage cells. Compared to the thermal mean energy of 0.026 eV at room temperature this barrier is large enough to keep electrons inside the secondary storage maximum.

6.1.2 Line direction

In the line direction, the lateral modulation of the electric potential is created by the positive space charge of the channel notch and guide implants and by the negative space charge of the channel stop implant. Therefore, the barrier height between two neighboring pixels is determined by the dose in these implants. The higher the implantation dose in the p channel stops and in the n channel notches and guides, the larger is the amount of active space charge in the depleted bulk below the register side. Both the implantation doses in the channel forming implants and the register voltages for a given pnCCD design

are chosen such that the lateral barrier height between two storage cells is similar for the charge transfer and for the line direction.

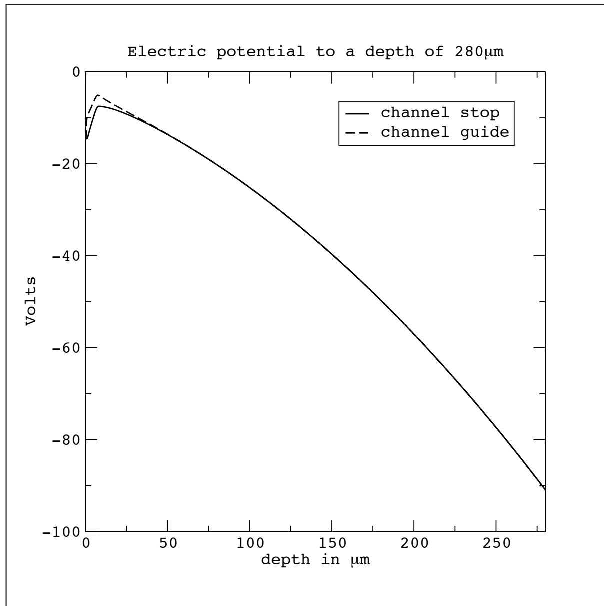

Figure 6.15: *Plots of the electric potential along cuts from the register side to the back contact. Here the potential is shown for cuts starting from below a channel guide and a channel stop.*

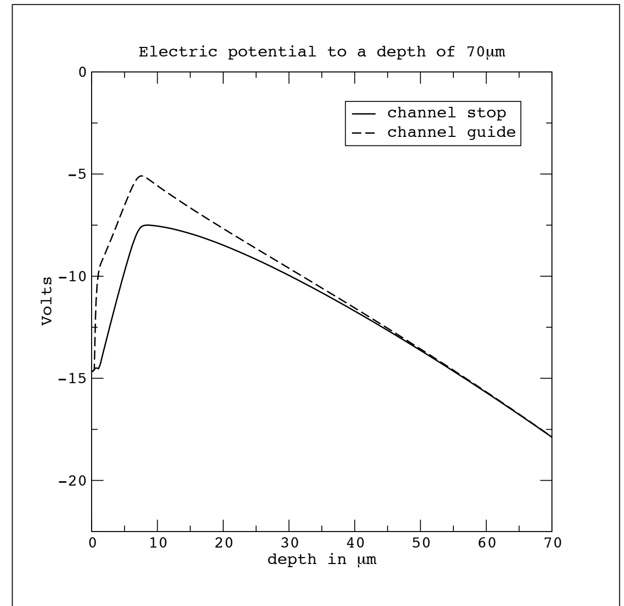

Figure 6.16: *The same plots as in fig. 6.15 but to a depth of 70 µm. Note the similarity to plot 6.6 and that the differences of the potential below the channel guide and –stop vanish in a depth of about 50 µm.*

Figures 6.15, 6.16, 6.17 and 6.18 show the electric potential in a cut along a storage register for the case of double register storage. A comparison of figures 6.6 and 6.16 shows the same absolute depth of -5.2 V of the storage maximum. Figure 6.17 shows that the channel notch implant creates an additional positive 'dip' in the electric potential maximum caused by the channel guide implant. The dip created by the channel notch defines the transfer channel along which the signal electrons are moved to the readout anodes.

The lateral electric potential barrier between two pixels in the transfer channel depth of 7 µm is 2.4 V. In a depth of 50 µm, the lateral barrier height between two pixels is 0.024 V. For an electron, this is a barrier of 0.024 eV which is slightly smaller than the mean thermal energy of 0.026 eV at room temperature. Electrons can thus pass the barrier between two pixels by thermal motion if the distance to the register side is more than 50 µm. At smaller distances from the register side, the lateral drift field becomes sufficiently large to prevent electrons from passing the barrier between two pixels. The mean lateral drift field from the channel stop to the channel notch is found from dividing the lateral barrier height by the distance from the channel stop to the channel notch. With a barrier height of 2.4 V in the depth of the transfer channel and the given channel stop to notch distance of 37.5 µm, the mean lateral drift field has a value of 640 V/cm in a depth of 7 µm from the register side.

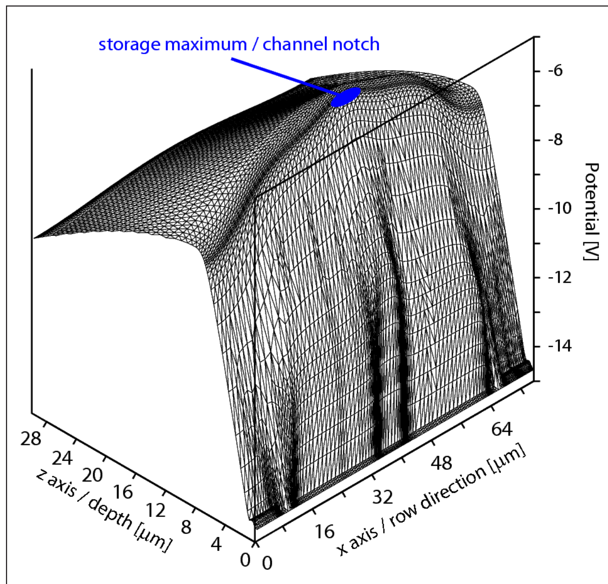

Figure 6.17: *Electric potential below a channel guide in the 75 µm pixel pnCCD. The channel notch implant results in a narrow potential minimum for electrons.*

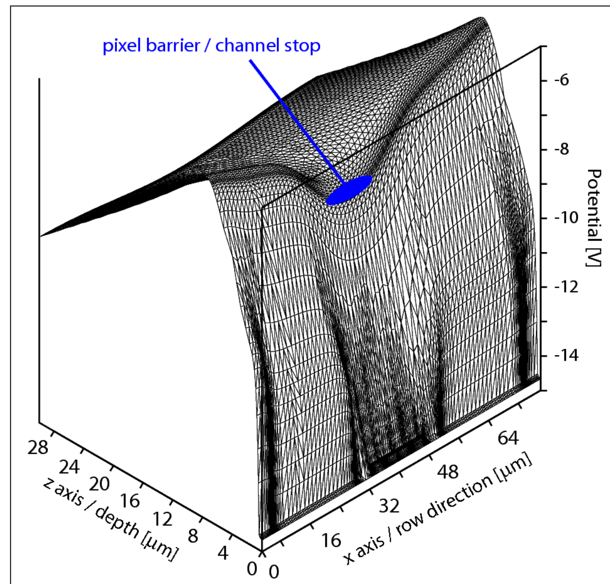

Figure 6.18: *Electric potential below a channel stop in the 75 µm pixel pnCCD. The negative space charge of the channel stop creates a potential barrier for electrons.*

6.2 Simulations of charge drift and diffusion

The TeSCA software determines the solution for the motion of free electrons and holes in the electric potential inside the two dimensional simulation region. In order to simulate the detection of photons, charge carriers can be generated at an arbitrary position of the grid. Therefore, the complete process from the generation of electron hole pairs to the collection of the electrons in the storage cells can be studied.

The solution for the collection of signal electrons was determined for sets of photon absorption positions with a given z–coordinate value (depth from the register side) and with different x–coordinate values (position along the line direction or along the charge transfer direction in the pixel array). These solutions for the final charge distribution in the two–dimensional simulation domains were evaluated in order to obtain profiles of the charge collection function. The accuracy of the simulated profiles was analyzed in a comparison with the measured ccf profiles.

6.2.1 Simulation principle

TeSCA performs device simulations in two dimensional domains where the simulation region is either a two dimensional plane or a cylindrical volume. In a two dimensional domain, the x–axis can be treated as the radial coordinate while the (vertical) z–axis of the domain corresponds to the z–axis in cylinder coordinates. This facilitates the correct solution of the Poisson and continuity equations for problems with a cylindrical symmetry,

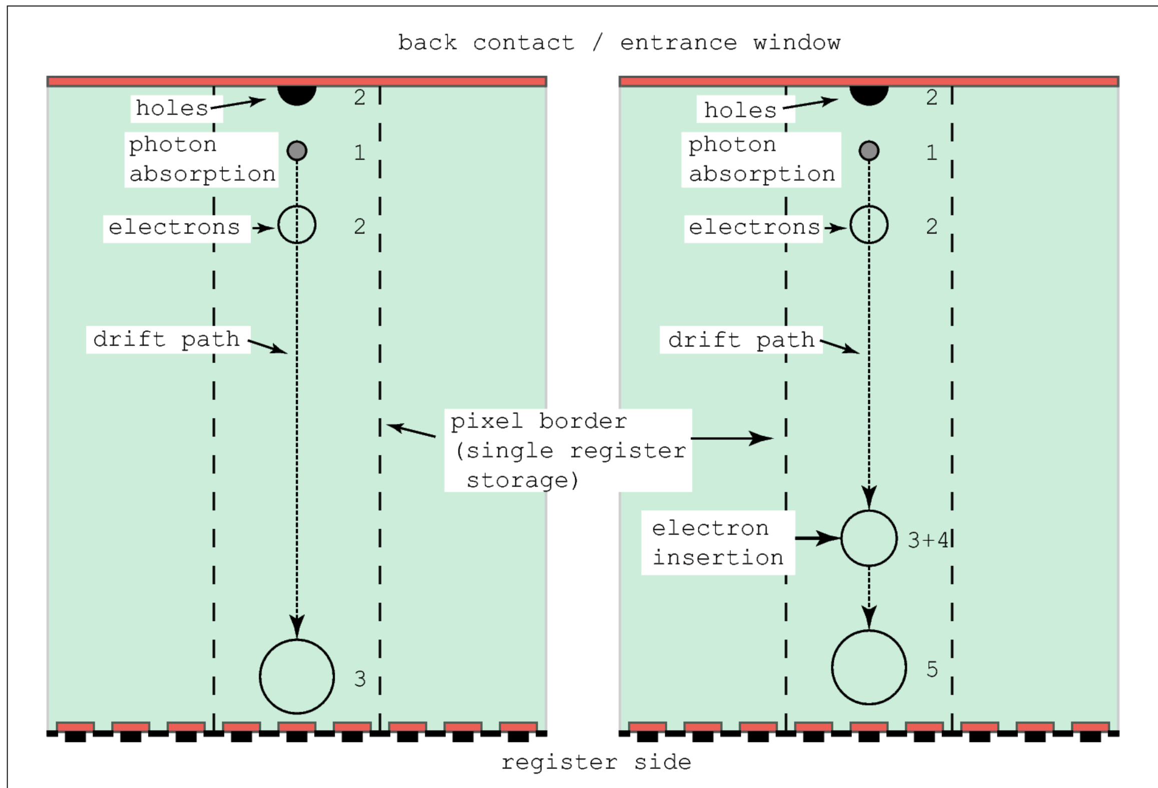

Figure 6.19: *Two possible ways to simulate the drift and collection of a signal electron cloud. On the left hand side, a direct approach is shown. An electron hole cloud is generated in the correct absorption depth (1) and the simulation software calculates the complete process from separation of the electron hole cloud (2), its drift and expansion (3) and the collection in the pixel structure (4). This approach does not work because of incorrect treatment of electrostatic repulsion and limitations of the computer hardware. On the right hand side, the approach chosen for this thesis is shown. The physical process is the same, but the expansion of the signal electron cloud along 2/3 and more of its drift distance is simulated separately (section 6.2.3). In the second stage, the signal electron cloud is inserted in the correct depth with the correct size (3+4) and the last part of the drift and the final collection process (5) is simulated in the two–dimensional pnCCD domain.*

e.g. the expansion of a spherical charge cloud. In this case, the effect of electrostatic repulsion in a charge cloud is correctly considered by the calculation (section 2.2.1.2) since the electric repulsion field is calculated for the charge density in a spherical volume. Diffusion is already correctly evaluated in a two dimensional domain since it only depends on the charge density profile in the radial direction (section 2.2.1.1). Electrostatic repulsion has the strongest effect directly after the separation of the electron hole cloud when the charge density has the highest value. Therefore, the simulations of the signal electron collection process are divided in two steps. In the first step, the expansion of the electron

cloud is simulated in a volume with cylindrical symmetry in order to correctly treat the effect of electrostatic repulsion. This step covers a time interval which is one half to two thirds of the electron drift time from the generation position to the register side. In the second step, the expanded charge cloud is inserted into the two dimensional CCD domain in order to obtain the result for the charge distribution over the pixels near the photon incidence position.

The expansion of a signal electron cloud is solved for a given drift time interval as indicated in the drawing on the right hand side of figure 6.19. The simulation region is a cylindrical volume of undoped bulk silicon where the electron cloud expands freely in the absence of an external electric field. The expansion of an electron cloud starts directly after the separation of the initial electron hole cloud. The electrons are thus inserted at the symmetry axis of the cylindrical domain, their initial distribution is a charge cloud with a radius of approximately 0.3 µm which is given by equation 1.10, section 1.3. Since the contributions of both diffusion and electrostatic repulsion are included in the calculation, the final size and form of the electron cloud represents an exact solution of the continuity equation 2.7 in section 2.2.1. At the end of the simulation, the size of the charge cloud is determined from a radial profile of the electron concentration. The time interval for the expansion is given by the electron drift time from the absorption depth of the photon to a given depth of typically 100 µm from the register side.

In the second step, the electron cloud with the known radius is inserted in the potential simulation of the pnCCD, compare the right hand side of figure 6.19. The insertion depth of typically 100 µm is chosen such that the lateral electric field component due to the pixel structure is still negligible. In the first section of the drift path to the register side, the electron cloud therefore still expands freely without the influence of a lateral electric field. The depth where the separation at the pixel borders begins is characterized by a deformation which destroys the spherical symmetry of the charge cloud. The separation depth can thus be identified with an evaluation of the position and the form of the electron cloud during its drift to the register side. At the end of the second simulation step, the signal electrons have reached the electric potential maxima of the storage cells. The final charge distribution is characterized by the amount of charge in the pixels near the insertion position of the electron cloud.

The two step approach relaxed the requirements for a high grid density along the drift path of the electron cloud. Since the electron cloud is inserted in the CCD domain after a time interval of approximately half of the total drift time, its radius is in the range of a few microns (section 2.2.1). The mean distance of the grid points in the drift path must be at maximum 1/5th of the charge cloud radius σ. Due to the larger size of the electron cloud at the time of its insertion in the CCD domain, the minimum required grid point distance can be increased. Later insertion of the electrons in the simulation region also means that the simulated drift distance from the electron insertion depth to the front side is shorter. Thus, the region where the grid needs to have a high density does not extend over the whole simulation domain. A lower maximum grid density in combination with a smaller region with an increased grid density means less computation effort in each simulation step and thus a shorter total computation time. Without the application of the two step

approach, simulations of the charge collection process are beyond the limitations of the available computation speed and memory.

6.2.1.1 Creating a simulation of the charge collection function

The basic data for a simulation of the charge collection function is delivered by a set of device simulations which are identical except for the photon incidence position. The ccf values are given by the ratio of the amount of electrons collected in a storage cell (pixel) to the total amount of generated electrons. These values are calculated for each simulated photon incidence position (x–coordinate of charge generation), compare the definition of the ccf in section 5.1.2.2. The z–coordinate of the signal electron generation position is given by the absorption length at the given photon energy. The x–coordinate range covers a width of 60 µm in the case of 51 µm pixels and 80 µm in the case of 75 µm pixels with a step size of 2 µm. A step size of 2 µm between two adjacent charge generation positions matches the spatial resolution of the mesh measurements.

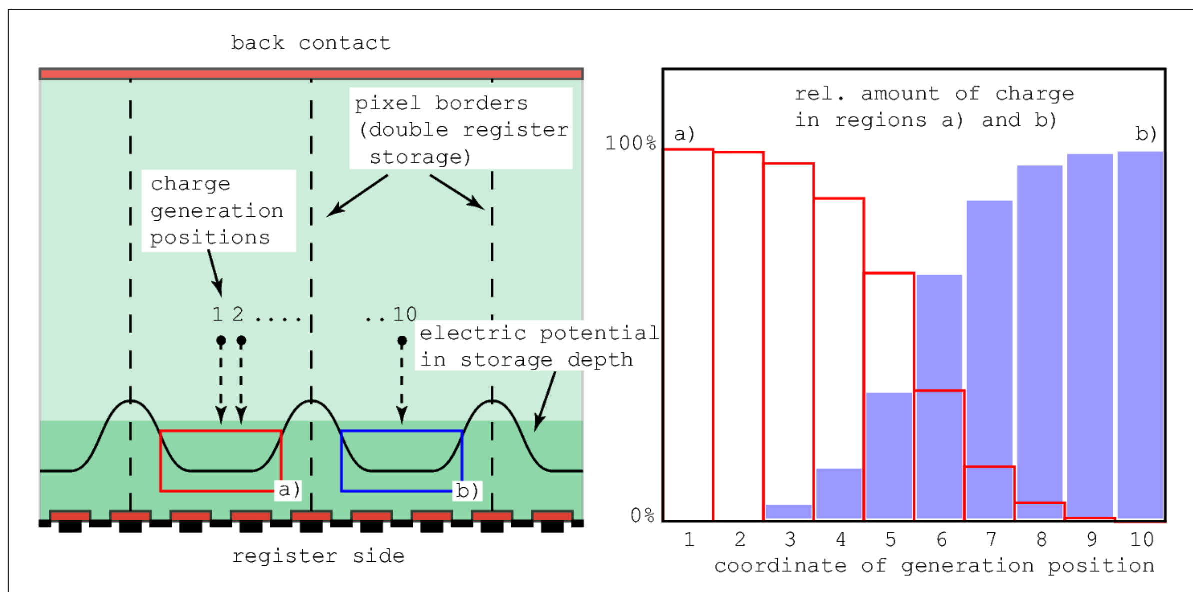

Figure 6.20: *Illustration of the set of device simulations that are used to simulate the charge collection function. Here, a simulation in the charge transfer direction is demonstrated for the case of double–register storage. Equidistant generation positions of a signal electron cloud are denoted with their index from 1 to 10. The pixel borders are defined by the potential barrier for electrons. Two rectangular regions are defined around the storage minima. On the right hand side, a graph shows the relative amount of charge in region a) and b) plotted over the charge generation positions on the x axis.*

Figure 6.20 shows how a set of individual charge drift and collection simulations is combined in a simulated ccf. The regions a) and b) in the simulation domain define sub-volumes which contain the storage cells for electrons. Integration of the charge density

over a sub-volume gives the total amount of charge in the storage cell inside of the volume. In the graph on the right hand side, the percentage of charge in the rectangular regions a) and b) is plotted as a function of the x–coordinate of charge generation. This graph shows how the amount of charge that reaches region a) decreases when the generation position moves to the right hand side of the x axis. The amount of charge that reaches region b) increases such that the sum of the charge in region a) and b) equals the total amount of generated signal electrons.

Since the electric potential in a pixel is symmetric to the pixel border, the distribution of signal charge is also symmetric to the pixel border. If the range of charge generation positions covers the width of one pixel in the x-direction, the values of the charge collection function can thus be calculated for a x axis coordinate range of two pixels. If the x–coordinate of the generated charge cloud lies in the middle of the pixel with region a) in figure 6.20, two ccf values can be calculated with the integrated charge values in the regions a) and b): I. The value of the ccf if a photon hits the middle of a pixel, it is given by $N_{\mathrm{el.}}(\mathrm{a})/N_{\mathrm{el.}}(\mathrm{total})$ where $N_{\mathrm{el.}}(\mathrm{a})$ is the number of electrons in region a) and $N_{\mathrm{el.}}(\mathrm{total})$ is the total number of generated electrons. II. The value of the ccf if a photon hits the middle of a neighboring pixel to the left of a pixel. It is given by $N_{\mathrm{el.}}(\mathrm{b})/N_{\mathrm{el.}}(\mathrm{total})$ where $N_{\mathrm{el.}}(\mathrm{b})$ is the number of electrons in region b). Due to the symmetry of the electric potential, this is the same result as the ccf value in the case that a photon hits the middle of a neighboring pixel on the right hand side. All simulations of charge collection functions were generated this way from a set of individual device simulations. This principle also applies to single–register storage and to simulation domains which represent the electric potential structure and the charge collection process in the line direction of a pnCCD.

6.2.2 Electron drift in the bulk

Electrons drift along the electric field which is given by the gradient of the electric potential inside of the pnCCD. The systematic motion in the electric field is superposed by the random motion due to the thermal energy of electrons. For a large number of electrons in a charge cloud, the random motion is described by the expansion due to diffusion. In a homogeneous electric field, the motion of an electron cloud is thus the superposition of drift, electrostatic repulsion, and diffusion expansion (section 2.2.1). If the electric field is not homogeneous, e.g. at the register side of a CCD, the free expansion of the electron cloud is suppressed. In a storage cell, the electrons are forced to collect at the point with the highest electric potential. At a pixel barrier, the lateral electric field divides the electron distribution in two parts on both sides of the barrier. Thus, the drift of the signal electrons in a pnCCD can be divided in two phases: In the first phase, the electron cloud drifts towards the register side and freely expands due to diffusion and electrostatic repulsion. In the second phase, the lateral field component of the register structure takes effect and it either collects all charge in one storage cell or it divides the charge cloud at the pixel borders. The depth where the second drift phase begins is defined as the 'separation depth' for signal electrons which drift towards the front side of the device.

6.2.2.1 Upper limit of the separation depth

For a correct simulation of charge splitting at the pixel borders, the electrons must be inserted in a depth that is larger than the separation depth. The lateral variations of the electric potential cause a drift field that moves electrons towards the middle of the pixels. As long as the amplitude of the potential variations is smaller than the thermal mean energy of the electrons, diffusion is stronger than the lateral drift force. For a decreasing depth from the front side, the lateral drift field becomes stronger. The upper limit for the separation depth is given by the depth where the lateral variations of the electron potential have the same value as the thermal mean energy of the electrons.

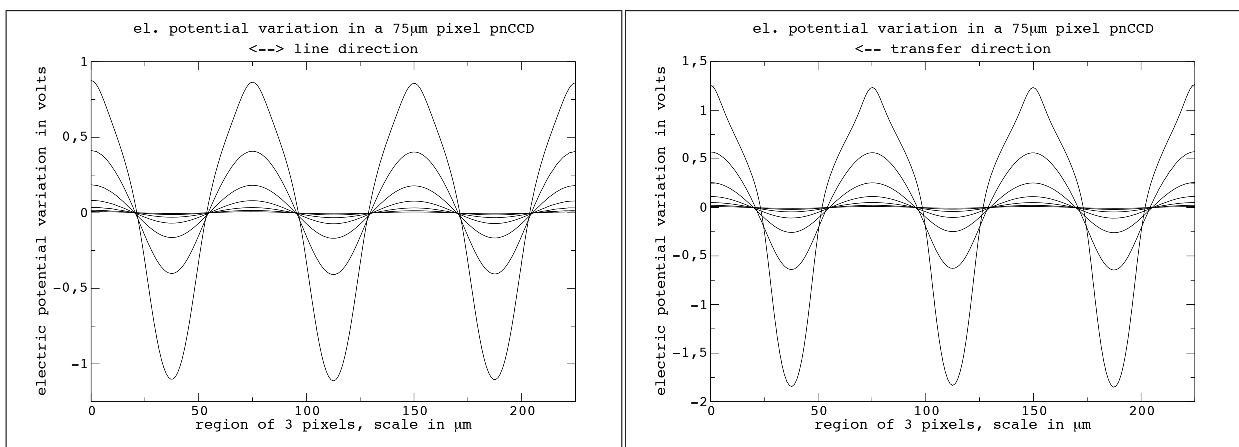

Figure 6.21: *Plot of the lateral variation of the electric potential along the line (left) and charge transfer (right) directions of a 75 µm pixel pnCCD. The plots show values of the electric potential in depths of 10 µm to 70 µm from the register side in steps of 10 µm. With increasing depth from the register side, the amplitude of the potential variation decreases until it looks like a straight line in a depth of 60 µm.*

Figures 6.21 and 6.23 show plots of the electric potential variation in different depths from the register side for the line and charge transfer directions. Both plots show the electric potential variation for the case of double register storage and cover the full width of the simulation region which is three pixels in both cases. The used operation voltages are the same as in the mesh measurements done with the 75 µm and 51 µm pixel pnCCDs: $V_{\mathrm{back}} = -90$ V, $\mathrm{Phi}_{123} = -15$ V and $\Delta\mathrm{Phi}_{123} = -6$ V for the 75 µm pixel pnCCD and $V_{\mathrm{back}} = -250$ V, $\mathrm{Phi}_{123} = -15$ V and $\Delta\mathrm{Phi}_{123} = -4$ V for the 51 µm pixel pnCCD. The curves with the largest amplitude in figures 6.21 (75 µm pixels) and 6.23 (51 µm pixels) show the potential variation in a depth of 10 µm from the register side. The amplitude decreases monotonously with an increasing depth from the register side. In both cases of 75 µm and 51 µm pixel size, the lateral potential variations are negligible in a depth greater than the side length of a pixel. This means that in a distance from the register side which is greater than the width of a pixel, the electric potential is only a function of the depth but not a function of the lateral coordinates in the pixel array.

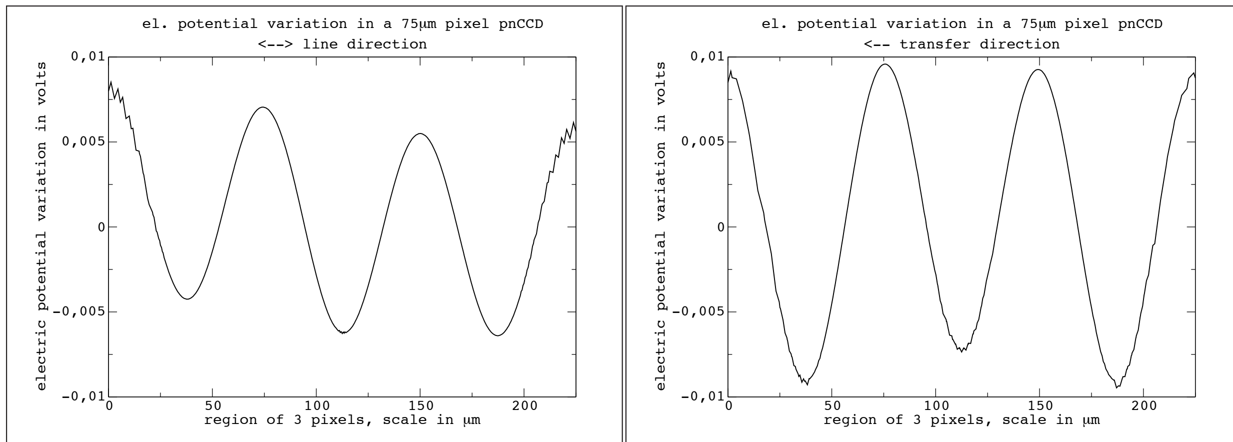

Figure 6.22: *Plot of the lateral variation of the electric potential in a depth of 70 µm from the register side, as shown in figure 6.21 but with a smaller y–axis range which makes the variations of the potential visible. The maximum excursion of the potential is just below 0.02V but over a region 25 µm wide, it is only 0.014V. This is value close to 0.013V, the thermal voltage of an electron at 153K.*

In order to resolve the remaining lateral change of the electric potential in a depth of 70 µm and 50 µm, figures 6.22 and 6.24 have a y axis range of 0.02 V to 0.05 V. In the 75 µm pixel CCD, the maximum excursion of the lateral electric potential variations is 0.02 V over the full width of the simulation region. In the 51 µm pixel CCD, the maximum variation of the electric potential over the width of the simulation region is 0.03 V in a depth of 50 µm from the register side. At 180 K, the lowest temperature which was applied in the CCD simulations, the thermal mean energy of an electron is 0.016 eV. The observed lateral variations of the potential of an electron are between 0.02 eV and 0.03 eV and thus in the order of magnitude of the thermal energy of the simulated signal electrons. This is at the threshold where a separation of the signal charge cloud by the lateral drift field is possible. Therefore, signal electron clouds are not separated before they reach a distance from the register side which is equal to the pixel size. As stated above, the calculation of the signal electron drift must start before the lateral drift field of the pixel structure takes effect. This requirement is fulfilled with an electron insertion depth of 100 µm in the simulations of 75 µm pixel CCDs and an insertion depth of 70 µm in the simulations of 51 µm pixel CCDs.

6.2.2.2 Electron drift velocity in the bulk

The drift velocity of electrons v_{e^-} is a function of the electric field. For low values of the field strength $\mathcal{E}$, v_{e^-} is proportional to $\mathcal{E}$. However, as the electric field strength increases, the drift mobility begins to decrease when the electron drift velocity approaches the saturation value. At a typical operation temperature of 193 K (-80 °C) and for a drift field strength of 2000 V/cm or less, the electron drift velocity can be calculated with the

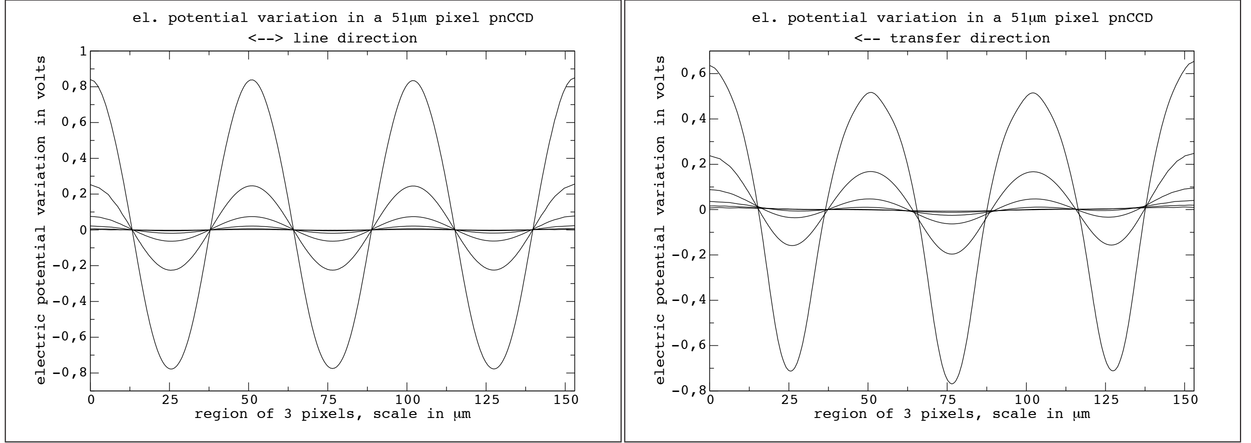

Figure 6.23: *Plot of the lateral variation of the electric potential along the line (left) and charge transfer (right) directions of a 51 µm pixel pnCCD. The plots show values of the electric potential in depths of 10 µm to 60 µm from the register side in steps of 10 µm. With increasing depth from the register side, the amplitude of the potential variation decreases until it looks like a straight line in a depth of 60 µm. Note the numerical errors causing lower values in the middle of the plot.*

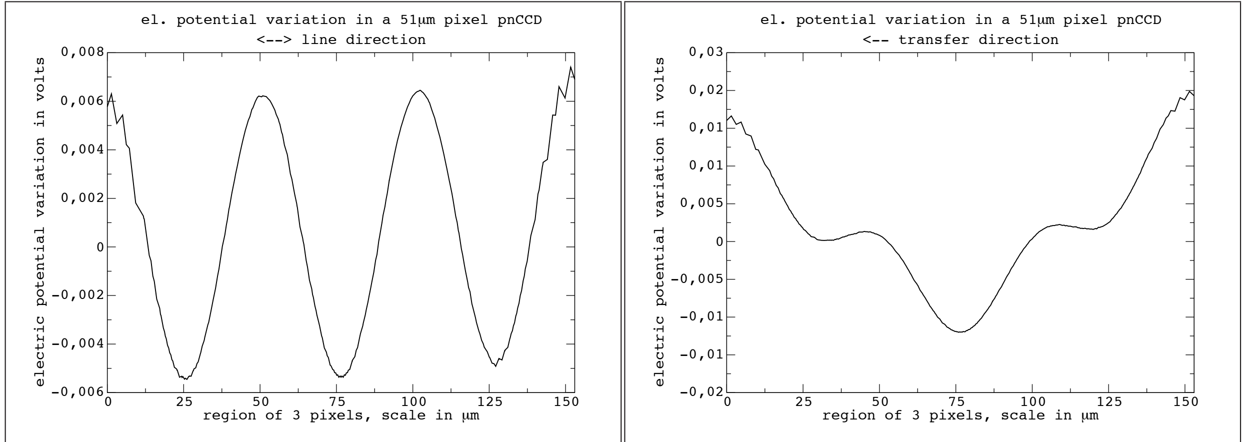

Figure 6.24: *Plot of the lateral variation of the electric potential in a depth of 50 µm from the register side, as shown in figure 6.23 but with a y–axis range which makes the variations of the potential visible. The maximum excursion of the potential is around 0.025V but over a region 25 µm wide, it is only 0.01V. This value is below 0.015V, the thermal voltage of an electron at 180K.*

linear relation $v_{e^-} = -\mu_n \cdot \mathcal{E}$. For $T = 193\,\mathrm{K}$, the mobility model of Arora [28] gives a mobility of $3612\,\mathrm{cm^2/Vs}$ and the corresponding drift velocity of electrons at $\mathcal{E} = 2000\,\mathrm{V/cm}$ is $7.2 \cdot 10^6\,\mathrm{cm/s}$. In section 2.2.1, the effect of the saturation of the electron drift velocity is discussed. According to [25, 26], the saturation drift velocity for electrons at 200 K is $1.0 \cdot 10^7\,\mathrm{cm/s}$. If the linear drift velocity model is used, this corresponds to an electric

field strength of 2770 V/cm at a temperature of 193 K. The device simulation software TeSCA calculates the drift velocity with the linear model $v_{e^-} = -\mu_n \cdot \mathcal{E}$. Thus, at a drift field strength of 3000 V/cm and more, the calculated electron drift velocity is above the saturation value of $1.0 \cdot 10^7$ cm/s given in [25, 26].

Since TeSCA supplies the values of the electric field strength at every point in the simulation domain, the corresponding drift velocity can be evaluated and compared with the saturation value. Figure 6.25 shows two plots of the electric drift field in the simulated pnCCDs. The x axis of the plots shows the depth from the register side of the simulation regions. Simulations of the 75 µm pixel device with 280 µm substrate thickness were performed for a back contact voltage of -90 V and a temperature of 193 K and 153 K. In the 51 µm pixel CCD simulations with a substrate thickness of 450 µm, back contact voltages V_{back} of -180 V and -250 V were applied and the substrate temperature is 180 K. In the plot on the right hand side of figure 6.25, the electric field is plotted for the case of $V_{\mathrm{back}} = -250$ V. The substrate temperatures and the corresponding electron mobilities are 193 K and 3612 cm²/Vs, 180 K and 4234 cm²/Vs and 152 K and 6140 cm²/Vs. The critical depth d_{vsat} where the drift velocity reaches the saturation value is thus 125 µm (193 K, $V_{\mathrm{back}} = -90$ V) or 25 µm (153 K, $V_{\mathrm{back}} = -90$ V) in the CCD with 280 µm substrate thickness. In the CCD with 450 µm substrate thickness, the critical depth d_{vsat} is 30 µm (180 K, $V_{\mathrm{back}} = -250$ V). Therefore the signal electrons reach their saturation velocity over most of the drift distance from the back side to the register side. In the pnCCD simulations, it was assumed that the mobility changes only in the direction of the drift

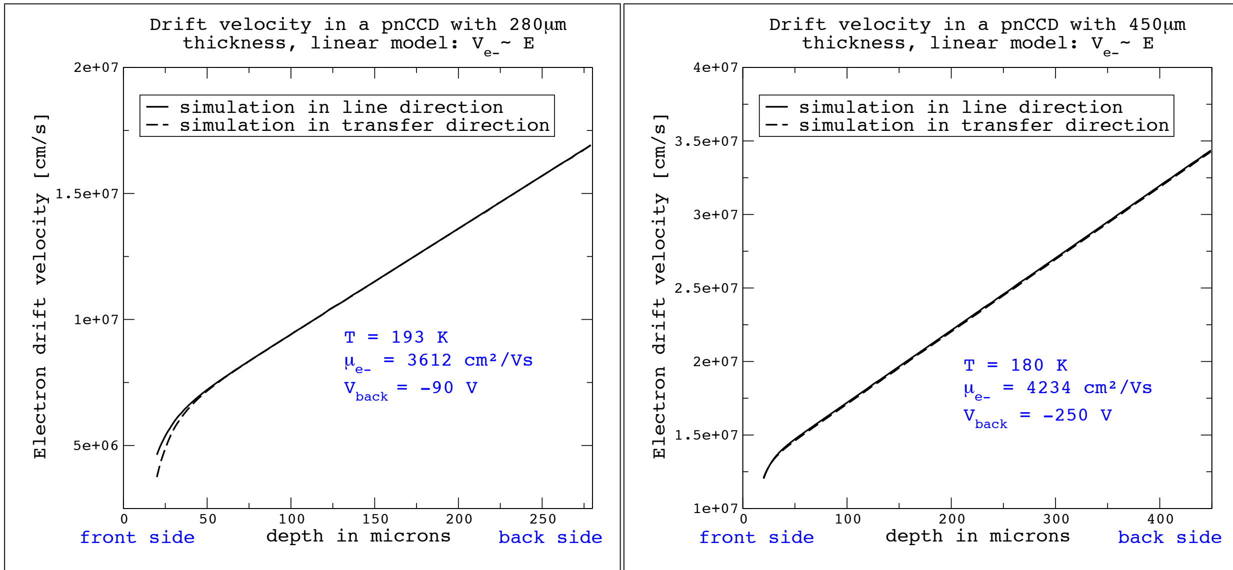

Figure 6.25: *Plots of the electron drift velocity in the bulk of a pnCCD with 280* µm *thickness and 75* µm *pixels (left) and a pnCCD with 450* µm *thickness and 51* µm *pixels (right). Both plots show the values for simulations in line– and transfer direction. Over most of the drift distance, the electron velocity calculation with* $v_{e^-} = \mu_e \cdot \mathcal{E}$ *delivers values above the saturation velocity of* $1.0 \cdot 10^7$ cm/s.

field. For the calculation of the expansion of an electron cloud in the lateral direction, the mobility value given by the model in [28] was used. The ccf simulations provide a means to investigate the prediction of a saturation velocity for electrons. Both the linear relation between the electric field and the drift velocity and drift with a saturation velocity of $1.0 \cdot 10^7$ cm/s were assumed for the calculation of the signal electron drift time. However, when the charge cloud was 'inserted' in the CCD domain, the linear drift model applied by TeSCA had to be used. The corresponding total drift times from the entrance window to the register side are in the range from 2 ns to 5 ns.

6.2.3 Numeric simulations of the charge cloud expansion

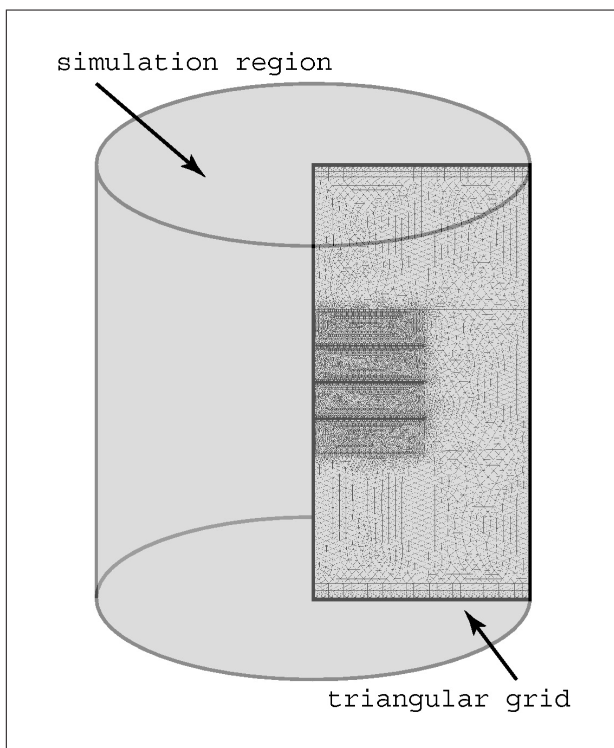

Figure 6.26: *Sketch of the physical geometry of a cylindrical simulation region in TeSCA. The grid of the simulation domain is still two–dimensional but all equations are rewritten from Cartesian to cylindrical coordinates. Charge is generated at half the height of the domain's left border. A part of the domain around the position of charge generation is discretized by a finer grid to suppress numerical errors. In addition the size of the domain is chosen sufficiently large to avoid letting the charge get into contact with its borders. Physically, the domain is defined to be a piece of intrinsic silicon free of any impurity. At the top and at the bottom, it is terminated by aluminum contacts with a fixed potential of 0 V.*

In the first step of the signal charge collection simulations, the solution for the expansion of the charge cloud is calculated in a cylindrical domain of undoped silicon, compare section 6.2.1. The resulting charge cloud size defines the initial charge distribution in the second simulation step. The parameters which determine the expansion of an electron cloud over a given time interval Δt are the electron mobility $\mu_{\mathrm{n}}(T)$, the temperature T, the number of electrons n_{e^-} and the initial size of the electron distribution. All simulations started with a spherical Gaussian electron distribution that has a sigma radius of 0.5 µm. As stated in the preceding section 6.2.2.2, it was assumed that the mobility in the lateral direction is not influenced by the vertical drift field. Due to the low bulk donor concentration of $1.0 \cdot 10^{12}\,\mathrm{cm}^{-3}$, the influence of the dopant ion concentration can also be neglected. The electron mobility $\mu_{\mathrm{n}}(T)$ is thus only a function of T.

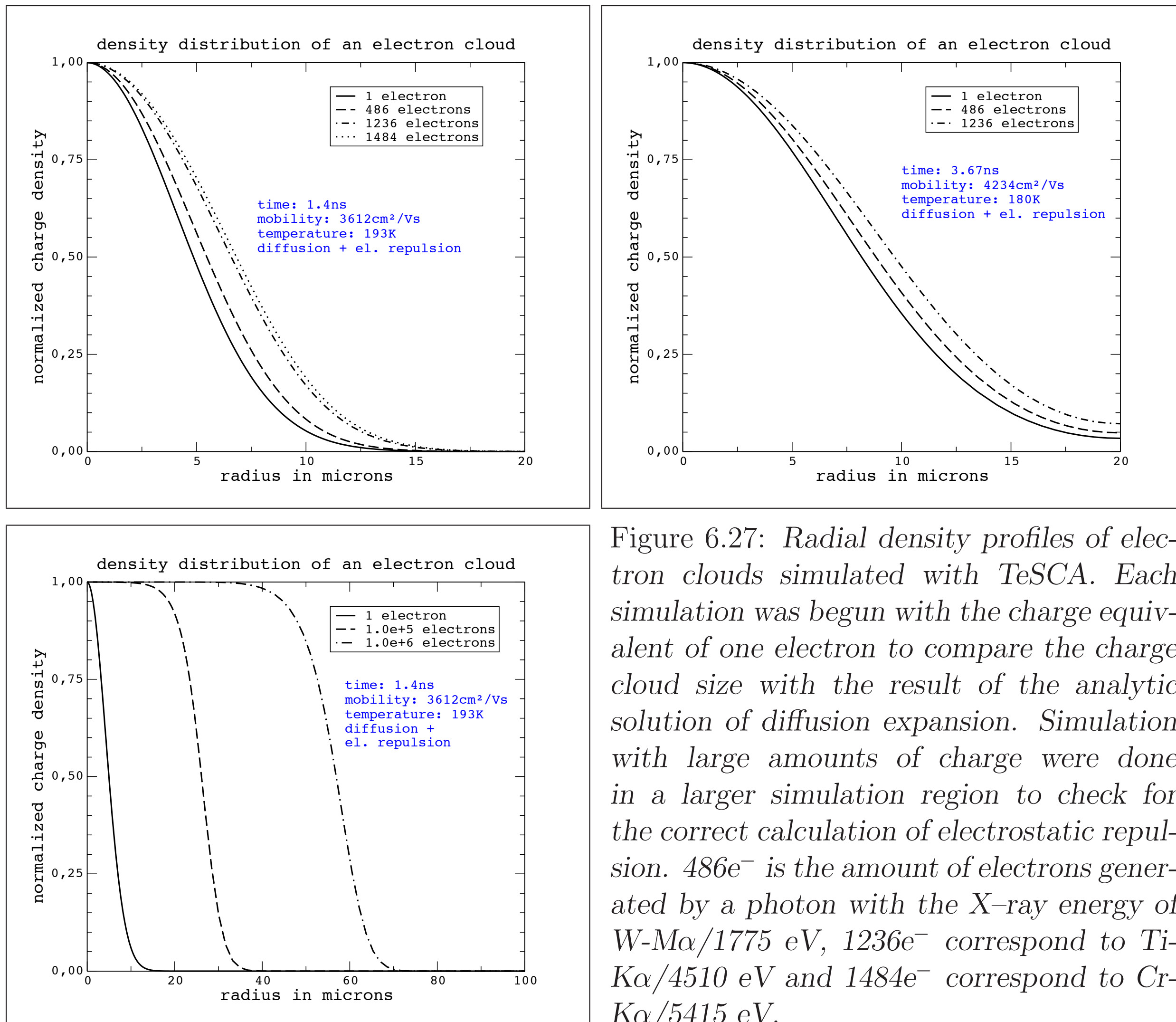

Figure 6.27: *Radial density profiles of electron clouds simulated with TeSCA. Each simulation was begun with the charge equivalent of one electron to compare the charge cloud size with the result of the analytic solution of diffusion expansion. Simulation with large amounts of charge were done in a larger simulation region to check for the correct calculation of electrostatic repulsion. 486e$^-$ is the amount of electrons generated by a photon with the X–ray energy of W-Mα/1775 eV, 1236e$^-$ correspond to Ti-Kα/4510 eV and 1484e$^-$ correspond to Cr-Kα/5415 eV.*

For the interpretation of the results, one has to consider that electrons are treated as a 'continuum' by the TeSCA software. Even the charge equivalent of a single electron can expand due to electrostatic repulsion and diffusion. This facilitates the comparison of the simulation result with the analytical solution for diffusion expansion. Since the amount of charge in a 'single electron cloud' is extremely small, electrostatic repulsion does not contribute to the expansion process. The charge cloud size after a given time interval must equal the analytical result given in section 2.2.1.1, equation 2.11. For the other case that electrostatic repulsion dominates the expansion process, a large number of $1.0 \cdot 10^5$ to $1.0 \cdot 10^5$ electrons is simulated and the resulting distribution is compared to the analytical result of equation 2.14.

Figure 6.26 shows the simulation region with the two–dimensional grid that represents the z– and the radial coordinate of the cylindrical region. At the left side of the domain is a more dense region where the charge is generated. This part needs to be discretized with a

finer grid than the outer parts of the region. At the beginning of the simulation, the charge is concentrated in a small volume in the center of the cylinder. The charge distribution in a small volume is correctly modeled only if the distance of the grid points is smaller than the size of the charge distribution. One starts with a Gaussian charge cloud which has a σ radius of 0.5 µm. This radius corresponds to the size of a charge cloud upon its generation by an X–ray photon. Accordingly the mean grid point distance in the central part of the simulation region was set to 0.15 µm.

time $1.4 \cdot 10^{-9} s$, temperature 193 K, electron mobility μ_{n} 3612 cm^2/Vs				
number of electrons ⟶	$1e^-$	$486e^-$	$1236e^-$	$1484e^-$
sigma–radius of charge cloud ⟶	4.14 µm	4.67 µm	5.58 µm	5.79 µm
analytical sigma–radius result ⟶	4.11 µm			

time $3.67 \cdot 10^{-9} s$, temperature 180 K, electron mobility μ_{n} 4234 cm^2/Vs				
number of electrons ⟶	$1e^-$	$486e^-$	$1236e^-$	
sigma–radius of charge cloud ⟶	6.97 µm	7.51 µm	8.24 µm	
analytical sigma–radius result ⟶	6.95 µm			

time $1.4 \cdot 10^{-9} s$, temperature 193 K, electron mobility μ_{n} 3612 cm^2/Vs				
number of electrons ⟶	$1e^-$	10^5e^-	10^6e^-	
fwhm of charge cloud ⟶	9.94 µm	52.4 µm	113.8 µm	
analytical fwhm result ⟶	9.68 µm	53.0 µm	114.0 µm	

Table 6.1: *Simulated charge cloud radii as either σ values of a Gaussian charge cloud or 1/2 FWHM values of a spherical charge cloud. The values are extracted from the data sets shown in fig. 6.27. In all cases the analytical– and simulation results differ by less than 3% .*

Results of simulations for typical expansion times of $1.4 \cdot 10^{-9}$ s in a pnCCD with 280 µm thickness and a drift distance over 174 µm (linear drift model) and $3.67 \cdot 10^{-9}$ s in a pnCCD with 450 µm thickness and a drift distance over 367 µm (saturation drift model with $v_{\mathrm{e}} = 1.0 \cdot 10^7$ cm/s) are shown in the plots of figure 6.27. The expansion time intervals correspond to the drift time from the photon absorption depth to the insertion depth in the CCD simulations. In the case of the 75 µm pixel CCD with 280 µm substrate thickness, the drift time was calculated with the assumption that no electron drift velocity saturation occurs. In the 51 µm pixel device with 450 µm substrate thickness, a constant drift velocity at the saturation value of $1.0 \cdot 10^7$ cm/s was assumed (section 6.2.2.2). Since the resulting charge distribution has a Gaussian profile for the numbers of signal electrons created by the simulated photon energies of up to 5415 eV, the radius is parameterized with the value of σ. Table 6.1 lists the results for the charge cloud radius, for the case of a charge cloud containing the equivalent of one electron, the result of the analytical simulation is also shown. The simulations with larger electron numbers of $1.0 \cdot 10^5$ or $1.0 \cdot 10^6$ electrons resulted in a homogeneous spherical charge distribution which drops to zero over a distance of 20 µm. The size of this distribution was parameterized as the radius where the charge density drops to one half of the maximum value.

Both extreme cases of very small (1 e^-) or large ($\geq 1.0 \cdot 10^5$ e^-) amounts of charge were handled correctly by the TeSCA simulations. The maximum deviation between the analytical results for the σ radius of the Gaussian in the case of diffusion expansion of one electron is 2.7%. In the case of large amounts of electrons and expansion mainly due to electrostatic repulsion, the deviation of the simulation from the analytical calculation is 1.1%. This proves that both diffusion and electrostatic repulsion are handled correctly by the simulations. It also guarantees that the results for the cases where diffusion and electrostatic repulsion have a similar contribution to the expansion of the electron cloud are reliable. Calculations showed that an expanding charge cloud with up to 1484 electrons has a Gaussian radial profile. The maximum radius error of simulated expanding electron clouds with 486 to 1484 electrons is below 3%.

Chapter 7

Comparison of device simulations and analysis results

The reconstructed charge collection functions which were discussed in chapter 5 represent the final result of the signal charge collection process. Section 6.2.1 describes how profiles of the charge collection function are simulated for the charge transfer and the row/line direction. The difference between the measured and the simulated ccf profiles shows the accuracy of the applied physical and mathematical model. A device simulation which is verified with a comparison to the corresponding mesh measurement data provides the correct values of the electric potential inside of the simulated pnCCD. Furthermore, the charge collection process can be studied at each point in time from the generation of signal electrons to their collection in the storage cells of the pixel structure.

A similar method was applied in the analysis of measurements with front side illumination. A known coverage map of the hole positions and a model of the photon absorption in the structures on the register side were combined in a Monte–Carlo simulation. This simulation delivered a count map model which was compared with the measured count map. The best fit model for each measurement was then determined in order to find the thickness of the insensitive regions in the silicon substrate below the MOS–gates.

7.1 Evaluation of ccf simulations

Overlayed plots of the measured and the simulated charge collection function profiles provide a first, visual evaluation of the correctness of the simulation. In order to obtain values of the difference between data and simulation the simulated ccf was subtracted from the measured ccf and the result was plotted. These plots show the added errors of the measurement and the simulations and thus represent an upper limit of the simulation errors. Profiles of the error function hill model (section 5.2.2, equation 5.3) were fitted both to the simulated ccf profiles and to the profiles of the measured charge collection functions. The best fit models for the ccf profiles deliver the average sigma radius of a Gaussian charge cloud before it is separated at the pixel borders. The appropriate one–dimensional erf–hill

profile is given by:

$$\mathrm{ccf}_{\mathrm{mod}}(x;\sigma;x_0;x_1) = \frac{1}{2}\cdot\left(\mathrm{erf}(x;\sigma;x_0) - \mathrm{erf}(x;\sigma;x_1)\right) \quad (7.1)$$

The error function $\mathrm{erf}(x,\sigma,x_0)$ is defined as:

$$\mathrm{erf}(x;\sigma;x_0) = \frac{2}{\sqrt{\pi}}\cdot\int_0^{(x-x_0)/(\sqrt{2}\sigma)} e^{-t^2}dt \quad (7.2)$$

where σ parameterizes the size of the Gaussian charge cloud and x_0 and x_1 define the pixel borders with typical values of $x_0 = 1.0$ and $x_1 = 2.0$.

The measured two dimensional ccf is projected on the x axis (line direction) or on the y axis (charge transfer direction) in order to obtain one dimensional profiles. The projected values on the x axis or the y axis are averaged along the projection direction. Each projected value with a given coordinate on the x axis of the charge map is the average of the ccf values in the y coordinate range from $y = 1.33$ to $y = 1.66$, i.e. over one third of a pixel. Each projected value with a given coordinate on the y axis of the charge map is the average of the ccf values in the x coordinate range from $x = 1.33$ to $x = 1.66$.

The observed deviations between the measured ccf profiles and the best fit erf profiles are below 2% for all measurements conducted with the pnCCD C10_19_01 and below 5% for all measurements conducted with the pnCCD C11_11_85. These difference values of 2% and 5% are an estimate of the upper limit of the ccf reconstruction error (section 5.2.2) and thus contribute to the difference between the measured and the simulated charge collection functions. For the evaluation of the simulation errors, the expected reconstruction error contribution must be subtracted from the difference between the ccf measurements and the ccf simulations.

7.1.1 75 µm pixel pnCCD

CCD C10_19_01 (compare table 4.1) was simulated for operation temperatures of 153 K and 193 K. The back contact voltage V_{back} is -90 V in all simulations, the register contact voltages are $V_{\mathrm{storage}} = -15\,\mathrm{V}$ and $V_{\mathrm{barrier}} = -21\,\mathrm{V}$. The voltage at the silicon–oxide interface of the MOS–gates was set to -8 V because it was discovered that the potential at the interface is not 0 V, which is the voltage of the aluminum contacts on the oxide layers (section 7.3.1).

At the operation temperatures of 193 K and 153 K the electron mobility μ_{n} according to [28] is 3612 cm^2/Vs (193 K/-80℃) and 6140 cm^2/Vs (153 K/-120℃). These mobility values were used for the calculation of the drift velocity with the linear model $v_{\mathrm{e}^-} = -\mu_{\mathrm{n}}\cdot\mathcal{E}$. The simulation of the signal electron cloud expansion in the first and in the second charge collection simulation step (section 6.2.1) was also performed with $\mu_{\mathrm{n}}(193\,\mathrm{K}) = 3612\,\mathrm{cm}^2/\mathrm{Vs}$ and $\mu_{\mathrm{n}}(153\,\mathrm{K}) = 6140\,\mathrm{cm}^2/\mathrm{Vs}$.

Charge–cloud insertion depths around 100 µm from the register side were chosen for the applied two step simulation approach. In all simulations, the resulting sigma–radii of the

inserted electron clouds are above 4 µm. This is large enough to be correctly sampled by the triangular grid which has a maximum node distance of 1.2 µm along the drift path of the inserted charge cloud.

Plots of typical results of the measured and the simulated ccf profiles are shown in figure 7.1. These plots illustrate the accuracy of the ccf simulations. Plots that show the difference values $\mathrm{ccf}_{\mathrm{meas.}} - \mathrm{ccf}_{\mathrm{sim}}$ for all performed simulations are shown in figure 7.2. An overview of the measurement to simulation comparisons is listed in table 7.1 which shows the best fit σ values of the erf–hill model, eq. 7.1.

The graphs in figure 7.1 indicate the correctness of the simulation approach and the applied physical and mathematical model. The plots of the other comparisons between measurements and simulations are practically identical. A quantitative evaluation of the differences between the measurements and the simulations is facilitated by the plots in fig. 7.2. As expected, the errors given by the difference $\mathrm{ccf}_{\mathrm{meas.}} - \mathrm{ccf}_{\mathrm{sim}}$ have the maximum values near the pixel borders where the signal charge is splitted between neighboring pixels. The maximum error of the simulation is below 6%, the typical error is 4%. This also includes the measurement error, so the actual precision of the simulations is slightly better.

Table 7.1 shows the parameterization of the measurements and simulations with the erf–hill function defined in eq. 7.1. The maximum error is above 10% in three cases. For most simulations the error of σ_{line} and $\sigma_{\mathrm{chn.}}$ is between 4% and 9%. This shows that a parameterization of the charge collection function is needed for a meaningful judgment of the simulation accuracy.

In all ccf simulations, the value of σ_{line} and $\sigma_{\mathrm{chn.}}$ is systematically larger than in the measured profiles. A charge cloud that expands only due to diffusion grows with $\sqrt{t}$ and a charge cloud that expands only due to electrostatic repulsion grows with $\sqrt[3]{t}$. In the case that the value of σ obtained with the simulation is 10% larger than the measured value, this translates into a simulated drift time which is 21% larger (diffusion) or 33% larger (repulsion). A significant source of deviations between the ccf simulations and the measurements is the fact that the simulations are performed in two dimensional domains. Therefore, the observed maximum error of 12.6% of the charge cloud σ needs further investigation. Despite the observed errors of the charge cloud σ, the measured and the simulated ccf profiles are visually nearly identical with a maximum deviation of 6%.

7.1.2 51 µm pixel pnCCD

The 51 µm pixel pnCCD C11_11_85 was operated at a temperature of 180 K / -93℃. Table 4.7 lists the operating voltages of -250 V or -180 V for V_{back}, -15 V for V_{storage} and -19 V for V_{barrier}. The electric potential at the silicon–oxide interface of the MOS–gates was set to -8 V as in the case of the 75 µm pixel CCD simulations, compare section 7.3.1.

The mobility model from [28] delivers a value of $\mu_{\mathrm{n}} = 4234\,\mathrm{cm}^2/\mathrm{Vs}$ for the electron mobility. This value leads to a theoretical electron drift velocity above the saturation velocity of $1.0 \cdot 10^7\mathrm{cm/s}$ due to the drift field strength above $3000\,\mathrm{V/cm}$ in the bulk, compare section 6.2.2.2 and figure 6.25. It was therefore assumed that the electrons drift with the saturation velocity of $1.0 \cdot 10^7\mathrm{cm}/s$, suggested by [25] and [26]. Upon insertion

data type	X–ray line	T	stor. mode	σ_{line}	$\sigma_{\text{chn.}}$	$\Delta\sigma_{\text{line}}$	$\Delta\sigma_{\text{chn.}}$
measurement	W-Mα/1775 eV	193K	double reg.	6.96 µm	6.71 µm	-/-	-/-
simulation	W-Mα/1775 eV	193K	double reg.	7.36 µm	7.21 µm	5.7%	7.5%
measurement	W-Mα/1775 eV	193K	double reg.	6.80 µm	6.69 µm	-/-	-/-
simulation	W-Mα/1775 eV	193K	double reg.	7.36 µm	7.21 µm	8.2%	7.8%
measurement	W-Mα/1775 eV	193K	single reg.	6.93 µm	7.02 µm	-/-	-/-
simulation	W-Mα/1775 eV	193K	single reg.	7.36 µm	7.11 µm	6.3%	1.3%
measurement	W-Mα/1775 eV	193K	single reg.	6.95 µm	7.03 µm	-/-	-/-
simulation	W-Mα/1775 eV	193K	single reg.	7.37 µm	7.11 µm	6.0%	1.1%
measurement	W-Mα/1775 eV	153K	double reg.	6.85 µm	6.54 µm	-/-	-/-
simulation	W-Mα/1775 eV	153K	double reg.	7.23 µm	7.06 µm	5.5%	8.0%
measurement	Ti-Kα/4510 eV	193K	double reg.	7.48 µm	7.29 µm	-/-	-/-
simulation	Ti-Kα/4510 eV	193K	double reg.	8.19 µm	8.07 µm	9.5%	10.7%
measurement	Ti-Kα/4510 eV	193K	double reg.	7.41 µm	7.17 µm	-/-	-/-
simulation	Ti-Kα/4510 eV	193K	double reg.	8.19 µm	8.07 µm	10.5%	12.6%
measurement	Ti-Kα/4510 eV	193K	single reg.	7.49 µm	7.67 µm	-/-	-/-
simulation	Ti-Kα/4510 eV	193K	single reg.	8.19 µm	7.98 µm	9.3%	4.0%
measurement	Ti-Kα/4510 eV	193K	single reg.	7.47 µm	7.67 µm	-/-	-/-
simulation	Ti-Kα/4510 eV	193K	single reg.	8.19 µm	7.98 µm	9.6%	4.0%
measurement	Ti-Kα/4510 eV	193K	single reg.	7.49 µm	7.65 µm	-/-	-/-
simulation	Ti-Kα/4510 eV	193K	single reg.	8.20 µm	7.98 µm	9.5%	4.3%
measurement	Ti-Kα/4510 eV	153K	double reg.	7.42 µm	7.08 µm	-/-	-/-
simulation	Ti-Kα/4510 eV	153K	double reg.	7.94 µm	7.76 µm	7.0%	9.6%
measurement	Cr-Kα/5415 eV	193K	single reg.	7.59 µm	7.64 µm	-/-	-/-
simulation	Cr-Kα/5415 eV	193K	single reg.	8.21 µm	8.06 µm	8.2%	5.5%

Table 7.1: *Overview of the simulation results for the studied 75 µm pixel pnCCD. Each simulation is shown with the associated measurement in the row above and the errors of the resulting σ values of the charge collection function. Note that only in three cases the error of σ_{line} or $\sigma_{\text{chn.}}$ is above 10%.*

data type	X–ray line	T	stor. mode	σ_{line}	$\sigma_{\text{chn.}}$	$\Delta\sigma_{\text{line}}$	$\Delta\sigma_{\text{chn.}}$
measurement	W-Mα/1775 eV	180K	single reg.	9.13 µm	8.57 µm	-/-	-/-
simulation	W-Mα/1775 eV	180K	single reg.	8.85 µm	9.26 µm	-3.2%	8.1%
measurement	W-Mα/1775 eV	180K	double reg.	8.95 µm	8.68 µm	-/-	-/-
simulation	W-Mα/1775 eV	180K	double reg.	8.85 µm	8.77 µm	-1.1%	1.0%
measurement	W-Mα/1775 eV	180K	single reg.	10.48 µm	9.78 µm	-/-	-/-
simulation	W-Mα/1775 eV	180K	single reg.	9.16 µm	9.55 µm	-12.6%	-2.4%
measurement	Ti-Kα/4510 eV	180K	single reg.	9.50 µm	9.02 µm	-/-	-/-
simulation	Ti-Kα/4510 eV	180K	single reg.	9.56 µm	9.98 µm	0.6%	10.6%
measurement	Ti-Kα/4510 eV	180K	double reg.	9.37 µm	9.18 µm	-/-	-/-
simulation	Ti-Kα/4510 eV	180K	double reg.	9.56 µm	9.47 µm	2.0%	3.2%
measurement	Ti-Kα/4510 eV	180K	single reg.	10.85 µm	10.22 µm	-/-	-/-
simulation	Ti-Kα/4510 eV	180K	single reg.	9.81 µm	10.21 µm	-9.6%	-0.1%
measurement	Cr-Kα/5415 eV	180K	single reg.	9.45 µm	9.08 µm	-/-	-/-
simulation	Cr-Kα/5415 eV	180K	single reg.	9.67 µm	10.09 µm	2.3%	11.1%
measurement	Cr-Kα/5415 eV	180K	double reg.	9.39 µm	9.17 µm	-/-	-/-
simulation	Cr-Kα/5415 eV	180K	double reg.	9.67 µm	9.58 µm	3.0%	4.5%
measurement	Cr-Kα/5415 eV	180K	single reg.	10.99 µm	10.33 µm	-/-	-/-
simulation	Cr-Kα/5415 eV	180K	single reg.	9.91 µm	10.30 µm	-9.8%	-0.3%

Table 7.2: *Overview of the simulation results for the studied 51 µm pixel pnCCD. Below each row with measurement results, the results of the associated simulation are shown together with the errors of the ccf σ in line and channel direction. The errors are below 10% in most cases, the highest accuracy of the simulations obtained with double register storage. For simulations with single register storage, the value of σ_{line} is smaller than $\sigma_{\text{chn.}}$, this is in contradiction to the measurement results where the opposite is true.*

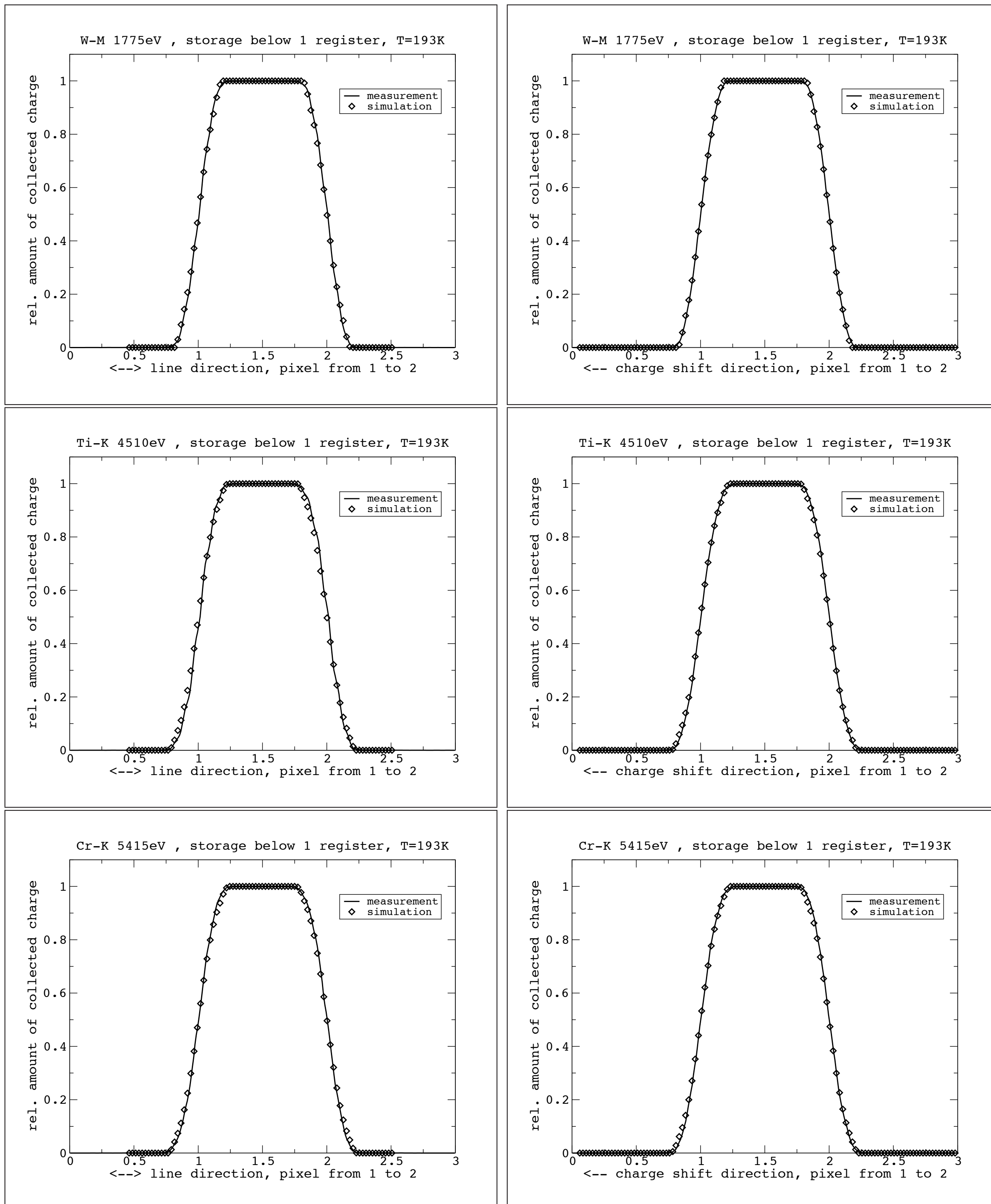

Figure 7.1: *A set of comparison plots showing profiles of the measured charge collection function and the outcome of two dimensional simulations. The accuracy of the simulations is so high that errors are only visible in a close inspection of the plots. Note the similarity of the plots, especially for X–ray energies of 4510 eV and 5415 eV.*

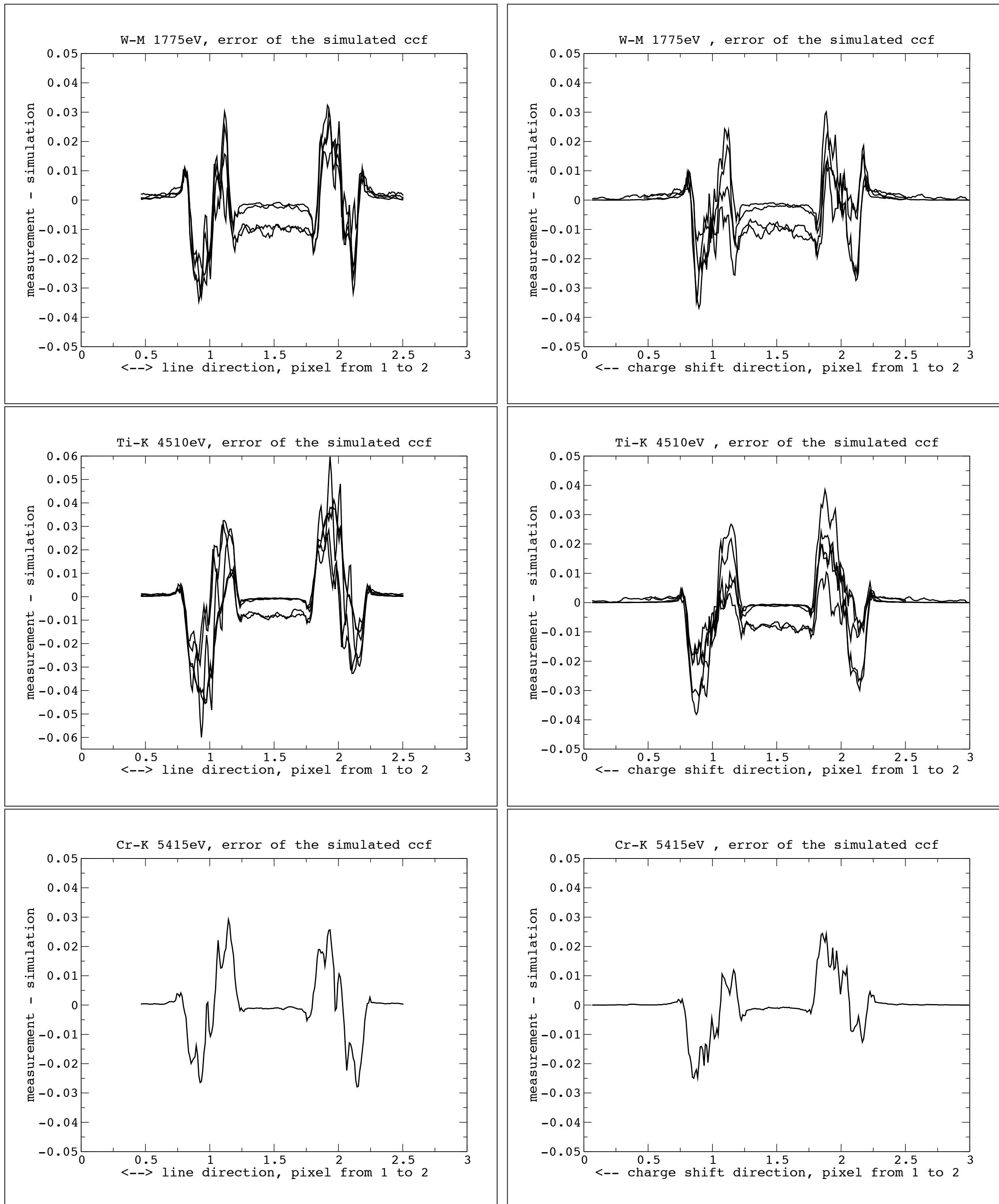

Figure 7.2: *Difference values* $\mathrm{ccf_{meas}} - \mathrm{ccf_{sim}}$ *of all comparisons done with simulations and measurements of a 75 µm pixel pnCCD. No energy dependency of the error values is seen, a maximum error of 4% is only exceeded at 4510 eV in the plot showing the line direction.*

of the charge cloud in the CCD domain, the linear drift velocity model $v_{e^-} = -\mu_n \cdot \mathcal{E}$ was applied by the simulation software TeSCA. For a back contact voltage of $V_{back} = -250\,V$, the insertion depth is 70 µm, in the case of $V_{back} = -250\,V$ the insertion depth is 100 µm, measured as the distance from the register side. The choice of the insertion depth is thus a compromise: The calculated linear drift velocity is above the saturation value over nearly the whole thickness of the pnCCD. However, the charge cloud needs to be inserted in the pnCCD simulation before it is separated by the lateral electric field of the pixel structure on the register side, section 6.2.2.1.

The used drift velocity model thus has a major influence on the results of the ccf simulations of the 51 µm pixel device. The plots in figure 7.3 indicate that the used drift model with a saturation drift velocity of $1.0 \cdot 10^7$cm/s delivers results which are close to the measurements. Figure 7.4 shows the difference values (measured ccf) - (simulated ccf) for all performed simulations. These deviations are are below 9% in the line direction and below 7% in the charge transfer direction. The visible oscillations of the difference values are due to reconstruction errors which result from irregularities in the mesh. Figure 7.4 shows that oscillations of the measurement to data differences occur especially in the ccf profiles which represent the line direction. The amplitude of these reconstruction error artifacts is 2% which results in an effective deviation between the simulated and the measured ccf of 7% and 5% in the line and the transfer direction respectively. A precision of the ccf simulations between 5% and 7% is close to the simulation accuracy observed for 75 µm pixel simulations.

The measured and simulated ccfs were fitted with the error function profile defined in equation 7.1. The fit results support the conclusion that the accuracy of the ccf simulations is in the same range for the 75 µm and 51 µm pixel CCDs. Table 7.2 shows both the values of σ_{line} and $\sigma_{channel}$ and the errors of the σ values of the simulated charge collection functions. In most cases the error of the σ values is below 10%, the maximum error is 12.6%. The simulations with double register storage are more accurate with a maximum error of 4.5%. This shows that the simple assumption of a constant electron drift velocity in the high drift field region is a good approximation to the real drift process. For the numerical calculation of the lateral expansion of a signal electron cloud, the electron mobility value $\mu_n(180\,\mathrm{K}) = 4234\,\mathrm{cm}^2/\mathrm{Vs}$ was used. The observed effective charge cloud sizes can only be explained if the relation $v_{e^-} = -\mu_n \cdot \mathcal{E}$ is invalid in the direction of large drift fields $\mathcal{E}$. Instead, v_{e^-} reaches a saturation value of $1.0 \cdot 10^7$ cm/s. Perpendicular to the drift direction, in the plane of the pixel array, the charge cloud expansion due to diffusion and electrostatic repulsion is not influenced by the drift field strength and the relation $v_{e^-} = -\mu_n \cdot \mathcal{E}$ is valid.

7.1.3 Reconstruction of the photon conversion position

An important aspect of the application of pnCCDs in X–ray astronomy experiments is their use as imaging detectors. The pixel size is usually adapted to the focal plane resolution of the X–ray optics. In experiments requiring different levels of spatial resolution, a method which increases the position resolution beyond the limits of the pixel size makes the existing pnCCD designs more universal. The application of the mesh method for the reconstruction

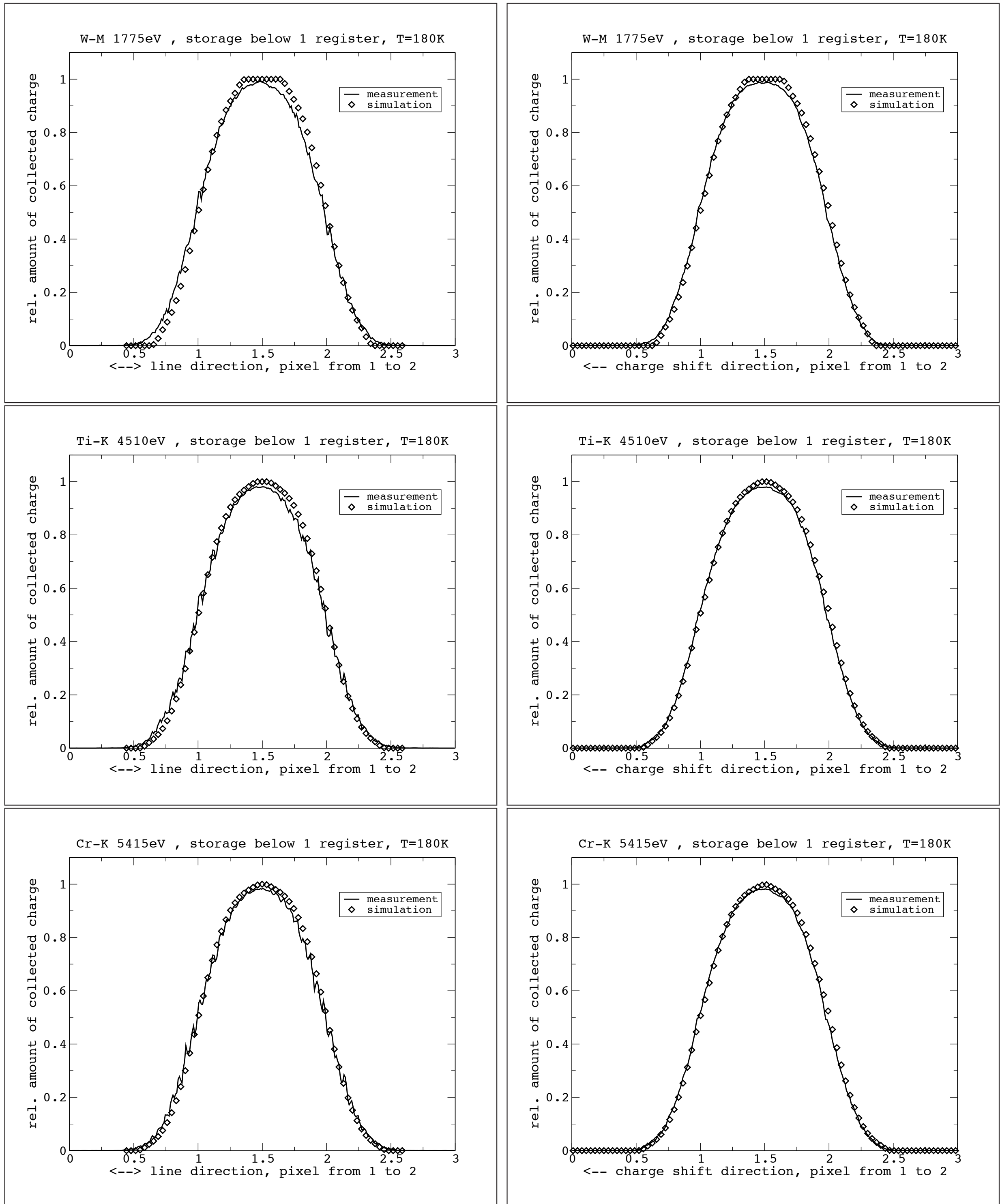

Figure 7.3: *Plots of measured and simulated charge collection functions of the studied 51 µm pixel pnCCD. The measurements and simulations are done with single register storage and a back contact voltage of -180V. As with the 75 µm pixel device, the accuracy is difficult to judge by these plots because the simulations match the measured ccf–curves quite well. Differences are best visible at an energy of 1775 eV.*

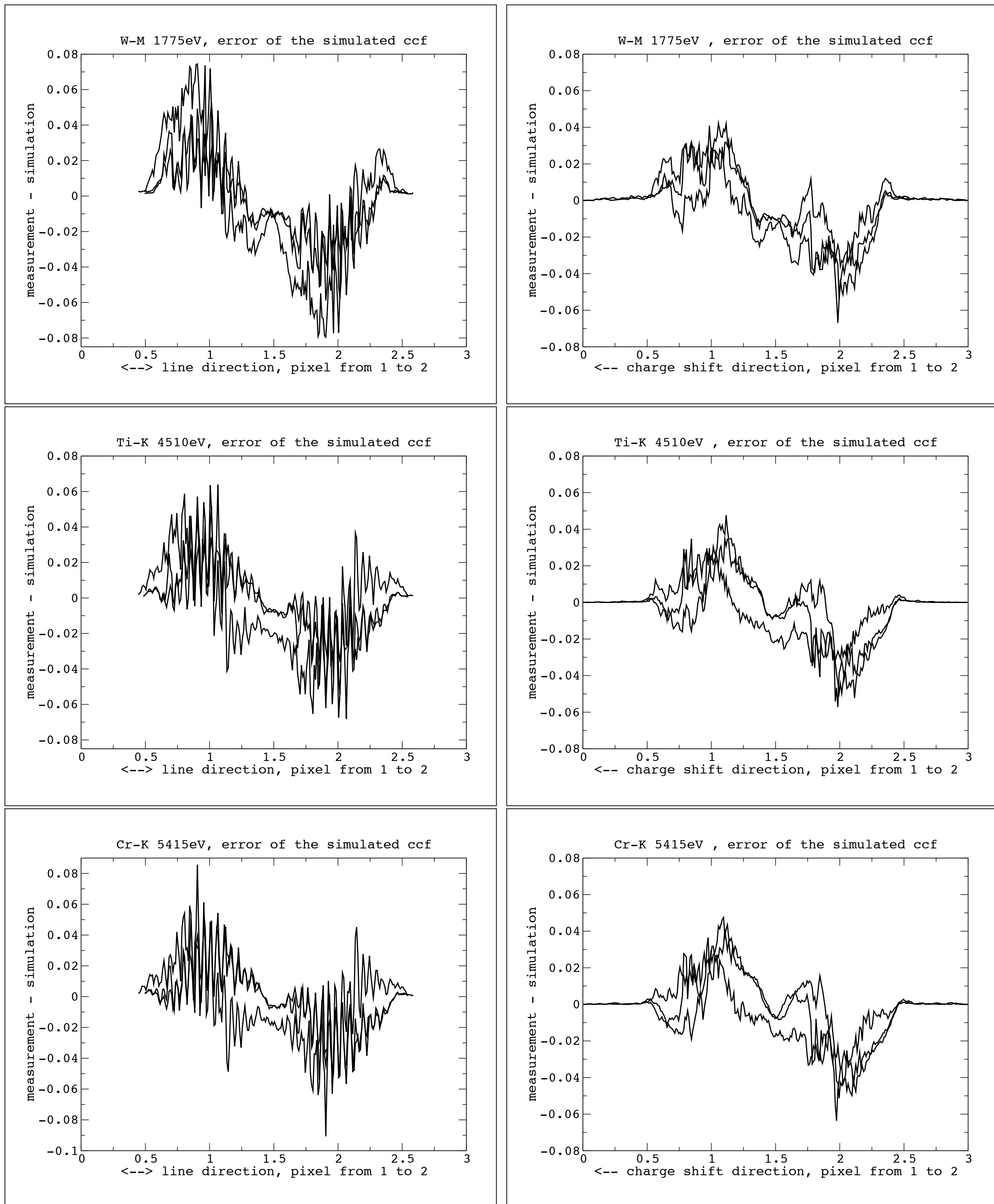

Figure 7.4: *Differences of the measured and simulated ccf for all simulations of a 51 µm pixel pnCCD. The plots are ordered by the used X–ray energies with the lowest at the top. It turns out that the accuracy of the simulated ccf values does not depend on the X–ray energy. The strong oscillations of the error values in the line direction are the result of measurement errors due to deformations of the mesh.*

of X–ray photon conversion positions is discussed for the case of MOS–CCDs as X–ray detectors in [38].

In the case of a double event, the position reconstruction method which is based on ccf measurements with the mesh method works as follows: If a X–ray photon causes a double split event, the pulse heights of the contributing pixels are between 0 and 1. A pulse height value of 1 corresponds to the total pulse height of the pattern. The ratios of the pulse heights in the contributing pixels to the total pulse height of the pattern correspond to values of the charge collection function. A double split event with equal pulse heights of both pixels corresponds to a ccf value of 0.5 and thus an conversion position on the border between the pixels. Pulse height ratios larger than 0.5 correspond to conversion positions inside of a pixel, pulse height ratios smaller than 0.5 correspond to photons with conversion positions in the neighboring pixel. For triple or quad split events, a position reconstruction in both coordinate directions is possible. In order to get the x–coordinate of the photon, the pulse heights of the pixels with identical x–coordinates are summed up. This results in two pulse height values with neighboring x–coordinate values. The x–coordinate of the photon is then calculated in the same way as for left–right double split pattern. In the y–direction, the pulse heights of the pixels with identical y–coordinates are summed up. The ccf value in the y–direction is calculated as the ratio of the summed up pulse heights to the total pulse height. The obtained ccf value is then identified with the y–coordinate of the photon.

The position reconstruction model for a given photon energy, temperature and for specific contact voltages requires the charge collection function profiles in the line and the channel direction. Instead of mesh measurements, numerical device simulations can be performed in order to obtain the required ccf profiles. Here, both mesh measurements and ccf simulations for the given operating conditions are available for two different pnCCDs. The position reconstruction results which are obtained with the measured and simulated ccfs are compared in order to translate ccf simulation errors into position reconstruction errors. Division of the error of the simulated ccf by the slope of the measured ccf results in a distance on the x axis. This distance is the position reconstruction error. The derivative of eq. 7.1 gives the slope of the charge collection function:

$$\frac{d\,\mathrm{ccf}_{\mathrm{mod}}(x;\sigma;x_0;x_1)}{dx} = \frac{1}{\sqrt{2\pi}\cdot\sigma}\cdot\left(e^{-(x-x_0)^2/(2\sigma^2)} - e^{-(x-x_1)^2/(2\sigma^2)}\right) \tag{7.3}$$

Where σ is the measured average sigma–radius of a charge cloud and x_0 and x_1 are the pixel borders where $\mathrm{erf}_{\mathrm{mod}}$ has the value 0.5. We look at equation 7.3 for $x = x_0$. Then the second part with x_1 has a value close to zero and can be neglected. The slope of the error function hill at $x = x_0$ is thus:

$$\frac{d\,\mathrm{ccf}(\sigma;x=x_0)}{dx} = \frac{1}{\sqrt{2\pi}\cdot\sigma} \tag{7.4}$$

At $x = x_1$ the slope is the same but with the opposite sign. With this slope, errors of the simulated ccf values can be transformed into position reconstruction errors on the x–axis.

Equation 7.4 can be modified to obtain the conversion formula:

$$\Delta x(\sigma; x = x_0) = \sqrt{2\pi} \cdot \sigma \cdot \Delta\mathrm{ccf}(\sigma; x = x_0) \tag{7.5}$$

This formula, tables 7.1 and 7.2 and figures 7.2 and 7.4 provide the information to calculate the position reconstruction errors which result from the errors of the ccf simulations.

The larger the ccf error Δccf or the value of σ, the larger the position reconstruction error Δx. Typical values of σ are around 7.5 µm for the 75 µm pixel device, the maximum σ is 8.2 µm. The error of the simulated ccf is around 3.5% for this pixel size, with a maximum value of 6%. Combining these values gives a typical position reconstruction error of 0.7 µm and a maximum error of 1.3 µm. Higher position reconstruction errors are expected for the studied 51 µm pixel pnCCD due to the larger σ values. Typical values of σ for the 51 µm pixel CCD are 9.5 µm and the maximum σ is 11 µm. At the same time, the errors of the simulated ccf are around 4% with a maximum value of 9%. The result is a larger position reconstruction error of 1 µm in most cases, the maximum expected error is 2.5 µm.

The position reconstruction error values provide a direct interpretation of the accuracy of the ccf simulations. The maximum relative position reconstruction error is 5% in the case of the CCD with 51 µm pixels. However, in most cases the position reconstruction error is 2% of the pixel side length. In the case of simulations of the 75 µm pixel pnCCD, a reconstruction accuracy better than 1.7% of the pixel side length is possible even in the worst case. In the case of a position reconstruction error of 5%, the position resolution is 1/20th of a pixel in the regions where split events occur.

If the position reconstruction is performed with the measured ccf, the reconstruction error is due to the signal noise σ_{noise}. In order to obtain the resulting position reconstruction error, the value Δccf in equation 7.5 is replaced with $\Delta\mathrm{ccf}(\sigma_{\mathrm{noise}})$. $\Delta\mathrm{ccf}(\sigma_{\mathrm{noise}})$ is the measurement error given by the ratio of the noise contribution of all pixel signals in an X–ray event to the total signal height. In the case of a quad event, Δccf is approximated by $\Delta\mathrm{ccf}(\sigma_{\mathrm{noise}}) = \sqrt{4} \cdot \sigma_{\mathrm{noise,mean}}/U_{\mathrm{photon}}[e^-]$ where $\sigma_{\mathrm{noise,mean}}$ is the mean noise of all pixels and $U_{\mathrm{photon}}[e^-]$ is the total signal pulse height in units of electrons. Current pnCCDs have a mean noise of less than $3\,e^-$ ENC. For a photon energy of 1 keV and a charge cloud σ of 11 µm, this translates in a reconstruction error Δx of 0.6 µm. At 5 keV and the same charge cloud size and noise, Δx has decreased to 0.12 µm. A position reconstruction accuracy of better than 1 µm can thus be achieved if the measured ccf is used as the relation of split ratios to photon conversion positions.

For a device thickness of 450 µm and a back contact voltage of -250 V, the charge cloud radius σ at 4.5 keV has an average value of 9.1 µm (table 5.8). If the pixel side length is 36 µm and the charge cloud size is 9 µm, a ccf value of 0.91 results if a photon is converted in the middle of a pixel. In this case 9% of the signal charge are distributed outside of the pixel. If the charge is evenly distributed over the eight pixels surrounding the central pixel, each pixel obtains more than 1% of the signal charge. At a photon energy of 5 keV and a noise σ of $3\,e^-$ ENC, the $4 \cdot \sigma_{\mathrm{noise}}$ detection threshold is 0.9%. This means each pixel has an event hit. Photons which are converted at other positions than the pixel middle deposit even more than 9% of the signal charge in the neighboring pixels. All photons thus

generate split events where the conversion position can be reconstructed with an accuracy of 1 µm.

7.2 Separation process of a charge cloud

In section 5.2.2 the 'error function hill' model of the charge collection function is introduced. This model is a good approximation to the charge collection functions of the evaluated pnCCDs with a pixel size of 75 µm and 51 µm. The basic assumption which leads to this ccf model is that the signal electrons expand in a charge cloud with a Gaussian radial profile while they drift towards the register side of a pnCCD. In a given distance from the register side, called the 'separation depth', charge clouds which arrive near the pixel borders are distributed over the neighboring pixels. Integration of the charge density over the depth coordinate z gives a surface charge density which corresponds to the projection of the charge cloud on the pixel array. The amount of electrons collected in a pixel is given by the integration of this surface charge density over the area of the pixel. Only if a photon has an conversion position close to the middle of a pixel, all of the generated signal electrons are collected in a single pixel.

The mesh experiment and the reconstructed charge collection function values represent the final distribution of the signal electrons after a charge cloud is separated at the pixel borders. In order to obtain a time resolved representation of the charge collection process in a pnCCD, a numerical device simulation is needed. The correctness of the device simulations presented here was evaluated in the comparison of the measured ccf profiles with the simulated ccf profiles. The verified device simulations provide the correct values of the charge density in the CCD at each moment from the generation of the signal charge to its final collection in the storage cells.

An evaluation of the dynamic behavior of the signal charge density during the charge collection process identifies the depth where a charge cloud begins to be separated by the pixel borders. Knowledge of this depth, which is the separation depth mentioned above, allows for the creation of a simple charge collection model in pnCCDs. In the simplified model, no numerical device simulation of a pnCCD is needed. It is based on the assumption that a signal electron cloud drifts to the front side and expands due to electrostatic repulsion and diffusion. When the charge cloud reaches the separation depth, it is splitted at the pixel borders.

Figures 7.5 and 7.6 show plots of the charge density in a region of 65x65 µm^2 inside of a 75 µm pixel CCD and a 51 µm pixel CCD respectively. Each column of plots is extracted from a simulation where an X–ray photon with an energy of 4510 eV creates the signal electrons exactly on the border between two pixels. The y coordinate axis shows the depth from the register side, the x coordinate axis shows the position in the line direction (the left hand column) or in the charge transfer direction (the middle and right hand columns). The middle of the x–axis corresponds to the geometrical pixel border which is either a p–doped channel stop, the barrier register (double register storage) or a MOS–gate (single register storage). The time interval between the plots in figure 7.5 is 0.2 ns. In figure 7.6,

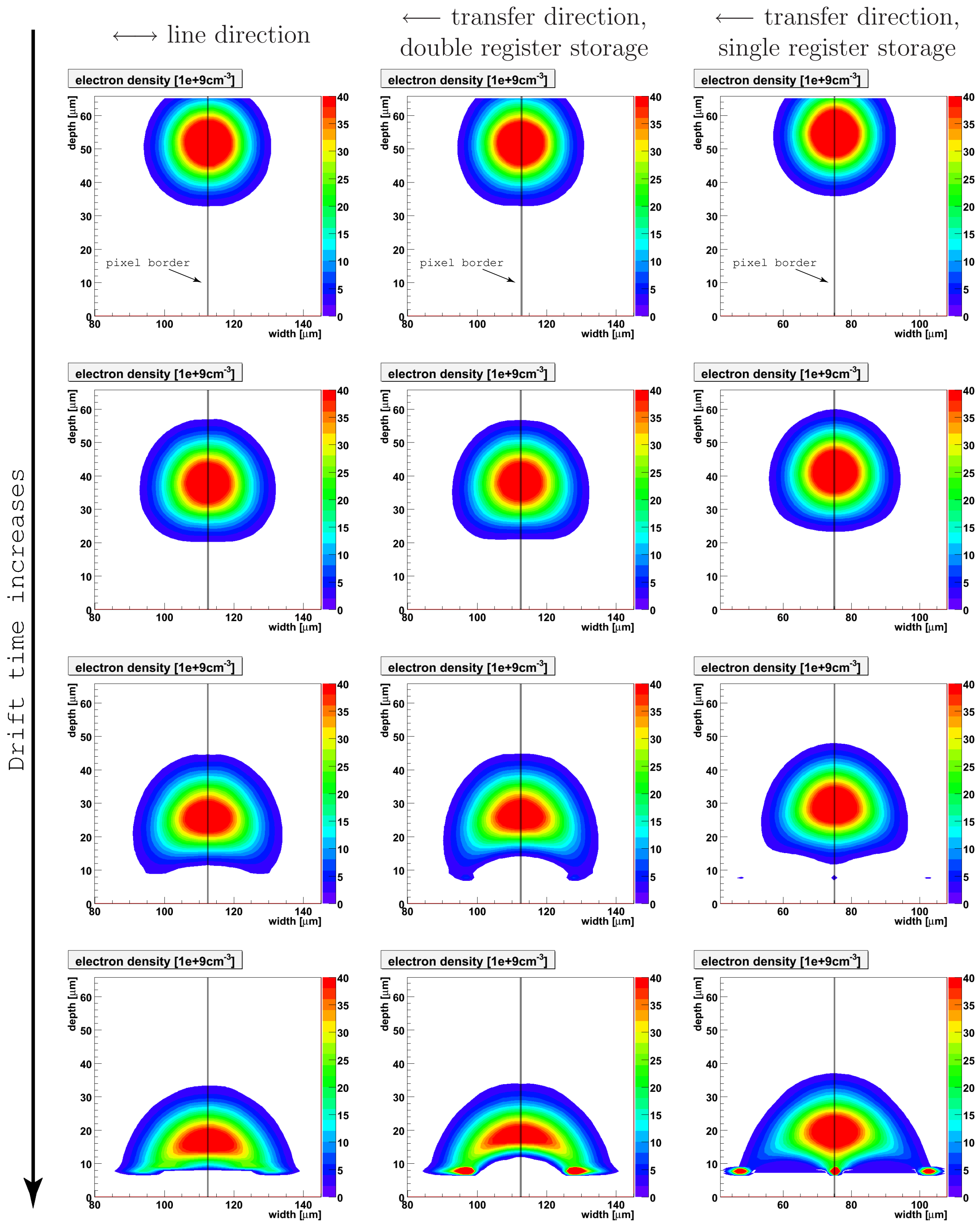

Figure 7.5: *Plots of a charge cloud in different depths from the front side of the simulated 75 µm pixel pnCCD. The plots are arranged in columns showing the drift of the charge cloud towards the register side. The X–ray photon energy is Ti–Kα/4510 eV in all simulations.*

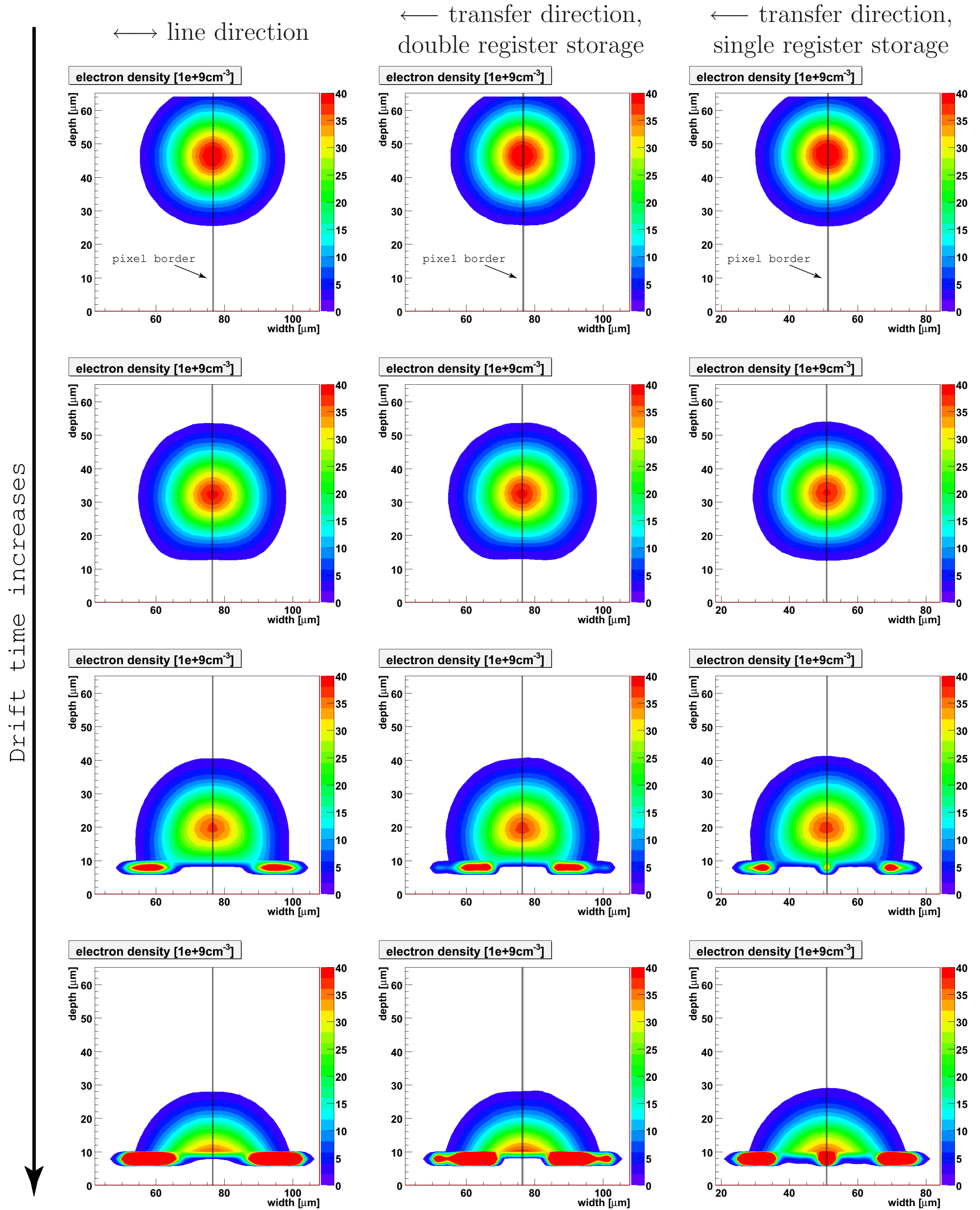

Figure 7.6: *Plots of a charge cloud in different depths from the front side of the simulated 51 µm pixel pnCCD. As in figure 7.5, the plots in each column show the drift of a charge cloud towards the register side. The photon energy is 4510 eV.*

the time step between the upper two plots of each column is 0.15 ns while the last two time steps between the lower three plots have a length of 0.1 ns.

In the depth where a deformation of the signal electron cloud at the side facing the x axis becomes visible, the lateral drift field begins to split the charge cloud at the pixel border. This is the separation depth where the lateral drift field is stronger than electrostatic repulsion and diffusion. If the lateral drift field becomes stronger than the radial expansion process of a charge cloud, radial expansion is stopped and the charge cloud can be considered as being 'cut' at the pixel border. This effect is visible both in figure 7.5 and 7.6. In the case of the 75 µm pixel simulations, the separation starts in a depth of 25 µm from the register structure. This is one third the width of a pixel or the width of one shift register, including the MOS–gate. In this depth the lower border of the former radial symmetric charge cloud begins to be distorted. The simulations of a 51 µm pixel device presented in figure 7.6 show the same effect. In all three simulations, the separation begins in a depth of 15 µm from the register side which is slightly less than one third of the pixel size.

The charge collection process in a pnCCD can thus be simplified as the separation of a signal electron cloud in a depth which is equal to one third of the pixel side length, measured from the register side. The size of the charge cloud in the separation depth is defined by the drift time, the electron mobility, the number of signal electrons and by the temperature. The drift time can be calculated if the back contact and the register contact voltages, the bulk acceptor concentration and the electron drift velocity as a function of the electric field are known. The electric field in the bulk can be calculated with the analytical solution presented in section 2.2, equations 2.5 and 2.6. Therefore, the simplified charge collection model does not require a pnCCD simulation in order to deliver the charge collection function at a given set of operation parameters.

7.3 Photon absorption in the front-side structure

A reverse mounted frame store pnCCD with 75 µm pixels was prepared for mesh measurements with illumination from the register side (CCD C10_19_16 in table 4.1). The idea behind this experiment is that with the mesh–method, not only the distribution of signal charges in a pixel can be measured but also the absorption of photons in the layers on the register side. An application of this method to MOS–CCDs is presented in [53]. The qualitative interpretation of the measurement results for a pnCCD is presented in section 5.3.2.

A cut of the surface structure of the used pnCCD is shown in figure 5.23 and on the left hand side of figure 7.9. Both the thicknesses and the materials of the surface layers are defined in the device design data. Measurements of the dimensions and the thicknesses of the layers are performed during the production process in order to control if the design data is correctly reproduced. These measurements deliver the actual lateral dimensions and thicknesses of the structures on the register side. Therefore, the analysis of the mesh measurements with front side illumination focuses on the structure of the electric potential

below the MOS–gates and on the region directly below the p+ register contacts.

7.3.1 Electric potential at the front side

Figures 6.13 to 6.12 in section 6.1.1 show the values of the electric potential below the MOS–gates for a voltage of 0 V of the electron layer below the oxide–silicon interface.

The electron layer below the MOS–gates is capacitively coupled to the aluminum contacts of the MOS–gates and to the two neighboring p+ register contacts. Due to the negative voltage of the register contacts, a slightly negative potential $V_{\mathrm{el.layer}}$ of the electron layer due to capacitive coupling is expected. As a first estimate, it was assumed that $V_{\mathrm{el.layer}}$ is -8 V, slightly less than one half of the average register voltage of -20 V to -22 V where $V_{\mathrm{storage}} = -17\,\mathrm{V}$ and $V_{\mathrm{barrier}} = -25\,\mathrm{V}$. Device simulations with both a potential of 0 V and -8 V in the electron layer were performed. The comparison of the simulation results shows the influence of the interface potential on the potential values in the bulk below the MOS–gates. Even if the voltage of the electron layer is -8 V, the MOS–gates still insulate the neighboring register contacts. This is visible in the plots shown in figure 7.7 which show the region below the MOS–gates for double register storage and a MOS–gate voltage of -8V. The saddle point is the maximum of a potential barrier of 5.2 V between the registers and the maximum of a potential barrier of 2.5 V or more between the transfer channel and the MOS–gates.

Figure 7.8 shows two plots of the electric potential below the middle of the MOS–gates as a function of the depth. The saddle point of the potential is identical to the local potential minimum in the plots. This minimum is in a depth of 2 µm to 4 µm below the oxide–silicon interface at 0 µm. If signal electrons are created in a depth which is closer to the surface than the saddle point of the electric potential, they drift to the silicon–oxide interface. Once the electrons are collected at the MOS–gate, the photon signal is lost. Therefore the region below the MOS–gates from the surface to the depth z_{MOS} is an insensitive region of the device. The value of z_{MOS} is thus given by the depth of the saddle point of the electric potential. The width of the insensitive region is equal to the width of the oxide layer. In the absorption model of the register side, this region is approximated as a rectangle with the width of the gate oxide and the depth of the local potential maximum for electrons.

The location of the minimum of the electric potential which is plotted in figure 7.8 depends both on the voltage of the neighboring register contacts and on the voltage of the electron layer below the oxide–silicon interface. The distance z_{MOS} of the electric potential minimum from the front side decreases if the register voltage is increased to more positive values. If the voltage of the electron layer is decreased to more negative values, the electric potential minimum moves closer to the front side. While the voltages of the register contacts are defined by the register voltage supplies, the voltage of the electron layer can differ from the MOS–gate supply. However, the value of this voltage can be related to the depth z_{MOS} of the saddle point which is predicted by the device simulations. The value of z_{MOS} is given by the absorption model which correctly reproduces the measured absorption of photons in the front side structures. Mesh measurements with front side illumination thus facilitate the determination of the voltage of the electron layer below the MOS–gates.

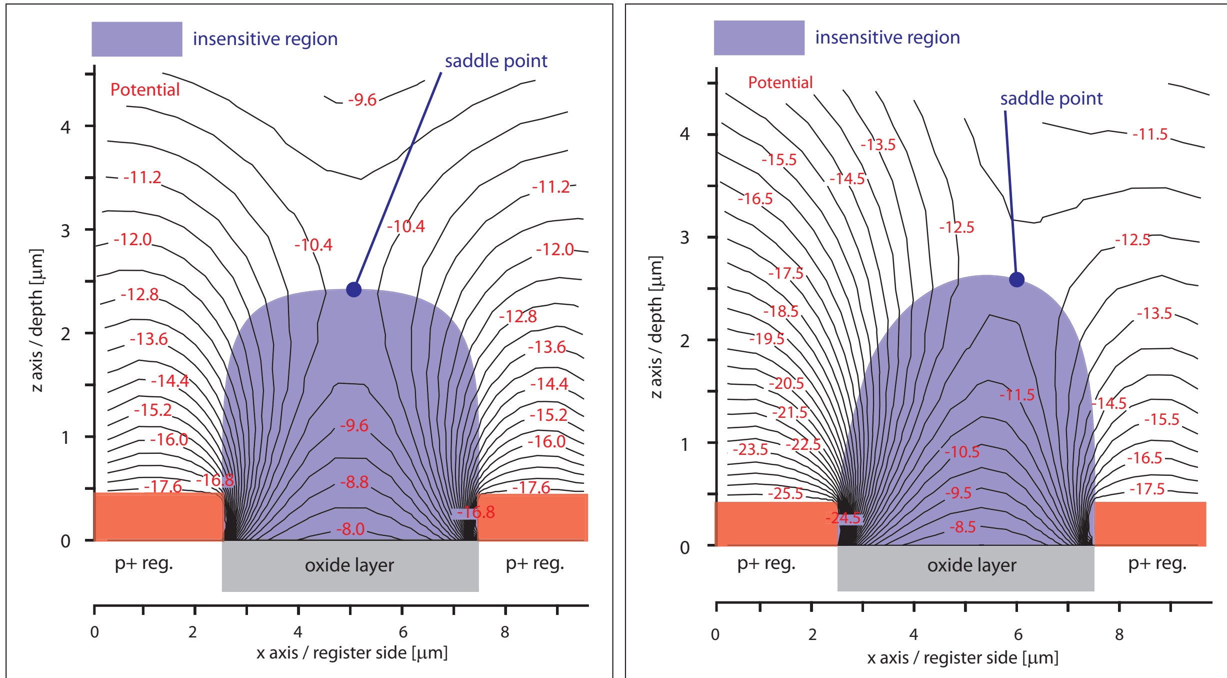

Figure 7.7: *Electric potential below the MOS–gates of the 75 µm pixel device in a region 10 µm wide and 5 µm deep. Both plots are for operation in double register storage mode with a MOS–gate voltage of -8V. In the left plot the potential between the two storage registers is shown. The right plot shows the electric potential between a barrier and a storage register. Note that despite the negative voltage, the neighboring registers are still insulated from each other and that electrons cannot be exchanged between the transfer channel and the electron layer below the oxide–silicon interface.*

The contour plots of fig. 7.7 show the field free region in the undepleted part of the p+ register implants. The absence of a drift field is indicated by the regions free of contour lines left and right to the MOS–gates. In the region where the p+ contacts are not depleted, signal electrons recombine with the surplus of free holes. Numerical device simulations (figure 7.7) predict a thickness of 0.4 µm for this insensitive region.

7.3.1.1 Absorption model of the register structure

An absorption model of the front side structure is needed for the simulation of count maps. If the correct absorption model is used for the simulations, the intensity profiles of the measured count maps for each photon energy are reproduced. Since the geometrical structure of the surface layers is known, the absorption model consists of the fixed layer structure at the surface and two types of structures with an unknown insensitive thickness. As shown in the discussion of the simulation results in section 6.1.1 and 7.3.1 these insensitive regions of the silicon bulk are located below the MOS–gates and in the p+ register implants. The measured absorption of photons in these layers can be transformed into the values of their

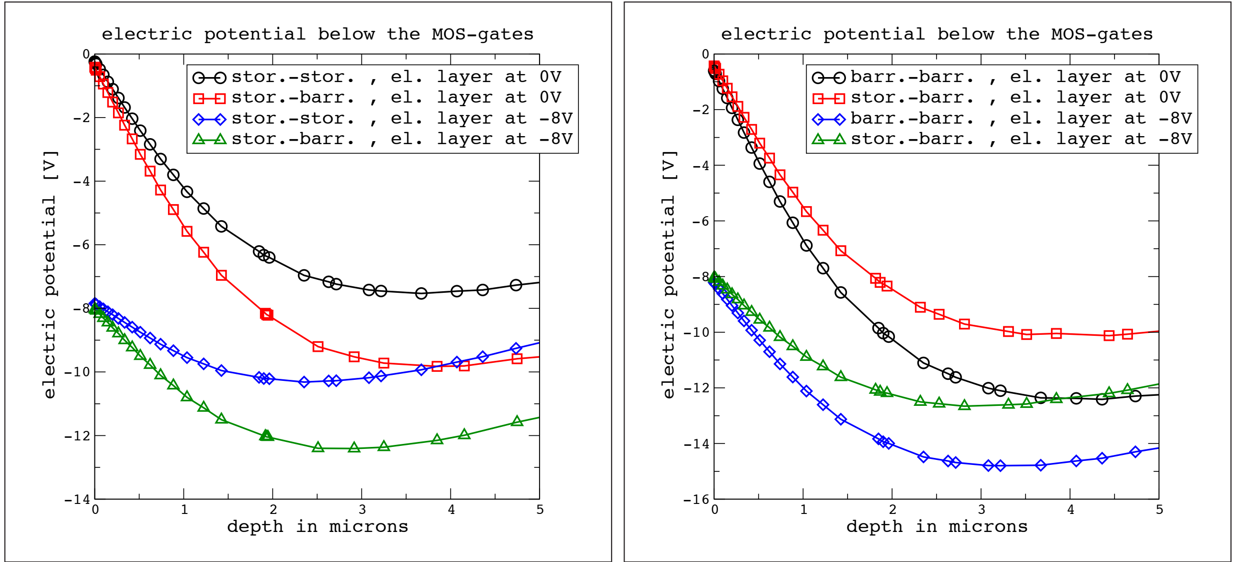

Figure 7.8: *Plots of the electric potential up to a depth of 5 µm below the middle of the MOS–gates. The left plot shows the potential in the case of double register storage, the case of single register storage is shown in the right plot. The depth where the potential is most negative is the saddle point also visible in the plots of figure 7.7. Electrons created by photons absorbed below this depth drift to the oxide–silicon interface at the front side. Electrons created beyond this depth are collected in the potential minima of the neighboring pixels. The saddle point moves towards the front surface if the voltage of the electron layer below the oxide–silicon interface becomes more negative.*

thickness z_{MOS} and $z_{\mathrm{p+}}$. The value of z_{MOS} is related to the surface potential below the MOS–gates and the value of $z_{\mathrm{p+}}$ is related to the acceptor concentration profile in the register implants. The correct values of z_{MOS} and $z_{\mathrm{p+}}$ are found if the absorption model is adjusted such that the measured intensity profiles of the count maps are reproduced by the simulations.

In the first step of the creation of the absorption model for a given X–ray photon energy, the transmission of photons through the insensitive regions is calculated. The transmission of radiation through a layer with the linear mass absorption coefficient $4\pi\beta/\lambda$ and the thickness w is given by equation 3.2, repeated here in a modified form as a transmission coefficient:

$$\theta_{\mathrm{abs}} = 1 - \exp(-\frac{4\pi\beta}{\lambda} \cdot w) = 1 - \exp(-\frac{4\pi\beta \cdot E \cdot 1.602 \cdot 10^{-19}}{h \cdot c} \cdot w) = \theta_{\mathrm{abs}}(E; \beta; w) \quad (7.6)$$

where E is the X–ray photon energy in eV, β is a material constant, λ is the wavelength and w the thickness of the layer. Stacked layers of different materials and thicknesses have the transmission:

$$\theta_{\mathrm{abs}}(E; \beta_1; \beta_2; \ldots; \beta_n; w_1; w_2; \ldots; w_n) = \\ \theta_{\mathrm{abs}}(E; \beta_1; w_1) \cdot \theta_{\mathrm{abs}}(E; \beta_2; w_2) \cdot \ldots \cdot \theta_{\mathrm{abs}}(E; \beta_n; w_n) \quad (7.7)$$

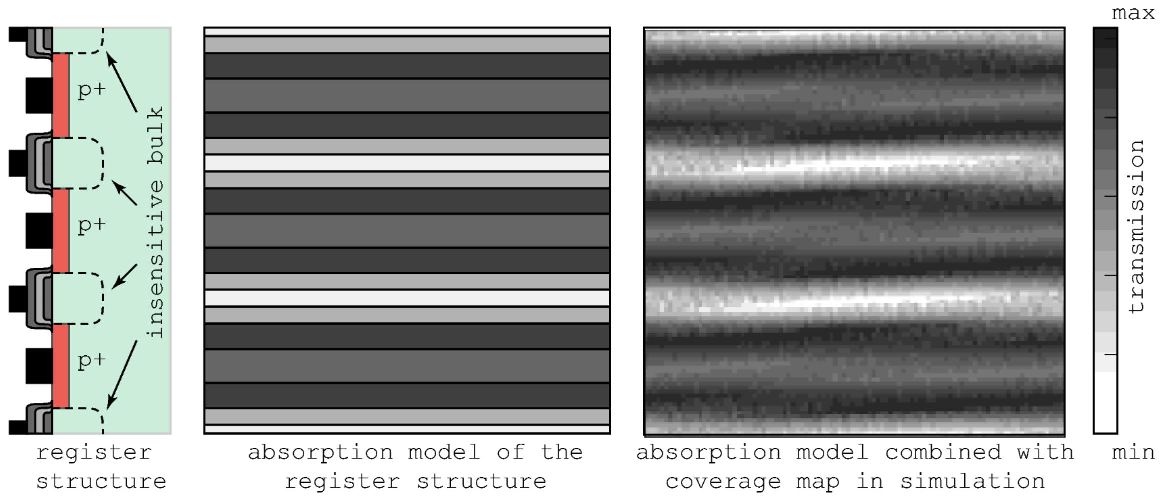

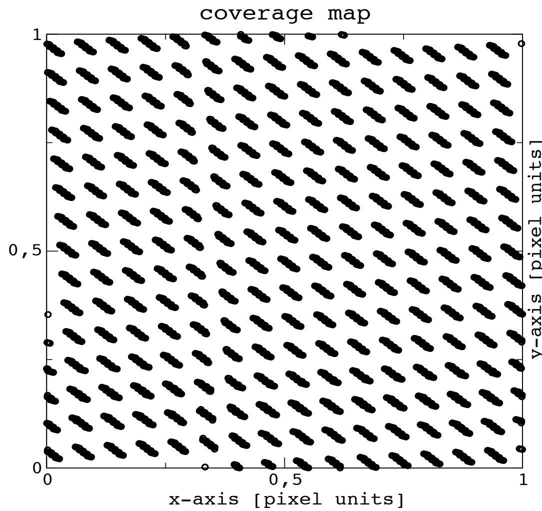

Figure 7.9: *Principle of the simulation of measurements with front side illumination. On the left hand side in the upper figure, the register structure of a pixel is shown as a cut along the transfer direction. To the right of the structure is a calculated transmission map that results from the geometry, material data and the photon absorption at the given energy. In the bottom left is the coverage map of a Cu-Lα/930 eV measurement. The transmission map combined with the coverage map in a Monte Carlo simulation delivers the count map shown on the right hand side in the upper drawing.*

This way the transmission of each layer is calculated with the known energy, thickness and material. Depending on the number and type of different layers for a given position along the transfer direction, the total transmission at this position is given by the multiplication of all transmission coefficients.

The absorption model is applied in a Monte–Carlo simulation in order to create a count map which represents the absorption model. In the Monte–Carlo simulation, the irregular illumination by the mesh holes is reproduced, compare figure 7.9. The illumination by the mesh holes is reconstructed from the hole coverage maps of the respective mesh measurements. At a given hole position in the coverage map, the photon conversion positions are distributed evenly in the area which is illuminated by the mesh hole. The transmission probability for each photon is proportional to the combined transmission coefficient $\theta_{\text{abs}}(E; \beta_1; \beta_2; \ldots; \beta_n; w_1; w_2; \ldots; w_n)$ of all insensitive layers below the conversion position. A large number of approximately 10^6 photons which pass through the mesh holes is gener-

ated in the Monte–Carlo simulation. For each photon, the transmission coefficient defines the detection probability. A random number in the range from 0 to 1 is then compared to the value of θ_{abs}. If the random number is smaller or equal than θ_{abs}, the photon detection is entered in the simulated count map. Finally, the simulated count map values are compared to the values of the measured count map.

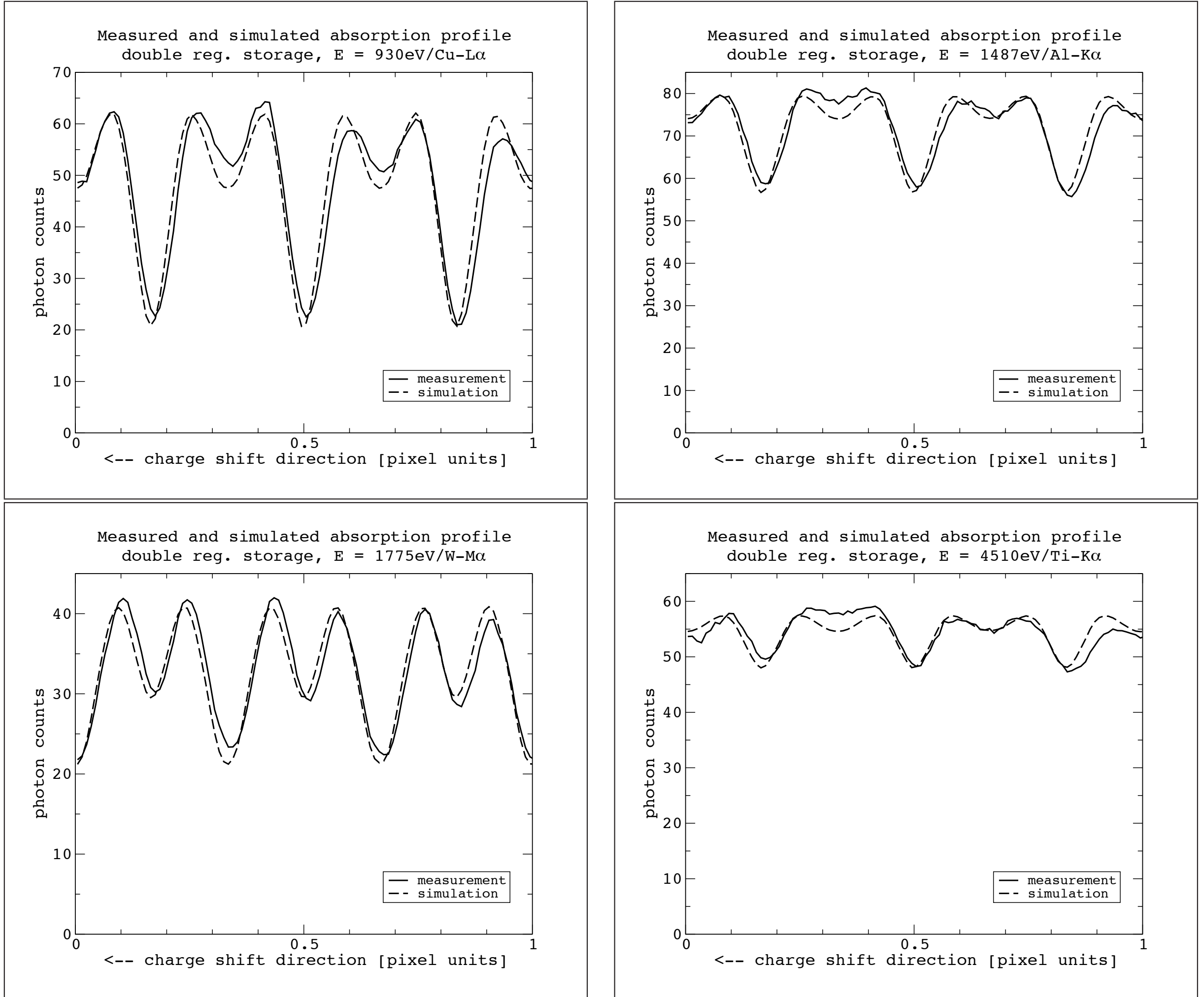

Figure 7.10: *Measured and simulated count profiles of the front side illuminated 75 µm pixel pnCCD. For higher X–ray energies, the contrast of the count rate profiles gets smaller. This directly shows that at higher energies, the front side measurement analysis is less sensitive to thickness variations of insensitive layers. Due to the lower contrast, fitting an absorption model to a count rate profile measured with a high X–ray photon energy is more sensitive to statistical uncertainties of the measured count rate.*

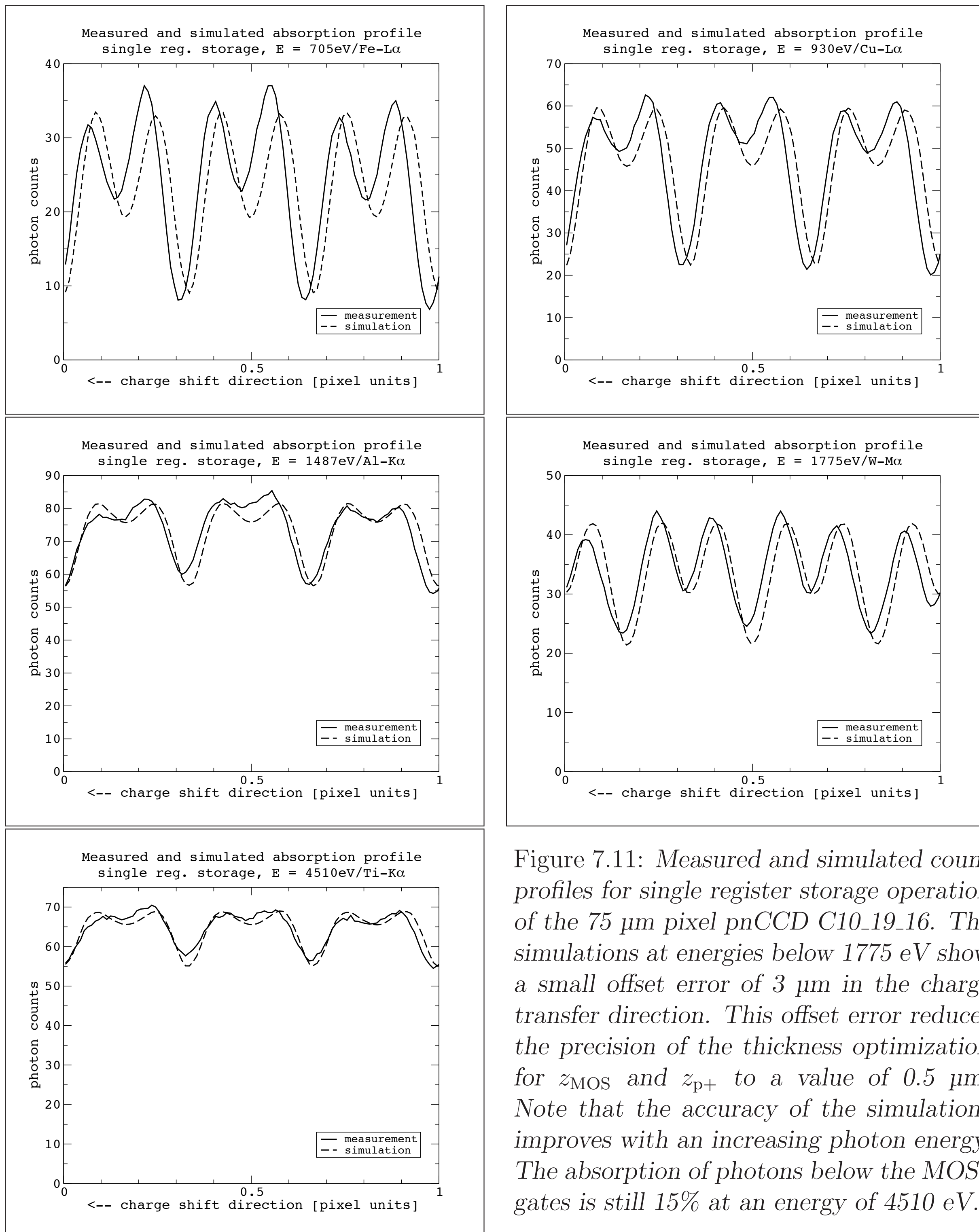

Figure 7.11: *Measured and simulated count profiles for single register storage operation of the 75 µm pixel pnCCD C10_19_16. The simulations at energies below 1775 eV show a small offset error of 3 µm in the charge transfer direction. This offset error reduces the precision of the thickness optimization for* z_{MOS} *and* $z_{\mathrm{p+}}$ *to a value of 0.5 µm. Note that the accuracy of the simulations improves with an increasing photon energy. The absorption of photons below the MOS–gates is still 15% at an energy of 4510 eV.*

7.3.2 Best fit parameters for the absorption model

In order to find the values of z_{MOS} and $z_{\mathrm{p+}}$, a set of absorption models was created. The parameter range of z_{MOS} is 2.5 µm to 4.5 µm and a step size of 0.25 µm was chosen. This step size is one half of the expected precision of the parameter optimization. The thickness $z_{\mathrm{p+}}$ of the insensitive layer in the p+ registers was set at 0.3 µm and 0.4 µm in two different simulation runs. The smallest squared sum of the differences between the measured and the simulated count map profiles indicates the correct values z_{MOS} and $z_{\mathrm{p+}}$.

The plots in figure 7.10 and in figure 7.11 show the measured count map profiles and the simulated count map profiles for double register storage and single register storage respectively. All simulated profiles which are plotted represent examples for the best fit values of z_{MOS}. In these plots, $z_{\mathrm{p+}}$ has a value of 0.3 µm in the case of double register storage and 0.4 µm in the case of single register storage. The accuracy of the simulated count map profiles is better than 10%. The range of the results for of z_{MOS} is maximally 1.0 µm for a given storage mode, all obtained results for z_{MOS} are shown in figure 7.12.

Note that for a photon energy of 705 eV / Fe-Lα and double register storage, no best fit profile was found. The simulated absorption at the MOS–gates was slightly smaller than in the measurements even if z_{MOS} was increased beyond 4.5 µm. Measurements of z_{MOS} become imprecise at this photon energy since they rely on an intensity measurement. Nearly all (94%) of the incident Fe-Lα photons are absorbed in the expected thickness of 3 µm insensitive silicon below the MOS–gates. Therefore, changes of z_{MOS} cause only small changes of the measured intensity which is already close to zero. Statistical variations of the count map values can thus prevent a successful modeling of the observed count map profile. In the case of single register storage, the mesh position reconstruction was difficult at energies below 1775 eV due to the small number of split events. This resulted in an error of the mesh offset which is visible in the plots for energies of 705 eV, 930 eV and 1487 eV in figure 7.11.

storage mode	energy range	number of results for z_{MOS}	$z_{\mathrm{p+}}$	z_{MOS}	variance / σ of z_{MOS}
1 register	705 eV – 4510 eV	5	0.4 µm	3.6 µm	0.38 µm
2 registers	930 eV – 4510 eV	4	0.4 µm	3.2 µm	0.24 µm
2 registers	930 eV – 4510 eV	4	0.3 µm	2.9 µm	0.15 µm

Table 7.3: *Best fit results for the values of z_{MOS} and $z_{\mathrm{p+}}$ in the absorption model. The value of $z_{\mathrm{p+}}$ was adjusted such that the variance σ of z_{MOS} is minimized. In the case of double register storage, no best fit result was found for a photon energy of 705 eV (Fe-Lα).*

The results for z_{MOS} are listed in table 7.3. For the case of double register storage, two results for different values of $z_{\mathrm{p+}}$ are listed. The results show that mean value of z_{MOS} depends on the storage mode and on the assumed value for $z_{\mathrm{p+}}$. The values for the thickness of the undepleted p+ register implants were chosen in order to minimize the variance $\sigma(z_{\mathrm{MOS}})$ of the results for z_{MOS}. For double register storage, values of both 0.3 µm and 0.4 µm resulted in a variance $\sigma(z_{\mathrm{MOS}})$ of less than 1/4 µm, compare figure 7.12. Since

the result for z_{MOS} depends on the value of $z_{\mathrm{p+}}$, the knowledge of the value of $z_{\mathrm{p+}}$ is a limiting factor for the measurement accuracy of z_{MOS}. The analysis which is presented here thus requires an assumption of the insensitive depth in the register contacts which is based on the performed device simulations.

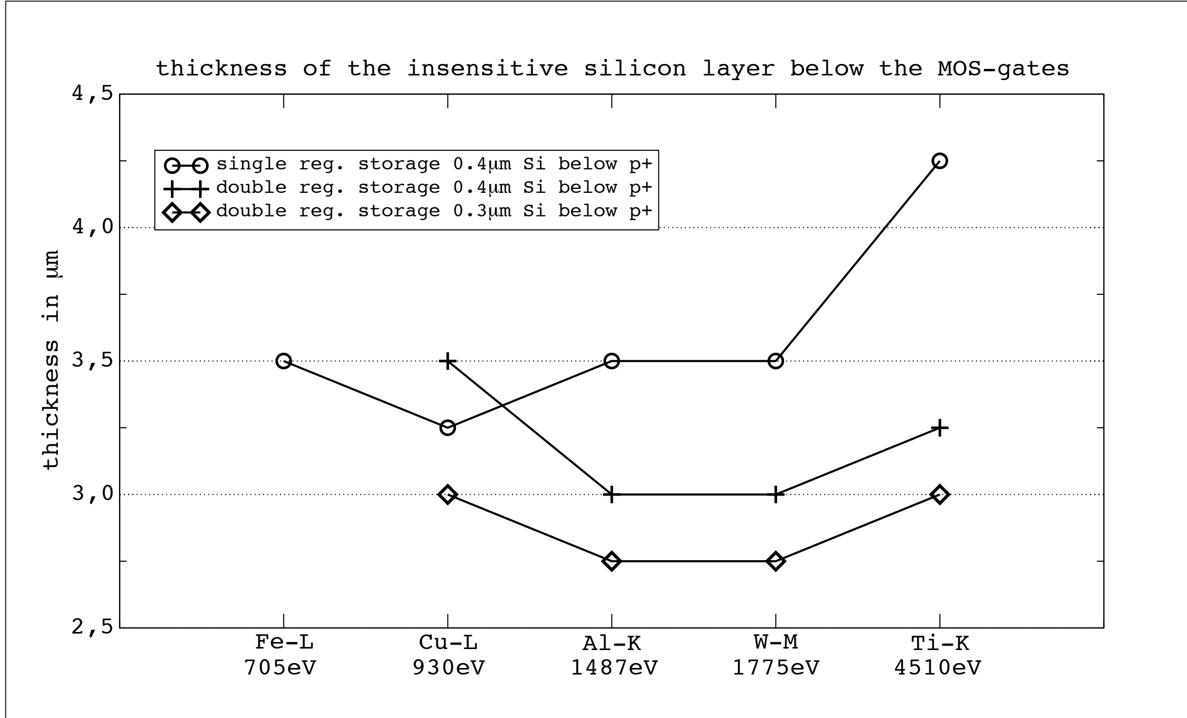

Figure 7.12: *Fit results for the insensitive silicon layer thickness below the MOS–gates. Results for both single and double register storage are shown. For double register storage a second set of values obtained with a different thickness of the undepleted layer below the p+ contacts is shown.*

The realized overall accuracy of better than 0.5 µm is sufficient to detect the dependency of z_{MOS} on the storage mode. Changing the storage mode from double to single register storage lowers the average voltage of the registers from -17 V to -19 V. The resulting increase of z_{MOS} is also observed in the device simulations shown in figure 7.8. A stronger effect which is predicted by the device simulations is the change of z_{MOS} with the potential $V_{\mathrm{el.layer}}$ of the electron layer below the MOS–gates. For $V_{\mathrm{el.layer}} = 0\,\mathrm{V}$, the simulations predict a value of $z_{\mathrm{MOS}} = 3.8$ µm (double register storage) and $z_{\mathrm{MOS}} = 4.2$ µm (single register storage). For $V_{\mathrm{el.layer}} = -8\,\mathrm{V}$, values of $z_{\mathrm{MOS}} = 2.5$ µm (double register storage) and $z_{\mathrm{MOS}} = 3.0$ µm (single register storage) are expected.

These values can be compared with the results of the absorption model fits (table 7.3) in order to find the value of V_{oxide}. The results for z_{MOS} obtained here suggest a value of $V_{\mathrm{el.layer}}$ which is between -3 V and -6 V. More measurements which facilitate a rigorous evaluation of the applied absorption model and the simulation model for the pixel shift are required in order to find a more precise result for $V_{\mathrm{el.layer}}$. The analysis presented here leads

to the conclusion that the electron layer is at a negative potential $V_{\mathrm{el.layer}}$ between -3 V and -8 V. The existence of an insensitive region below the MOS–gates is verified and measured with an accuracy of better than 0.5 µm. The measured thickness of the insensitive silicon layer is (3.2 ± 0.5) µm which is in agreement with the values of z_{MOS} that are predicted by numerical device simulations of the studied 75 µm pixel pnCCD.

Conclusion

This thesis draws its motivation from the need for an analysis method which characterizes the X–ray imaging properties of pnCCDs. In order to understand the physical mechanisms which are involved in the steps from the generation of signal charges to the finally measured pixel signal values, three aims were stated:

→ Establishment of a physical model for the signal charge cloud dynamics in fully depleted semiconductor detectors.

→ Development of a technique for the precise characterization of the imaging properties of a pixelized detector system.

→ Creation of an analytical tool for the detection and quantitative analysis of insensitive regions in the detector volume.

The work which was performed in order to accomplish these aims resulted in a physical model of the pnCCD which explains both the dynamics of signal electron clouds and the electric potential inside of the device. Two types of quantitative measurements and numerical device simulations provided the data which are required for the creation of this model:

→ The measurement of the amount of signal charge which is collected in a pixel as a function of the photon conversion position. This measurement is used to determine the size of a signal electron cloud in the moment when it is collected in the potential minima of the pixel structure.

→ The measurement of the detection efficiency as a function of the photon conversion position. Maps of the photon detection efficiency in a pixel as a function of the photon energy deliver the exact location and size of insensitive regions in the detector.

→ Numerical device simulations of the electric potential in a pnCCD and, in a second step, of the diffusion and drift of signal electrons in the depleted device volume. Comparisons of the simulations with the measurement data were used in order to evaluate the correctness of the physical device model.

It turns out that the imaging properties of a pnCCD are characterized by the size of a charge cloud when it is collected in a given pixel structure and by the electronic noise. Therefore, a model of the charge cloud dynamics as a function of (a) the electron mobility, (b) the photon energy, (c) the device temperature, and (d) the electric field strength was created. The validity of this model is illustrated by the accuracy of the numerical simulations when compared to the measurement results. Applications of pnCCDs benefit from the improved position reconstruction method which is based on measurements of the charge cloud size.

The achievements of this thesis are of value for both the user and the designer of pnCCDs and for the users of other pixelized solid state X–ray detectors:

→ The absolute size of a signal electron cloud after its drift from the photon conversion position to the pixel structure is predicted with an accuracy of 10%.

→ The conversion position of X–ray photons can be reconstructed with a precision of 1 µm in the case of a pixel size of 36 µm, an energy of 5 keV, and an electronic noise of 3 electrons ENC. The imaging properties which determine the parameters of the reconstruction algorithm can be directly measured with the experimental analysis developed in this thesis. This analysis and the associated position reconstruction method can be applied to any other X–ray detector with a rectangular pixel array.

→ Insensitive regions with a thickness of 3.2 µm a width of 5 µm and a length of 10 mm could be identified. The total volume of these insensitive regions corresponds to only 0.23% of the total device volume. This method can be applied to any other pixelized X–ray detector for the identification of insensitive regions.

The physical model of pnCCDs which is presented in this thesis permits to fully exploit the advantages of this detector. The high readout speed, good energy resolution close to the Fano limit, and the high sensitivity up to an energy of 20 keV are now combined with a position resolution in the order of 1 µm.

List of Figures

1.1 Energy levels in a pn-junction . . . 6
1.2 The sources of leakage current in a pn–junction . . . 8
1.3 Physical states of a MOS–capacitor . . . 9
1.4 Si–SiO_2 interface charge density and Voltage drop in a nMOS–structure . . . 11
1.5 Oxide charge in a MOS–capacitor . . . 13
1.6 Signal charge generation and collection in a fully depleted detector . . . 15
1.7 Clocking scheme of 3 phase CCD . . . 17
1.8 Principle of a p–channel MOS–CCD . . . 18
1.9 Sidewards depletion of double sided diode structures . . . 20
1.10 Electric potential in bulk of depleted silicon . . . 20
1.11 Principle of the pnCCD . . . 22
1.12 Principle of a pnCCD array . . . 23
1.13 Signal charge collection in a pnCCD . . . 24
1.14 Block diagram of a CAMEX channel . . . 25
1.15 The pnCCD for the eROSITA instrument . . . 27
1.16 The instrument concept of eROSITA . . . 27
1.17 XMM–type pnCCDs with CAMEX and TIMEX . . . 28
1.18 Closeup view of a 128 channel CAMEX ASIC . . . 28
1.19 framestore–pnCCD with 132 channel CAMEX ASIC . . . 28

2.1 end of pixel column with first amplifier stage . . . 32
2.2 end of pixel column, aluminum layers removed . . . 33
2.3 end of pixel column, channel guides and –stops . . . 33
2.4 single– and double register storage . . . 34
2.5 Bulk silicon with epi–layer . . . 37
2.6 Electric potential in n–doped silicon with an additional epi–layer . . . 39
2.7 Variation of the potential maximum with the back contact voltage . . . 39

3.1 Principle of the mesh experiment . . . 46
3.2 Example of a hole coverage map . . . 46
3.3 Radial intensity profiles with Fresnel diffraction at a circular aperture . . . 48
3.4 Topologies of valid X-ray event patterns . . . 49
3.5 Moiré patterns from mesh measurements with a 150µm pixel pnCCD . . . 50

3.6 Vector description of vertical moiré lines 52
3.7 Vector description of horizontal moiré lines 52
3.8 Detail of moiré pattern geometry 53
3.9 Moiré pattern: alignment angle of the mesh 54
3.10 How to find the offset of the mesh 55
3.11 Coverage map of real measurement with 150µm pixel pnCCD 56
3.12 Generation of reconstructed pixel maps 57
3.13 Interpolation of an irregular pixel map 58

4.1 Sketch of setup with detector and X-ray tube 62
4.2 View of the Rösti test facility 66
4.3 Measurement chamber and power supply rack 66
4.4 Vacuum flange with cooling mask and circuit boards 66
4.5 Inside of the measurement center 67
4.6 Cooling mask with V10 pnCCD and mesh holder 67
4.7 V9 pnCCD with mesh assembly 68
4.8 Reversed V10 pnCCD for front side illumination in cooling mask with cutouts 68
4.9 Copper frame and mesh holder for cooling mask of V10 and V11 pnCCDs . 68
4.10 Noise map of a frame 74
4.11 Offset map of a frame 74
4.12 Map of an uncorrected signal frame 74
4.13 Single pixel event 76
4.14 Double pixel event 76
4.15 Triple pixel event 76
4.16 Quadruple pixel event 76
4.17 Invalid triple pixel event 76
4.18 Invalid quad pixel event 76
4.19 Row scatter plot of a spectrum 77
4.20 Corrected Ti-Kα spectrum with pnCCD C10_19_01 79
4.21 Event count map of a measurement flat field illumination 80
4.22 Event count map of a measurement with illumination through the mesh . . 80

5.1 3x3 tiled single event map 82
5.2 3x3 tiled double event map 83
5.3 3x3 tiled triple event map 84
5.4 3x3 tiled quad event map 85
5.5 3x3 tiled event count map 86
5.6 Charge map for an area of 3x3 pixels 87
5.7 Explanation of the meaning of charge map values 87
5.8 Surface plot of the charge map 88
5.9 Cut through the charge map along the charge transfer direction 88
5.10 Estimation of the maximum position error 91
5.11 Difference of simulation data and fit model for a 75µm pixel pnCCD 93

5.12 Difference of simulation data and fit model for a 51µm pixel pnCCD 93
5.13 Influence of the signal threshold on the single map 94
5.14 Ti-Kα event maps of the 150µm pixel XMM–type pnCCD 96
5.15 Ti-Kα event maps of the 75µm pixel frame store pnCCD 97
5.16 Ti-Kα event maps of the 51µm pixel frame store pnCCD 98
5.17 Ti-Kα event maps of the 150 µm pixel XMM–type pnCCD 100
5.18 Count map and y–profile of a measurement with a 150µm pixel pnCCD . . 102
5.19 Count map and y–profile of a measurement with a 75µm pixel pnCCD . . 102
5.20 Count map and y–profile of a measurement with a 51µm pixel pnCCD . . 102
5.21 Rejecting X–ray events due to pattern pileup 103
5.22 Count maps of a 75µm pixel pnCCD reconstructed from data with front side illumination 104
5.23 Cut through a pnCCD pixel along the charge transfer direction 105
5.24 Difference between fit and reconstruction of the charge collection function of a 150 µm pixel pnCCD with double register storage 107
5.25 Difference between fit and reconstruction of the charge collection function of a 75 µm pixel pnCCD with double register storage 107
5.26 Difference between fit and reconstruction of the charge collection function of a 75 µm pixel pnCCD with single register storage 107
5.27 Difference between fit and reconstruction of the charge collection function of a 51 µm pixel pnCCD with single register storage 107
5.28 Difference between fit and reconstruction of the charge collection function of a 150 µm pixel pnCCD with single register storage 110
5.29 Difference between fit and reconstruction of the charge collection function of a 75 µm pixel pnCCD with single register storage and front side illumination 110

6.1 Bulk silicon with epi–layer 115
6.2 Simulation region in channel direction 116
6.3 Simulation region in line direction 116
6.4 Boundary conditions for device simulation 117
6.5 Bulk potential in 75 µm pixel pnCCD 118
6.6 Detail of bulk potential close to register side 118
6.7 Potential below two storage registers in a 75 µm pixel pnCCD 120
6.8 Potential below a storage register in a 75 µm pixel pnCCD 120
6.9 Potential below a barrier register in a 75 µm pixel pnCCD 120
6.10 Potential below two barrier registers in a 75 µm pixel pnCCD 120
6.11 Electric potential below a MOS–gate in a 75 µm pixel pnCCD 121
6.12 Contour plot of the electric potential below a MOS–gate 121
6.13 Asymmetric potential below a MOS–gate in a 75 µm pixel pnCCD 122
6.14 Contour plot of the asymmetric potential below a MOS–gate 122
6.15 Bulk potential in a simulation of a cut in line direction 123
6.16 Bulk potential below a channel stop and channel guide 123
6.17 Potential below a channel guide in a 75 µm pixel pnCCD 124

6.18 Potential below the channel stop in a 75 µm pixel pnCCD 124
6.19 Different approaches to the simulation of signal charge drift and collection 125
6.20 Configuration of a series of device simulations to model the charge collection function 127
6.21 Lateral electric potential in a 75 µm pixel pnCCD in line and transfer direction 129
6.22 Lateral electric potential in a 75 µm pixel pnCCD in line and transfer direction in a depth of 70 µm 130
6.23 Lateral electric potential in a 51 µm pixel pnCCD in line and transfer direction 131
6.24 Lateral electric potential in a 51 µm pixel pnCCD in line and transfer direction in a depth of 50 µm 131
6.25 Electron drift velocity in the bulk of a pnCCD with 280 µm thickness and a pnCCD with 450 µm thickness 132
6.26 Cylindrical region for simulations of the charge cloud expansion for different amounts of signal electrons 133
6.27 Radial profiles of electron clouds after given times after their generation . . 134

7.1 Measured and simulated ccf profiles for a 75 µm pixel pnCCD 142
7.2 Plots of the differences between measured and simulated ccfs for all simulations of a 75 µm pixel pnCCD 143
7.3 Measured and simulated ccf profiles for a 51 µm pixel pnCCD 145
7.4 Plots of the differences between measured and simulated ccfs for all simulations of a 51 µm pixel pnCCD 146
7.5 Separation of a charge cloud close to the register structure in a 75 µm pixel pnCCD 150
7.6 Separation of a charge cloud close to the register structure in a 51 µm pixel pnCCD 151
7.7 Contour line plots of the electric potential below the MOS–gates 154
7.8 Electric potential to a depth of 5 µm below the middle of the MOS–gates . 155
7.9 Principle of the simulation of X–ray photon absorption in the register structure 156
7.10 Count profile measurements and simulations of the front side illuminated 75 µm pixel CCD with double register storage 157
7.11 Count profile measurements and simulations of the front side illuminated 75 µm pixel CCD with single register storage 158
7.12 Best fit results for the thickness of the insensitive silicon layer below the MOS–gates in both single– and double register storage mode 160

Bibliography

[1] L. Strüder, H. Bräuniger, et al. A 36 cm^2 large monolithic pn-charge-coupled device x-ray detector for the European XMM satellite mission. *Rev. Sci. Instrum.*, 68:4271, 1997.

[2] H. Tsunemi, K. Yoshita, and S. Kitamoto. New technique of the X-ray efficiency measurement of a Charge-Coupled Device with a subpixel resolution. *Jpn. J. Appl. Phys.*, 36:2906, 1997.

[3] Gerhard Lutz. *Semiconductor radiation detectors, device physics.* Springer Verlag, Berlin, Heidelberg, 2001.

[4] Sima Dimitrijev. *Understanding semiconductor devices.* Oxford University Press, New York / Oxford, 2000.

[5] S. M. Sze. *Physics of semiconductor devices.* John Wiley & Sons, New York, 1981.

[6] E. H. Nicollian and J. R. Brews. *MOS (metal oxide semiconductor) physics and technology.* John Wiley & Sons, New York, 1982.

[7] H. He, T. Zhang, R. Shang, and S. Xu. A detailed study of the interaction mechanisms for Si(li) detector response functions by the direct Monte Carlo approach. *Nucl. Instr. and Meth. A*, 272:847–854, 1988.

[8] William R. Leo. *Techiques for nuclear and particle physics experiments, a how–to approach.* Springer Verlag, Berlin / Heidelberg / New York, 1994.

[9] Peter Lechner. *Zur Ionisationsstatistik in Silicium.* PhD thesis, Technische Universität München, 1998.

[10] S. M. Seltzer and J. H. Hubbell. Tables and graphs of photon mass attenuation coefficient and mass energy-absorption coefficients for photon energies 1 keV to 20 MeV for elements Z = 1 to 92 and some dosimetric materials. Presented at the 51st National Meeting of the Japanese Society of Radiological Technology, April 14-16, 1995.

[11] W. S. Boyle and G. E. Smith. Charge coupled semiconductor devices. *Bell Syst. Tech. J.*, 49:587, 1970.

[12] E. Gatti and P. Rehak. Semiconductor Drift Chamber – an application of a novel charge transport scheme. *Nucl. Instr. and Meth. A*, 225:608–614, 1984.

[13] L. Strüder et al. The MPI/AIT X-ray imager – high speed pn CCDs for X-ray detection. *Nucl. Instr. and Meth. A*, 288:227–235, 1990.

[14] E. Pinotti et al. The pn-CCD on-chip electronics. *Nucl. Instr. and Meth. A*, 326:85–91, 1993.

[15] W. Buttler, G.Lutz, H. Bergmann, H. Dietl, D. Hauff, P. Holl, and P. F. Manfredi. Low noise-low power monolithic multiplexing readout electronics for silicon strip detectors. *Nucl. Instr. and Meth. A*, 273:778–783, 1988.

[16] S. Herrmann, W. Buttler, R. Hartmann, P. Holl, N. Meidinger, and L. Strüder. Mixed signal pnCCD readout ASIC for the future X–ray astronomy mission eROSITA. *Nucl. Sci. Symp. 2007 Conference Record*, 3:2398–2403, 2008.

[17] R. Hartmann, H. Gorke, N. Meidinger, H. Soltau, and L. Strüder. Results of a fast pnCCD detector system. *Proc. SPIE 5903*, Astronomical Adaptive Optics Systems and Applications II:59030N–1 – N–9, 2005.

[18] R. Hartmann, W. Buttler, H. Gorke, S. Herrmann, P. Holl, N. Meidinger, H. Soltau, and L. Strüder. A high speed pnCCD detector system for optical applications. *Nucl. Instr. and Meth. A*, 568:118–123, 2006.

[19] N. Meidinger et al. Fast large–area spectroscopic and imaging CCD detectors for X–ray astronomy with eROSITA and for exploration of the nanocosmos. *Proc. SPIE 6686*, UV, X–ray, and Gamma–Ray Space Instrumentation for Astronomy XV:66860H–1 – H–10, 2007.

[20] P. Predehl et al. eROSITA. *Proc. SPIE 6266*, Space Telescopes and Instrumentation II: Ultraviolet to Gamma Ray:62660P–1 – P–10, 2006.

[21] M. Pavlinski, G. Hasinger, et al. Spectrum–RG/eROSITA/Lobster astrophysical mission. *Proc. SPIE 6266*, Space Telescopes and Instrumentation II: Ultraviolet to Gamma Ray:62660O–1 – O–11, 2006.

[22] A. Müller and G. Hasinger. Evolution of supermassive black holes. arXiv:0708.0942v1 [astro-ph], 2007.

[23] Henry N. Chapman et al. Femtosecond time–delay X–ray holography. *Nature*, 448:676–679, 2007.

[24] Siegfried Selberherr. *Analysis and simulation of semiconductor devices*. Springer Verlag, Wien / New York, 1984.

[25] C. Canali, C. Jacoboni, F. Nava, G. Ottaviani, and A. Alberigi-Quaranta. Electron drift velocity in silicon. *Phys. Rev. B*, 12(4):2265–2284, 1975.

[26] C. Jacoboni, C. Canali, G. Ottaviani, and A. Alberigi-Quaranta. A review of some charge transport properties of silicon. *Solid State El.*, 20:77–89, 1977.

[27] S. F. Liotta and A. Majorana. High field mobility and diffusivity of electron gas in silicon devices. *ArXiv Condensed Matter e-prints*, 2000.

[28] N. D. Arora, J. R. Hauser, and D. J. Roulston. Electron and hole mobilities in silicon as a function of concentration and temperature. *IEEE Trans. Electron Devices*, ED-29:292–295, 1982.

[29] E. Gatti, A. Longoni, P. Rehak, and M. Sampietro. Dynamics of electrons in drift detectors. *Nucl. Instr. and Meth. A*, 253:393–399, 1987.

[30] H. Tsunemi, J. Hiraga, K. Yoshita, and S. Kitamoto. Where are the X-ray event grades formed inside the pixel of the Charge-Coupled Device? The behaviour of the primary charge cloud inside the Charge-Coupled Device. *Jpn. J. Appl. Phys.*, 37:2734, 1998.

[31] H. Tsunemi, K. Yoshita, A. D. Short, P. J. Bennie, M. J. L. Turner, and A. F. Abbey. X-ray measurement of the subpixel structure of the XMM EPIC MOS CCD. *Nucl. Instr. and Meth. A*, 437:359, 1999.

[32] Heinz Niedrig, editor. *Bergmann • Schaefer, Lehrbuch d. Experimentalphysik, Optik*. Walter de Gruyter, Berlin / New York, 1993.

[33] B. L. Henke, E.M. Gullikson, and J.C. Davis. X-ray interactions: photoabsorption, scattering, transmission, and reflection at E=50-30000 eV, Z=1-92. *Atomic Data and Nuclear Data Tables*, 54:no. 2, 181–342, 1993.

[34] B. L. Henke, E. M. Gullikson, and J. C. Davis. X-ray interactions with matter. http://www-cxro.lbl.gov/optical_constants/, 2007.

[35] K. D. Mielenz. Numerical evaluation of diffraction integrals. *J. Res. Natl. Inst. Stand. Technol.*, 105:581, 2000.

[36] K. Yoshita, H. Tsunemi, K. C. Gendreau, G. Pennington, and M. W. Bautz. Direct measurements at the sub-pixel level of the X-ray detection efficiency of the CCD on board the ASCA satellite. *IEEE Trans. Nucl. Sci.*, 45:915, 1998.

[37] H. Tsunemi, J. Hiraga, K. Mori, K. Yoshita, and E. Miyata. Diagnostics of the CCD using the mesh experiment. *Nucl. Instr. and Meth. A*, 436:32, 1999.

[38] Junko Hiraga. *Diagnostics of the X-ray CCD with subpixel resolution*. PhD thesis, Osaka University, 2002.

[39] K. Yoshita, H. Tsunemi, K. C. Gendreau, and M. W. Bautz. Improvement of the position resolution of the CCD for X-ray use. *IEEE Trans. Nucl. Sci.*, 46:100, 1999.

[40] Siegmund Brandt. *Datenanalyse, mit statistischen Methoden und Computerprogrammen*. BI–Wissenschafts–Verlag, Mannhein / Leipzig / Wien / Zürich, 1992.

[41] G. W. Fraser, A. F. Abbey, A. Holland, K. McCarthy, A. Owens, and A. Wells. The X–ray energy response of silicon Part A. Theory. *Nucl. Instr. and Meth. A*, 350:368–378, 1994.

[42] D. R. Lide and H. P. R. Frederikse, editors. *CRC handbook of chemistry and physics*. CRC Press, Boca Raton / NewYork, 1997.

[43] H. Bräuninger et al. First results with the pn–CCD detector system for the XMM satellite misssion. *Nucl. Instr. and Meth. A*, 326:129–135, 1993.

[44] Martin Popp. *Untersuchung und analytische Modellierung der Systemantwort von pn–CCD Detektoren*. PhD thesis, Ludwig–Maximilians–Universität München, 2000.

[45] U. G. Briel et al. Calibration and preliminary results on the performance of the XMM EPIC PN flight camera: imaging modes. *Proc. SPIE Vol. 3445, p. 38-49, EUV, X-Ray, and Gamma-Ray Instrumentation for Astronomy IX, Oswald H. Siegmund; Mark A. Gummin; Eds.*, pages 38–49, November 1998.

[46] K. Dennerl, U. G. Briel, F. Haberl, G. D. Hartner, N. Krause, M. Popp, and V. E. Zavlin. Determination and correction of the charge transfer efficiency of the pn-CCD camera. *Proc. SPIE Vol. 3765, p. 232-243, EUV, X-Ray, and Gamma-Ray Instrumentation for Astronomy X, Oswald H. Siegmund; Kathryn A. Flanagan; Eds.*, pages 232–243, October 1999.

[47] J. Englhauser. HLL–SAS: standard analysis software for pnCCD data. Private communication, MPI semiconductor lab, 2004.

[48] R. Andritschke and G. Hartner. New version of the standard analysis software. Private communication, MPI semiconductor lab, 2005.

[49] Norbert Meidinger. *Strahlenhärte von Röntgen–Sperrschicht–CCD-Detektoren*. PhD thesis, Technische Universität München, 2003.

[50] P. Holl. PixelMC, a Monte–Carlo simulation of pnCCDs. Private communication, MPI semiconductor lab, 2005.

[51] N. Kimmel, R. Hartmann, P. Holl, N. Meidinger, and L.Strüder. Reconstruction method for the charge collection function of pnCCDs using data obtained with the mesh experiment. *Nucl. Instr. and Meth. A*, 569:134–140, 2006.

[52] H. Gajewski, B. Heinemann, H. Langmach, R. Nuernberg, G. Telschow, and K. Zacharias. WIAS–TeSCA Handbuch. TeSCA software package, 1996.

[53] M. Pivovaroff, S. Jones, M. Bautz, S. Kissel, G. Prighozin, G. Ricker, H. Tsunemi, and E. Miyata. Measurement of the subpixel structure of AXAF CCDs. *IEEE Trans. Nucl. Sci.*, 45:164, 1998.

Danksagung

An dieser Stelle möchte ich mich bei all denen herzlich bedanken, die zum Gelingen dieser Arbeit beigetragen haben:

Herr Prof. Dr. Strüder hat mir die erst Möglichkeit gegeben, diese Arbeit am Halbleiterlabor durchzuführen. Er war jederzeit ein Ansprechpartner für konstruktive Disskussionen und hat diese Arbeit unterstützt, wie ich es mir nicht besser wünschen konnte.

Herr Dr. Norbert Meidinger war mein „Zweitbetreuer" und mit seinem besonderen Interesse am Thema stets ein hervorragender Diskussionspartner. Er hat mich in die Bedienung aller pnCCD–relevanten Hardware eingeführt, alle möglichen und unmöglichen Fragen beantwortet und auch sonst bestens unterstützt.

Bei Herrn Prof. Dr. Ullrich Pietsch möchte ich mich für seine Arbeit als zweiter Gutachter und für die Einladungen zu den Vorträgen an der Universität Siegen bedanken.

Herr Robert Hartmann hatte als Hardware– und pnCCD–Spezialist auf alle technischen Fragen eine Antwort parat. Mein besonderer Dank gilt für seine stets wirkungsvolle und schnelle Hilfe an den Laboraufbauten.

Herr Rainer Richter führte mich in die Verwendung der Simulationssoftware „TeSCA" ein und erweiterte mein Wissen über Halbleiterbauelemente in zahlreichen Gesprächen.

Herr Dr. Gerhard Lutz hat sich stets Zeit genommen, um Fragen zu den physikalischen Grundlagen des Ladungstransports in Silizium zu beantworten. Insbesondere möchte ich mich für die gemeinsamen Diskussionen zur Interpretation der Simulationsergebnisse bedanken.

Bei der Firma PNSensor und stellvertretend Frau Dr. Heike Soltau möchte ich mich für einen Teil der Förderungsdauer bedanken.

Der Technologie und stellvertretend Herrn Dr. Florian Schopper danke ich für die Herstellung der pnCCDs, ohne die es diese Doktorarbeit nicht gäbe.

Herr Danilo Miessner baute in der Montagetechnik alle pnCCDs auf, so daß ich damit auch die Messungen für diese Arbeit durchführen konnte.

Herrn Olaf Hälker und Herrn Sven Herrmann danke ich für die Anfertigung der elektronischen Komponenten für den Meßaufbau und die Beantwortung aller Fragen zur Funktion der Ausleseelektronik.

Herrn Dr. Robert Andritschke danke ich für seine Arbeit als aufmerksamer Korrekturleser.

Meinen Kolleginnen und Kollegen aus der Diplomanden– und Doktorandengruppe, stellvertretend davon Gabi Schächner, Thomas Lauf, Stefan Rummel und Stefan Wölfel danke ich für die schöne Zeit und die Hilfe bei den kleinen Problemen im Doktorandenalltag.

Herr Admir Ramic und Herr Peter Holl hielten stets Rechner und Netzwerk instand, ohne die heute in der Wissenschaft nichts mehr möglich ist.

In der Hoffnung, niemanden vergessen zu haben, möchte ich mich bei allen Leuten im Halbleiterlabor für die freundliche und kooperative Arbeitsatmosphäre bedanken.

Zum Schluss gilt mein Dank natürlich der Unterstützung meiner Eltern und meiner Familie, die mein Interesse an der Physik über all die Jahre stets gefördert haben.